

PREPARATION OF PIGMENTS FOR SPACE-STABLE THERMAL CONTROL COATINGS

June 1, 1968 through March 31, 1972

Contract No. NAS8-21317

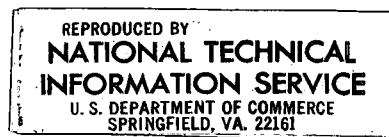
Funded Under Code 124-09-18-1200-25-9-004-028-2510

Prepared by

W. B. Campbell
R. G. Smith

of

The Ohio State University
Research Foundation
Columbus, Ohio



to

NATIONAL AERONAUTICS AND SPACE ADMINISTRATION

George C. Marshall Space Flight Center
Marshall Space Flight Center, Alabama

May 1972

(NASA-CR-124067) PREPARATION OF PIGMENTS
FOR SPACE-STABLE THERMAL CONTROL COATINGS
Final Report, 1 Jun. 1968 - 31 Mar. 1972
(Ohio State Univ. Research Foundation)

188 p HC

N73-18144

Unclas
16854

CSCIL 07A

G3/06

PREPARATION OF PIGMENTS FOR SPACE-STABLE THERMAL CONTROL COATINGS

June 1, 1968 through March 31, 1972

Contract No. NAS8-21317

Funded Under Code 124-09-18-1200-25-9-004-028-2510

Prepared by

W. B. Campbell

R. G. Smith

of

The Ohio State University
Research Foundation
Columbus, Ohio

**Details of illustrations in
this document may be better
studied on microfiche**

to

NATIONAL AERONAUTICS AND SPACE ADMINISTRATION

George C. Marshall Space Flight Center
Marshall Space Flight Center, Alabama

May 1972

ABSTRACT

The identification and control of vapor phase reaction kinetics to produce pigments by homogeneous nucleation have been achieved. A vapor phase apparatus has been designed, fabricated, and calibrated through 1800°C. Vapor phase reactions have been analyzed, calculations have been made, and powders of alumina, rutile, zinc orthotitanate (in a mixed phase) calcium tungstate, and lanthana have been produced by homogeneous nucleation. Electron microscopy shows uniform particle morphology and size and supports anticipated advantages of vapor-phase homogeneous nucleation; namely, purity, freedom from defects, and uniform particle sizing without grinding.

descriptors:

Thermal control space-stable pigments, Vapor phase, Nucleation, Alumina, Rutile, Zinc Orthotitanate, Lanthana, Calcium Tungstate, Ceramics, Gas Mixing

FOREWORD

This report was prepared by The Ohio State University Research Foundation, under NASA Contract No. NAS8-21317, entitled, "Preparation of Pigments for Space-Stable Thermal Control Coatings," This reports covers the period from June 1, 1968 through March 31, 1972.

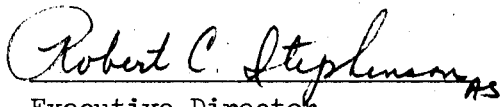
Dr. William B. Campbell was the principal investigator for this program. He was ably assisted by R. G. Smith, J. K. Cochran, J. W. Hinton, S. G. Nychas, J. E. Seaver, J. W. Randall, R. J. Versic and J. E. Burroughs. Full or partial support from this program provided the means for R. G. Smith, J. K. Cochran, J. W. Hinton, S. G. Nychas and R. J. Versic to fulfill the requirements for the Doctor of Philosophy degree. The Master of Science degree was received by J. W. Randall.

This work was performed under the Space Sciences Laboratory of the George C. Marshall Space Flight Center. Mr. Daniel W. Gates was the Contracting Officer's Technical Representative and the Project Manager.

Respectfully submitted
OSU Research Foundation

William B. Campbell, Ph.D.
Associate Professor

Approved:


Executive Director
OSU Research Foundation

SUMMARY

The development of vapor phase technology in the preparation of space-stable pigments has been demonstrated by the production of very fine powders with discrete morphology and an average particle size in the range of 0.35 to 2.5 μ .

The critical parameters for the controlled production of rutile and alumina have been used as the basis for the development of mono-sized particles of zinc orthotitanate. Zinc orthotitanate (Zn_2TiO_4) has been found to be one of the better space-stable pigments for use in thermal-control paints of low α and low α/ϵ ratio (solar absorptance and infrared emittance). Because of these stringent requirements, the development of vapor phase reactions to produce calcium tungstate and lanthana by homogeneous nucleation was included in this program.

Vapor phase apparatus has been designed, fabricated, and calibrated. Vapor phase reactions have been analyzed, calculations have been made, and powders of alumina, rutile, zinc orthotitanate (in a mixed phase), calcium tungstate and lanthana have been produced by homogeneous nucleation. Submicron size particles required for efficient scattering of solar radiation in the 0.35 to 2.5 μ wavelength range have been produced. Excellent sub-angular morphology was exhibited in the electron photomicrographs.

TABLE OF CONTENTS

<u>Section</u>	<u>Page</u>
I INTRODUCTION	1
A. Program Objective	2
B. Survey of Literature	3
1. Pigment Properties for Thermal Control of Space Vehicles	3
2. Phase Equilibrium in the ZnO-TiO ₂ System	4
3. Vapor Phase Powder Technology Departments	6
II PRINCIPLES OF VAPOR PHASE POWDER PRODUCTION	7
A. Thermodynamics of Aluminum Oxide (Al ₂ O ₃) Reaction	7
B. Thermodynamics of Titanium Dioxide (TiO ₂) Reaction	7
C. Thermodynamics of Zinc Orthotitanate Reactions	10
D. Thermodynamics of Calcium Tungstate (CaWO ₄) Reactions	14
E. Thermodynamics of Lanthanum Oxide (La ₂ O ₃) Reactions	24
F. Reactor Design, Mixing and Heat Transfer	33
1. Thermodynamic and Transport Properties	33
2. Reactor Gas Mixing	41
3. Reactor Mixing for Zn ₂ TiO ₄	60
III EXPERIMENTAL PROCEDURE	67
1. Reactor	67
2. Powder-Gas Separation	70
3. Gas Scrubbers	83
4. Chlorinator	85
5. Gas Temperature Measurement	89
6. Gas Flow Control	89
7. Operation Procedure for Vapor Phase Runs	94
IV EXPERIMENTAL RESULTS	95
A. Aluminum Oxide (Al ₂ O ₃) Production and Characterization	95
1. Aluminum Oxide Production	95
2. Aluminum Oxide Characterization	95

TABLE OF CONTENTS - (Continued)

<u>Section</u>	<u>Page</u>
B. Titanium Dioxide (TiO_2) Powder Production and Characterization	102
1. Titanium Dioxide Powder Production	102
2. Titanium Dioxide Powder Characterization	105
C. Zinc Orthotitanate (Zn_2TiO_4) Powder Production and Characterization	121
1. Using Zinc Metal as the Zinc Vapor Species	121
2. Using Zinc Chloride as the Zinc Vapor Species	125
D. Calcium Tungstate (CaWO_4) Powder	131
E. Lanthanum Oxide (La_2O_3) Powder	131
V CONCLUSIONS AND RECOMMENDATIONS	139
A. Conclusions	139
1. Aluminum Oxide Powder	139
2. Titanium Dioxide	139
3. Zinc Orthotitanate	139
4. Calcium Tungstate	140
5. Lanthanum Oxide	140
B. Recommendations	140
VI REFERENCES	141
APPENDIX A Free Energy Values Used in Thermodynamic Calculations	145
APPENDIX B Computer Program Source List for Calculation of Equilibrium Constants and Free Energy Values	149
APPENDIX C Computer Source List for Program	153
APPENDIX D Aluminum Oxide X-Ray Diffraction Patterns	165
APPENDIX E Titanium Dioxide X-Ray Diffraction Patterns	169
APPENDIX F Zinc Orthotitanate X-Ray Diffraction Patterns	173

LIST OF FIGURES

<u>Figure No.</u>		<u>Page</u>
1	System ZnO-TiO ₂ . Inset Shows Alternative Incongruent Melting of Zn ₂ TiO ₄	5
2	Equilibrium Concentrations of Zn ₂ TiO ₄ as a Function of System Conditions	15
3	Equilibrium Constant as a Function of Temperature for Zn ₂ TiO ₄ Formation	16
4	Vapor Pressure of CaCl ₂	20
5	Free Energies of WCl ₂ , WCl ₅ , and WCl ₆	21
6	Equilibrium Concentration of CaWO ₄	22
7	Equilibrium Constant as a Function of Temperature for CaWO ₄	23
8	Vapor Pressure of LaCl ₃ vs. Temperature	27
9	Equilibrium Concentration of La ₂ O ₃ as a Function of System Conditions	28
10	Equilibrium Constant as a Function of Temperature for La ₂ O ₃	29
11	Proposed Reactor Configuration	43
12	View A ¹ A ¹ of Figure 11	43
13	Geometry Used for Mixing Calculations	47
14	The Intensity and Scale of Segregation During Mixing	47
15	Preliminary Reactor Design. Mixing of Stream 2	49
16	Preliminary Reactor Design. Mixing of Stream 1	50
17	Geometry Nomenclature for Round Jet	52
18	Geometry for Round Jet	52
19	Velocity at the Center Line and Width Variation for Downstream of Central Jet	54

LIST OF FIGURES - (Continued)

<u>Figure No.</u>		<u>Page</u>
20	Peripheral Jets	56
21	Variation of Axial Turbulence Intensity Along the Jet Center Line with X	58
22	Geometry for Calculating Residence Time in Reactor	59
23	Mixing of Central Jet	61
24	Reactor Configuration for the Production of Zn_2TiO_4	62
25	Reactor Mixing Performance for Zn_2TiO_4 Production	66
26	Temperature Profile of Silicon Carbide Resistance- Heated Furnace	68
27	22-inch Molybdenum-Wound Furnace	69
28	Modified SiC Furnace Reactor	71
29	Modified Molybdenum-Wound Furnace	72
30	Temperature Profile of Molybdenum-Wound Furnace with Seven Inch Isothermal Zone	73
31	Molybdenum-heated Reactors with Pump and Flow Controls	74
32	Induction Furnace Reactor	75
33	Temperature Profile of Induction Furnace	76
34	Induction System	77
35	Characteristics of Particles and Particle Dispersoids	79
36	Sonic Agglomerator	81
37	Cyclone Collector	82
38	Typical Laboratory Scrubber	84
39	Double-Stage Chlorinator	86
40	Double-Stage Chlorinator	87

LIST OF FIGURES - (Continued)

<u>Figure No.</u>		<u>Page</u>
41	Apparatus for Chlorination Efficiency Determinations	88
42	Actual Temperature Inside Reaction Tube vs Temperature Outside Reaction Tube for Various Gas Flow Rates	90
43	Temperature Profile of Vapor Phase Reaction Furnace	91
44	Vapor Phase Apparatus	92
45	Gas Flow Control Panel	92
46	Vapor Phase System	93
47	Electron Photomicrograph of Alumina Powder, 67,200X	98
48	Electron Photomicrograph of Alumina Powder, 43,400X	99
49	Electron Photomicrograph of Alumina Powder, 92,000X	100
50	Electron Photomicrograph of Alumina Powder, 43,400X	101
51	Particle Size Probability Plot of Alumina Powders	103
52	Anatase Morphology in Titania Powders, 59,000X	107
53	Typical Micrograph of Rutile Powder, Run T-8, 40,000X	108
54	Typical Micrograph of Rutile Powder, Run T-6, 40,000X	109
55	Typical Micrograph of Rutile Powder, Run T-10, 40,000X	110
56	Typical Micrograph of Rutile Powder, Run T-11, 40,000X	111
57	Typical Particle Size Distributions of Rutile Powders	112
58	Effect of Temperature and Residence Time on Particle Size of Vapor-Grown Rutile	113
59	Volume Growth Rate versus Temperature for Titania Runs	114
60	Injector Modification for Rutile Studies	116
61	Typical Micrograph of Rutile Powder, Run T-24, 40,000X	117
62	Typical Micrograph of Rutile Powder, Run T-21, 40,000X	118

LIST OF FIGURES - (Continued)

<u>Figure No.</u>		<u>Page</u>
63	Typical Micrograph of Rutile Powder, Run T-25, 23,000X	119
64	Effect of Residence Time and Injector Length on Particle Size of Rutile	120
65	Zinc Evaporation Rate vs Temperature at 50 mmHg	123
66	Schematic of Powder Deposition Zones	124
67	Electron Photomicrograph, Run Zn_2TiO_4 -1, Zone 3, 40,000X	126
68	Electron Photomicrograph, Run Zn_2TiO_4 -1, Zone 3, 82,000X	127
69	Scanning Electron Micrograph, Sample ZOT-12, 500X	132
70	Scanning Electron Micrograph, Sample ZOT-12, 1000X	132
71	Scanning Electron Micrograph, Sample ZOT-12, 5000X	133
72	Scanning Electron Micrograph, Sample ZOT-12, 10,000X	133
73	Scanning Electron Micrograph, Sample CW-1, 1000X	134
74	Scanning Electron Micrograph, Sample CW-1, 3000X	134
75	Scanning Electron Micrograph, Sample CW-1, 5000X	135
76	Scanning Electron Micrograph, Sample LA-16, 500X	137
77	Scanning Electron Micrograph, Sample LA-16, 3000X	137
78	Scanning Electron Micrograph, Sample LA-20, 500X	138
79	X-ray Diffractometer Trace of Vapor Grown Aluminum Oxide Powder from Run VA-10	166
80	X-ray Diffraction Pattern for Alumina, Run VA-10	167
81	X-ray Diffractometer Trace of Vapor Grown Rutile Powder from Run TiO_2 -1	170
82	X-ray Diffraction Pattern for Titania, Run TiO_2 -1	171
83	X-ray Diffractometer Trace of Oxides from Run Zn_2TiO_4 -2, Showing Zn_2TiO_4 as the Major Phase	174
84	X-ray Diffraction Pattern for Zinc Orthotitanate, Run Zn_2TiO_4 -1	175

LIST OF TABLES

Table No.		Page
I	Free-Energy Changes and Equilibrium Constants for Aluminum Oxide Reactions	8
II	Free-Energy Changes and Equilibrium Constants as a Function of Temperature for Titanium Dioxide Production	9
III	Free-Energy Changes and Equilibrium Constants as Functions of Temperature for Zinc Orthotitanate Production Using Zinc Metal	11
IV	Free-Energy Changes and Equilibrium Constants as Functions of Temperature for Zinc Orthotitanate Production Using Zinc Chloride	12
V	Estimate of Maximum Free Energy of Zinc Orthotitanate	13
VI	Thermodynamic Data for Calcium Tungstate System	17
VII	Thermodynamic Data for Calcium Oxide Chlorination	18
VIII	Thermodynamic Data for Calcium Oxide Chlorination	19
IX	Thermodynamic Data for Lanthanum Oxide System	25
X	Thermodynamic Data for Lanthanum Oxide Chlorination	26
XI	Free-Energy Change and Equilibrium Constant for Chlorination of La_2O_3 with Carbon	30
XII	Free-Energy Change and Equilibrium Constant for Chlorination of La_2O_3 with CO_2	31
XIII	Estimate of Maximum Free-Energy of LaOCl	32
XIV	Free-Energy Changes and Equilibrium Constants for LaOCl	34
XV	Free-Energy Changes and Equilibrium Constants for LaOCl	35
XVI	Free-Energy Changes and Equilibrium Constants for LaOCl	36
XVII	Free-Energy Changes and Equilibrium Constants for La_2O_3 Production from LaOCl	37
XVIII	Free-Energy Changes and Equilibrium Constants for La_2O_3 Production	38

LIST OF TABLES - (Continued)

<u>Table No.</u>		<u>Page</u>
XIX	Free-Energy Changes and Equilibrium Constants for LaOCl Production for LaCl ₃	39
XX	Estimated Transport Properties	42
XXI	Intensity of Segregation from Equation (65)	59
XXII	Free-Energy Changes and Equilibrium Constants as a Function of Temperature for Aluminum Oxide Production	96
XXIII	Conditions for Aluminum Oxide Powder Production	97
XXIV	Free-Energy Changes and Equilibrium Constants as a Function of Temperature for Titanium Dioxide Production	104
XXV	System Conditions for TiO ₂ Pigment Production	106
XXVI	Particle Size Variation with Injector Length	115
XXVII	System Conditions and Phase Analysis for Runs Using Metallic Zinc as the Zinc Vapor Species	122
XXVIII	System Conditions and Phase Analysis for Runs Using Oxide to Produce Zinc Chloride	128
XXIX	System Conditions and Phase Analysis for Runs Using Zinc Orthotitanate to Produce Zinc Chloride	130
XXX	System Conditions and Phase Analysis of CaWO ₄ Run	131
XXXI	System Conditions and Phase Analysis for La ₂ O ₃ Runs	136
XXXII	Free Energy Values Used in Thermodynamic Calculations	147
XXXIII	X-ray Powder Diffraction Data for Alumina, Run No. VA-10	167
XXXIV	X-ray Powder Diffraction Data for Titanium, Run No. TiO ₂ -1	171
XXXV	X-ray Powder Diffraction Data for Zinc Orthotitanate, Run Zn ₂ TiO ₄ -1	175

PREPARATION OF PIGMENTS FOR SPACE-STABLE THERMAL CONTROL COATINGS

I. INTRODUCTION

During the past decade, efforts have been directed toward producing thermal control coatings which are stable to solar radiation in space. Inorganic pigments, once believed to be extremely stable, have been shown to be subject to ultraviolet and proton degradation. The degradation mechanism appears related to the strong absorption of high-energy ultraviolet radiation and may result from a defect structure in the pigment crystals. Crystal size, structural integrity, and surface condition apparently influence the performance and degradation resistance of a pigment.

The primary purpose of a thermal control coating is to reflect as much radiation as possible. Maximum reflectance is obtained when the particle size of the pigment is of the same order of magnitude as the wavelength of the incident radiation. For solar radiation, the maximum intensity is between 0.35 and 2.5 microns.

In the past eight years, the major emphasis in pigment research for thermal control coatings has been on zinc oxide which has consistently shown the greatest stability to ultraviolet irradiation in a vacuum. Of the new pigments under investigation, zinc orthotitanate has shown considerable promise as a new, potentially stable white pigment.

The first zinc orthotitanate (Zn_2TiO_4) pigment powder was prepared by mixing ZnO and TiO_2 (anatase) in the mole ratio (2:1). Residual ZnO was removed by washing with acetic acid (complete removal is seldom achieved). Stoichiometric considerations suggest that residual TiO_2 remains, that other titanates are formed, or that titanium is present in interstitial solid solution in the orthotitanate lattice.¹ Subsequent, solid state reactions have reportedly reduced the stoichiometric effects.²

Zinc orthotitanate is not completely space-stable and will degrade under space simulation. One of the primary factors believed responsible for promoting damage to the pigment powder is grinding; however, the extraction with acetic acid and washing are other important variables. A grinding or mulling operation is usually employed to obtain submicron-size particles that produce the efficient scattering of solar radiation in the 0.35 to 2.5 μ wavelength range.

The development of vapor-phase technology in the preparation of space-stable pigments has been demonstrated by the production of rutile powders having discrete morphology. Powders produced by homogeneous nucleation in the vapor phase have controlled chemical composition; are monosized crystalline particles of controlled particle size; and retain

their structural integrity. The ability of the vapor phase process to control the parameters that influence reflectance provides many advantages in comparison to other powder production techniques. Systematic variations of particle size have been controlled with hot zone temperature, residence time, and injector design. The current investigation was designed to study the production of stable pigments for thermal control coatings. Materials include zinc titanates, calcium tungstate and lanthanum oxide.

Two major limitations retarding the production of multiple oxides and rare earth compounds; gas mixing and halide generation have been studied. A detailed mixing study has been performed and a reactor designed from the results of this study. Halide generation of multiple chlorides has been achieved by the direct chlorination of the multiple oxide. Calcium tungstate has been produced as a major phase in the jet mixing reactor. Zinc orthotitanate and lanthanum oxide were obtained as minor phases only. Reaction kinetics were limiting in production of multiple oxide phases.

A. PROGRAM OBJECTIVE

Since 1960 several exploratory investigations have established the feasibility of production of highly reproducible materials by vapor-phase reactions. Also, the morphology of vapor-phase productions has been controlled in these rapid reaction systems. Product morphology has ranged from whiskers to bulk crystals to monodisperse powders.

The objective of this investigation is to apply the vapor-phase technology developed in earlier investigations to the products of space-stable pigments of zinc titanates, zirconates, etc. The primary material system to be considered is zinc orthotitanate; however, rutile, aluminum oxide, calcium tungstate and lanthanum oxide are included.

Zinc orthotitanate (Zn_2TiO_4), which was found to be one of the better space-stable pigments of low α and low α/ϵ ratios (solar absorptance and infrared emittance), was selected as the primary material for production by homogeneous nucleation in a quantity sufficient for pigment evaluation.

The vapor reaction system has the potentials of close control of chemical composition, production of monosized crystalline particles, and retention of structural integrity -- all with sizeable production batches.

B. SURVEY OF LITERATURE

1. Pigment Properties for Thermal Control of Space Vehicles

Temperature requirements for space vehicles impose stringent restrictions on the properties of thermal control coatings. Satellites containing electronic equipment must maintain temperatures of -10°C to 100°C and should be kept in the temperature range of 20° to 40°C for reliable operation. Manned space vehicles must maintain an even more narrow temperature range and must not exceed 45°C for more than a few minutes.³

The average equilibrium surface temperature of a vehicle in space is given by the following general equation:³

$$T = \sqrt{\frac{(\alpha/\epsilon)(P_s + P_a) + P_e}{A\sigma}} \quad (1)$$

where

- α = solar absorptivity of external body surface;
- ϵ = hemispherical emittance of external body surface, assumed to be equal to the absorptance of the Earth-emitted radiation;
- P_s = direct solar radiation incident upon the body;
- P_a = Earth-reflected solar radiation upon the body;
- P_e = Earth-emitted radiation incident upon the body;
- A = surface area of the body; and
- σ = Boltzman's constant.

To maintain low temperatures in a space vehicle, a coating of low (α/ϵ) ratio and a low α is desired, as predicted by Eq. (1). A number of inorganic ceramic pigments, including zinc orthotitanate, possess low α/ϵ ratios.

In recent years inorganic pigments, once believed to be extremely stable, have been shown to be subject to ultraviolet and proton degradation. Considering the mechanisms involved, pigments having a minimum of structural defects would be the most space stable. When pigments degrade, the solar absorption (α_s) increases, thereby increasing the α/ϵ ratio.

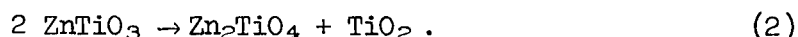
The primary purpose of a thermal control coating is to reflect as much radiation as possible; thereby preventing the radiation from reaching the interior of the space vehicle. The most important factor to consider in the reflectivity of a two-phase coating are (1) the particle size of the pigment, (2) the relative index of refraction of the pigment and the binder, and (3) the volume of the pigment present

in the coating.⁴ Maximum backscattering or reflectance is obtained when the particle size of the pigment is of the same order of magnitude as the wavelength of the incident radiation. For solar radiation, the maximum intensity is between 0.35 and 2.5 μ .

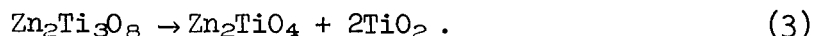
For greatest reflectance, the index of refraction of the pigment should be significantly higher than that of the binder and the volume of particles should be as great as possible. A pigment suitable for a thermal control coating should (1) have a low (α/ϵ) ratio, (2) be stable when subjected to ultraviolet radiation in a vacuum, (3) have a particle size in the 0.35 to 2.5 μ range, and (4) have a high index of refraction.

2. Phase Equilibrium in the ZnO-TiO₂ System

Compounds reported for the ZnO-TiO₂ system are zinc orthotitanate (Zn₂TiO₄), zinc metatitanate (ZnTiO₃), and zinc sesquititanate (Zn₂Ti₃O₈). The study of phase equilibria in the ZnO-TiO₂ system made by Dulin and Rase⁵ shows decomposition of zinc metatitanate into zinc orthotitanate and rutile at approximately 900°C (see Fig. 1) by the following reaction:



In the composition region ZnO·TiO₂ to ZnO·2TiO₂, Bartram and Slepety's⁶ report the formation of Zn₂Ti₃O₈ as the predominant phase from 600 to 900°C. Like the metatitanate, the sesquititanate becomes unstable in the temperature region 900° - 1000°C. At temperatures greater than 1000°C, the sesquititanate decomposes to orthotitanate and rutile by the following reaction:



The presence of Zn₂Ti₃O₈ may have been overlooked because of similarity between Zn₂TiO₄ and Zn₂Ti₃O₈ structures. Variations in X-ray data have been previously attributed to solid solution of TiO₂ in Zn₂TiO₄ instead of Zn₂Ti₃O₈. One point on which there is general agreement is that zinc orthotitanate is the only stable zinc oxide-titania compound above 1000°C.

The structures of zinc orthotitanate, zinc metatitanate, and zinc sesquititanate are inverse spinel, hexagonal, and defect spinel, respectively. Zinc orthotitanate with an inverse spinel structure has 32 oxygen atoms in an approximately cubic close-packing arrangement, with 8 Zn²⁺ ions in A sites with tetrahedral coordination, and 8 Zn²⁺ + 8 Ti⁴⁺ ions distributed randomly in B sites with octahedral coordination to the oxygen atoms. Zinc sesquititanate crystallizes in a defect spinel structure with 8 Zn²⁺ ions in the tetrahedral positions and

ZnO-TiO₂

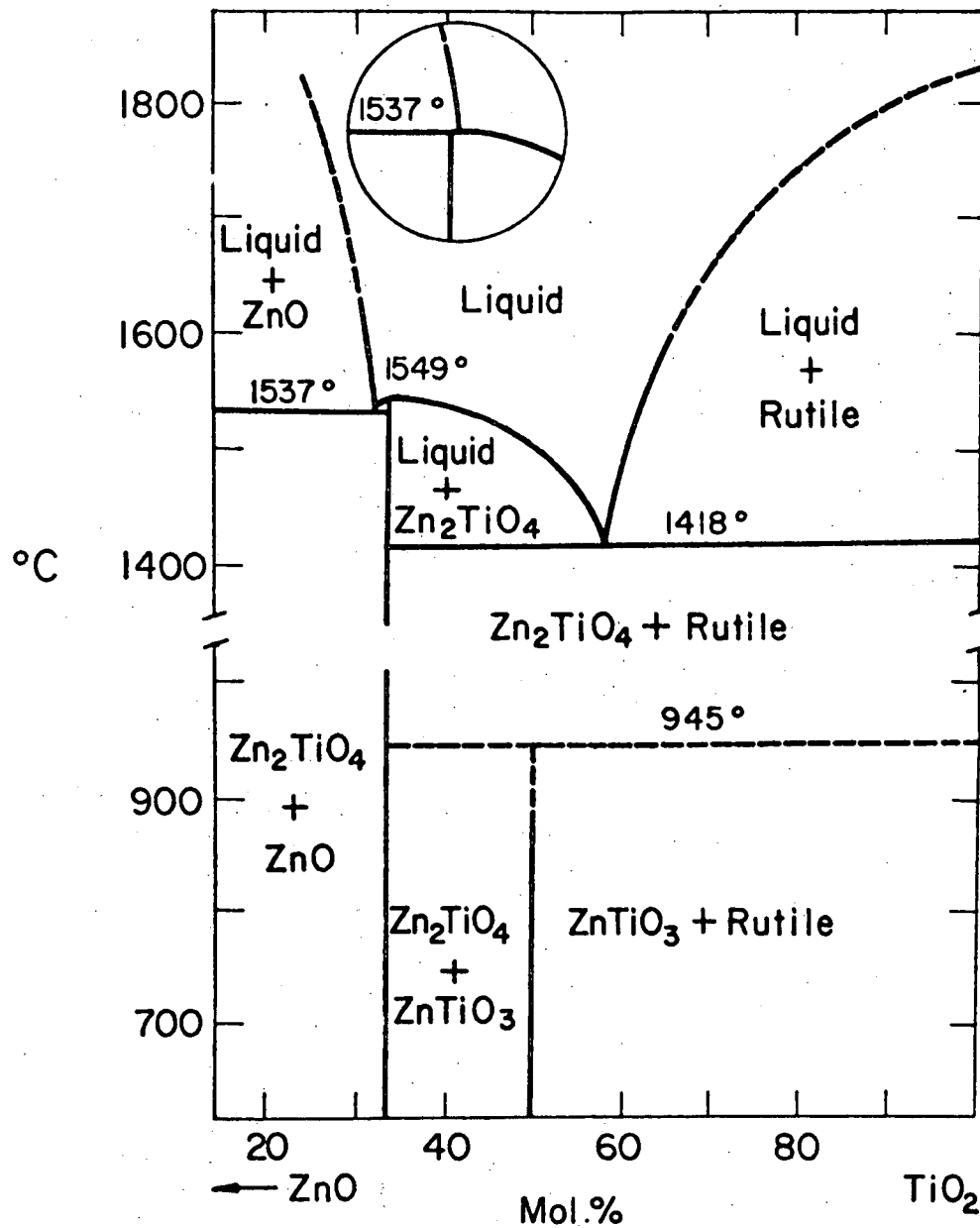


Fig. 1 - System ZnO-TiO₂. Inset Shows Alternative Incongruent Melting of Zn₂TiO₄.⁶

12 Ti^{4+} ions occupying the octahedral positions. Zinc metatitanate has an ilmenite-type structure.

3. Vapor Phase Powder Technology Developments

Aluminum oxide powder was produced by Campbell⁷ from homogeneous nucleation in the vapor phase. Aluminum chloride, carbon dioxide, and hydrogen were reacted in an isothermal hot zone. Variables such as temperature, gas velocity, system pressure, and gas composition were shown to be controlling parameters for powder and whisker growth.

Schaffer and Jones⁸ produced other oxide powders (i.e., SiO_2 , ZrO_2 , TiO_2 , and ZnO and the double oxide ZnTiO_3) using a halide hydrolysis reaction and subsequent homogeneous nucleation of the powder in the gas phase using equipment similar to that of Campbell. Both chlorination and vaporization of zinc were used for production of ZnO and ZnTiO_3 . Chlorination of zinc, proved unsatisfactory because of its high vapor pressure. Vaporization of zinc proved difficult to control because other reacting gases passed over its surface and oxide formation limited evaporation.

Vapor-grown zinc oxide pigmenting powders are produced in large quantities commercially by reaction of zinc oxide with coal at elevated temperatures. The coal reduces zinc oxide to zinc metal vapor, and the zinc vapor is later reoxidized to form zinc oxide powder by homogeneous nucleation.

II. PRINCIPLES OF VAPOR PHASE POWDER PRODUCTION

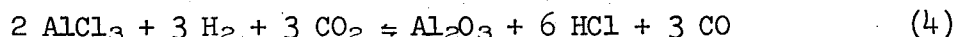
The fundamental considerations for a vapor phase reaction system are

- (1) the thermodynamic behavior of the system at selected temperatures;
- (2) the kinetics of nucleation, reaction, and evaporation; and
- (3) a basis for process control.

Formation of desired products may be accomplished by introducing suitable metal vapor species into a heated reaction zone at constant temperature and pressure followed by H_2 and CO_2 to provide the remaining reactants necessary to cause homogeneous nucleation. By carrying out the chemical reaction in a zone of constant temperature and pressure, the equilibrium conditions of the reaction can be predicted from thermodynamics. Appendix A, B and C contain the data, and computer source listings used in the following calculations.

A. THERMODYNAMICS OF ALUMINUM OXIDE (Al_2O_3) REACTION

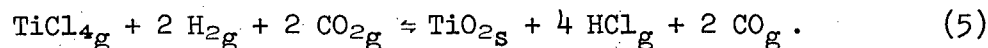
Aluminum oxide powders can be prepared by the following reaction:



The reaction free energy and equilibrium constant over the temperature range 500-2000°K, are summarized in Table I.

B. THERMODYNAMICS OF TITANIUM DIOXIDE (TiO_2) REACTION

Titanium dioxide (rutile) powder has been formed by homogeneous nucleation according to the reaction:



The free energy change over the temperature range of 300 to 2000°K reported in Table II.

Table I - Free-Energy Changes and Equilibrium Constants for Aluminum Oxide Reactions

T (°C)	T (°K)	ΔG° Reaction* (kcal/mole)	K_p Reaction*
227	500	-63.3	3.3×10^{27}
727	1000	-75.8	3.0×10^{16}
927	1200	-80.2	3.4×10^{14}
1127	1400	-85.4	1.8×10^{13}
1227	1500	-87.6	5.0×10^{12}
1327	1600	-90.5	2.0×10^{12}
1427	1700	-92.6	6.9×10^{11}
1527	1800	-94.6	2.7×10^{11}
1627	1900	-97.4	1.4×10^{11}
1727	2000	-100.0	7.4×10^{10}

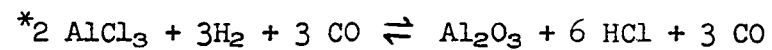
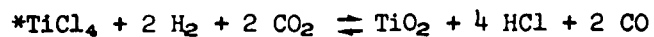


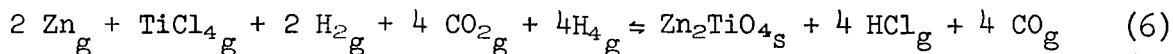
Table II - Free-Energy Changes and Equilibrium Constants as a Function of Temperature for Titanium Dioxide Production

T (°C)	T (°K)	ΔG° Reaction* (kcal/mole)	K_p Reaction*
27	300	- 4.60	2.25×10^3
127	400	-10.55	5.82×10^5
227	500	-17.15	3.14×10^7
327	600	-18.20	4.27×10^8
427	700	-21.85	6.64×10^8
527	800	-25.45	8.98×10^8
627	900	-28.90	1.04×10^7
727	1000	-32.10	1.04×10^7
827	1100	-35.55	1.16×10^7
927	1200	-39.39	1.49×10^7
1027	1300	-42.30	1.29×10^7
1127	1400	-45.90	1.46×10^7
1227	1500	-49.15	1.45×10^7
1327	1600	-53.25	1.88×10^7
1427	1700	-56.45	1.81×10^7
1527	1800	-60.60	2.28×10^7
1627	1900	-64.50	2.63×10^7
1727	2000	-67.40	2.32×10^7

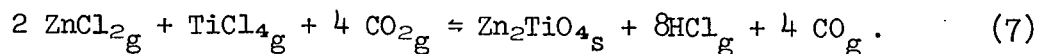


C. THERMODYNAMICS OF ZINC ORTHOTITANATE REACTIONS

The suitability of the thermodynamics for the zinc-titania system has been established by thermodynamic calculation and previous investigations. Two reactions were considered for production of zinc orthotitanate; i.e.,



and



By summing the free energies of the products of the reactions and subtracting the sum of the free energies of the reactants, the free energy changes for Eqs. (6) and (7) were obtained from room temperature to 2000°K. These values are summarized in Tables III and IV. Free-energy data^{9,10} were available for all the compounds in Eqs. (6) and (7) except Zn_2TiO_4 . An estimate for Zn_2TiO_4 was made using the following reaction:



This reaction occurs above 780°C¹¹ and thus the free energy of one mole of Zn_2TiO_4 must be more negative than the sum of the free energies of two moles of ZnO and one of TiO_2 . Assuming that the free energy change for reaction (8) is at least -5,000 cal/mole Zn_2TiO_4 , a free-energy value for Zn_2TiO_4 was calculated, as summarized in Table V.

As indicated in Tables III and IV, the free-energy changes for Eqs. (6) and (7) are substantially negative with large equilibrium constants above 1300°K (1023°C). Thus the thermodynamics are favorable for the formation of Zn_2TiO_4 above 1000°C where Zn_2TiO_4 is the only stable zinc titanate compound.

Growth conditions for zinc orthotitanate within pressure and temperature ranges of the system were calculated by a CDC 6600 computer using program EQUICA. Program EQUICA is designed to compute the equilibrium compositions of a given set of reaction species by minimizing the Gibb's free energy. The input data consisted of:

- a) possible species formed within the system
- b) Gibb's free energy values for these species
- c) temperature

Table III - Free-Energy Changes and Equilibrium Constants as Functions of Temperature for Zinc Orthotitanate Production Using Zinc Metal

T (°C)	T (°K)	ΔG° Reaction* (kcal/mole)	K_p Reaction*
27	300	-38.90	2.19×10^{28}
127	400	-46.25	1.87×10^{25}
227	500	-50.15	8.36×10^{21}
327	600	-50.90	3.48×10^{18}
427	700	-54.15	8.09×10^{16}
527	800	-56.85	3.40×10^{15}
627	900	-59.50	2.82×10^{14}
727	1000	-61.80	3.22×10^{13}
827	1100	-63.75	4.65×10^{12}
927	1200	-66.19	1.14×10^{12}
1027	1300	-68.00	2.71×10^{11}
1127	1400	-69.70	7.61×10^{10}
1227	1500	-71.65	2.76×10^{10}
1327	1600	-74.25	1.39×10^{10}
1427	1700	-75.85	5.65×10^9
1527	1800	-78.30	3.22×10^9
1627	1900	-80.80	1.97×10^9
1727	2000	-81.90	8.92×10^8

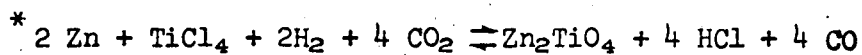


Table IV - Free-Energy Changes and Equilibrium Constants as Functions of Temperature for Zinc Orthotitanate Production Using Zinc Chloride

T (°C)	T (°K)	ΔG° Reaction* (kcal/mole)	K _p Reaction*
27	300	47.00	5.27×10^{-35}
127	400	31.55	5.76×10^{-18}
227	500	16.45	6.44×10^{-8}
327	600	13.10	1.69×10^{-5}
427	700	4.65	3.53×10^{-2}
527	800	- 3.05	6.81×10
627	900	-10.70	3.97×10^2
727	1000	-17.80	7.77×10^3
827	1100	-26.91	2.22×10^5
927	1200	-36.91	5.28×10^8
1027	1300	-45.28	4.10×10^7
1127	1400	-54.54	3.27×10^8
1227	1500	-63.25	1.65×10^9
1327	1600	-70.85	4.77×10^9
1427	1700	-76.85	7.60×10^9
1527	1800	-84.30	1.72×10^{10}
1627	1900	-91.60	3.45×10^{10}
1727	2000	-96.90	3.89×10^{10}

* $2 \text{ZnCl}_2 + \text{TiCl}_4 + 4 \text{H}_2 + 4 \text{CO}_2 \rightleftharpoons \text{Zn}_2\text{TiO}_4 + 8 \text{HCl} + 4 \text{CO}$

Table V - Estimate of Maximum Free Energy of Zinc Orthotitanate
(Assuming $\Delta G_R = -5000$ cal/mole Zn_2TiO_4)

Temperature		$2 \Delta G^\circ_{ZnO}$ (kcal/mole)	$\Delta G^\circ_{TiO_2}$ (kcal/mole)	$\Delta G^\circ_{Zn_2TiO_4}$ Estimate* (kcal/mole)
$^\circ K$	$^\circ C$			
300	27	-152.20	-212.00	-369.60
400	127	-149.30	-207.90	-362.20
500	227	-142.60	-203.60	-351.20
600	327	-137.90	-199.30	-342.20
700	427	-133.20	-194.30	-333.15
800	527	-121.00	-190.75	-323.75
900	627	-123.00	-186.55	314.50
1000	727	-118.00	-182.35	-305.35
1100	827	-112.20	-178.00	-295.20
1200	927	-106.80	-173.89	-285.69
1300	1027	-101.40	-169.55	-275.95
1400	1127	- 95.80	-165.45	-266.25
1500	1227	- 90.20	-161.20	-256.40
1600	1327	- 84.40	-157.25	-246.65
1700	1427	- 78.80	-153.10	-236.90
1800	1527	- 73.20	-149.35	-227.55
1900	1627	- 67.60	-145.25	-217.85
2000	1727	- 62.00	-141.15	-208.15

* $\Delta G^\circ_{Zn_2TiO_4} = 2 \Delta G_{ZnO} + \Delta G_{TiO_2} - 5000$ cal/mole Zn_2TiO_4

- d) pressure
- e) initial estimate of the composition of these species.

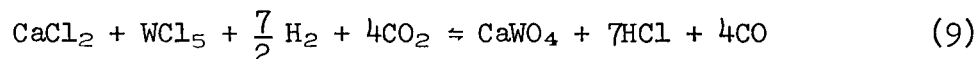
The output consisted of:

- a) the equilibrium concentrations of the species
- b) equilibrium constants
- c) partial pressure of the species
- d) the total pressure.

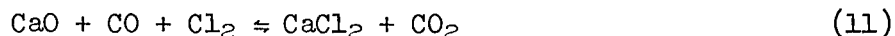
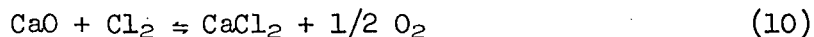
Figure 2 shows the equilibrium concentration of zinc orthotitanate for various temperatures and system pressures. Figure 3 shows the equilibrium constant for zinc orthotitanate formation for various temperatures.

D. THERMODYNAMICS OF CALCIUM TUNGSTATE (CaWO_4) REACTIONS

The computer output for the summary reaction



shows thermodynamic feasibility at all temperatures, Table VI. Calcium chloride cannot be obtained by chlorinating calcium metal because the metal has a higher vapor pressure than CaCl_2 . Chlorination of CaO offers two possibilities,



Both reactions are thermodynamically favored at all temperatures, Tables VII and VIII. The vapor pressure of calcium chloride, Figure 4, requires temperatures above 1600°C for sufficient volatility.

Generating tungsten chloride, WCl_5 , by chlorination of tungsten metal is feasible due to the low vapor pressure of the metal. Various lower chlorides may be formed as intermediate compounds, but WCl_5 has the lowest free energy above 400°C , Figure 5.

Growth conditions for CaWO_4 were calculated using program EQUICA. The equilibrium concentration of CaWO_4 as a function of temperature and pressure is shown in Figure 6. Figure 7 shows the equilibrium constant for CaWO_4 formation at various temperatures.

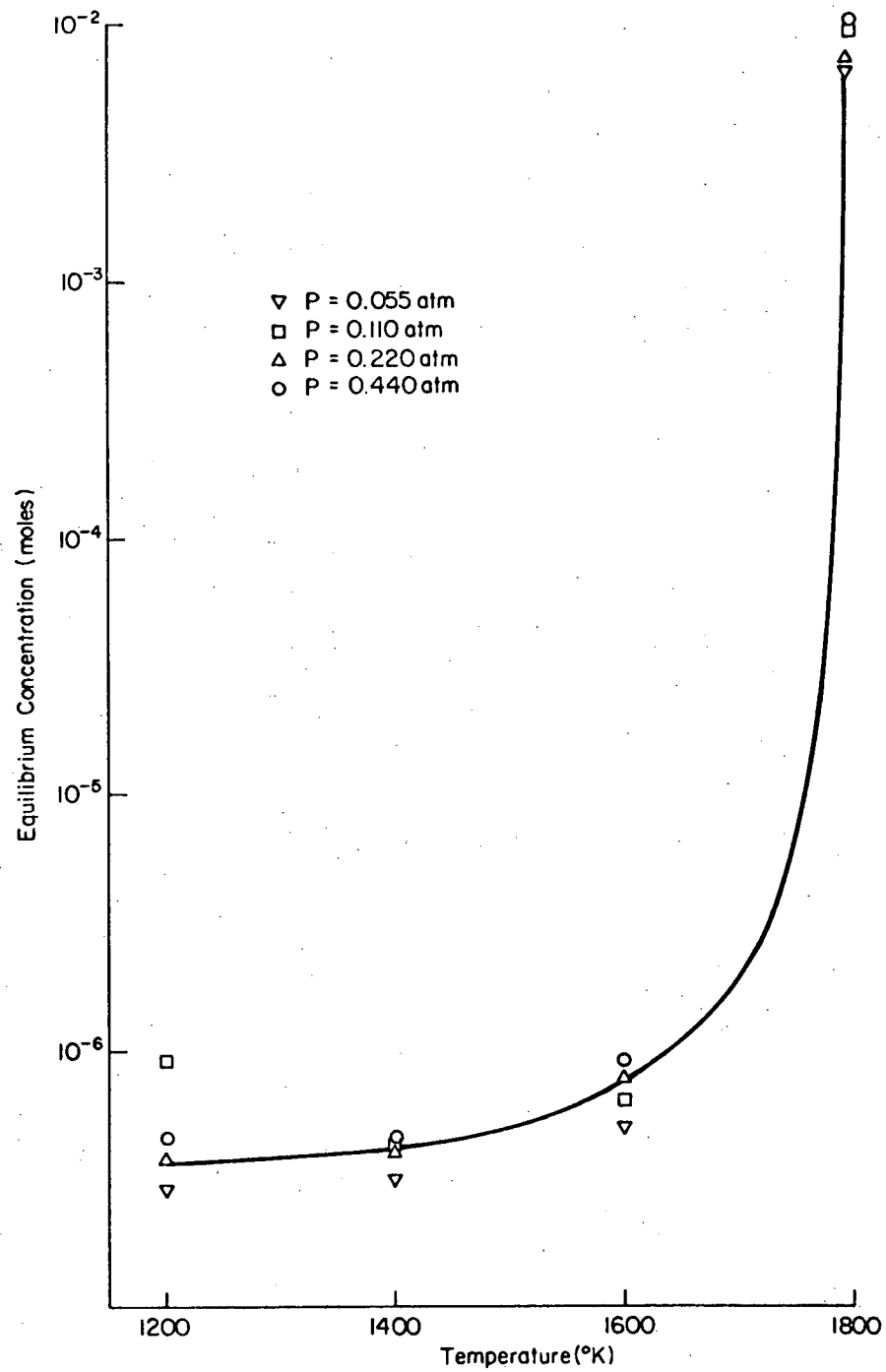


Fig. 2 - Equilibrium Concentrations of Zn_2TiO_4 as a Function of System Conditions

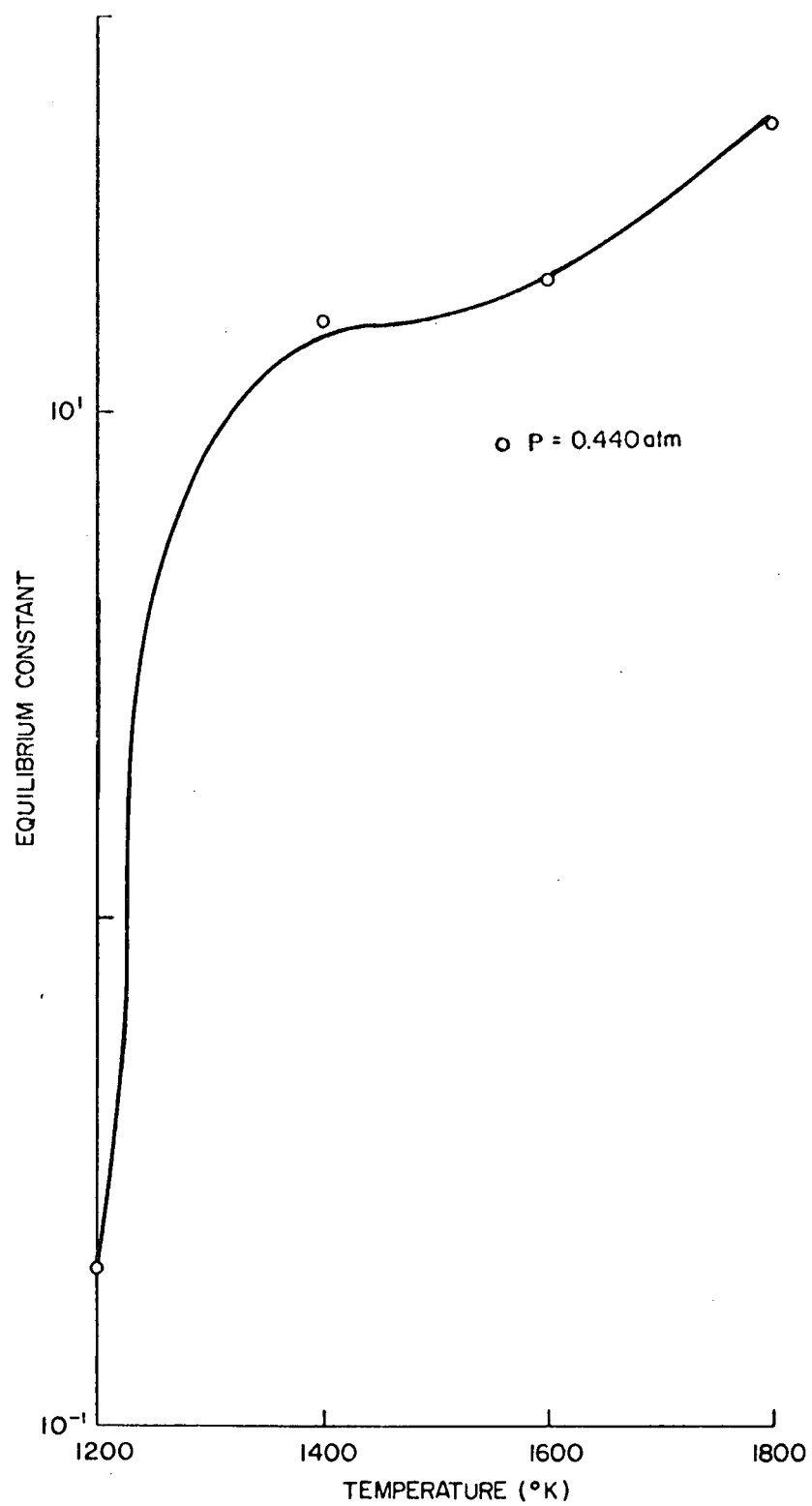


Fig. 3 - Equilibrium Constant as a Function of Temperature for Zn_2TiO_4 Formation

Table VI - Thermodynamic Data for Calcium
Tungstate System (CaWO_4)

THE FOLLOWING DATA IS FOR THE REACTION

REACTANTS	2 CaCl_2	2 WCl_5	7 H_2	8 CO_2
PRODUCTS	2 CaWO_4	EST 14 HCl	8 CO	
DELTA G IS	-11200 CALORIES AT	300 DEGREES	KELVIN AND THE	EQUILIBRIUM CONSTANT IS 0.1445E+09
DELTA G IS	-36000 CALORIES AT	400 DEGREES	KELVIN AND THE	EQUILIBRIUM CONSTANT IS 0.4689E+20
DELTA G IS	-70400 CALORIES AT	500 DEGREES	KELVIN AND THE	EQUILIBRIUM CONSTANT IS 0.5948E+31
DELTA G IS	-80200 CALORIES AT	600 DEGREES	KELVIN AND THE	EQUILIBRIUM CONSTANT IS 0.1641E+30
DELTA G IS	-95300 CALORIES AT	700 DEGREES	KELVIN AND THE	EQUILIBRIUM CONSTANT IS 0.5708E+30
DELTA G IS	-110000 CALORIES AT	800 DEGREES	KELVIN AND THE	EQUILIBRIUM CONSTANT IS 0.1130E+31
DELTA G IS	-124100 CALORIES AT	900 DEGREES	KELVIN AND THE	EQUILIBRIUM CONSTANT IS 0.1374E+31
DELTA G IS	-137600 CALORIES AT	1000 DEGREES	KELVIN AND THE	EQUILIBRIUM CONSTANT IS 0.1196E+31
DELTA G IS	-152100 CALORIES AT	1100 DEGREES	KELVIN AND THE	EQUILIBRIUM CONSTANT IS 0.1667E+31
DELTA G IS	-165500 CALORIES AT	1200 DEGREES	KELVIN AND THE	EQUILIBRIUM CONSTANT IS 0.1394E+31
DELTA G IS	-176800 CALORIES AT	1300 DEGREES	KELVIN AND THE	EQUILIBRIUM CONSTANT IS 0.5312E+30
DELTA G IS	-189100 CALORIES AT	1400 DEGREES	KELVIN AND THE	EQUILIBRIUM CONSTANT IS 0.3329E+30
DELTA G IS	-200900 CALORIES AT	1500 DEGREES	KELVIN AND THE	EQUILIBRIUM CONSTANT IS 0.1877E+30
DELTA G IS	-216400 CALORIES AT	1600 DEGREES	KELVIN AND THE	EQUILIBRIUM CONSTANT IS 0.3642E+30
DELTA G IS	-228300 CALORIES AT	1700 DEGREES	KELVIN AND THE	EQUILIBRIUM CONSTANT IS 0.2251E+30
DELTA G IS	-243000 CALORIES AT	1800 DEGREES	KELVIN AND THE	EQUILIBRIUM CONSTANT IS 0.3211E+30
DELTA G IS	-258900 CALORIES AT	1900 DEGREES	KELVIN AND THE	EQUILIBRIUM CONSTANT IS 0.6064E+30
DELTA G IS	-271500 CALORIES AT	2000 DEGREES	KELVIN AND THE	EQUILIBRIUM CONSTANT IS 0.4684E+30

Table VII - Thermodynamic Data for Calcium
Oxide Chlorination

THE FOLLOWING DATA IS FOR THE REACTION					
REACTANTS	1 CAO	1 CL2			
PRODUCTS	1 CaCl2	1 O2			
DELTA G IS	-35300 CALORIES	AT 300 DEGREES KELVIN AND THE	EQUILIBRIUM CONSTANT IS	0.5226E	26
DELTA G IS	-34100 CALORIES	AT 400 DEGREES KELVIN AND THE	EQUILIBRIUM CONSTANT IS	0.4295E	19
DELTA G IS	-33100 CALORIES	AT 500 DEGREES KELVIN AND THE	EQUILIBRIUM CONSTANT IS	0.2946E	15
DELTA G IS	-32100 CALORIES	AT 600 DEGREES KELVIN AND THE	EQUILIBRIUM CONSTANT IS	0.4936E	12
DELTA G IS	-31250 CALORIES	AT 700 DEGREES KELVIN AND THE	EQUILIBRIUM CONSTANT IS	0.5721E	10
DELTA G IS	-30300 CALORIES	AT 800 DEGREES KELVIN AND THE	EQUILIBRIUM CONSTANT IS	0.1898E	09
DELTA G IS	-29500 CALORIES	AT 900 DEGREES KELVIN AND THE	EQUILIBRIUM CONSTANT IS	0.1459E	03
DELTA G IS	-28500 CALORIES	AT 1000 DEGREES KELVIN AND THE	EQUILIBRIUM CONSTANT IS	0.1695E	07
DELTA G IS	-28100 CALORIES	AT 1100 DEGREES KELVIN AND THE	EQUILIBRIUM CONSTANT IS	0.3832E	06
DELTA G IS	-27900 CALORIES	AT 1200 DEGREES KELVIN AND THE	EQUILIBRIUM CONSTANT IS	0.1207E	06
DELTA G IS	-27850 CALORIES	AT 1400 DEGREES KELVIN AND THE	EQUILIBRIUM CONSTANT IS	0.4721E	05
DELTA G IS	-27900 CALORIES	AT 1500 DEGREES KELVIN AND THE	EQUILIBRIUM CONSTANT IS	0.2228E	05
DELTA G IS	-27500 CALORIES	AT 1600 DEGREES KELVIN AND THE	EQUILIBRIUM CONSTANT IS	0.1162E	05
DELTA G IS	-27500 CALORIES	AT 1700 DEGREES KELVIN AND THE	EQUILIBRIUM CONSTANT IS	0.5710E	04
DELTA G IS	-27300 CALORIES	AT 1800 DEGREES KELVIN AND THE	EQUILIBRIUM CONSTANT IS	0.3433E	04
DELTA G IS	-27200 CALORIES	AT 1900 DEGREES KELVIN AND THE	EQUILIBRIUM CONSTANT IS	0.2065E	04
DELTA G IS	-27000 CALORIES	AT 2000 DEGREES KELVIN AND THE	EQUILIBRIUM CONSTANT IS	0.1346E	04
				0.9926E	03

Table VIII - Thermodynamic Data for Calcium
Oxide Chlorination

Reproduced from
best available copy.

THE FOLLOWING DATA IS FOR THE REACTION

REACTANTS	1 CAO	1 CL2	1 CO
PRODUCTS	1 CACL2	1 CO2	
DELTA G IS	-96750 CALORIES AT 300 DEGREES KELVIN AND THE	EQUILIBRIUM CONSTANT IS	0.3077E 71
DELTA G IS	-93400 CALORIES AT 400 DEGREES KELVIN AND THE	EQUILIBRIUM CONSTANT IS	0.1085E 52
DELTA G IS	-90400 CALORIES AT 500 DEGREES KELVIN AND THE	EQUILIBRIUM CONSTANT IS	0.3289E 40
DELTA G IS	-87200 CALORIES AT 600 DEGREES KELVIN AND THE	EQUILIBRIUM CONSTANT IS	0.5824E 32
DELTA G IS	-84200 CALORIES AT 700 DEGREES KELVIN AND THE	EQUILIBRIUM CONSTANT IS	0.1953E 27
DELTA G IS	-81100 CALORIES AT 800 DEGREES KELVIN AND THE	EQUILIBRIUM CONSTANT IS	0.1437E 23
DELTA G IS	-78200 CALORIES AT 900 DEGREES KELVIN AND THE	EQUILIBRIUM CONSTANT IS	0.9798E 19
DELTA G IS	-75150 CALORIES AT 1000 DEGREES KELVIN AND THE	EQUILIBRIUM CONSTANT IS	0.2663E 17
DELTA G IS	-72600 CALORIES AT 1100 DEGREES KELVIN AND THE	EQUILIBRIUM CONSTANT IS	0.2664E 15
DELTA G IS	-70400 CALORIES AT 1200 DEGREES KELVIN AND THE	EQUILIBRIUM CONSTANT IS	0.6647E 13
DELTA G IS	-68150 CALORIES AT 1300 DEGREES KELVIN AND THE	EQUILIBRIUM CONSTANT IS	0.2871E 12
DELTA G IS	-66350 CALORIES AT 1400 DEGREES KELVIN AND THE	EQUILIBRIUM CONSTANT IS	0.2283E 11
DELTA G IS	-64250 CALORIES AT 1500 DEGREES KELVIN AND THE	EQUILIBRIUM CONSTANT IS	0.2301E 10
DELTA G IS	-61700 CALORIES AT 1600 DEGREES KELVIN AND THE	EQUILIBRIUM CONSTANT IS	0.2682E 09
DELTA G IS	-59700 CALORIES AT 1700 DEGREES KELVIN AND THE	EQUILIBRIUM CONSTANT IS	0.4738E 08
DELTA G IS	-57550 CALORIES AT 1800 DEGREES KELVIN AND THE	EQUILIBRIUM CONSTANT IS	0.9730E 07
DELTA G IS	-55350 CALORIES AT 1900 DEGREES KELVIN AND THE	EQUILIBRIUM CONSTANT IS	0.2329E 07
DELTA G IS	-53250 CALORIES AT 2000 DEGREES KELVIN AND THE	EQUILIBRIUM CONSTANT IS	0.6597E 06

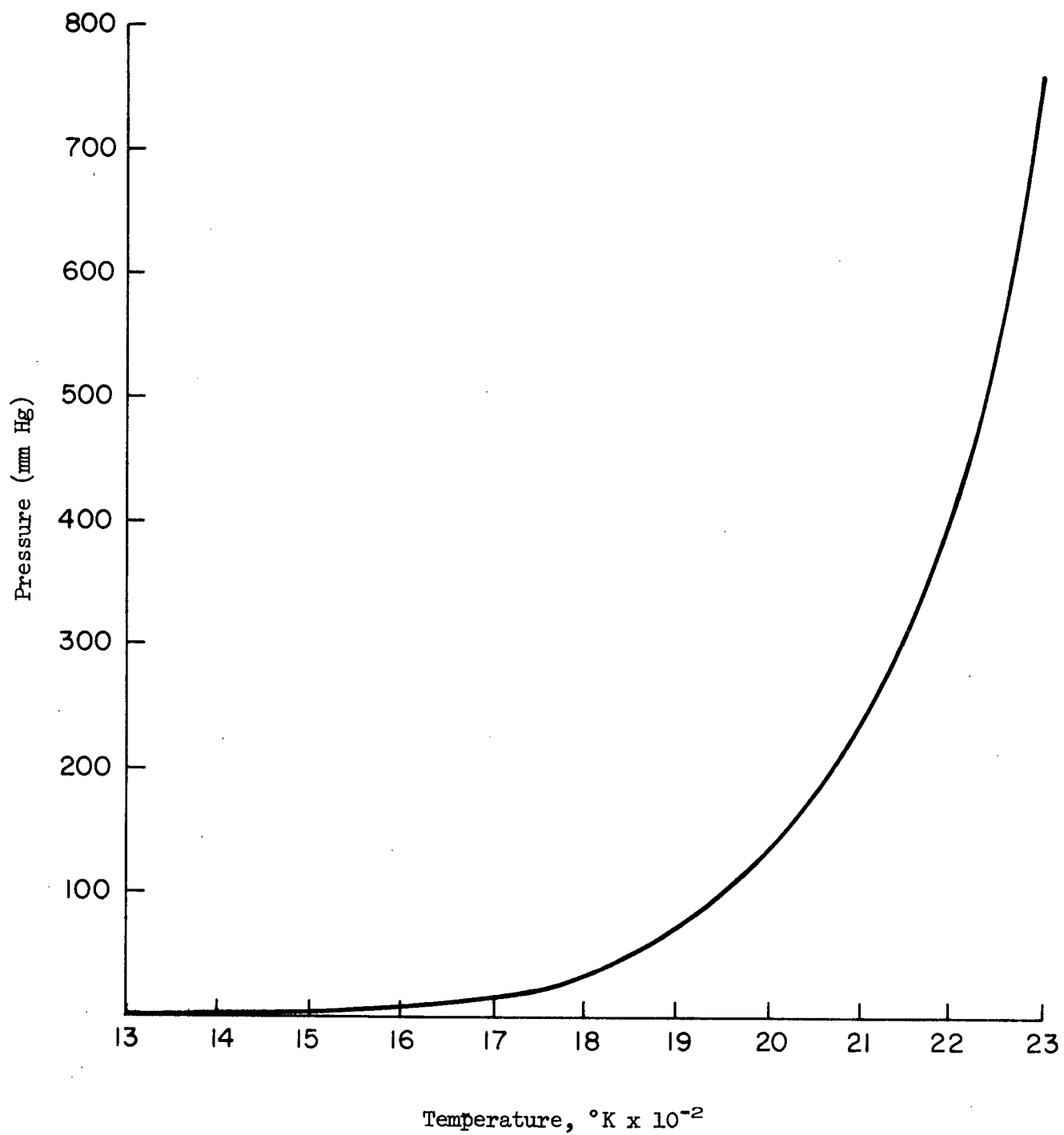


Fig. 4 - Vapor Pressure of CaCl₂

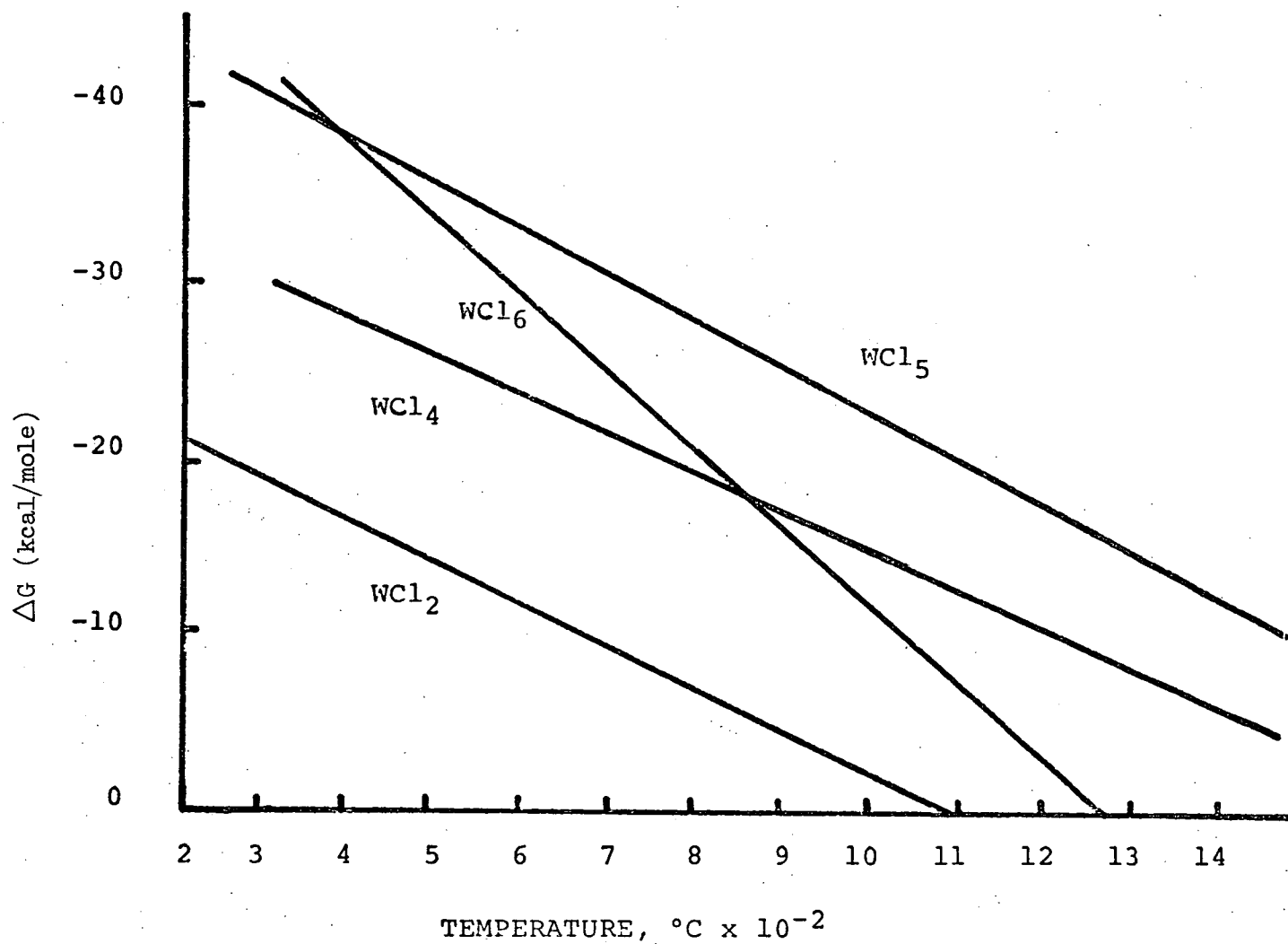


Fig. 5 - Free Energies of WCl_2 , WCl_4 , WCl_5 , and WCl_6

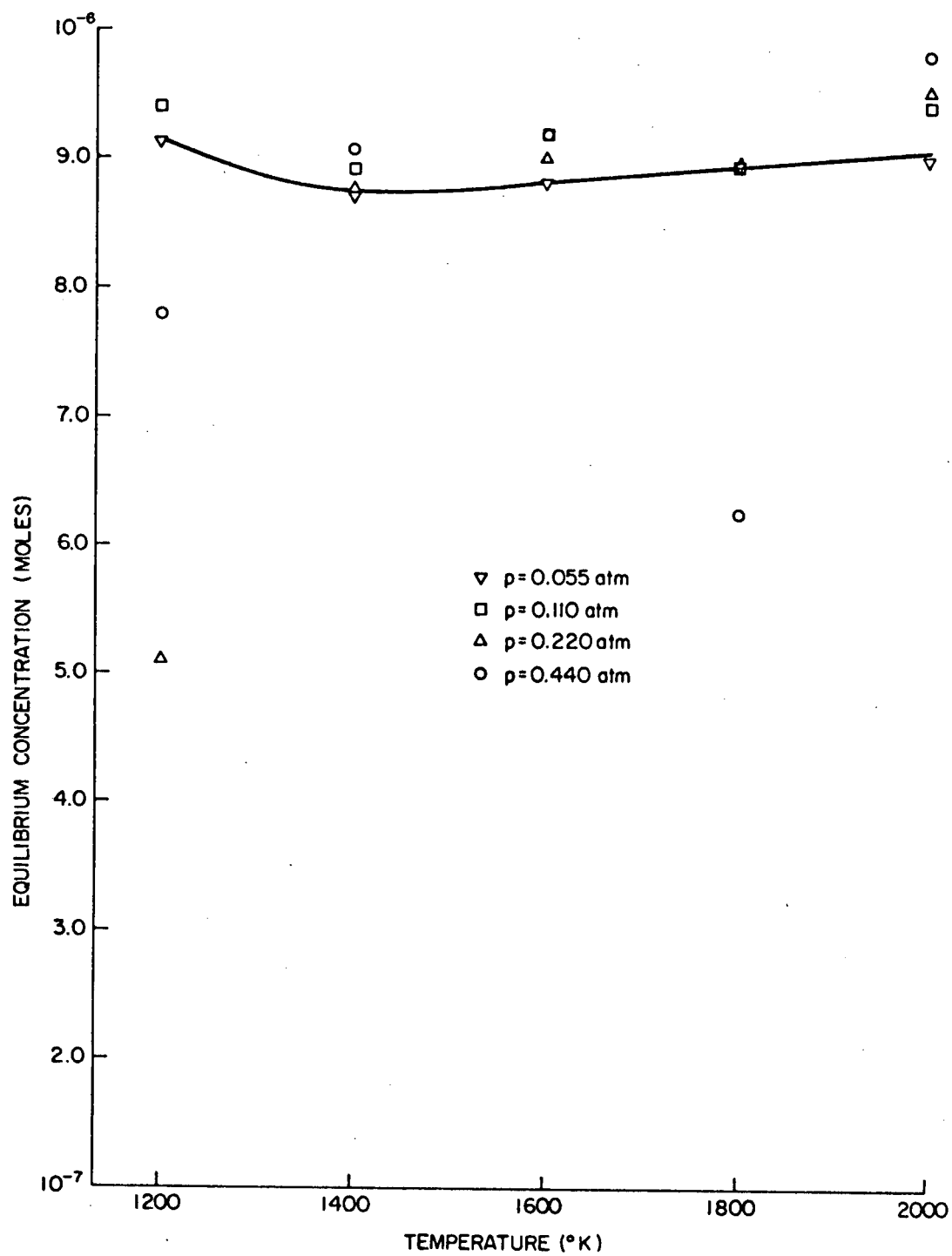


Fig. 6 - Equilibrium Concentration of CaWO_4

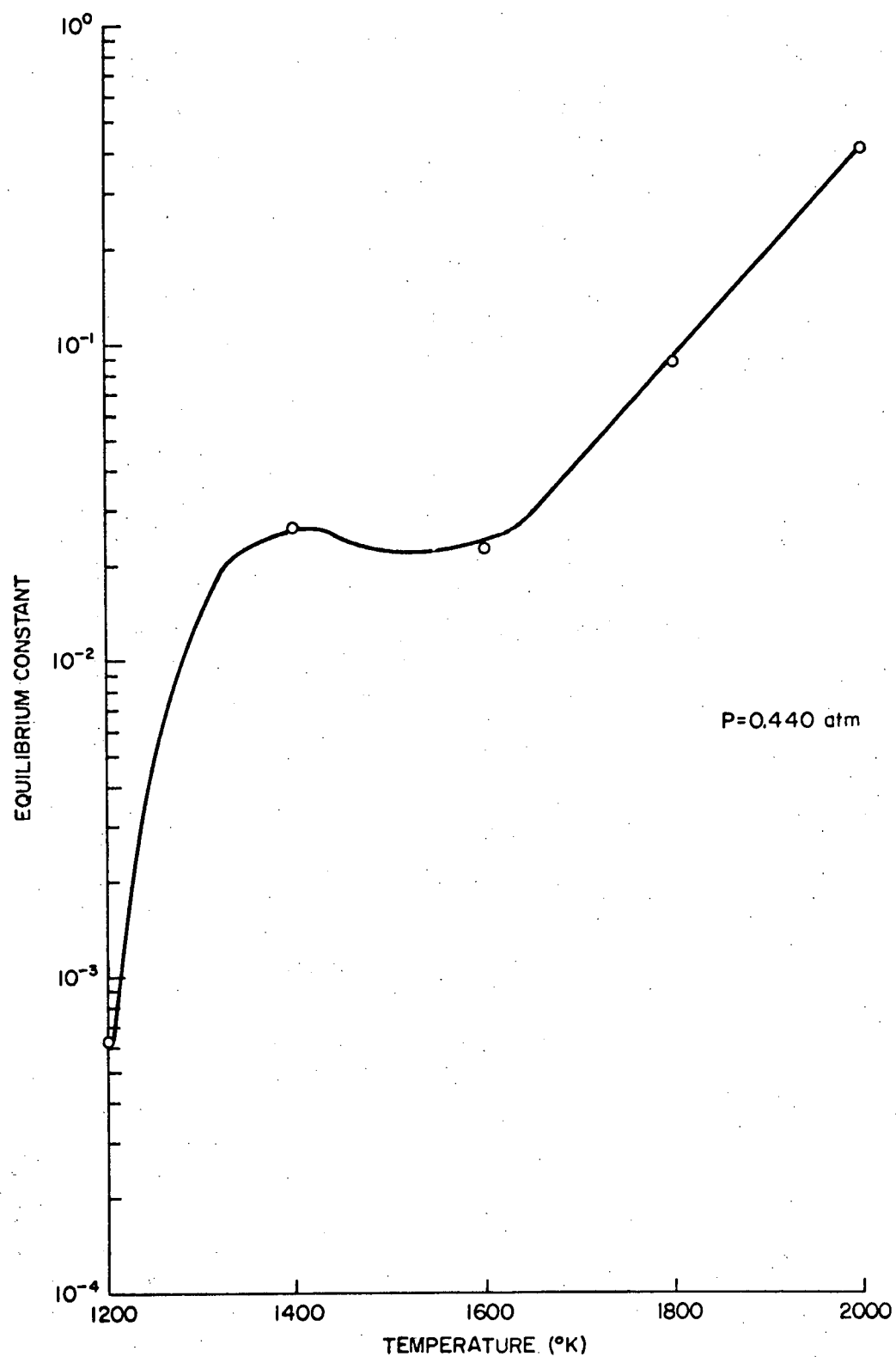
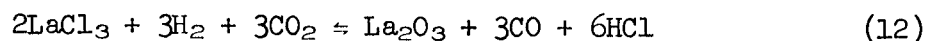


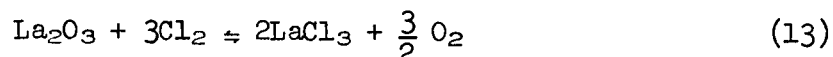
Fig. 7 - Equilibrium Constant as a Function of Temperature for CaWO_4

E. THERMODYNAMICS OF LANTHANUM OXIDE (La_2O_3) REACTIONS

The summary reaction for vapor phase production of lanthana powders,



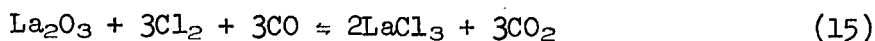
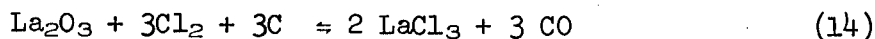
was introduced into the IBM 360/75 program for computing thermodynamic reaction free energies and equilibrium constants. The data output, Table IX, shows that temperatures above 1600°C are necessary to make the reaction thermodynamically favored. Lanthanum chloride, LaCl_3 , can be obtained by chlorination of La_2O_3 ,



which is thermodynamically feasible at all temperatures, Table X. The vapor pressure of lanthanum chloride, Figure 8, indicates that chlorination above 1500°C will be required to ensure volatilization of the chloride. These restrictions on chlorination and reaction pose severe technical problems in the vapor phase reaction system now employed.

Growth conditions for La_2O_3 were calculated using program EQUICA. The equilibrium concentration of La_2O_3 as a function of temperature and pressure is shown in Figure 9. Figure 10 shows the equilibrium constant for Ca_2O_3 formation at various temperatures.

In addition to the production of lanthanum chloride by reaction (13), lanthanum chloride was produced by the following reactions:



Thermodynamic data for reactions (14) and (15) are summarized in Tables XI and XII, respectively.

LaOCl Reactions

Since LaOCl occurred frequently in the La_2O_3 runs, the thermodynamics of possible reactions were considered. Free-energy data were not available for LaOCl and an estimate was made using the following reaction



Assuming that the free-energy change is at least $-10,000$ cal/mole, a free-energy value for LaOCl was calculated and summarized in Table XIII. Possible reactions occurring in the chlorinator are:

Table IX - Thermodynamic Data for Lanthanum
Oxide System (La_2O_3)

THE FOLLOWING DATA IS FOR THE REACTION				
REACTANTS	2 LaCl_3	3 CO_2	3 H_2	
PRODUCTS	1 La_2O_3	6 HCl	3 CO	
DELTA G IS	121850 CALORIES	AT 300 DEGREES	KELVIN AND THE	EQUILIBRIUM CONSTANT IS 0.0
DELTA G IS	113100 CALORIES	AT 400 DEGREES	KELVIN AND THE	EQUILIBRIUM CONSTANT IS 0.1585E-61
DELTA G IS	98800 CALORIES	AT 500 DEGREES	KELVIN AND THE	EQUILIBRIUM CONSTANT IS 0.6471E-43
DELTA G IS	93700 CALORIES	AT 600 DEGREES	KELVIN AND THE	EQUILIBRIUM CONSTANT IS 0.7362E-34
DELTA G IS	83750 CALORIES	AT 700 DEGREES	KELVIN AND THE	EQUILIBRIUM CONSTANT IS 0.7078E-26
DELTA G IS	72500 CALORIES	AT 800 DEGREES	KELVIN AND THE	EQUILIBRIUM CONSTANT IS 0.1557E-19
DELTA G IS	65400 CALORIES	AT 900 DEGREES	KELVIN AND THE	EQUILIBRIUM CONSTANT IS 0.1310E-15
DELTA G IS	55350 CALORIES	AT 1000 DEGREES	KELVIN AND THE	EQUILIBRIUM CONSTANT IS 0.7985E-12
DELTA G IS	45300 CALORIES	AT 1100 DEGREES	KELVIN AND THE	EQUILIBRIUM CONSTANT IS 0.9977E-09
DELTA G IS	37400 CALORIES	AT 1200 DEGREES	KELVIN AND THE	EQUILIBRIUM CONSTANT IS 0.1542E-06
DELTA G IS	31650 CALORIES	AT 1300 DEGREES	KELVIN AND THE	EQUILIBRIUM CONSTANT IS 0.4772E-05
DELTA G IS	26100 CALORIES	AT 1400 DEGREES	KELVIN AND THE	EQUILIBRIUM CONSTANT IS 0.8419E-04
DELTA G IS	20150 CALORIES	AT 1500 DEGREES	KELVIN AND THE	EQUILIBRIUM CONSTANT IS 0.1159E-02
DELTA G IS	13100 CALORIES	AT 1600 DEGREES	KELVIN AND THE	EQUILIBRIUM CONSTANT IS 0.1624E-01
DELTA G IS	8000 CALORIES	AT 1700 DEGREES	KELVIN AND THE	EQUILIBRIUM CONSTANT IS 0.9364E-01
DELTA G IS	1650 CALORIES	AT 1800 DEGREES	KELVIN AND THE	EQUILIBRIUM CONSTANT IS 0.6304E 00
DELTA G IS	-4850 CALORIES	AT 1900 DEGREES	KELVIN AND THE	EQUILIBRIUM CONSTANT IS 0.3613E 01
DELTA G IS	-10250 CALORIES	AT 2000 DEGREES	KELVIN AND THE	EQUILIBRIUM CONSTANT IS 0.1319E 02

Table X - Thermodynamic Data for Lanthanum
Oxide Chlorination

THE FOLLOWING DATA IS FOR THE REACTION

REACTANTS	1 LA2O3	3 CL2	
PRODUCTS	2 LACL3	3 O2	
DELTA G IS	-74000 CALORIES AT	300 DEGREES KELVIN AND THE	EQUILIBRIUM CONSTANT IS 0.8193E 54
DELTA G IS	-72900 CALORIES AT	400 DEGREES KELVIN AND THE	EQUILIBRIUM CONSTANT IS 0.6824E 40
DELTA G IS	-70300 CALORIES AT	500 DEGREES KELVIN AND THE	EQUILIBRIUM CONSTANT IS 0.5378E 31
DELTA G IS	-68800 CALORIES AT	600 DEGREES KELVIN AND THE	EQUILIBRIUM CONSTANT IS 0.1155E 26
DELTA G IS	-66500 CALORIES AT	700 DEGREES KELVIN AND THE	EQUILIBRIUM CONSTANT IS 0.5807E 21
DELTA G IS	-62600 CALORIES AT	800 DEGREES KELVIN AND THE	EQUILIBRIUM CONSTANT IS 0.1267E 18
DELTA G IS	-62700 CALORIES AT	900 DEGREES KELVIN AND THE	EQUILIBRIUM CONSTANT IS 0.1686E 16
DELTA G IS	-59400 CALORIES AT	1000 DEGREES KELVIN AND THE	EQUILIBRIUM CONSTANT IS 0.9615E 13
DELTA G IS	-56700 CALORIES AT	1100 DEGREES KELVIN AND THE	EQUILIBRIUM CONSTANT IS 0.1846E 12
DELTA G IS	-56300 CALORIES AT	1200 DEGREES KELVIN AND THE	EQUILIBRIUM CONSTANT IS 0.1797E 11
DELTA G IS	-57000 CALORIES AT	1300 DEGREES KELVIN AND THE	EQUILIBRIUM CONSTANT IS 0.3831E 10
DELTA G IS	-58500 CALORIES AT	1400 DEGREES KELVIN AND THE	EQUILIBRIUM CONSTANT IS 0.1358E 10
DELTA G IS	-59300 CALORIES AT	1500 DEGREES KELVIN AND THE	EQUILIBRIUM CONSTANT IS 0.4372E 09
DELTA G IS	-59900 CALORIES AT	1600 DEGREES KELVIN AND THE	EQUILIBRIUM CONSTANT IS 0.1523E 09
DELTA G IS	-61400 CALORIES AT	1700 DEGREES KELVIN AND THE	EQUILIBRIUM CONSTANT IS 0.7837E 08
DELTA G IS	-62400 CALORIES AT	1800 DEGREES KELVIN AND THE	EQUILIBRIUM CONSTANT IS 0.3776E 08
DELTA G IS	-63400 CALORIES AT	1900 DEGREES KELVIN AND THE	EQUILIBRIUM CONSTANT IS 0.1965E 08
DELTA G IS	-64000 CALORIES AT	2000 DEGREES KELVIN AND THE	EQUILIBRIUM CONSTANT IS 0.9867E 07

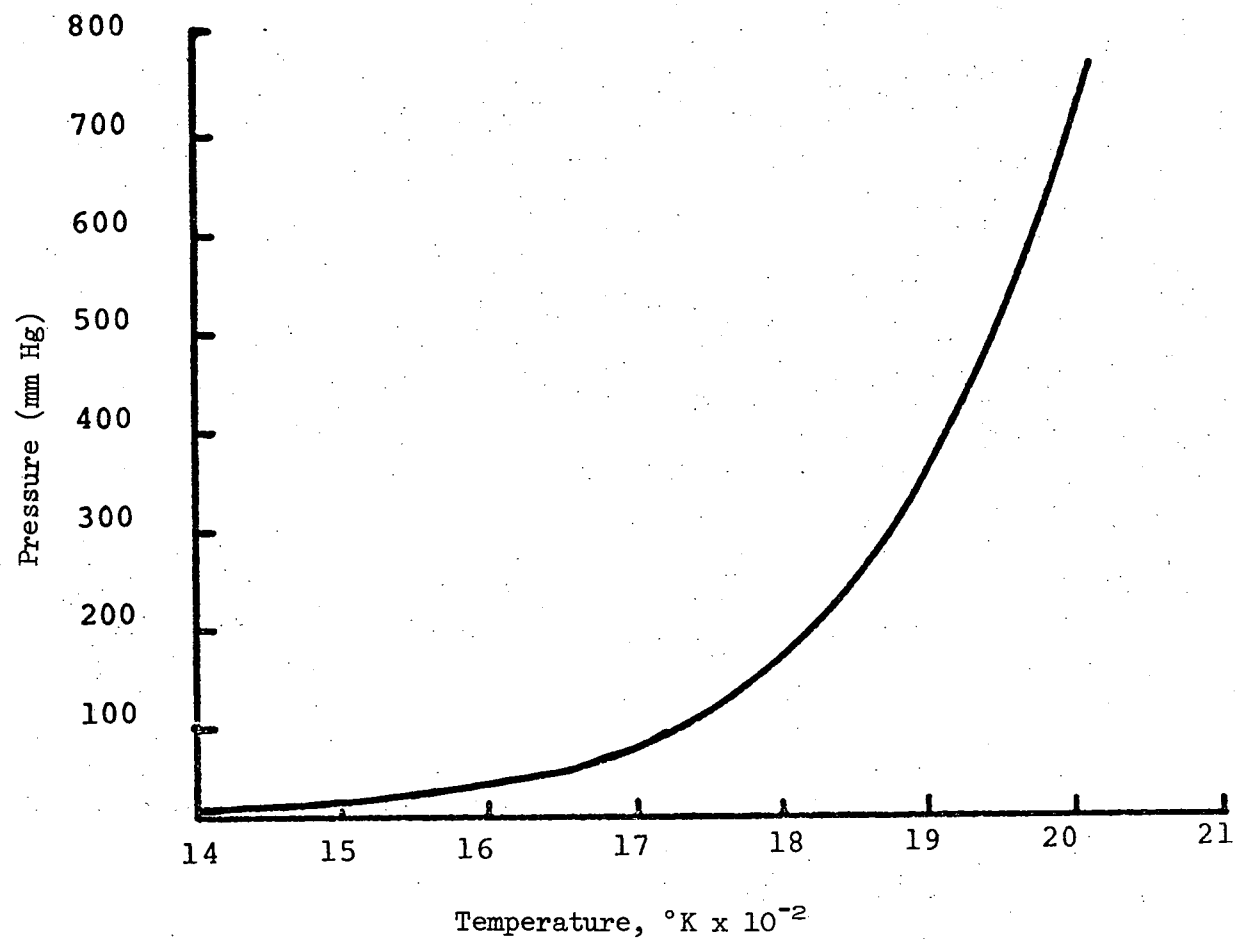


Fig. 8 - Vapor Pressure of LaCl_3 vs. Temperature

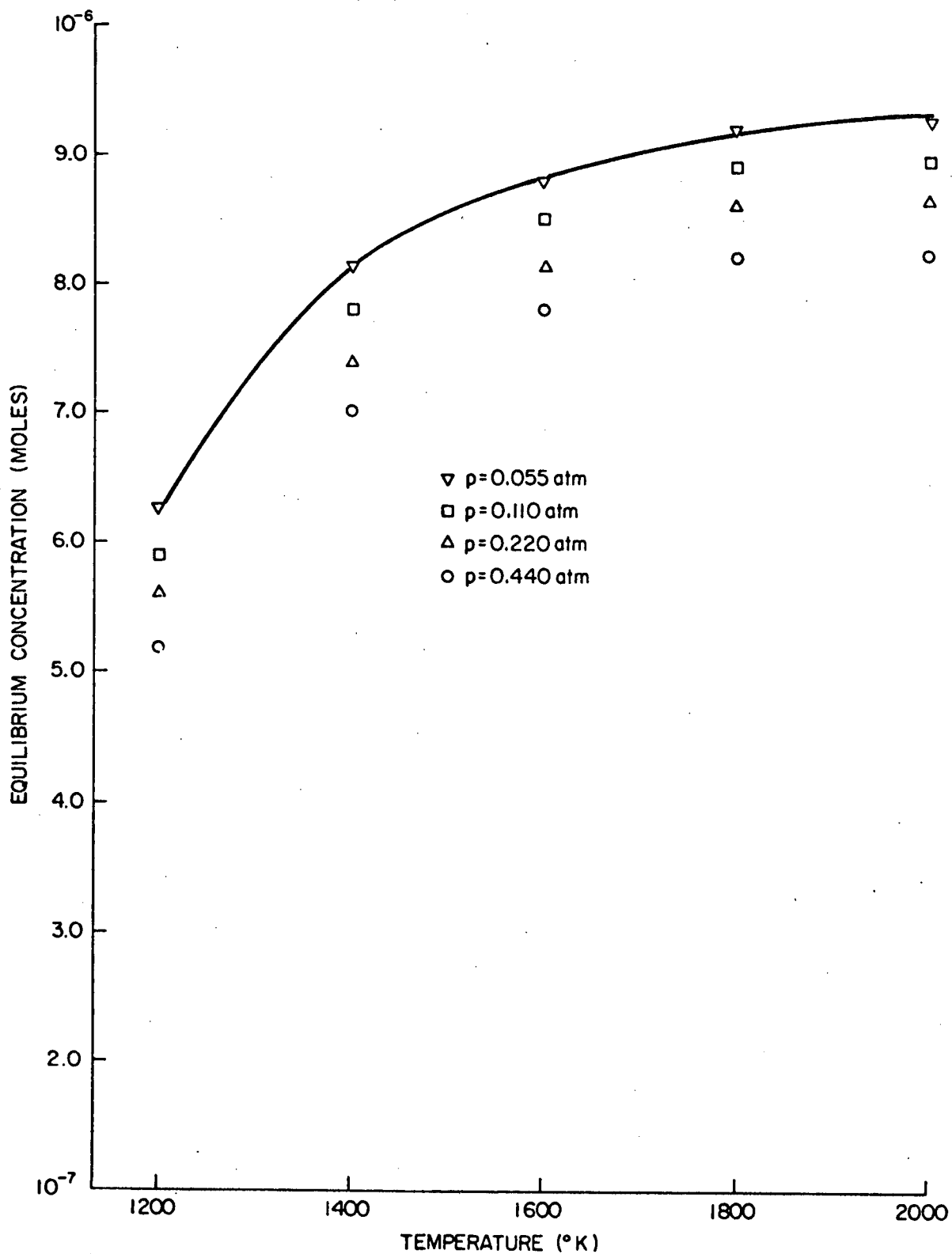


Fig. 9 - Equilibrium Concentration of La_2O_3 as a Function of System Conditions

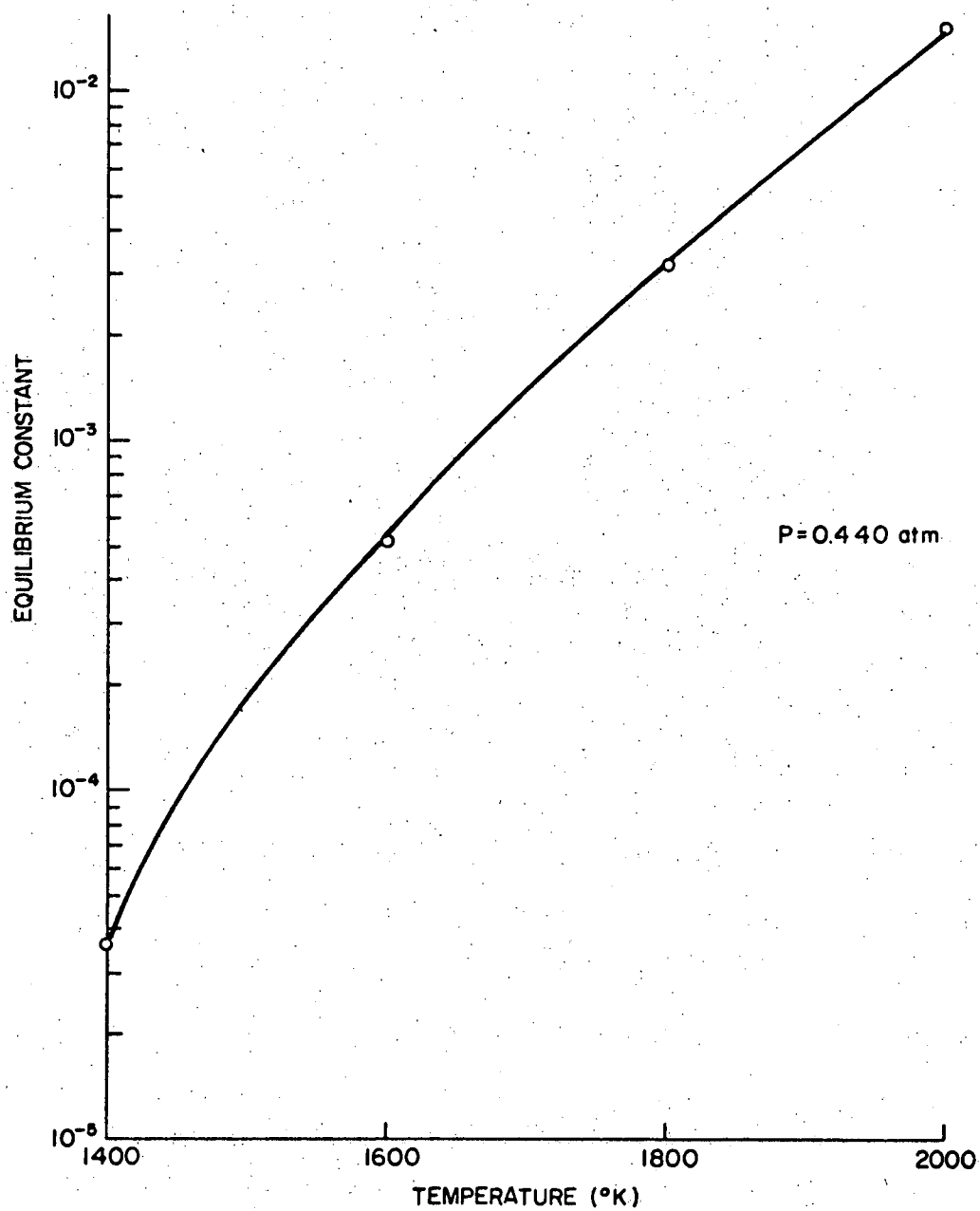


Fig. 10 - Equilibrium Constant as a Function of Temperature for La_2O_3

Table XI - Free-Energy Change and Equilibrium Constant
for Chlorination of La_2O_3 with Carbon*

T(°C)	T(°K)	ΔG° Reaction (kcal/mole)	K_p Reaction
227	500	-181.60	7.24×10^{75}
327	600	-186.85	1.16×10^{68}
427	700	-191.15	4.84×10^{59}
527	800	-193.70	8.33×10^{52}
627	900	-200.25	4.28×10^{48}
727	1000	-203.25	2.65×10^{44}
827	1100	-207.00	1.35×10^{43}
927	1200	-212.75	5.63×10^{38}
1027	1300	-200.05	9.73×10^{36}
1127	1400	-227.25	3.01×10^{35}
1227	1500	-234.50	1.48×10^{34}
1327	1600	-241.70	1.04×10^{33}
1427	1700	-249.35	1.15×10^{32}
1527	1800	-256.35	1.34×10^{31}
1627	1900	-263.65	2.13×10^{30}
1727	3000	-270.25	3.42×10^{29}

* $\text{La}_2\text{O}_3 + 3\text{Cl}_2 + 3\text{C} \rightleftharpoons 2\text{LaCl}_3 + 3\text{CO}$

Table XIII - Free-Energy Change and Equilibrium Constant
for Chlorination of La_2O_3 with CO^*

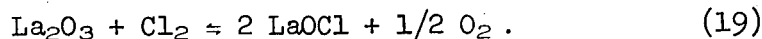
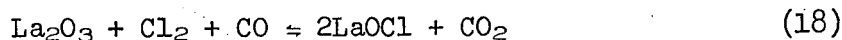
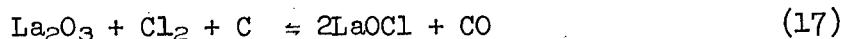
T(°C)	T(°K)	ΔG° Reaction (kcal/mole)	K_p Reaction
327	600	-234.10	7.24×10^{75}
427	700	-225.35	2.31×10^{70}
527	800	-215.06	5.50×10^{58}
627	900	-208.80	5.10×10^{50}
727	1000	-199.35	3.73×10^{43}
827	1100	-190.20	6.20×10^{37}
927	1200	-183.80	3.00×10^{33}
1027	1300	-178.05	8.62×10^{29}
1127	1400	-174.06	1.46×10^{27}
1227	1500	-168.35	3.39×10^{24}
1327	1600	-162.50	1.58×10^{22}
1427	1700	-158.00	2.06×10^{20}
1527	1800	-153.15	3.95×10^{18}
1627	1900	-147.85	1.02×10^{17}
1727	2000	-142.75	3.98×10^{15}

* $\text{La}_2\text{O}_3 + 3\text{Cl}_2 + 3\text{CO} \rightleftharpoons 2\text{LaCl}_3 + 3\text{CO}_2$

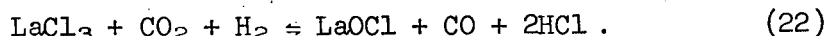
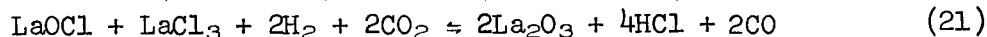
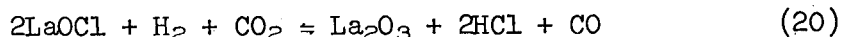
Table XIII - Estimate of Maximum Free-Energy of LaOCl*

T(°K)	T(°C)	$\Delta G^\circ \text{ LaCl}_3$ (kcal/mole)	$\Delta G^\circ \text{ La}_2\text{O}_3$ (kcal/mole)	$\Delta G^\circ \text{ LaOCl}$ Estimate (kcal/mole)
300	27	-238.30	-402.60	-223.63
400	127	-233.00	-393.10	-218.70
500	227	-227.40	-384.50	-213.97
600	327	-222.70	-376.60	-209.77
700	427	-217.30	-368.10	-205.13
800	527	-211.30	-360.00	-200.43
900	627	-207.00	-351.30	-196.10
1000	727	-200.90	-342.40	-191.10
1100	827	-195.80	-334.90	-186.90
1200	927	-191.60	-326.90	-182.83
1300	1027	-188.00	-319.00	-179.00
1400	1127	-184.50	-310.50	-175.00
1500	1227	-180.90	-302.50	-171.13
1600	1327	-177.20	-294.50	-167.23
1700	1427	-173.70	-286.00	-163.23
1800	1527	-170.20	-278.00	-159.40
1900	1627	-166.70	-270.00	-155.57
2000	1727	-163.00	-262.00	-151.67

* $\Delta G^\circ \text{ LaOCl} = 1/3 \Delta G^\circ \text{ La}_2\text{O}_3 + 1/3 \Delta G^\circ \text{ LaCl}_3 = -10,000 \text{ cal/mole LaOCl}$



Thermodynamic data for reactions (17), (18) and (19) are summarized in Tables XIV, XV, and XVI, respectively. Possible reactions occurring in the reaction zone are:



Thermodynamic data are summarized in Tables XVII, XVIII and XIX.

F. REACTOR DESIGN, MIXING AND HEAT TRANSFER

Prior experience in the area of particle production by vapor-phase reaction has shown that mixing of reactants was limited. To improve the mixing of reactant gases, a detailed study was performed and the results were used to design a reactor to provide suitable mixing of the gaseous species.

1. Thermodynamic and Transport Properties

Energy balances, fluid-mechanical, mixing and heat transfer calculations require the knowledge of thermodynamic and transport properties. Densities of reactants and products as well as heat capacities, viscosities, thermal conductivities and mass diffusivities were calculated or estimated whenever not available in literature.

a. Viscosity

For the estimation of gas viscosity at low densities, the following formula was used,¹²

$$\mu = 2.6693 \times 10^{-5} \frac{\sqrt{MT}}{\sigma^2 \Omega_\mu} \quad (23)$$

Table XIV - Free-Energy Changes and Equilibrium Constants
for LaOCl*

T(°C)	T(°K)	ΔG° Reaction (kcal/mole)	K_p Reaction
27	300	-77.47	2.75×10^{56}
127	400	-79.30	2.14×10^{48}
227	500	-80.53	1.60×10^{35}
327	600	-82.28	9.43×10^{29}
427	700	-83.72	1.38×10^{26}
527	800	-84.57	1.27×10^{23}
627	900	-86.75	1.17×10^{21}
727	1000	-87.75	1.51×10^{19}
827	1100	-89.00	4.83×10^{17}
927	1200	-90.92	3.63×10^{16}
1027	1300	-93.35	4.95×10^{15}
1127	1400	-95.75	8.88×10^{14}
1227	1500	-98.17	2.01×10^{14}
1327	1600	-100.57	5.47×10^{13}
1427	1700	-103.12	1.81×10^{13}
1527	1800	-105.45	6.37×10^{12}
1627	1900	-107.88	2.57×10^{12}
1727	2000	-110.08	1.07×10^{12}

* $\text{La}_2\text{O}_3 + \text{Cl}_2 + \text{C} \rightleftharpoons 2\text{LaOCl} + \text{CO}$

Table XV - Free-Energy Changes and Equilibrium Constants
for LaOCl *

T(°C)	T(°K)	ΔG° Reaction (kcal/mole)	K_p Reaction
27	300	-106.12	7.24×10^{75}
127	400	-103.60	4.07×10^{56}
227	500	-100.73	1.08×10^{44}
327	600	-98.03	5.15×10^{35}
427	700	-95.12	5.00×10^{28}
527	800	-91.67	1.11×10^{25}
627	900	-89.60	5.75×10^{21}
727	1000	-86.45	7.86×10^{18}
827	1100	-83.40	3.73×10^{16}
927	1200	-81.27	6.34×10^{14}
1027	1300	-79.35	2.19×10^{13}
1127	1400	-78.00	1.51×10^{12}
1227	1500	-76.12	1.23×10^{11}
1327	1600	-74.17	1.35×10^{10}
1427	1700	-72.67	2.20×10^9
1527	1800	-71.05	4.24×10^8
1627	1900	-69.28	9.34×10^7
1727	2000	-67.58	2.43×10^7

* $\text{La}_2\text{O}_3 + \text{Cl}_2 + \text{CO} \rightleftharpoons 2\text{LaOCl} + \text{CO}_2$

Table XVI - Free-Energy Changes and Equilibrium Constants
for LaOCl^*

T(°C)	T(°K)	ΔG° Reaction (kcal/mole)	K_p Reaction
27	300	-44.67	3.48×10^{31}
127	400	-44.30	1.61×10^{24}
227	500	-43.43	9.70×10^{18}
327	600	-42.93	4.37×10^{15}
427	700	-42.16	1.47×10^{13}
527	800	-40.87	1.47×10^{11}
627	900	-40.90	8.56×10^9
727	1000	-39.80	5.00×10^8
827	1100	-38.90	5.36×10^7
927	1200	-38.77	1.15×10^7
1027	1300	-39.00	3.61×10^6
1127	1400	-39.50	1.47×10^6
1227	1500	-39.77	6.23×10^5
1327	1600	-39.97	2.88×10^5
1427	1700	-40.47	1.60×10^5
1527	1800	-40.80	9.00×10^4
1627	1900	-41.13	5.39×10^4
1727	2000	-41.33	3.29×10^4

* $\text{La}_2\text{O}_3 + \text{Cl}_2 \rightleftharpoons 2\text{LaOCl} + 1/2 \text{O}_2$

Table XVII - Free-Energy Changes and Equilibrium Constants
for La_2O_3 Production from LaOCl *

$T(^{\circ}\text{C})$	$T(^{\circ}\text{K})$	ΔG° Reaction (kcal/mole)	K_p Reaction
27	300	60.62	6.88×10^{-45}
127	400	57.70	2.96×10^{-32}
227	500	52.93	7.26×10^{-24}
327	600	51.23	2.17×10^{-17}
427	700	47.92	1.09×10^{-15}
527	800	44.17	8.58×10^{-13}
627	900	41.80	7.06×10^{-11}
727	1000	38.45	3.95×10^{-9}
827	1100	35.10	1.06×10^{-7}
927	1200	32.47	1.22×10^{-6}
1027	1300	30.55	7.31×10^{-6}
1127	1400	28.76	3.31×10^{-5}
1227	1500	26.72	1.28×10^{-4}
1327	1600	24.37	4.69×10^{-4}
1427	1700	22.67	1.22×10^{-3}
1527	1800	20.55	3.20×10^{-3}
1627	1900	18.38	7.68×10^{-3}
1727	2000	16.58	1.54×10^{-2}

* $2 \text{LaOCl} + \text{H}_2 + \text{CO}_2 \rightleftharpoons \text{La}_2\text{O}_3 + 2 \text{HCl} + \text{CO}$

Table XVIII - Free-Energy Changes and Equilibrium Constants
for La_2O_3 Production*

T(°C)	T(°K)	ΔG° Reaction (kcal/mole)	K_p Reaction
27	300	91.23	3.40×10^{-67}
127	400	85.40	2.17×10^{-47}
227	500	75.89	6.85×10^{-34}
327	600	72.47	4.00×10^{-27}
427	700	65.83	2.78×10^{-21}
527	800	58.33	1.16×10^{-16}
627	900	53.60	9.62×10^{-14}
727	1000	46.90	5.61×10^{-11}
827	1100	40.20	1.03×10^{-8}
927	1200	34.93	4.34×10^{-7}
1027	1300	31.10	5.90×10^{-6}
1127	1400	27.40	5.28×10^{-5}
1227	1500	23.43	3.85×10^{-4}
1327	1600	18.73	2.76×10^{-3}
1427	1700	15.33	1.07×10^{-2}
1527	1800	11.10	4.49×10^{-2}
1627	1900	6.77	1.67×10^{-1}
1727	2000	3.17	4.51×10^{-1}

* $\text{LaOCl} + \text{LaCl}_3 + 2\text{H}_2 + 2\text{CO}_2 \rightleftharpoons \text{La}_2\text{O}_3 + 4\text{HCl} + 2\text{C}$

Table XIX - Free-Energy Changes and Equilibrium Constants
for LaOCl Production from LaCl₃*

T(°C)	T(°K)	ΔG° Reaction (kcal/mole)	K_p Reaction
27	300	30.62	4.94×10^{-23}
127	400	27.70	7.31×10^{-16}
227	500	22.93	9.44×10^{-11}
327	600	21.23	1.84×10^{-8}
427	700	17.92	2.54×10^{-6}
527	800	14.17	1.35×10^{-4}
627	900	11.80	1.36×10^{-3}
727	1000	8.45	1.42×10^{-2}
827	1100	5.10	9.70×10^{-2}
927	1200	2.47	3.55×10^{-1}
1027	1300	0.55	8.08×10^{-1}
1127	1400	-1.35	1.60
1227	1500	-3.28	3.01
1327	1600	-5.63	5.88
1427	1700	-7.33	8.77
1527	1800	-9.45	1.40×10^1
1627	1900	-11.62	2.17×10^1
1727	2000	-13.42	2.93×10^1

* $\text{LaCl}_3 + \text{CO}_2 + \text{H}_2 \rightleftharpoons \text{LaOCl} + \text{CO} + 2\text{HCl}$

in which $\mu [=] \text{g cm}^{-1} \text{ sec}^{-1}$, $T [=] ^\circ\text{K}$, $\sigma [=] \text{\AA}$ and Ω_μ is a slowly varying function of the dimensionless temperature KT/ϵ .¹³ Values of ϵ/K and collision diameter, σ , were calculated from

$$\epsilon/K = 1.15 T_b, \sigma = 1.166 (\tilde{V}_b)_{\text{liq}}^{1/3} \quad (24)$$

in which ϵ/K and T_b are in $^\circ\text{K}$, $\sigma [=] \text{\AA}$, and $\tilde{V} [=] \text{cm}^3 (\text{g-mole})^{-1}$. For multicomponent gas mixtures, the semi-empirical formula of Wilke¹⁴ was used.

$$\mu_{\text{mix}} = \frac{\sum_{i=1}^n \frac{x_i \mu_i}{\sum_{j=1}^n x_j \phi_{ij}}}{\sum_{j=1}^n x_j \phi_{ij}} \quad (25)$$

where

$$\phi_{ij} = \frac{1}{\sqrt{8}} \left(1 + \frac{M_i}{M_j} \right)^{-1/2} \left[1 + \left(\frac{\mu_i}{\mu_j} \right)^{1/2} \left(\frac{M_j}{M_i} \right)^{1/4} \right]^2 \quad (26)$$

and n is the number of chemical species in the mixture; x_i and x_j are the mole fractions of species i and j ; μ_i , μ_j and M_i , M_j are the viscosities and molecular weights respectively.

b. Thermal Conductivity

The Eucken approximation for estimating thermal conductivity of a polyatomic gas at low density was used.¹⁵

$$k = (C_p + 5/4 R) \mu/M \quad (27)$$

where

μ = viscosity
 M = molecular weight
 R = gas content
 C_p = heat capacity.

For a gas mixture (n-components),

$$k_{\text{mix}} = \frac{\sum_{i=1}^n \frac{x_i k_i}{\sum_{j=1}^n x_j \phi_{ij}}} \quad (28)$$

where x_i , x_j and ϕ_{ij} are as in equations (25) and (26).

c. Mass Diffusivity

The following formula for the estimation of mass diffusivity of gases at low density was used.¹⁶

$$D_{AB} = 0.0018583 \frac{\sqrt{T^3 \left(\frac{1}{M_A} + \frac{1}{M_B} \right)}}{P \sigma_{AB}^2 \Omega_D} \quad (29)$$

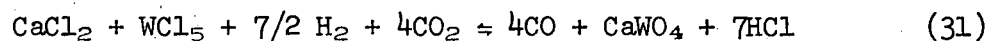
where

$$\sigma_{AB} = 1/2 (\sigma_A + \sigma_B), \quad (30)$$

$T [=]$ °K, M_A , M_B are molecular weights of A and B, $p [=]$ atm, $\sigma_{AB} [=]$ Å, Ω_D is a dimensionless function of temperature, and $D_{AB} [=]$ cm²/sec. A summary of transport properties are listed in Table XX.

2. Reactor Gas Mixing

Past experience in the area of gas phase particle production¹⁷ had shown that mixing of reactants was indeed limited. A detailed study of this problem was undertaken to design a reactor which would provide adequate mixing of the reactants and increase the product yield. The example product was CaWO₄, produced by the overall reaction.



Thermodynamic calculations, previous experience and existing experimental facilities dictated the choice of operating conditions, as well as the reactor configuration. Fluid mechanical and mixing calculations determined

Table XX - Estimated Transport Properties

Species	Viscosity μ $\text{g cm}^{-1} \text{sec}^{-1}$	Mass Diff. D_{AB} cm^2/sec	Temperature $^{\circ}\text{K}$	Kinematic Viscosity $\mu/\rho, \text{cm}^2/\text{sec}$
CaCl_2	3.49×10^{-4}		2,073	5.33×10^{-2}
WCl_5	6.20×10^{-4}		2,073	2.91×10^{-2}
CaCl_2 } WCl_5 }		(at $p = 1.0 \text{ atm}$) 0.37	2,073	
O_2	8.0×10^{-4}		2,073	
CO_2	4.9×10^{-4}		2,073	3.26
CO_2	5.24×10^{-4}		1,598	
H_2	2.65×10^{-4}		1,598	
ZnCl_2	5.10×10^{-4}		1,598	
TiCl_4	4.60×10^{-4}		1,598	

the efficiency for the degree of mixing under the chosen operating conditions and reactor configuration.

In Figs. 11 and 12, the proposed reactor configuration is shown. One gas stream is composed of $\text{O}_2 + \text{CO}_2$, and the other gas stream is composed of $\text{CaCl}_2 + \text{WCl}_5 + \text{H}_2$. Two heat sources were considered: an induction furnace and a oxy-hydrogen flame. A preliminary reactor design was based on stoichiometric reactant flow rates to give a first estimate of reactor dimensions. Heat balance calculations gave information of the additional flow rates of oxy-hydrogen flame. The oxy-hydrogen flame would provide heat for the reaction and create instability and turbulence at the central jet. Revised calculations based on the new rates provided the final reactor configurations and dimensions.

Preliminary Reactor Design: The selected operating conditions were:

Pressure: 0.5 atm

Temperature: 2,074°K

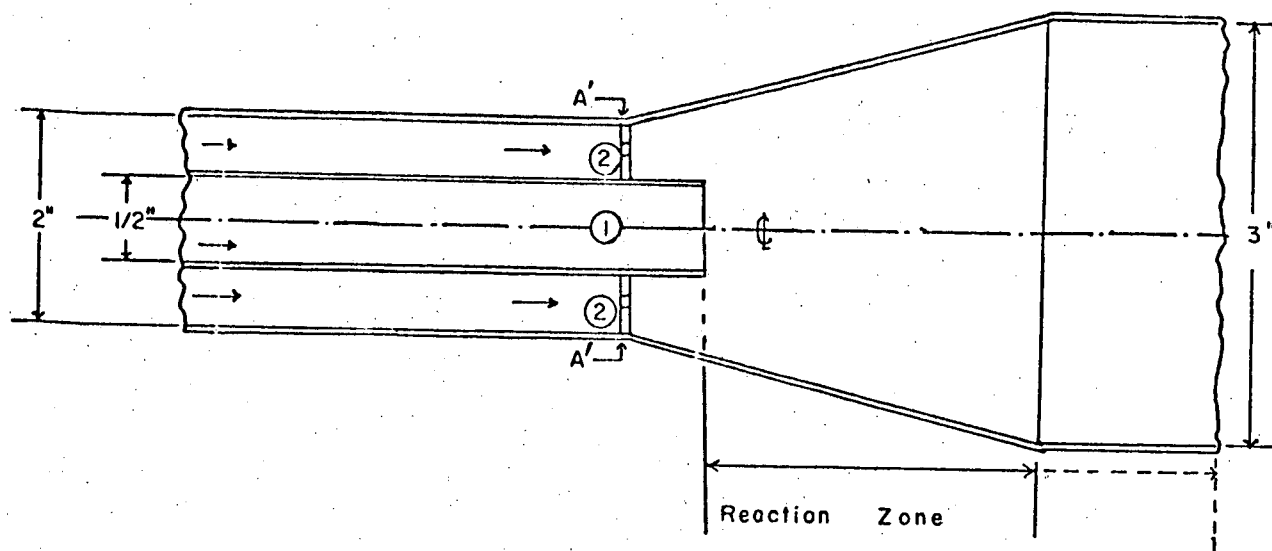


Fig. 11 - Proposed Reactor Configuration

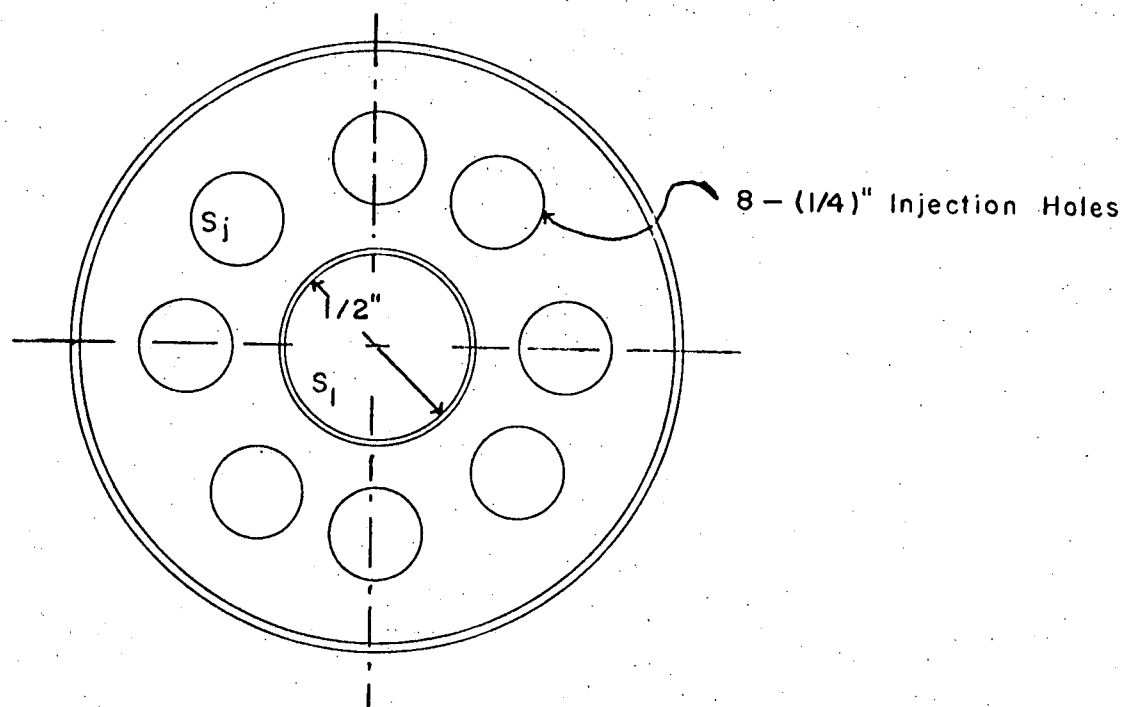


Fig. 12 - View A¹A¹ of Figure 11

Gas flow rates:

CO ₂	800	cc/min	(STP)
CaCl ₂	200	" "	"
WCl ₅	200	" "	"
H ₂	700	" "	"

Stream 1 forms a jet issuing from a 1/2" I.D. tube (central jet) with a volumetric flow rate of $V_1 = 1.2 \times 10^4$ cc/min and an average issuing velocity of $\bar{v}_1 = 1.57 \times 10^4$ cm/sec under the selected operating conditions. Stream 2 is split into eight jets issuing from eight 1/4" orifices (peripheral jets) with a total volumetric flow rate of $V_2 = 1.66 \times 10^4$ cc/min and an average issuing velocity of 1.11×10^2 cm/sec.

The density and kinematic viscosity of Stream 2 was calculated as $P_2 = 2.18 \times 10^{-4}$ g/cc and $\nu_2 = 1.7$ cm²/sec respectively; and that of Stream 1 as $P_1 = 1.2 \times 10^{-4}$ gm/cc and $\nu_1 = 3.26$ cm²/sec, respectively. Hence the Reynolds numbers of the jets are based on their issuing velocity and diameter.

$$\text{Central jet: } (N_{Re})_1 = \frac{(157) (1/2 \times 2.54)}{3.26} = 49 \quad (32)$$

$$\text{Peripheral jets: } (N_{Re})_2 = \frac{(111) (1/4 \times 2.54)}{1.70} = 41 \quad (33)$$

Since the transition Reynolds number for a free jet is approximately 30, turbulent velocity fluctuations should be present outside of the jets potential core. Assuming that Stream 1 has fully occupied the cross sectional area of the divergent nozzle of the reactor (Fig. 11); the time (equivalently, the length of the mixing zone) for a prescribed degree of mixing may be determined.

The terminology of mixing may cause confusion, since there is generally a free interchange of words (e.g., blending, mixing, dispersion) and their meanings. Brodkey¹⁸ defines "mixing to mean any blending into one mass and mixture as a complex of two or more ingredients which do not have a fixed proportion to one another and which, however thoroughly comingled, are conceived as retaining a separate existence". The ultimate in any mixing process is submicroscopic homogeneity with molecules uniformly distributed over the field. Molecular diffusion will always be the controlling factor and when it is very slow, turbulence can speed up the diffusion by increasing the transfer area. It is the dispersive action inherent in turbulence that enhances the molecular diffusion.

Criteria characterizing the quality of mixing are defined for the purpose of this report;¹⁹ their mathematical treatments are available elsewhere.²⁰⁻²⁷

Scale of segregation: A measure of the size of the unmixed clumps of the pure components. As these clumps are dispersed, the scale of mixing is reduced. A linear scale, L_s , is defined as

$$L_s = \int g_s(r) d\vec{r} \quad (34)$$

where,

$$g_s(r) = \frac{\overline{a(\vec{x}) a(\vec{x} + \vec{r})}}{a'^2} \quad (35)$$

and

$a = c - \bar{c}$ = concentration fluctuation
 c = instantaneous concentration
 \bar{c} = time-average concentration
 a' = rms fluctuation $\equiv \sqrt{\bar{a}^2}$.

A volume scale, V_s , is defined as

$$V_s = \int 2\pi r^2 g_s(r) dr \quad (36)$$

where \vec{x} and \vec{r} are vector distances and $r = |\vec{r}|$.

Intensity of segregation: The effect of molecular diffusion on the mixing process is a measure of the difference in concentration between neighboring clumps of fluid. The intensity of segregation is defined as

$$I_s = \frac{a'^2}{a_o'^2} \quad (37)$$

The intensity of segregation is unity for complete non-mixing and equal to zero when the mixture is perfectly uniform ($a'^2 = 0$). Figure 14 is a schematic representation of the scale and intensity of segregation during a gas mixing process.

The statistical theory of turbulence suggests the following relations

$$I_s = e^{-t/\tau} \quad (38)$$

where

t = time of mixing
 τ = time constant

$$\tau = 1/2 \left[3 \left(\frac{5}{\Pi} \right)^{2/3} \left(\frac{L_s}{\epsilon} \right)^{1/3} + \left(\frac{\nu}{\epsilon} \right)^{1/2} \cdot \ln N_{sc} \right] \quad (39)$$

and

ν = kinematic viscosity = μ/ρ [=] cm²/sec
 N_{sc} = Schmidt number = ν/D
 D = molecular mass diffusivity [=] cm²/sec
 L_s = scale of segregation

The scale of segregation, L_s , can be estimated.

$$\left(\frac{5}{\Pi} \right)^{2/3} \left(\frac{L_s}{\epsilon} \right)^{1/3} = \frac{\lambda^2}{10\nu} = \frac{0.341 r_o}{\mu'} \quad (40)$$

$$\lambda^2 = 15\nu u'^2/\epsilon \quad (41)$$

where

λ = a microscale of mixing
 $u' = \sqrt{\bar{u}^2}$ = rms velocity fluctuation in the axial direction

In summary, the key to the mixing is the determination of the time constant, τ . From equation (38), the time of mixing may be calculated for any desired value of the intensity of segregation I_s , i.e., degree of mixing.

Mixing Calculations

Values of the intensity of segregation were calculated for different values of the rms value of the axial velocity fluctuation, u' . The geometry is shown in Figs. 11-13.

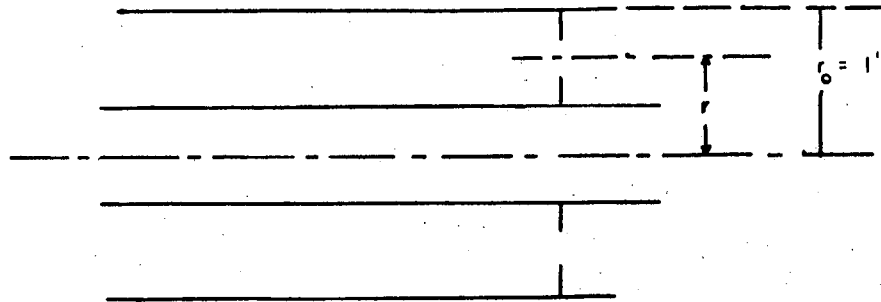


Fig. 13 - Geometry Used for Mixing Calculations

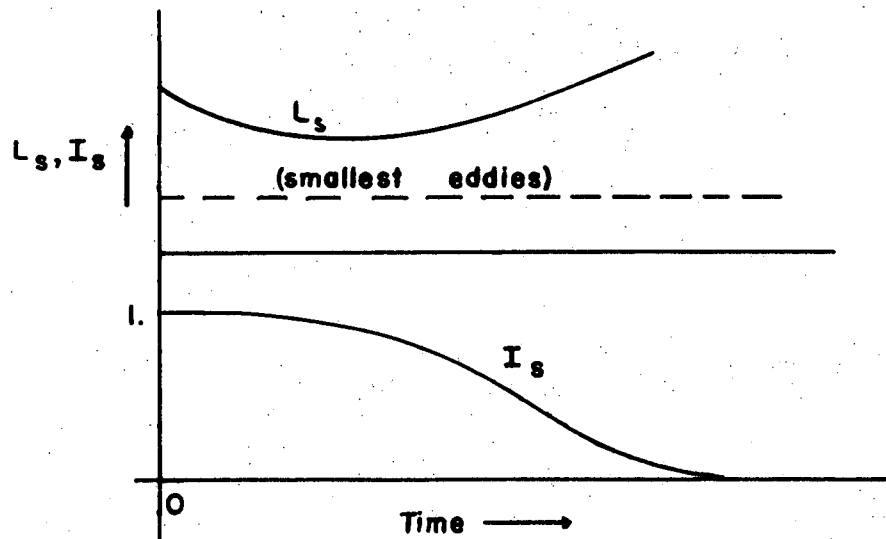


Fig. 14 - The Intensity and Scale of Segregation During Mixing²⁸

Two cases were considered:

(a) Mixing of the peripheral jets (1/4" nozzle) with surrounding gas considered as stagnant. Three values of u' were assumed; $u_1 = 0.05\bar{v}_2$, $u_2 = 0.025\bar{v}_2$ and $u_3 = 0.01\bar{v}_2$, where $\bar{v}_2 = 110$ cm/sec. Corresponding time constants were calculated: $\tau_1 = 0.236$ sec, $\tau_2 = 0.472$ sec, and $\tau_3 = 1.165$. Figure 15 summarizes the results of this case where the intensity of segregation is plotted against time.

(b) Mixing of the central jet with surrounding gas considered stagnant. Time constants of mixing were calculated as in the preceeding case with $\bar{v}_1 = 157$ cm/sec. The corresponding time constants were calculated as: $\tau_1 = 0.110$ sec, $\tau_2 = 0.332$ sec and $\tau_3 = 0.830$ sec. Figure 16 summarizes the results of this case.

The length of the reaction zone was calculated on the basis of mixing time (for a given intensity of segregation and an average flow velocity of both gas streams). For an 80% degree of mixing, i.e., $I_s = 0.2$, and an average gas velocity of 23.5 cm/sec the time of mixing was calculated as $t = 1.875$ sec. Taking $N = 2^*$, the dimensionless measure of mixing distance, σ ,

$$\sigma = k_0 u' t \quad (42)$$

drops from $\sigma = 6$ to $\sigma \approx 4.5^*$. Hence the actual mixing time is

$$t_{\text{mix}} = 1.875 \left(\frac{4.5}{6} \right) \approx 1.40 \text{ sec} \quad (43)$$

and the length of the mixing zone

$$L_m = (23.4 \text{ cm/sec}) (1.4 \text{ sec}) \approx 32.8 \text{ cm} . \quad (44)$$

These preliminary reactor design data formed the basis for subsequent reactor design.

Reactor Design

The rms value of the axial velocity fluctuation, u' , varies with distance downstream in the reactor. Moreover due to the spreading of the central and peripheral jets, their average velocity also varies with distance downstream in the reactor. The spreading of the jets is not free, due to interactions of two adjacent peripheral jets and the

* [29]

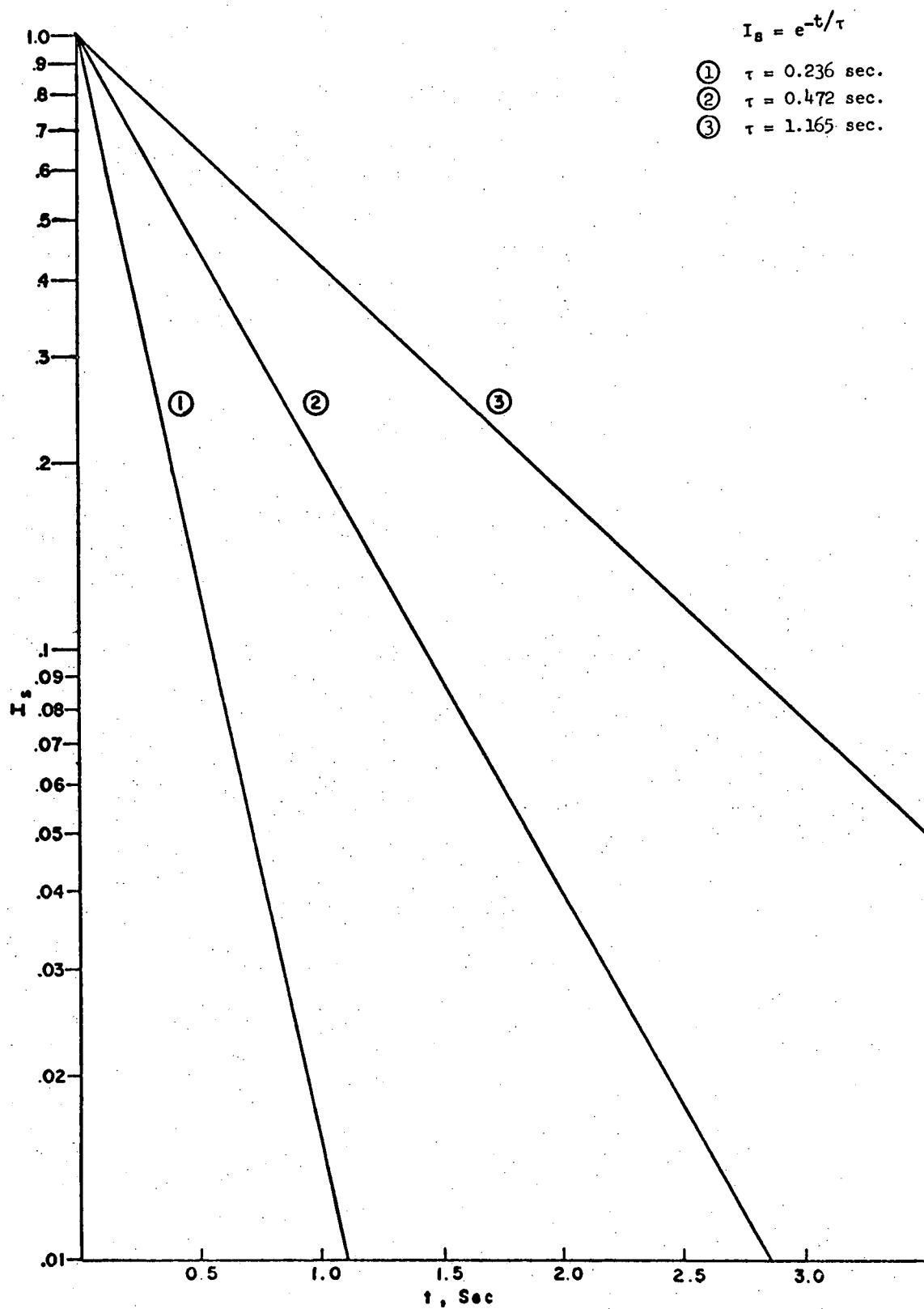


Fig. 15 - Preliminary Reactor Design. Mixing of Stream 2

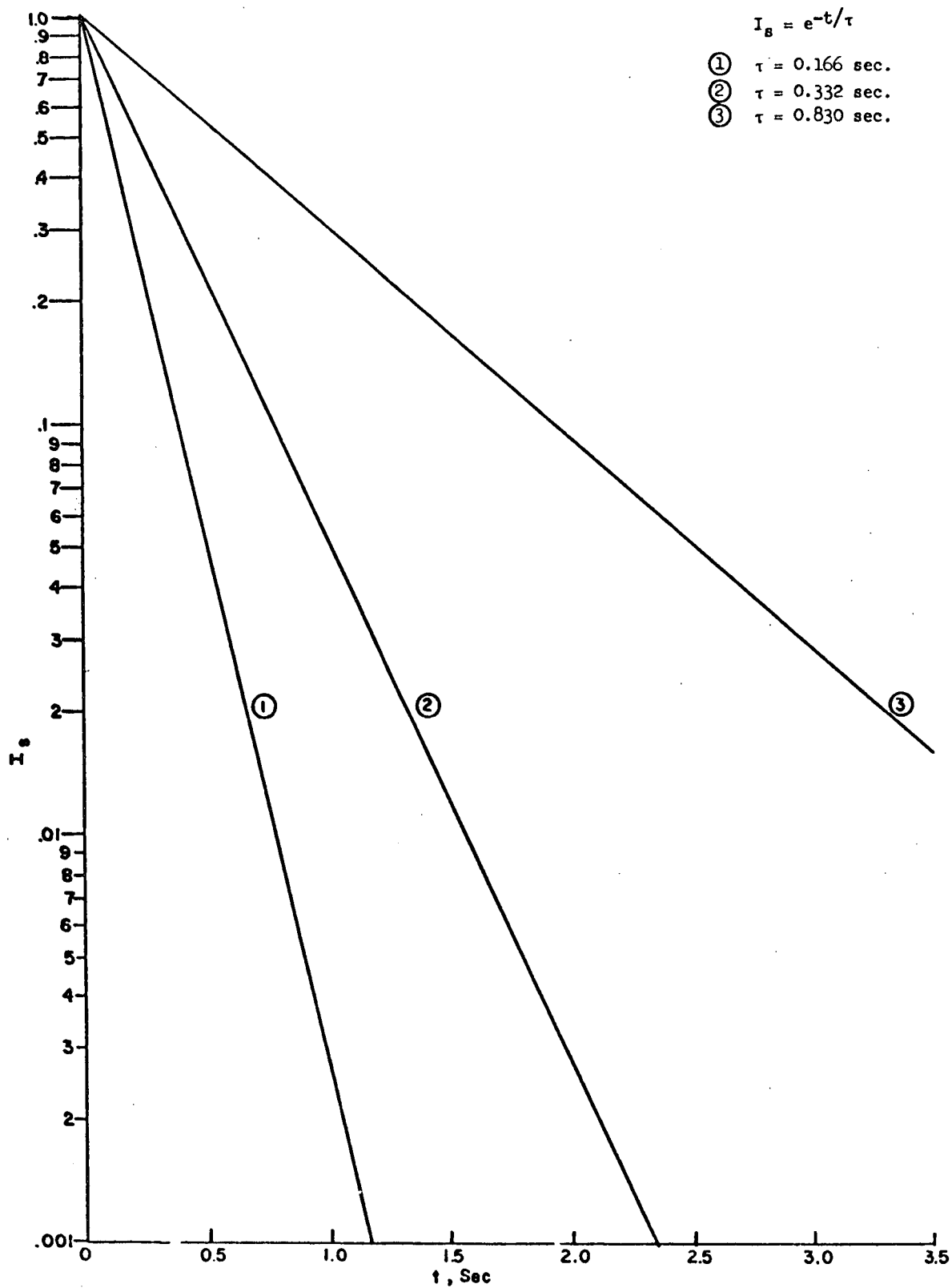


Fig. 16 - Preliminary Reactor Design. Mixing of Stream 1

central jet. Thus, the flow field becomes extremely complicated and almost hopeless from an exact analytical point of view.

Semi-empirical approximations have been used as well as reasonable simplifications to make the problem tenable. An energy (heat) balance around the reactor established the heat requirements being supplied by the oxy-hydrogen flame, thus revising the flow rates in the central jet.

There is a wealth of information concerning free turbulence and especially round free jets.³⁰⁻³² Figures 17 and 18 show the nomenclature and configurations used in these calculations.

The jet issues with a velocity v_p from an orifice with diameter, d , into a stream with uniform velocity v_s . In the jet region, the axial velocity component \bar{v}_x is assumed to be composed of the velocity v_s of the ambient stream and the velocity \bar{v}_1 , which is the deviation from the velocity v_s caused by the jet (Fig. 17). Close to the orifice, the turbulent mixing zone has zero width W ; this width $W(x)$ increases with increasing distance from the orifice to a distance x_c where the mixing zone covers the entire jet (Fig. 18). If the velocity distribution at the orifice is uniform, the velocity at the axis maintains its constant value v_p up to this distance x_c . Up to x_c , the jet contains a central potential core region. Farther downstream the velocity at the axis of the jet decreases with increasing distance.

The length of the core region, x_c , is determined mainly by the value of the ratio $\mu \equiv v_s/v_p$; one empirical correlation³³ is:

$$\frac{x_c}{d} = 4 + 12\mu \quad (45)$$

The velocity of the jet at the axis decreases hyperbolically with increasing downstream distance x ,

$$\frac{\bar{v}_{1,\max}}{v_p - v_s} = \frac{x_c}{x} \text{ for } x > x_c \quad (46)$$

and the change in jet width, W , is given by

$$\frac{W}{d} = \left(\frac{x}{x_c}\right)^{1-\mu} \text{ for } x > x_c \quad (47)$$

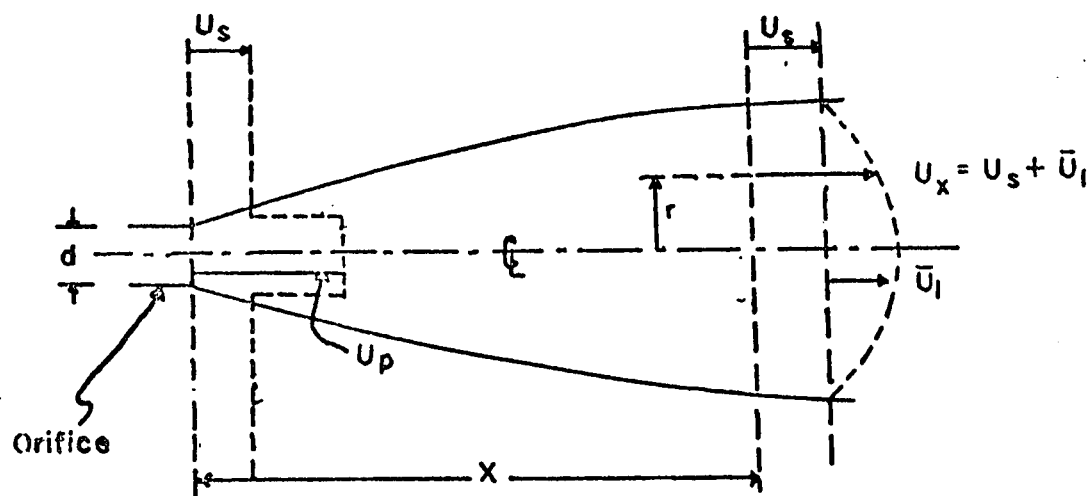


Fig. 17 - Geometry Nomenclature for Round Jet

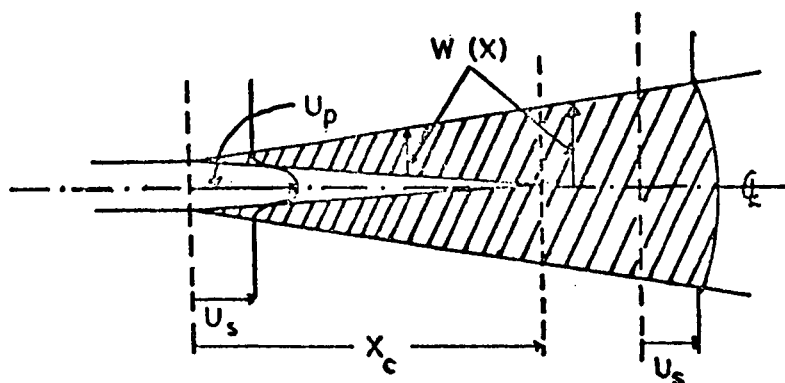


Fig. 18 - Geometry for Round Jet

The heat of reaction of the oxy-hydrogen flame was calculated as: -60.298 kcal/g-mole at $T = 2,073^\circ\text{K}$. From the heat balance calculations around the reactor it was determined that the amount of heat supplied by the oxy-hydrogen flame is

$$Q_f = 40 \text{ kcal/hr} \quad (48)$$

Hence the volumetric flow rates were revised.

$$V_1 = 1.373 \times 10^4 \text{ cc/min} \quad (49)$$

$$V_2 = 2.005 \times 10^4 \text{ cc/min} \quad (T = 2,073^\circ\text{K}, p = 0.5 \text{ atm}) \quad (50)$$

and the corresponding Reynolds numbers were calculated to be

$$N_{Re_1} = 56.2; N_{Re_2} = 37 \quad (51)$$

Under these new flow conditions v_p for the central jet was calculated as $v_p = 179.5 \text{ cm/sec}$. Since $\mu = v_s/v_p$ and downstream interaction between central and peripheral jets occurs, it is obvious that μ depends on x . An average value of μ was estimated on the basis of two limiting values of $v_s = 17.6 \text{ cm/sec}$ and $v_s = 134 \text{ cm/sec}$; for $\mu_{Avg} = 0.223$ the total velocity at the centerline, $(\bar{v}_x)_0 = \bar{v}_1 + v_s$, was calculated as

$$(\bar{v}_x)_0 = \frac{1,180}{x} + 40 \quad (52)$$

and the jet width as

$$W = 0.24 (x)^{0.777} \quad (53)$$

where $(\bar{v}_x)_0$ [=] cm/sec; x, w , [=] cm. The results are shown in Fig. 19. Similar calculations for the peripheral jets and available data,³⁴ gave $x_c = 8.5 \text{ cm}$, $\mu = 0.61$ and

$$(\bar{v}_x)_0 = \frac{374}{x} + 82 \quad (54)$$

$$W = 0.294 (x)^{0.39} \quad (55)$$

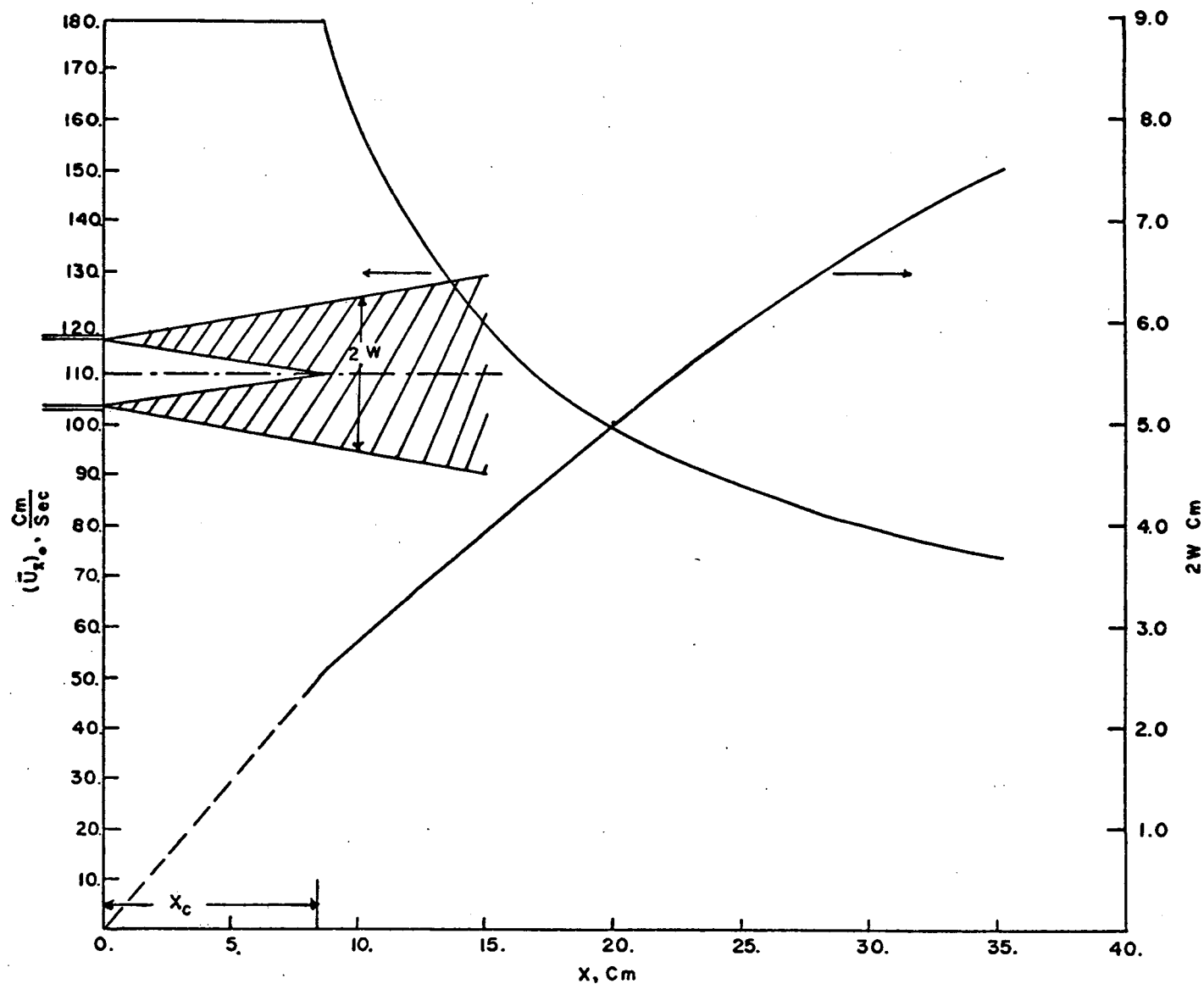


Fig. 19 - Velocity at the Center Line and Width Variation for Downstream of Central Jet

The results are shown in Fig. 20. The rms value u' was calculated using available data.³⁵ For the central jet and at a radial distance of $r = 1$ cm,

$$u' = \frac{1.8 \times 10^2}{(x - 1.02)} \sqrt{g_1 \left(\frac{r}{x - 1.02} \right)}; [=] \text{ cm/sec} \quad (56)$$

where $x [=]$ cm, and the function g was obtained from reference [36]. Since those data were for much higher jet Reynolds number, the predicted values of u' from equation (52) are rather high. Due to lack of other data this calculation was retained for comparison. Hinze³⁷ gives the following correlation for the axial (x -direction) eddy viscosity, $(\epsilon_m)_{xx}$.

$$(\epsilon_m)_{xx} = 0.013 v_p d; [=] \text{ cm}^2/\text{sec} \quad (57)$$

where $v_p [=]$ cm/sec and $d [=]$ cm.

The corresponding Reynolds (eddy) stresses are given by the well known expression

$$\overline{u_x u_x} = -(\epsilon_m)_{xx} \frac{dv}{dx} \quad (58)$$

Using Figs. 19 and 20 or equations (48) and (50), the velocity gradients at the centerline may be calculated. The following expressions for u' for both the central and peripheral jets can be obtained.

$$\text{Central jet: } u' = \frac{59}{x} \quad (59)$$

$$\text{Peripheral jets: } u' = \frac{20.3}{x} \quad (60)$$

where $x [=]$ cm, $u' [=]$ cm/sec. These results are summarized in Fig. 21. It is worth noticing that u' for the peripheral jets is lower than for the central jet. Half-way in the x -direction of a ~35 cm long reaction zone, $u' \approx 1.3$ cm/sec; the velocity $(\bar{v}_x)_0$ at the same x is 100 cm/sec [Fig. 20] or $u' \approx 0.013 (v_x)_0$.

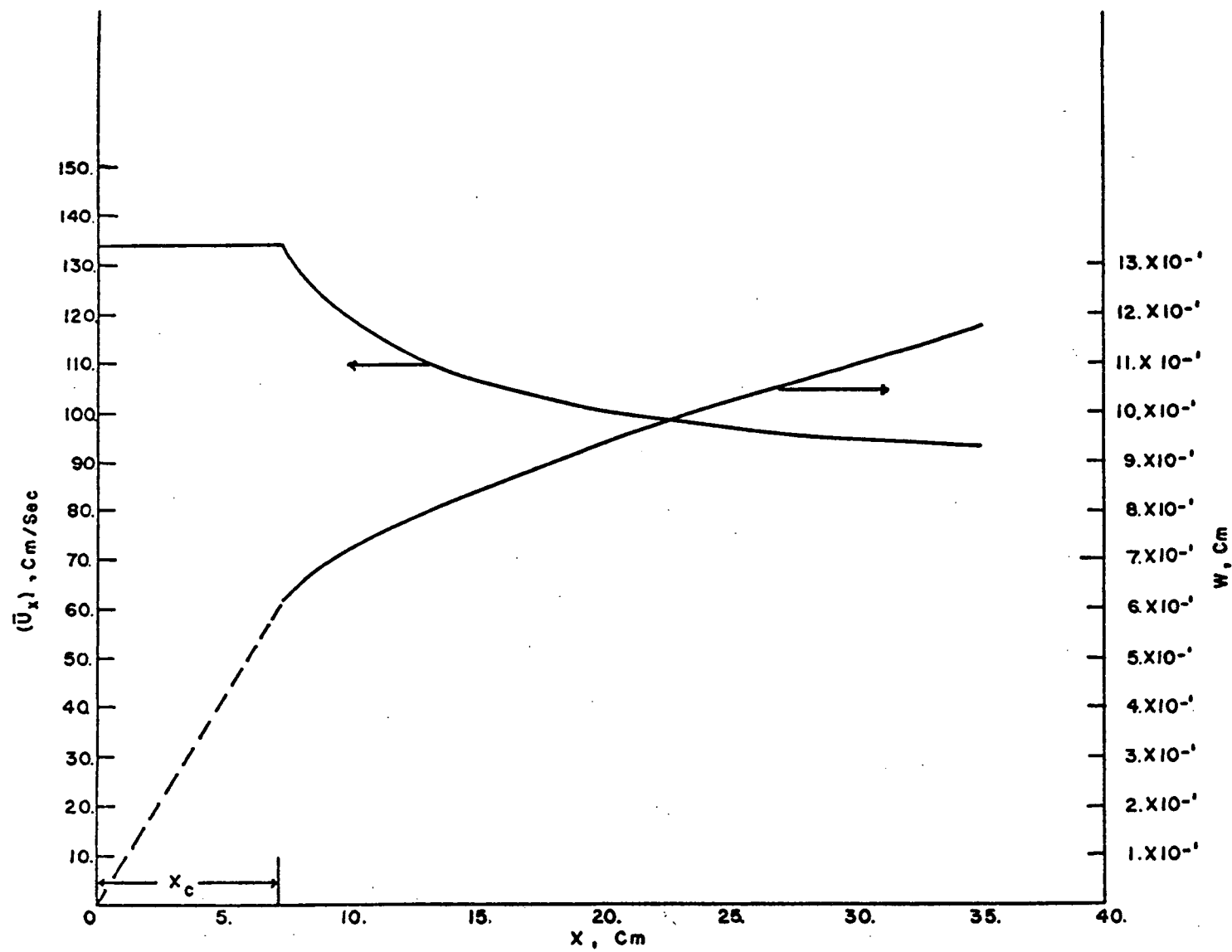


Fig. 20 - Peripheral Jets

From Fig. 21, one may graphically calculate a reactor length for a chosen intensity of segregation. Additionally, an analytic solution was attempted. For gases, with the Schmidt number very close to unity, equations (39) and (40) give for the time constant, τ ,

$$\tau = \frac{3}{2} \left(\frac{0.341 r_o}{u'} \right) \quad (61)$$

for $r_o = 1 \text{ inch} = 2.54 \text{ cm}$, and for the central jet (equation 24) $\tau = 0.022 x$, $x [=] \text{ cm}$ and $\tau [=] \text{ sec}$. The intensity of segregation becomes

$$I_s(x,t) = \exp \left[- \frac{t}{0.022x} \right] \quad (62)$$

The total volumetric flow rate (Streams 1 and 2) was

$$V = 1.373 \times 10^4 + 2.005 \times 10^4 = 3.378 \times 10^4 \text{ cc/min} = 5.62 \times 10^2 \text{ cc/sec} \quad (63)$$

From the geometry shown in Fig. 22, it is easily seen that $R = 2.54 + (1.27/L)x [=] \text{ cm}$. If $v = v(x)$ is the average velocity based on the total cross sectional area,

$$v(x) = \frac{dx}{dt} = \frac{V [=] \text{ cc/sec}}{\pi R^2} = \frac{562}{\pi \left(2.54 + \frac{1.27}{L} x \right)^2} \quad (64)$$

If $L = 35 \text{ cm}$, equation (64) represents the intensity of segregation as

$$I_s(x) = \exp[-0.279 (4.4 \cdot 10^{-3} x^2 + 9.2 \cdot 10^{-2} x + 6.45)] \equiv e^{-\psi} \quad (65)$$

where $x [=] \text{ cm}$ and $8.9 < x < 35$. Table XXI lists the values of $I_s(x)$ from equation (65).

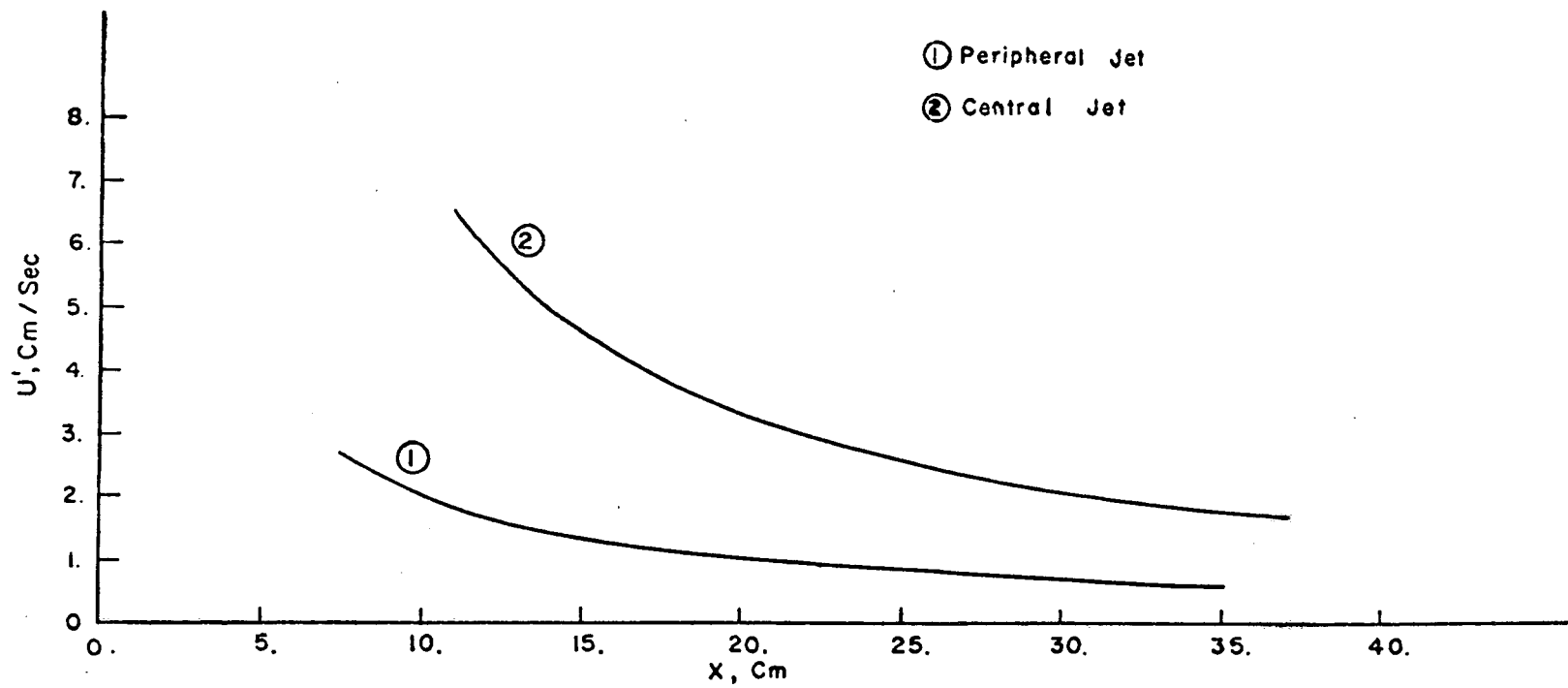


Fig. 21 - Variation of Axial Turbulence Intensity Along the Jet Center Line With X

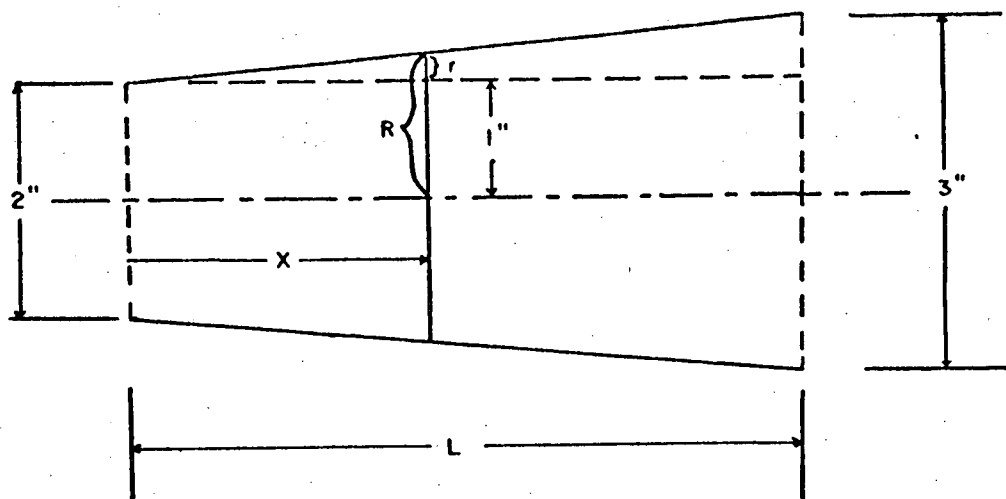


Fig. 22 - Geometry for Calculating Residence Time in Reactor

Table XXI - Intensity of Segregation from Equation (65)

$x [=] \text{cm}$	ψ	$I_s = e^{-\psi}$
9	2.13	0.119
10	2.16	0.115
15	2.47	0.094
20	2.78	0.072
25	3.21	0.040
30	3.77	0.023
35	4.20	0.016

It is obvious from Table XXI, that the calculation of time based on the total cross-sectional area gives high values for t , thus decreasing the intensity of segregation very rapidly.

Recent research³⁸ in gas jet mixing suggested that the length of the potential core $x_c \approx L_s \approx r_o$, at least for the initial period of mixing i.e., for $0 < x < x_c$. A conservative calculation performed on this basis resulted in the following. For the central jet and $0 < x < x_c = 8.9$ cm, $r_o \approx x_c$, $u' \approx 7$ cm/sec, the u' close to the end of the potential core [Fig. 21], the time constant, τ , was calculated.

$$\tau = \frac{(0.341) (8.9 \text{ cm})}{7 \text{ cm/sec}} = 0.434 \text{ sec} \quad (66)$$

For the region: $8.9 < x < 35$ cm, $r_o \approx 2.5$ inches = average of the two diameters of 2" and 3". $u' \approx 2$ cm/sec (i.e., u' at the end of the reaction zone)

$$\tau = \frac{(0.341) (6.35 \text{ cm})}{2 \text{ cm/sec}} = 1.07 \text{ sec} \quad (67)$$

The results for the intensity of segregation and time are shown in Fig. 23. A time for the central jet to travel the total length of the reactor was calculated.

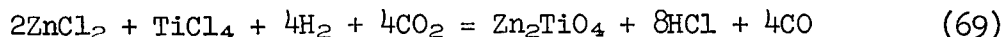
$$t = \frac{8.9 \text{ cm}}{179 \text{ cm/sec}} + \frac{(35-8.9) \text{ cm}}{93 \text{ cm/sec}} = 0.33 \text{ sec} \quad (68)$$

(see Fig. 19)

The corresponding intensity of segregation from Fig. 23 was $I_s \approx 0.66$, or 34% mixing.

3. Reactor Mixing for Zn_2TiO_4

The proposed CaWO_4 reactor mixing performance is estimated for the production on Zn_2TiO_4 according to the reaction:



The reactor configuration, gas flow rates, operating temperature and pressure are given in Fig. 24. The amounts of O_2 and H_2 in stream (1) are the ones for the oxy-hydrogen flame and for the purpose of this estimation they were based on heat supply of 40 kcal/hr by the oxy-hydrogen flame.

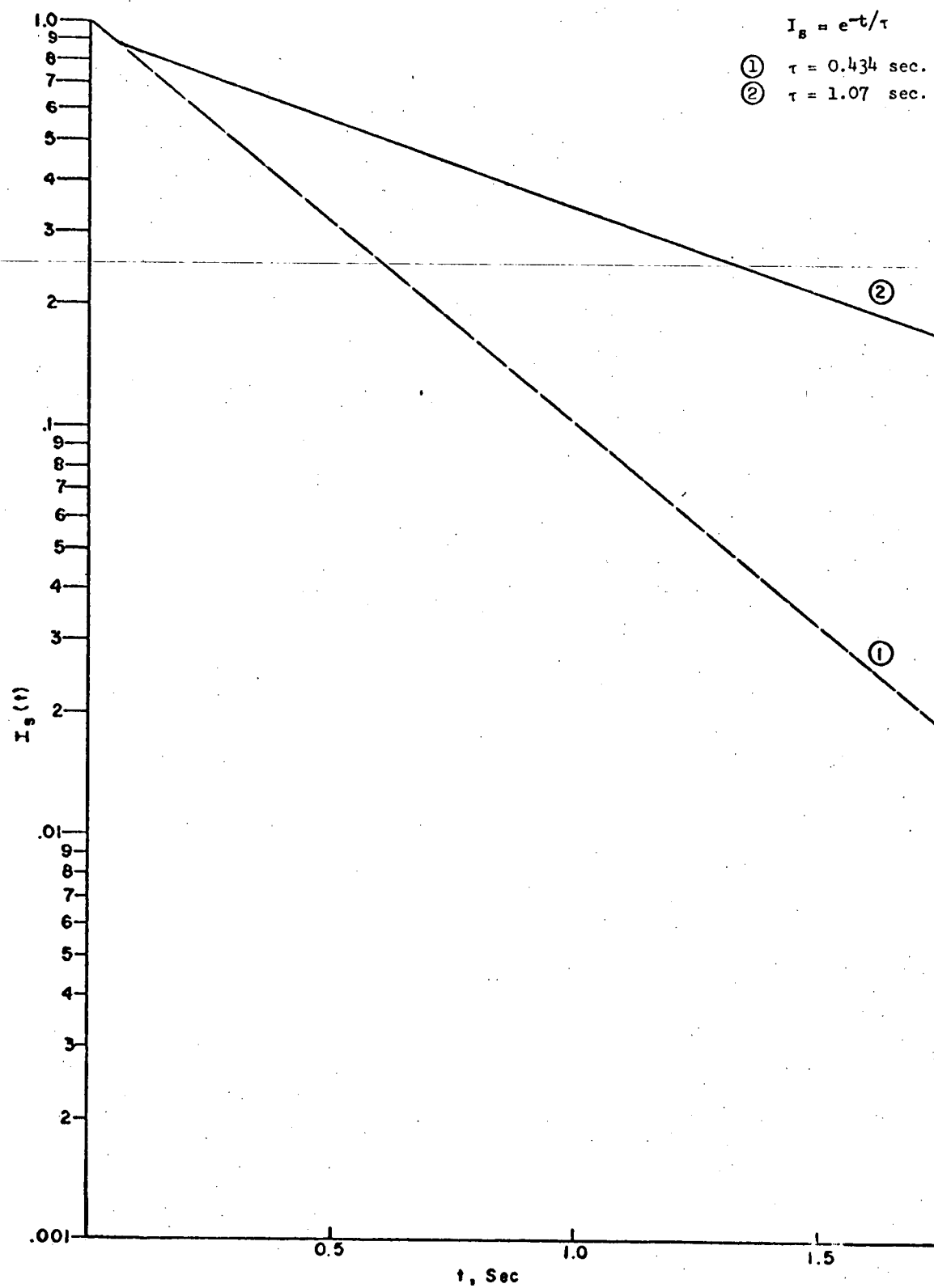


Fig. 23 - Mixing of Central Jet

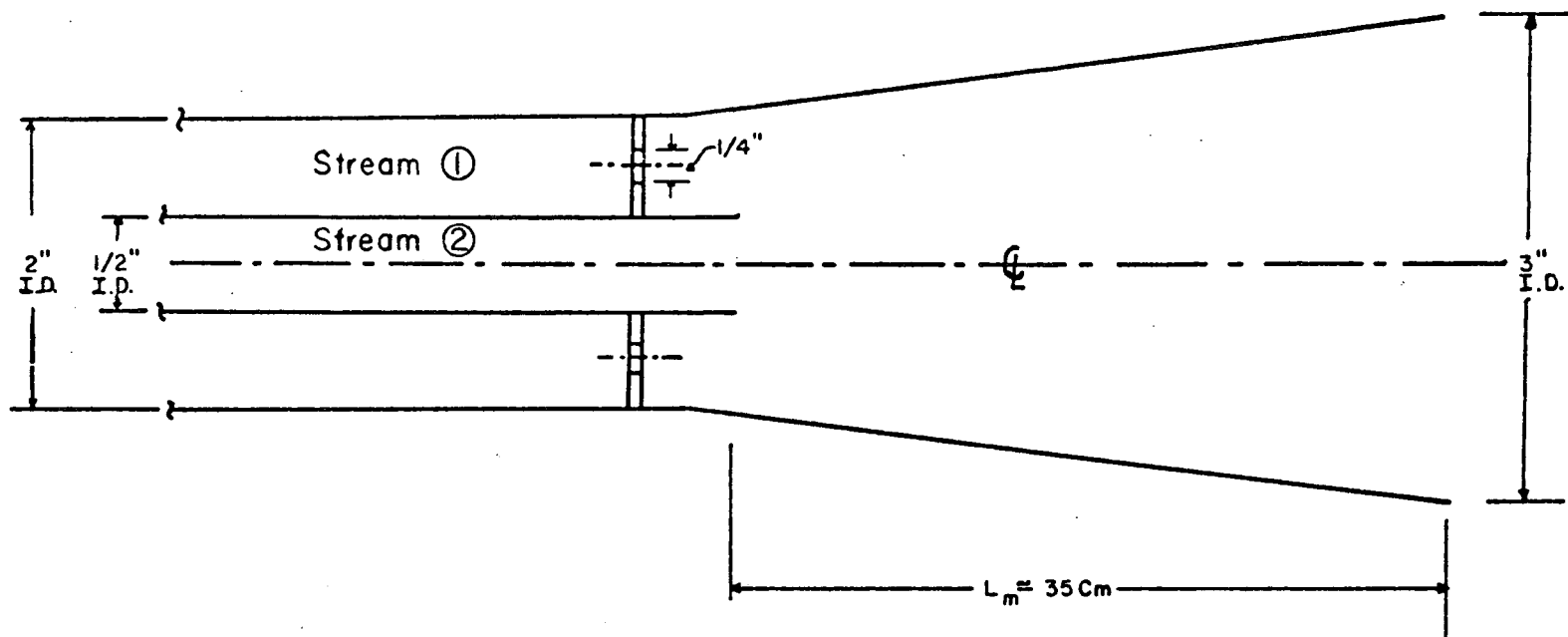


Fig. 24 - Reactor Configuration for the Production of Zn_2TiO_4

Gas flow rates

Stream (1):

ZnCl ₂	400	cc/min (STP)
H ₂	248	" "
CO ₂	400	" "
O ₂	124	" "

Stream (2):

TiCl ₄	200	cc/min (STP)
H ₂	800	" "

Temperature: 1,300°C

Pressure: 0.5 atm.

The volumetric flow rates of streams (1) and (2) at 1,300°C and 0.5 cc/min were calculated as:

$$V_1 = (1,172) \times \left(\frac{1}{0.5}\right) \left(\frac{1,598}{298}\right) \cong 12,480 \text{ cc/min} \quad (70)$$

$$V_2 = (1,000) \times \left(\frac{1}{0.5}\right) \left(\frac{1,598}{298}\right) \cong 10,700 \text{ cc/min} \quad (71)$$

The corresponding velocities of the central jet, \bar{v}_1 , and each of the eight peripheral jets were calculated (at the operating temperature and pressure)

$$\bar{v}_1 = \frac{(12,480 \text{ cc/min})}{(2.53 \text{ cm}^2) (60 \text{ sec/min})} = 82.3 \text{ cm/sec} \quad (72)$$

$$\bar{v}_2 = \frac{(8,460)}{(0.315) (60) (8)} = 56.0 \text{ cm/sec} \quad (73)$$

The kinematic viscosities of streams (1) and (2) were estimated as $\nu_1 = 1.77 \text{ cm}^2/\text{sec}$ and $\nu_2 = 1.38 \text{ cm}^2/\text{sec}$ (see Table XX) respectively. The corresponding Reynolds number of the central jet was calculated as $N_{Re} = 59$.

Jet mixing estimation

Equation (45) with a ratio of velocities $\mu = v_s/v_p$
= $56/82 = 0.68$, gives for the length x_c of the central jet core region.

$$x_c = (4 + 12 \times 0.68) \times (1.27) = 15.4 \text{ cm} \quad (74)$$

The velocity at the centerline of the jet $(\bar{v}_x)_o$ was calculated from equation (46) as:

$$\frac{(\bar{v}_x)_o - v_s}{v_p - v_s} = \frac{x_c}{x}$$

or

$$(\bar{v}_x)_o = \frac{400}{x} + 56; \text{ x [=] cm, } (\bar{v}_x)_o \text{ [=] cm/sec} \quad (75)$$

Equation (57) for the eddy viscosity $(\epsilon_m)_{xx}$ gave:

$$(\epsilon_m)_{xx} = (0.013) (82) (1.27) \cong 1.36 \text{ cm}^2/\text{sec} \quad (76)$$

From equation (75),

$$\frac{d(v_x)_o}{dx} = - \frac{400}{x^2} \quad (77)$$

which combined with equation (76) reduced equation (52) to:

$$u' = \sqrt{+ (1.36) \frac{400}{x^2}} = \frac{23.4}{x} \text{ [=] cm/sec; x [=] cm} \quad (78)$$

The time constant of mixing, τ , was calculated from equations (39) and (40) at a radial distance $r_o = 1 \text{ in.}$,

$$\tau = \frac{1}{2} \times \left[3 \times \frac{(0.341) (2.54)}{1.4} \right] = 0.93 \text{ sec} \quad (79)$$

The intensity of segregation

$$I_s = e^{-t/0.93}, t [=] \text{ sec} \quad (80)$$

is plotted vs mixing time in Fig. 25. At a downstream distance $x = 20$ cm, the velocity at the centerline of the central jet is: $(\bar{v}_x)_0 = 76$ cm/sec (from equation 75). This velocity was used to calculate a residence time in the reactor. This is a conservative estimate as far as mixing because the jet velocity drops continuously downstream, and the central jet is the faster one; in addition the velocity profile has its maximum at the center line of the jet reaching the value $v_s = 56$ cm/sec at the most, towards the boundaries of the expanding nozzle of the reactor. A mixing time based on the $L_m \approx 35$ cm reactor length and the volume velocity was calculated as $t = (35 \text{ cm})/(76 \text{ cm/sec}) \approx 0.46$ sec, giving $I_s \approx 0.60$ for the intensity of segregation, i.e., 40% mixing. Hence, even this conservation estimate gives an adequate degree of reactant mixing in the case of Zn_2TiO_4 production.

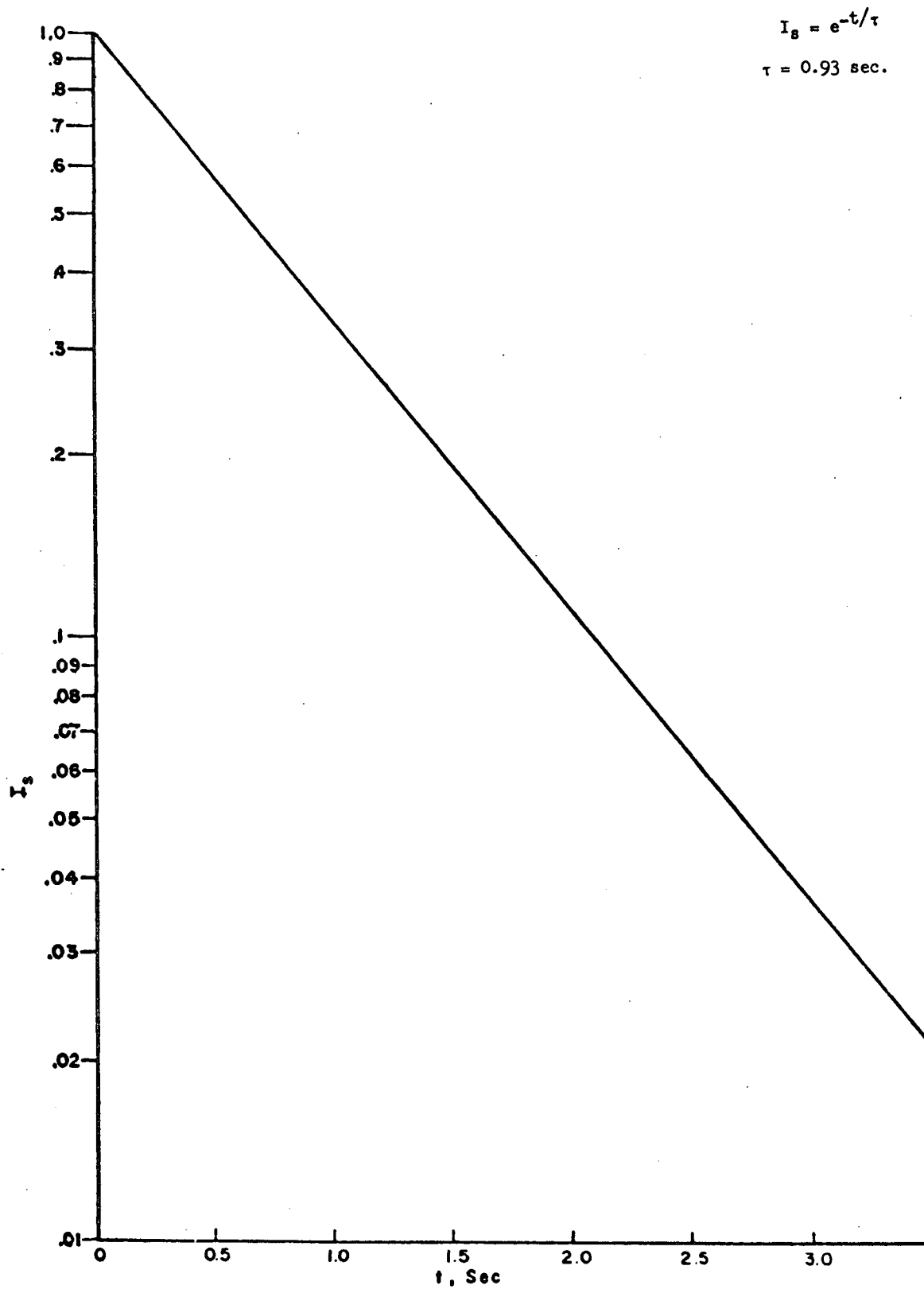


Fig. 25 - Reactor Mixing Performance for Zn_2TiO_4 Production

III. EXPERIMENTAL PROCEDURE

Serious experimental limitations of previous investigations were reviewed and analyzed. Methods for alleviating or circumventing these problems were based on improved component and process designs. The results of theoretical gas mixing studies were incorporated, as were new devices such as induction heated reactors and sonic agglomerators.

1. Reactor

A silicon carbide tube furnace 21 inches long and 2.25 inches ID was used to heat a high-purity, recrystallized Al_2O_3 tube 36 inches long with 38 mm ID and 46 mm OD. Reaction of gases and subsequent powder production occurred in a 6 inch hot zone. Use of a silicon carbide heating element provided a maximum temperature capability of 1500°C . Temperature was measured with a Pt-Pt 10% Rh thermocouple positioned between the Al_2O_3 tube and the SiC heating element in the center of the hot zone. The furnace was positioned vertically with the Al_2O_3 reaction tube passing through the center and extending four inches above the heating element. The tube furnace used to heat the zinc and zinc oxide extended below the SiC heating element.

Gases were introduced into the reaction zone at the bottom and passed up through the furnace. When zinc was used as the zinc vapor species, all other gases were introduced through a Al_2O_3 injector nozzle (6 mm x 10 mm) central to the zinc crucible and extending within one inch of the hot zone. The Al_2O_3 reaction tube was sealed with a stainless steel plate and a silicone rubber gasket. The top of the Al_2O_3 reaction tube (outlet) was connected to a stainless steel tee joint and sealed with a silicone rubber gasket. The branch of the tee was connected to a rubber vacuum hose and the run of the tee was used as a sight window.

Three reaction furnaces were designed and constructed to extend the range of system conditions for powder production. Intermediate temperatures to 1500°C were provided by a resistively-heated silicon carbide furnace. The silicon carbide element was thermally insulated with K-30 insulating fire brick. One-half of the symmetrical temperature profile, with maximums of 1050°C and 1200°C is shown in Fig. 26. Taking the effective isothermal hot zone as that length within 50°C of the maximum, a hot zone of approximately ten inches (25 cm) resulted.

Temperature capability was extended beyond 1800°C with a molybdenum-wound, hydrogen-protected furnace, Fig. 27. The 60-mil molybdenum wire was coiled about a wax core. Successive layers of Alundum cement containing 20 volume per cent of polyvinyl alcohol were built up on the molybdenum element, to a total thickness of 1-1/2 inches. The wax was melted, leaving a hollow tube of Alundum cement with the molybdenum wire firmly embedded in it. This element was centered in an

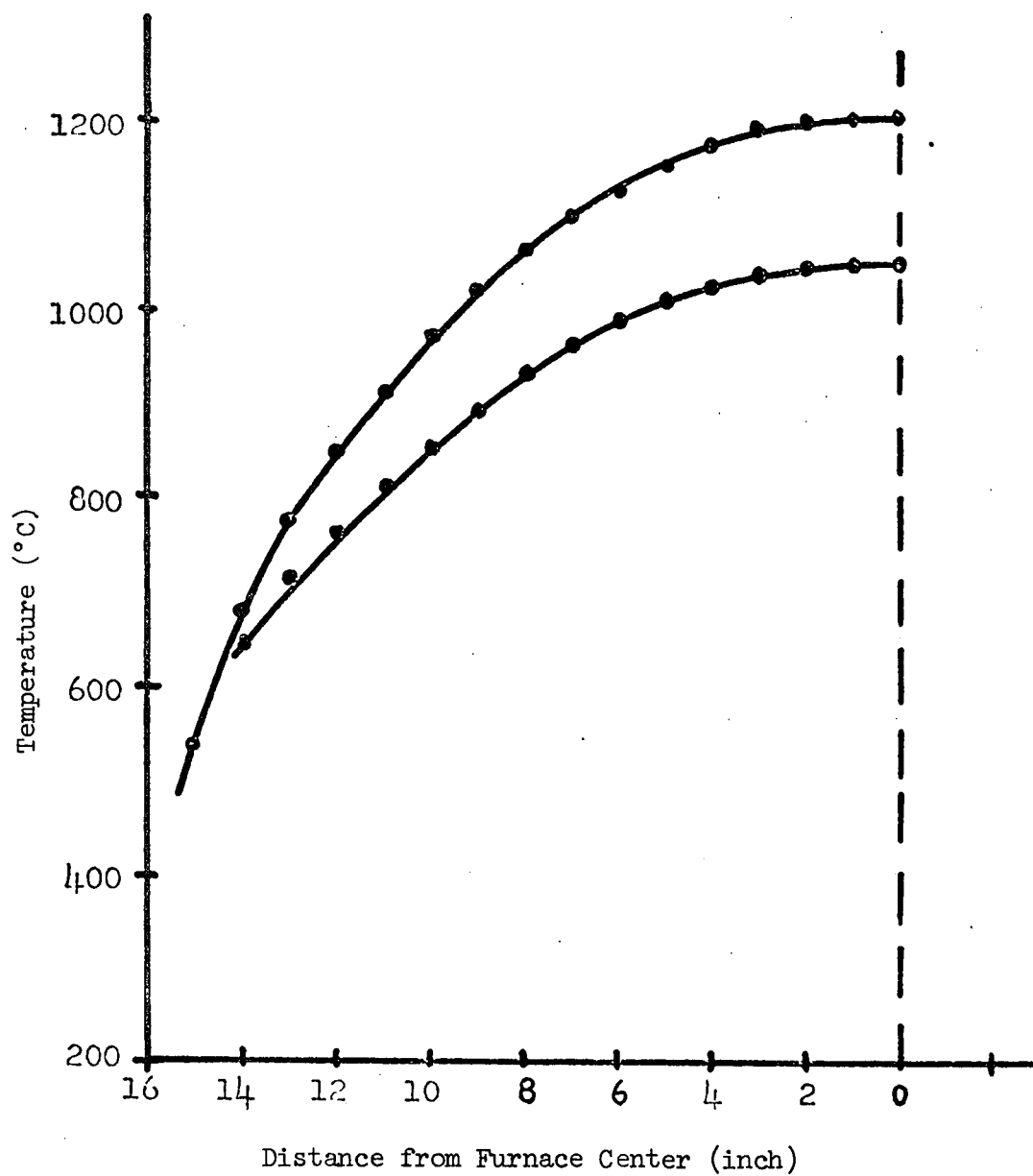


Fig. 26 - Temperature Profile of Silicon Carbide Resistance-heated Furnace

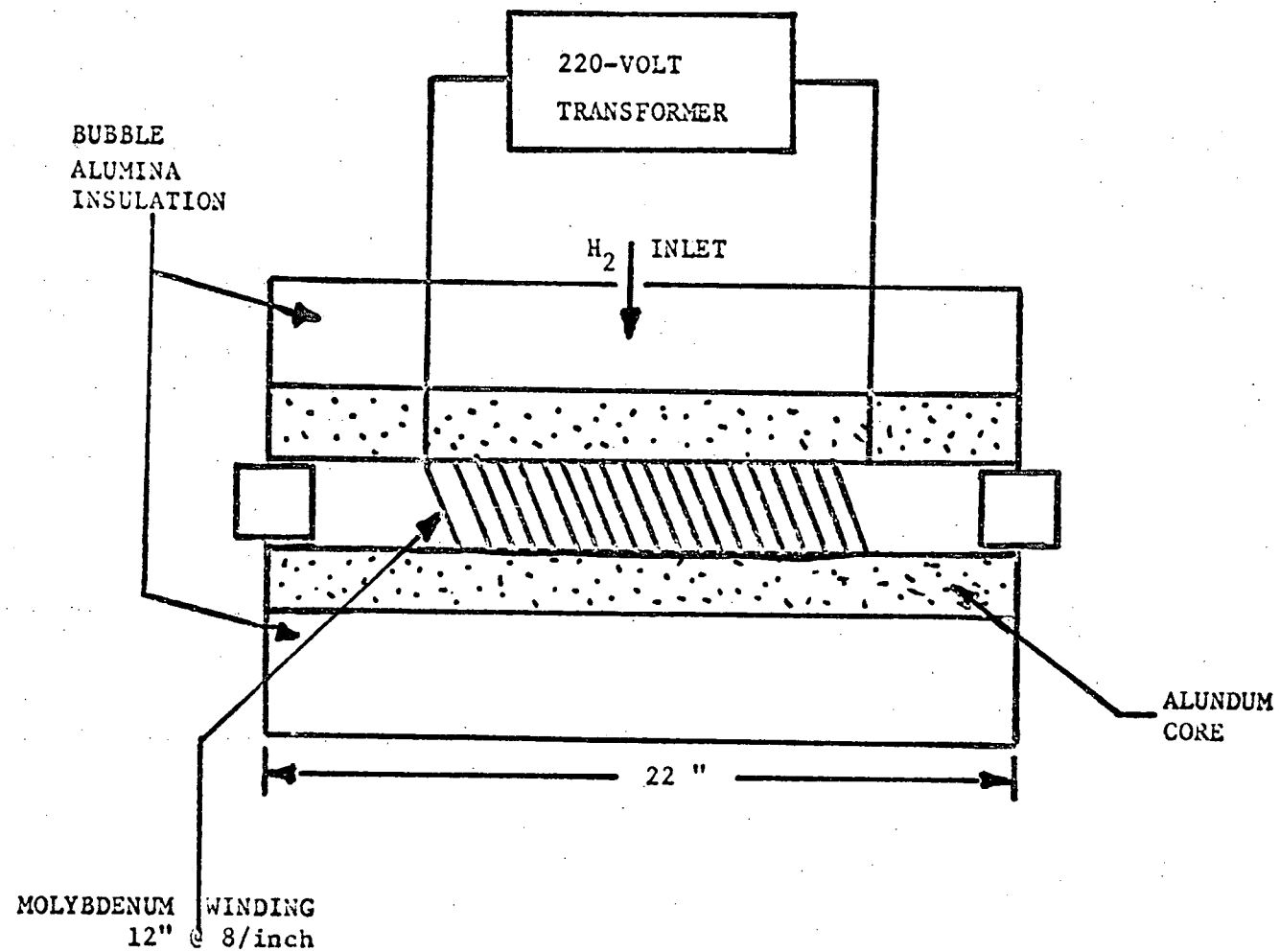


Fig. 27 - 22-inch Molybdenum-Wound Furnace

18-inch diameter drum, and the remaining volume filled with bubble alumina insulation. Electrical leadthroughs in the outer shell served as connections to the power supply. The drum was sealed and checked for gas-tightness.

The molybdenum element was protected from oxidation during firing by hydrogen. The polyvinyl alcohol burned out during the first firing, providing porosity in the core for flow of hydrogen over the element. Power was supplied by a variable transformer, and temperature was monitored with an optical pyrometer. Furnaces with four and seven inch isothermal zones were constructed.

Existing reactors heated by silicon carbide and molybdenum elements were modified to the configurations shown in Figs. 28 and 29. Respective temperature profiles of these reactors are shown in Figs. 26 and 30. In both instances, the halide is produced by passing chlorine through a bed of appropriate oxide. Figure 31 shows the arrangement of molybdenum-heated reactors with pumps and flow controls.

Operating temperature was extended beyond 1800°C by the construction of a high frequency, induction-heated reactor, Fig. 32. The temperature profile of the reactor is shown in Fig. 33. The arrangement of flow controls, pumps, furnace and sonic agglomerator are shown in Fig. 34.

The reactor contained an internal chlorinator for zinc oxide or zinc orthotitanate opening into a 13-inch long diverging nozzle which was the reaction zone. The chlorinator and nozzle were separated by an alumina disc. The reactor chamber was a three-inch diameter alumina tube. Radiation losses were minimized by two concentric molybdenum heat shields, .010" each. The reactor and heat shields were positioned within a 6.5-inch diameter fused silica tube. Argon flows prevented heat shield oxidation.

The induction power supply was a 15 kW, 10,000 Hz, motor generator feeding an eight tap autotransformer in a portable work station. The induction coil was 7 inches in diameter, 20 inches long, and contained 18 evenly spaced turns of 5/8" diameter copper tubing.

2. Powder-Gas Separation

A survey of the literature identified several methods of solid-gas separation.³⁹⁻⁵⁰ Four separation processes were considered; namely,

- (1) centrifugation,
- (2) electrostatic precipitation,
- (3) thermal precipitator, and
- (4) cyclone.

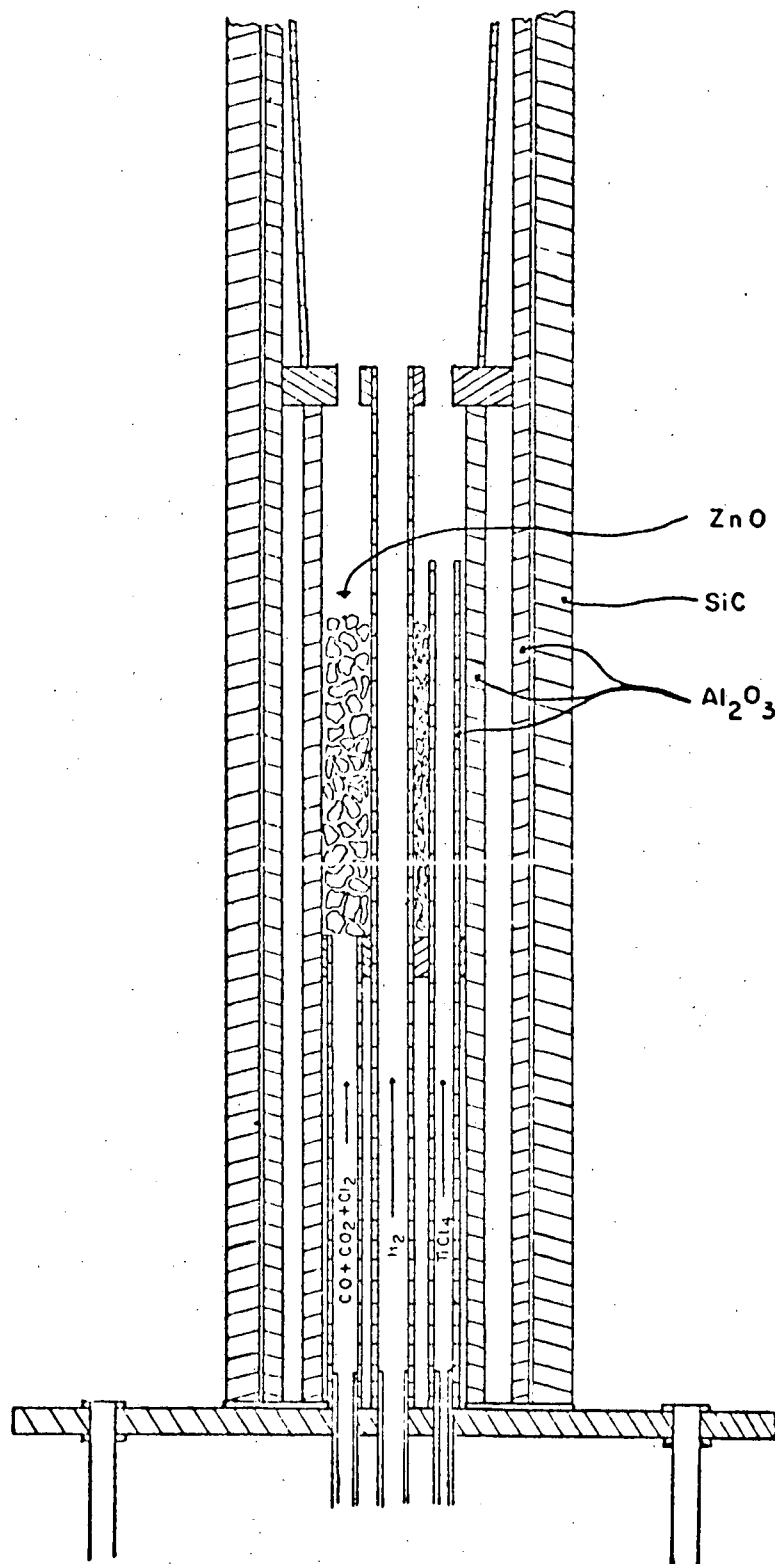


Fig. 28 - Modified SiC Furnace Reactor

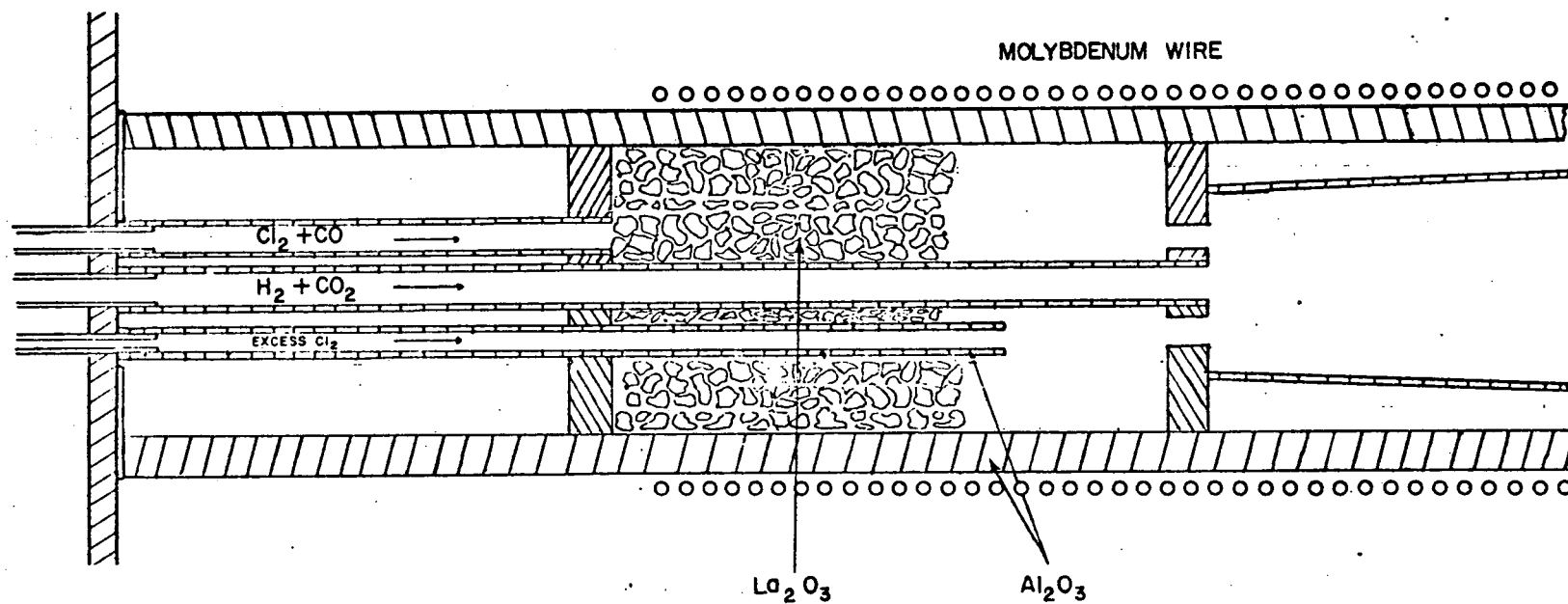


Fig. 29 - Modified Molybdenum-Wound Furnace

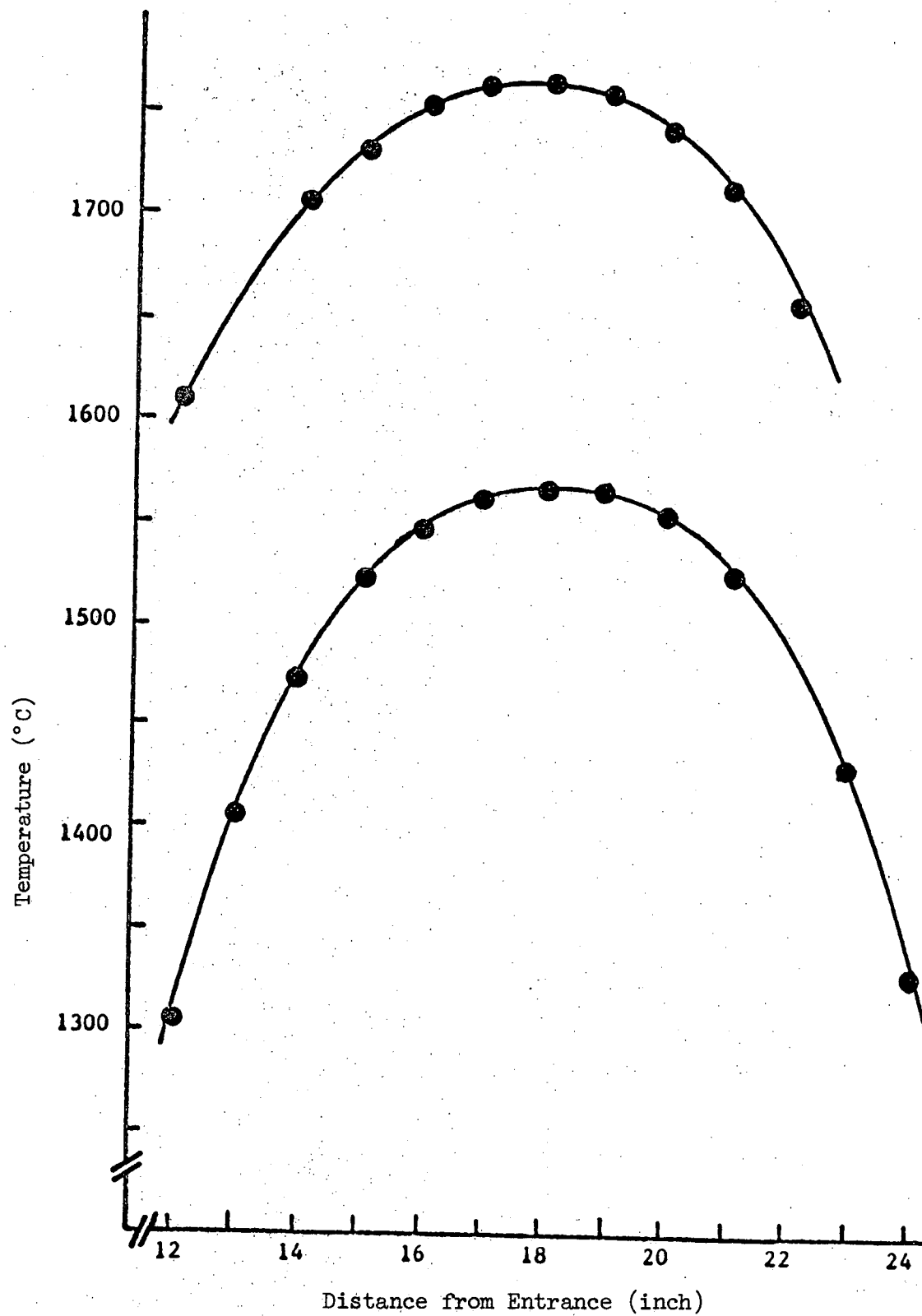


Fig. 30 - Temperature Profile of Molybdenum-Wound Furnace with Seven Inch Isothermal Zone

Reproduced from
best available copy.

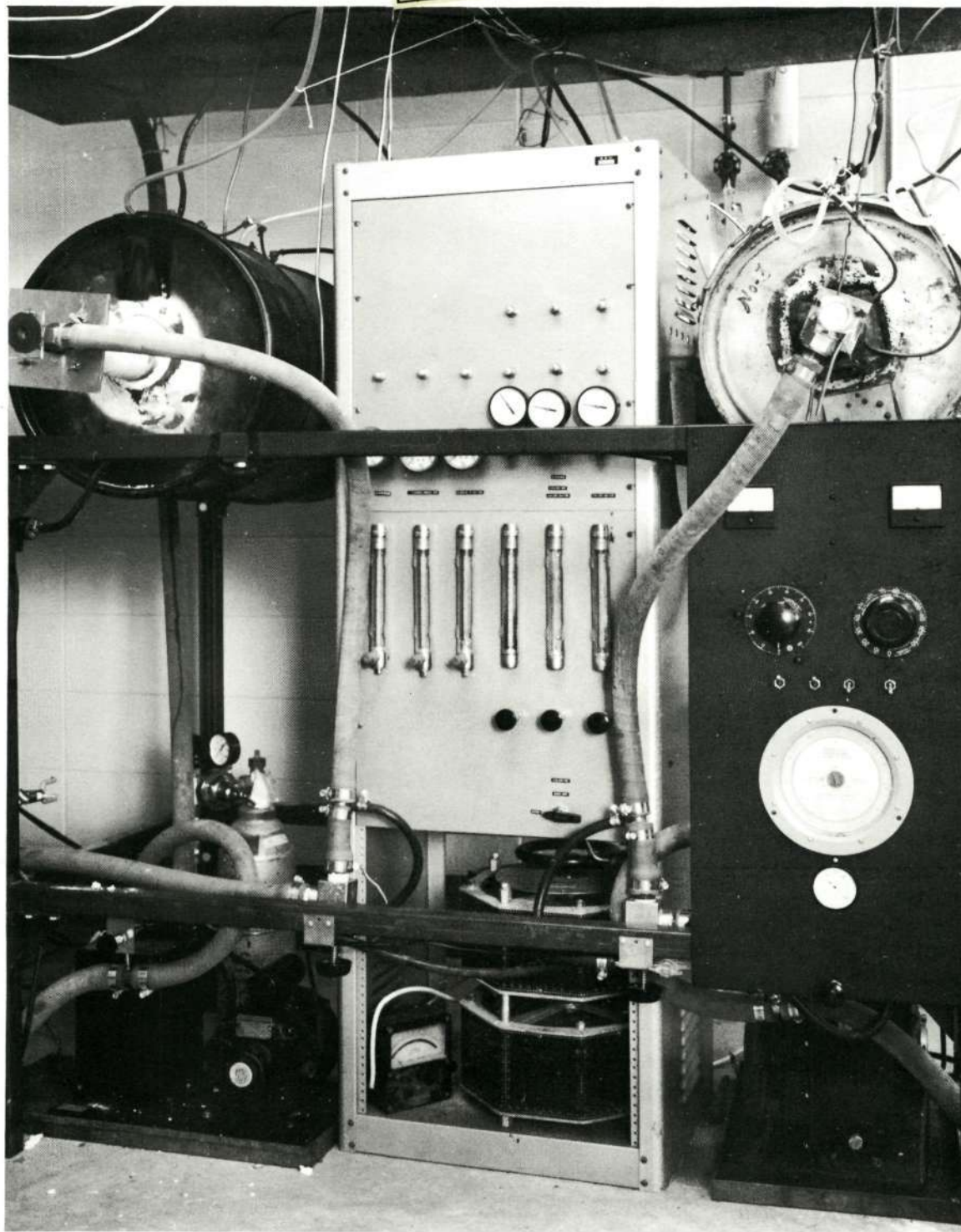


Fig. 31 - Molybdenum-Heated Reactors with Pump and Flow Controls

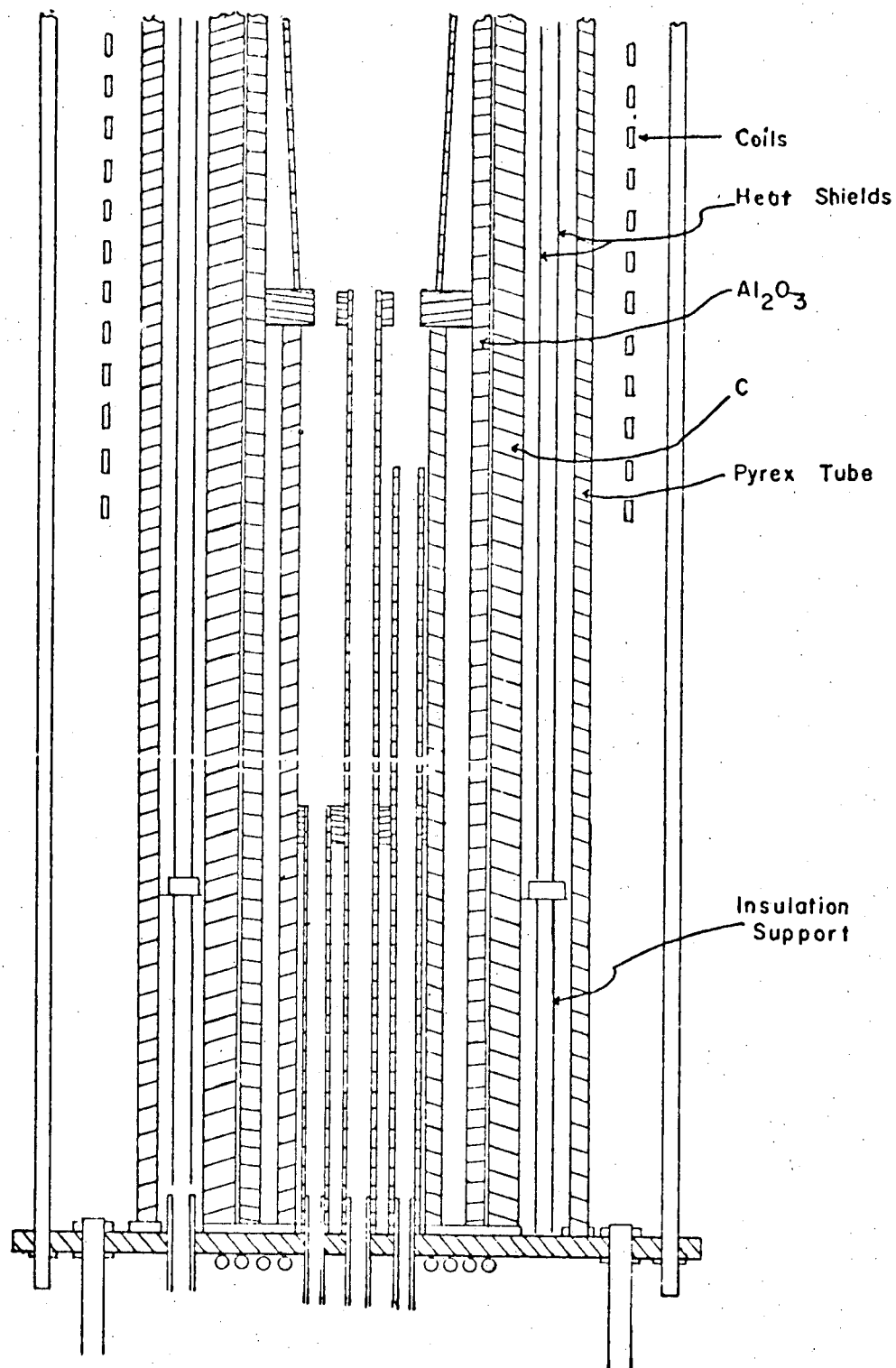


Fig. 32 - Induction Furnace Reactor

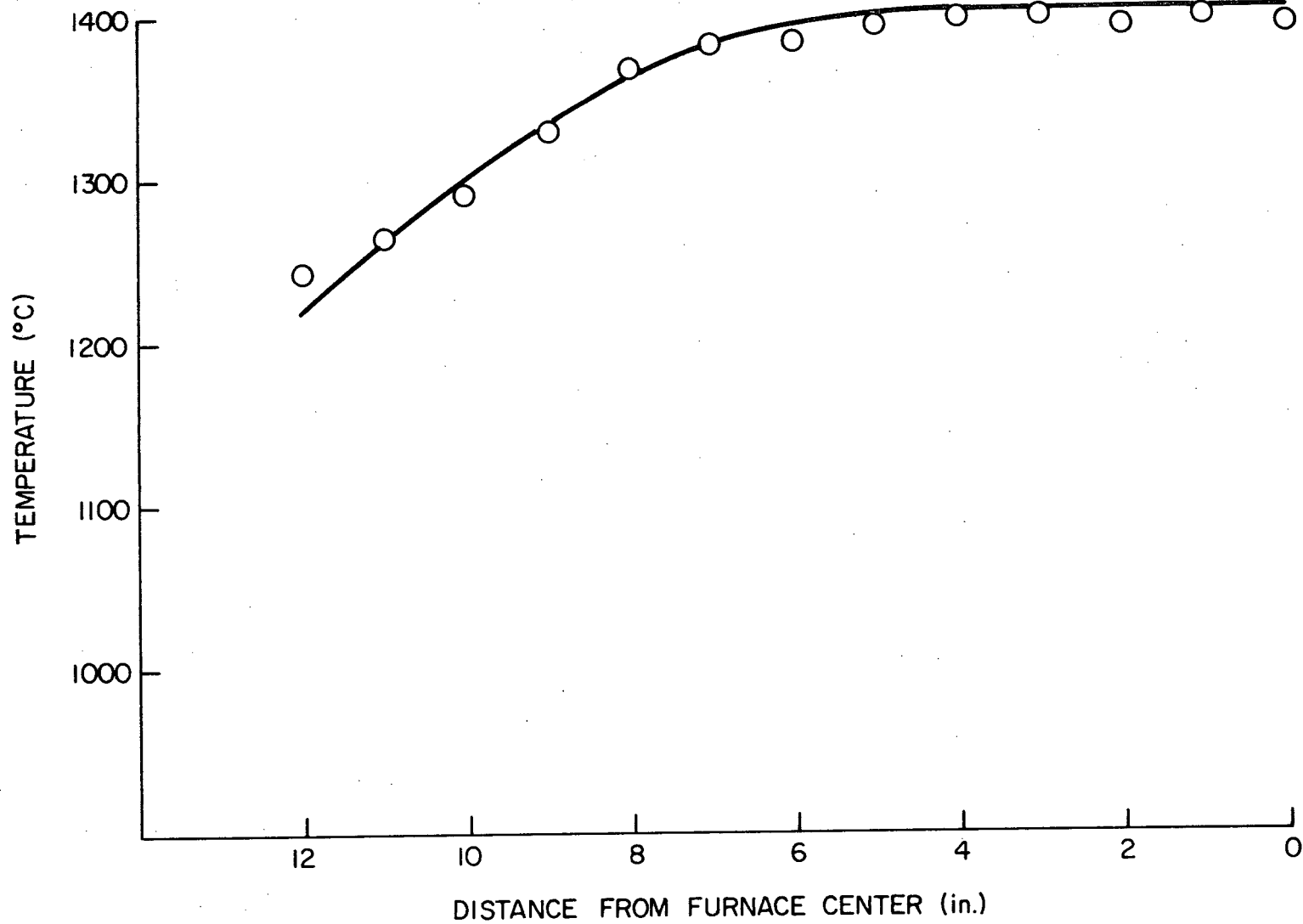
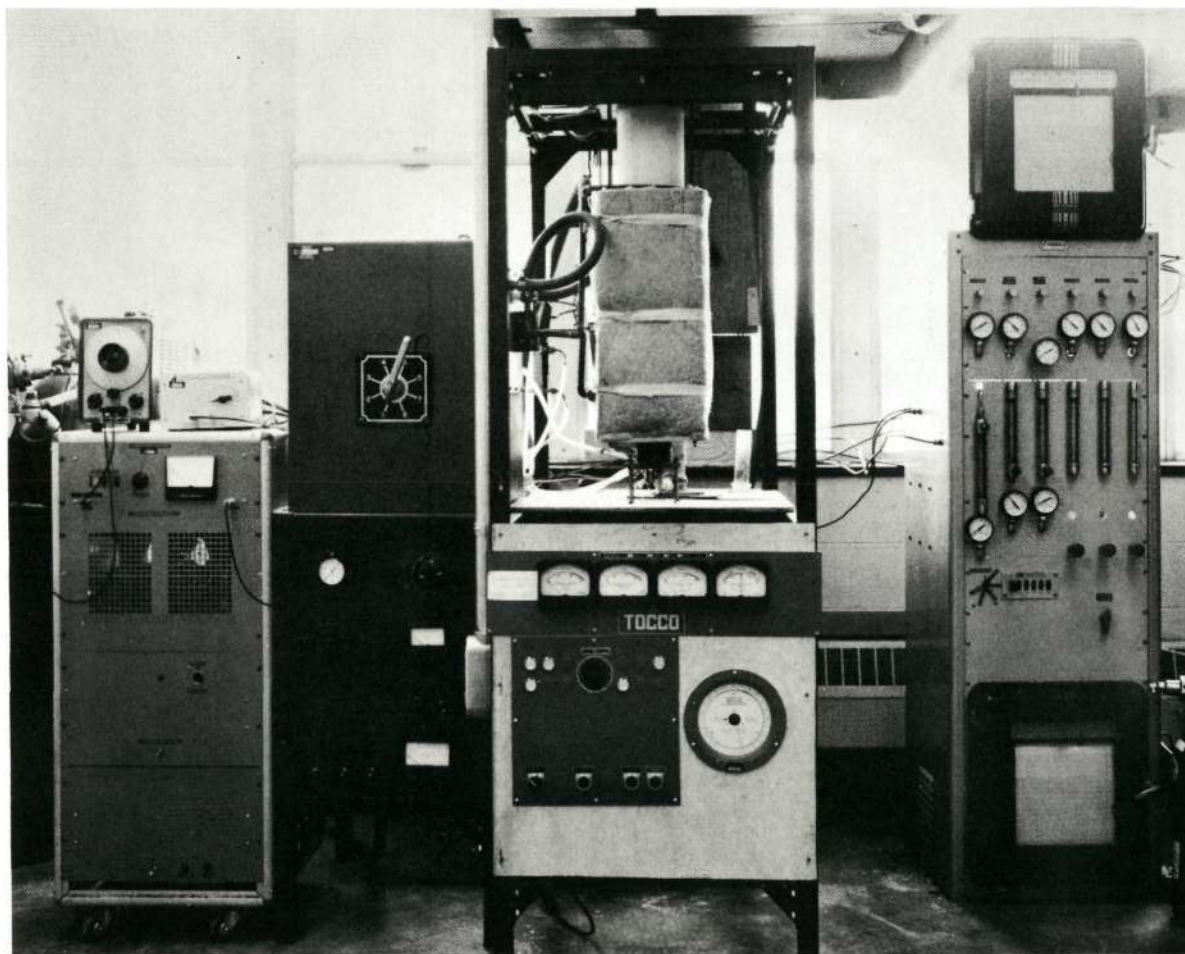


Fig. 33 - Temperature Profile of Induction Furnace



Reproduced from
best available copy.

Fig. 34 - Induction System

The performance of a particle collector is described by collection efficiency. Regardless of the figure of merit, performance is not a specific characteristic of a given collector but depends on the physical properties of the dispersoid. Figure 35 shows characteristics of particles and dispersoids together with the applicable types of gas cleaning. The primary distinguishing feature of gas dispersoids is particle size. The most widely used unit of particle size is the micron (μ). The particle size of a gas dispersoid is usually taken as the average or equivalent diameter of the particle.

The most widely used type of dust-collection equipment is the cyclone, in which dust-laden gas enters a cylindrical or conical chamber tangentially at one or more points and leaves through a central opening. The dust particles, by virtue of their inertia, will move toward the outside separator wall from which they are led into a receiver. At operating conditions commonly employed, the centrifugal separating force or acceleration may range from 5G, five times gravity, in very large diameter, low-resistance cyclones, to 2500G in very small, high-resistance units. In a cyclone, the gas path involves a double vortex with the gas spiralling downward at the outside and upward at the center. When the gas enters the cyclone, its velocity undergoes a redistribution so that the tangential component of velocity increases with decreasing radius as expressed by $V_{ct} \sim r^{-n}$. A cyclone is essentially a settling chamber in which gravitational acceleration is replaced by centrifugal acceleration.⁵¹

Various centrifugal collectors or cyclones have efficiencies of only 8-40% at one micron and fall rapidly with decreasing particle size. Electrostatic precipitation is limited by the high resistivity of the powder and the increased arc-over at reduced operating pressures. Of the remaining techniques, sonic agglomeration offers the greatest promise for laboratory collection. Construction is simple, even for corrosive service, and collection efficiency is independent of temperature.

A sonic agglomerator subjects the particle-laden gas stream to a standing acoustic wave. Vibration causes particle migration to the antinodes where flocculation occurs. Sonic flocculation is thought to result by a combination of: (a) co-vibration of the particles and gas, (b) sonic radiation pressure and (c) hydrodynamic forces between particles. The degree of flocculation is predictable from the geometry of the tube, the power input and the residence time of the gas stream. The flocs should be of sufficient size to permit collection by conventional means, as in a cyclone.

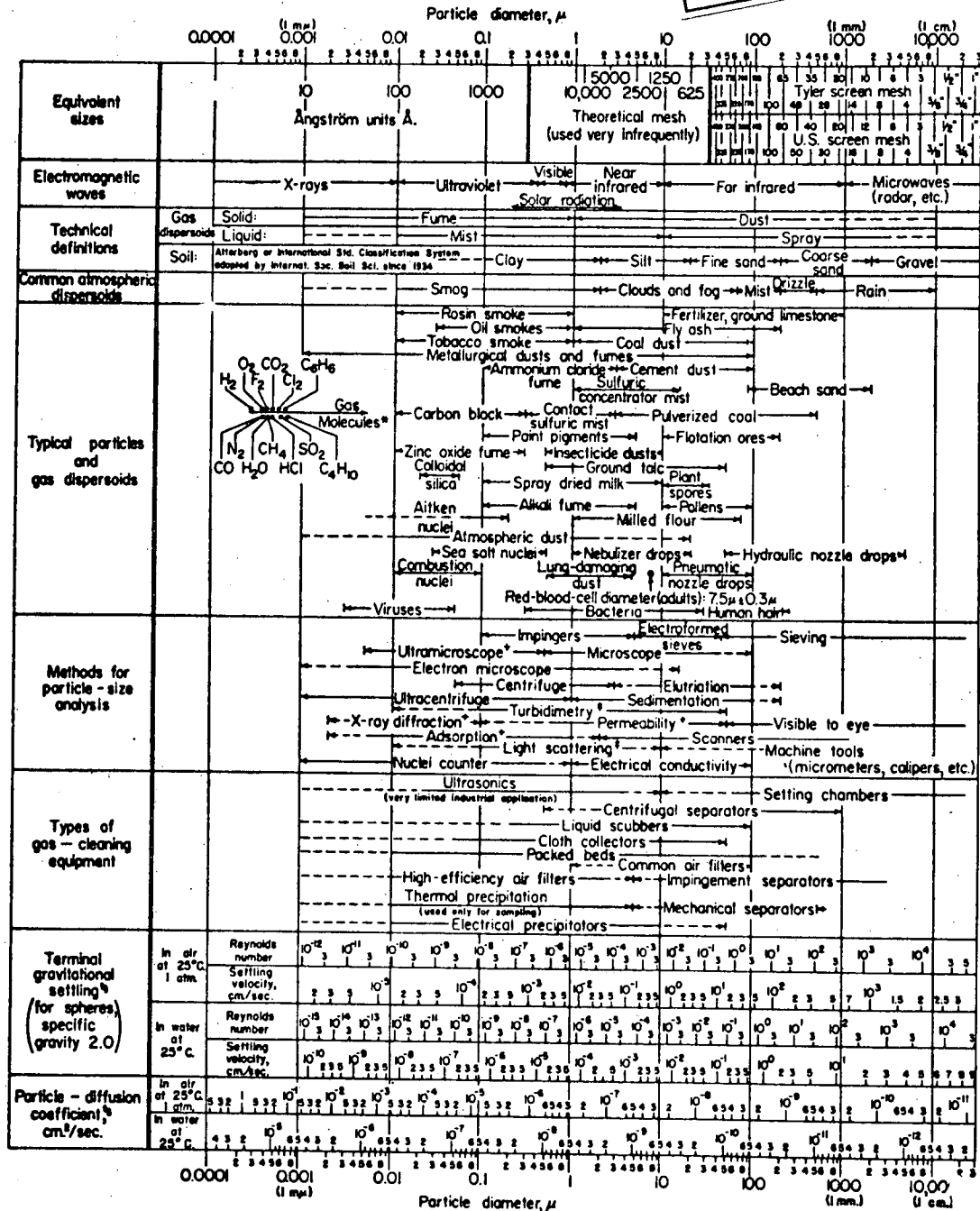
To determine the geometry of an agglomeration tower, an index of agglomeration, I_a , was defined such that

$$I_a = \frac{d}{d_o} \quad (81)$$

where

GAS-SOLIDS SEPARATIONS

Reproduced from
best available copy.



- * Molecular diameters calculated from viscosity data at 0°C.
- * Furnishes average particle diameter but no size distribution.
- * Size distribution may be obtained by special calibration.
- * Stokes-Cunningham factor included in values given for air but not included for water.

Fig. 35 - Characteristics of Particles and Particle Dispersoids.
(Courtesy of the Stanford Research Institute, prepared
by C. E. Lapple)⁵¹

d = final agglomerate diameter

d_0 = initial particle diameter

An index of 100 was necessary to change 0.1 micron powder into 10 micron agglomerates which can be collected by a cyclone. From Boucher⁵² an index of agglomeration of 100 required a residence time in the tower of about ten seconds. For typical flow rates of 100 cc per second, a tower volume of 1000 cc was needed to satisfy this requirement. Thus,

$$1000 = \frac{D^2 L}{4} \quad (82)$$

where

D = tower diameter

L = tower length

A diameter of 5.1 cm (2 inches) and length of 42 cm (16.5 inches) were chosen as the tower dimensions.

To determine the sonic power requirements, the coalescence constant, C , was determined. It is related to the index of agglomeration by

$$I_a = e^{(Ct/3)} \quad (83)$$

where t is the residence time. For $I_a = 100$ and $t = 10$ seconds, the coalescence constant, C , was 1.4. Boucher has shown that the average sound intensity, I , within the tower is:

$$I = C^2 \text{ watts/cm}^2 \quad (84)$$

The cross-sectional area of the tower, A , is 20 cm². Thus,

$$\text{Power (P)} = IA = 40 \text{ watts} \quad (85)$$

Based on the design considerations a sonic agglomerator, Fig. 36, was constructed. Sonic input was supplied to 11,000 Hz and power levels to 60 watts. A flexible Mylar film protected the generator from the gas stream and kept the system closed. A glass cyclone, Fig. 37 was placed downstream to collect the agglomerates.

Gases exiting the cyclone were passed through a liquid nitrogen cold trap to remove condensable vapors and prevent excessive pump oil

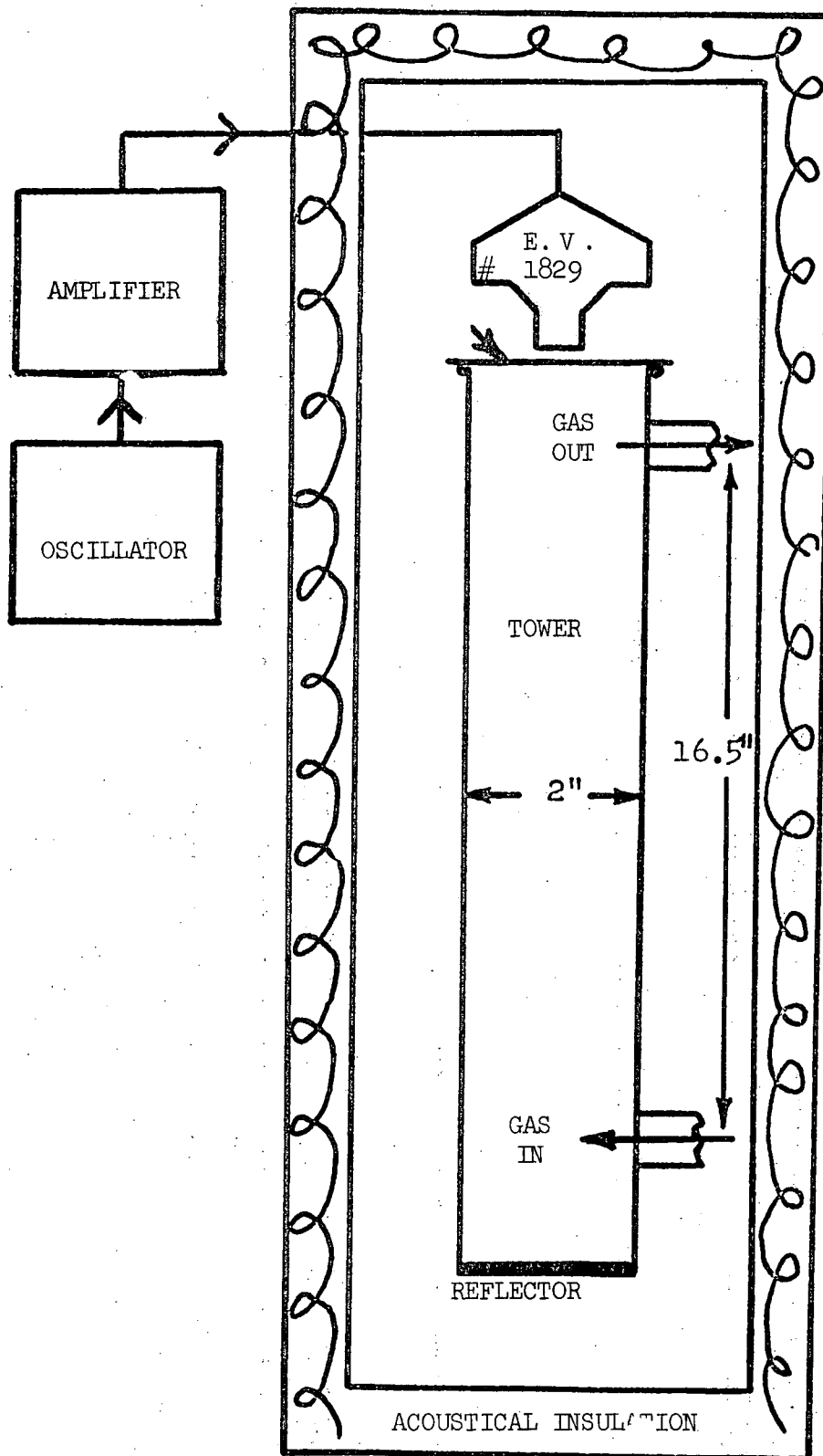


Fig. 36 - Sonic Agglomerator

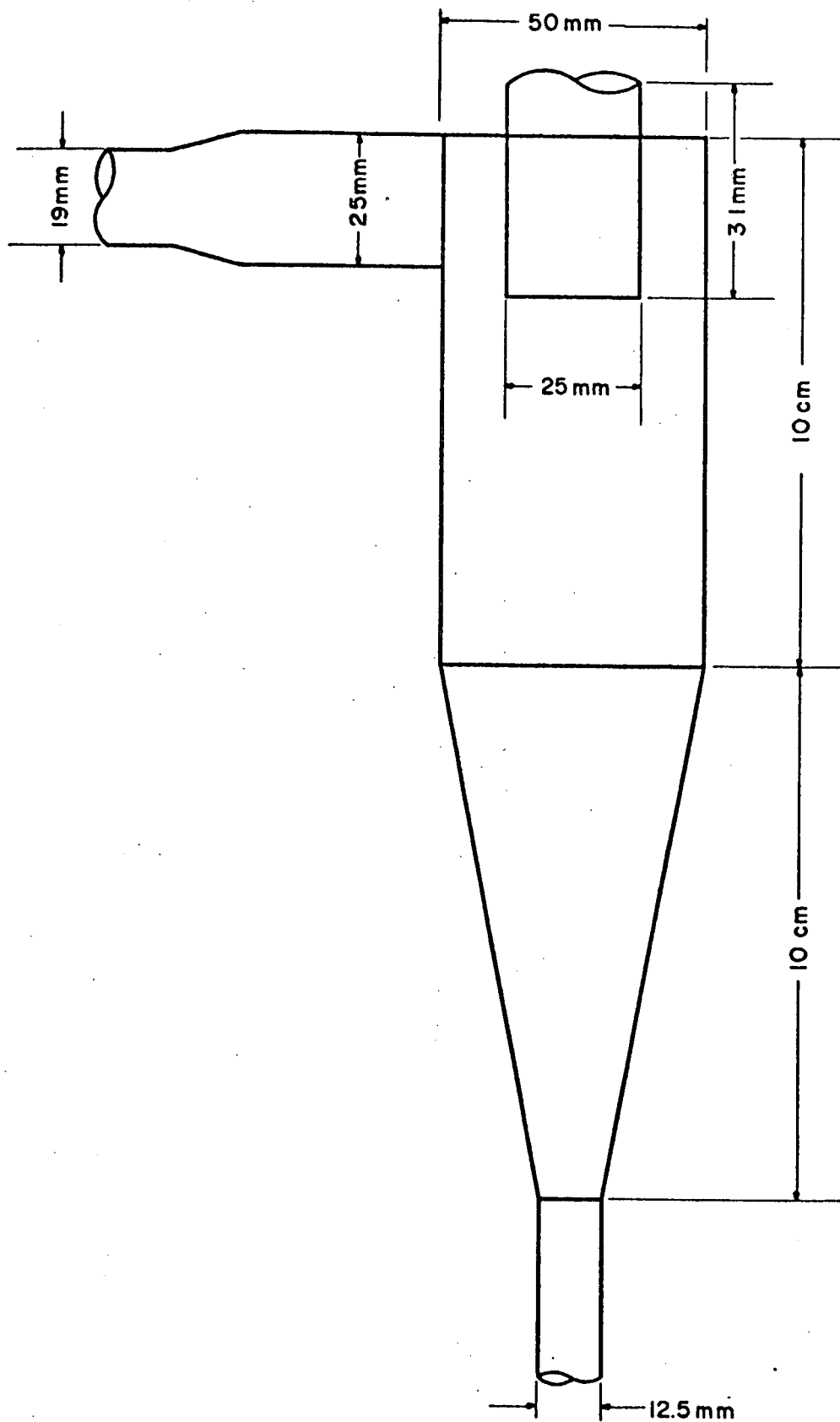


Fig. 37 - Cyclone Collector

contamination. Non-condensable vapors were vented to a hood. For continuous operation product gases would be separated, probably with a wet scrubber, and recirculated to complete the loop.

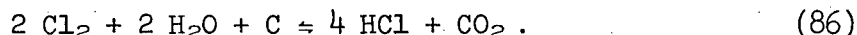
3. Gas Scrubbers

An on-line vapor phase reaction system should be equipped to separate, recover, or convert into useful products the gaseous HCl, Cl₂, and CO. A review of the literature to identify efficient and practical means of recovering product gases indicated some of the wet-scrubbing techniques to be⁵³⁻⁶²

- a. spray towers,
- b. deflection washers,
- c. mechanical (combination of dry and wet),
- d. atomizing (venturi throat-type), and
- e. wetted fibers and packed towers (only method described for acid mist removal).

in which a liquid is employed to achieve or assist in the removal of powders from gases. Figure 38 shows a block-type flow plan and a schematic of a typical laboratory-type scrubber. The basic and most essential part of this scrubber is the absorption tower, consisting of water flowing over activated charcoal.

The flows of the two fluids (water down and gas up) in the absorption tower are important. The water must flow at a minimum wetting rate (MWR) so that it wets all the charcoal. The relative flow of the two fluids (i.e., water and gas) must not be so large, however, that the upward flow of gas impedes the downward flow of water by bubbling through it, a point known as the flooding rate is reached, at which the flow of water is impeded. The tower is designed to operate at 0.2°C and remove HCl and Cl₂ from the gas stream. The HCl is removed by direct reaction with water. The absorption coefficient (that is, the solubility of HCl in water at 0°C and at 1/30 atm.) is 2.74 g/100 ml. The Cl₂ is removed by the reaction⁶³



Because the solubility of Cl₂ in H₂O is small, (i.e., ~ 0.1 g/100 ml at 0°C and 1/30 atm.) the above reaction will be the dominant mechanism for the removal of Cl₂ from the gas stream. With the HCl and Cl₂ removed from the gas stream, the gas out of the absorption tower consists of water vapor, CO, (from the original product gas) and CO₂ (from the Cl₂ reactions). At this point the gas stream is dried (possibly by 2 CaSO₄ drying column), and the CO-CO₂ mixture is passed through a separator.

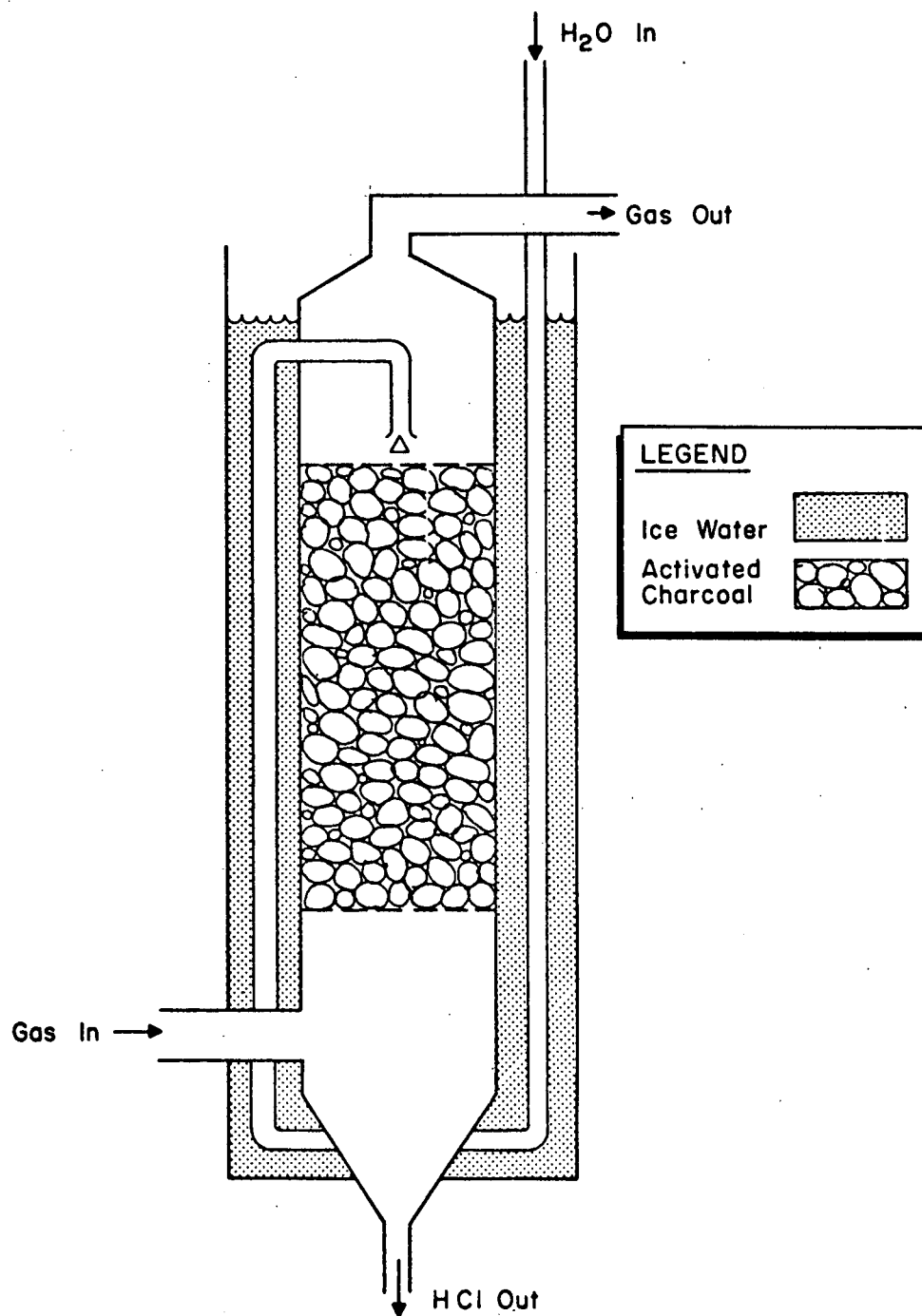
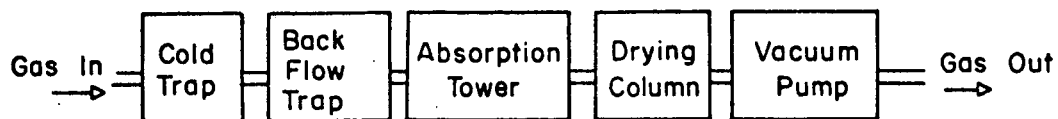


Fig. 38 - Typical Laboratory Scrubber

Using available data for gas inputs in the vapor phase-growth apparatus, approximately 4.3×10^{21} molecules/minute of solid species are produced. For example, for Zn_2TiO_4 this corresponds to $4 \times 4.30 \times 10^{21}$ molecules of HCl . By converting the number of HCl molecules to moles and then to grams, we get approximately 1.0 grams. If the solubility of HCl in water at 1/30 atm and 0°C is 2.74 gm HCl /100 ml water, then 1.04 gm dissolves in 38 ml of water. If an equal amount of HCl is produced by the Cl_2 reaction in the absorption tower, approximately 80 ml/min of water is necessary to remove the HCl and Cl_2 from the gas flow. Using a conservative safety factor (and realizing that the flow rates assumed in this treatment are high) 200 ml/min of water should be sufficient. The cold trap and back-flow trap upstream from the absorption tower are added variations that prevent solid particles from entering the absorption tower.

4. Chlorinator

A chlorinator for titanium was designed, fabricated, and installed on the apparatus. The chlorinator was electrically insulated by wrapping pressed Fiberfrax around the surface; Kanthal wire was wrapped over the Fiberfrax. The chlorinator was thermally insulated by wrapping the Kanthal wire-wrapped chlorinator with Kaowool blanket-type insulation. The chlorinator temperature profile was stabilized and calibrated. Because of a temperature drop at the outlet end of the chlorinator, the Kanthal wrapping was modified. The rewrapped Kanthal was stabilized and calibrated.

A double-stage chlorinator, Figs. 39 and 40, was constructed for the production of Zn_2TiO_4 . The purpose of the double-stage chlorinator was to chlorinate zinc oxide and titanium dioxide, and produce a homogeneous mixture of zinc chloride and titanium tetrachloride before the chlorides entered the reaction zone.

To establish a controlled halide flow to the reaction chamber, the conversion of chlorine to metal chloride must be determined. To measure the conversion efficiency, a chlorinator was constructed as shown in Figure 41. The Inconel chamber containing the metal was fitted with thermowells for accurate mapping of radial and longitudinal temperatures. External heating with asbestos-insulated Nichrome wire maintained the chlorinator and transfer lines at the desired temperature. A Pyrex condenser immersed in liquid nitrogen was used to collect the chloride. The conversion efficiency was calculated as the ratio of the actual weight of chloride in the condenser to the theoretical weight for 100% conversion.

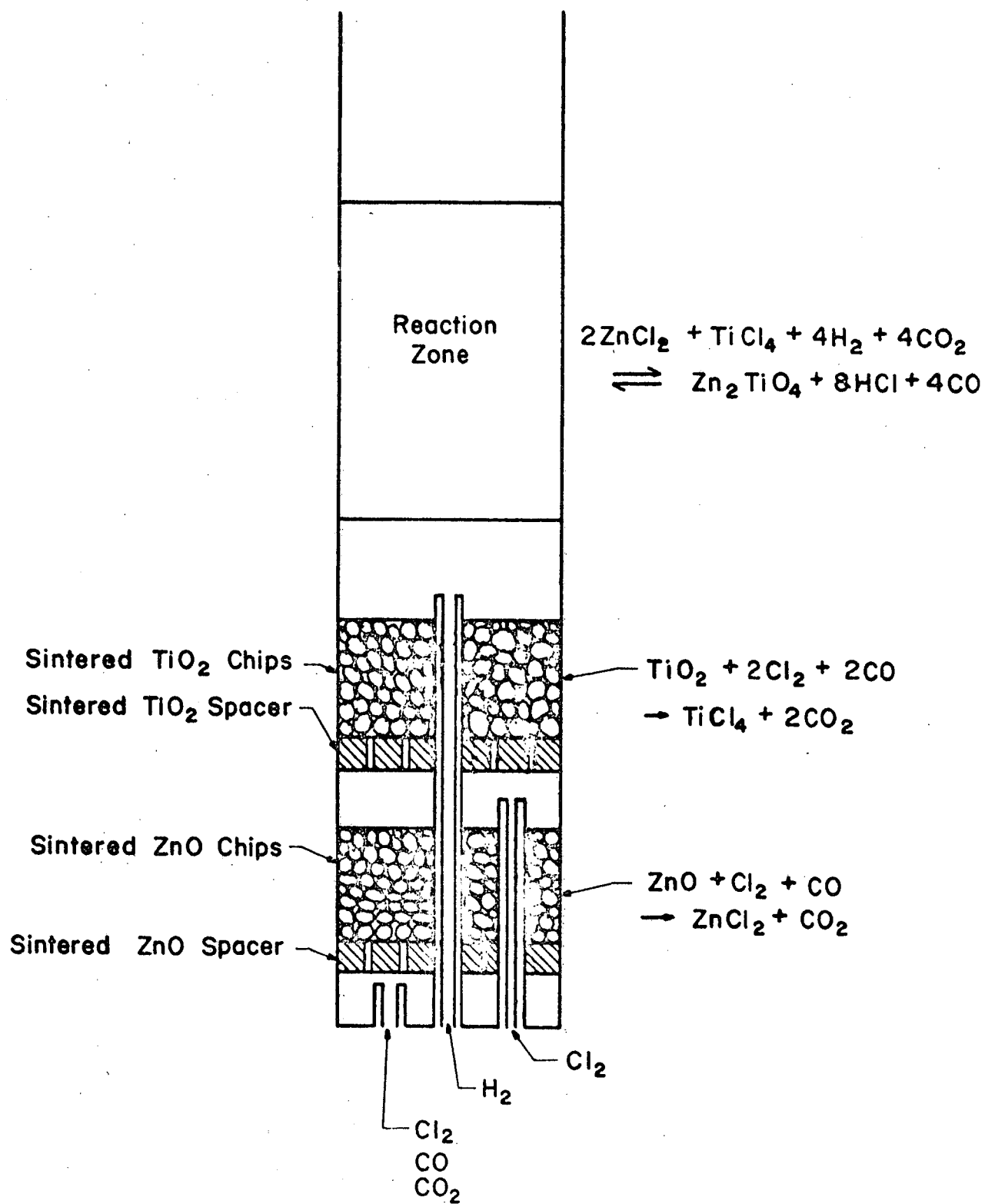


Fig. 39 - Double-Stage Chlorinator

Reproduced from
best available copy. 

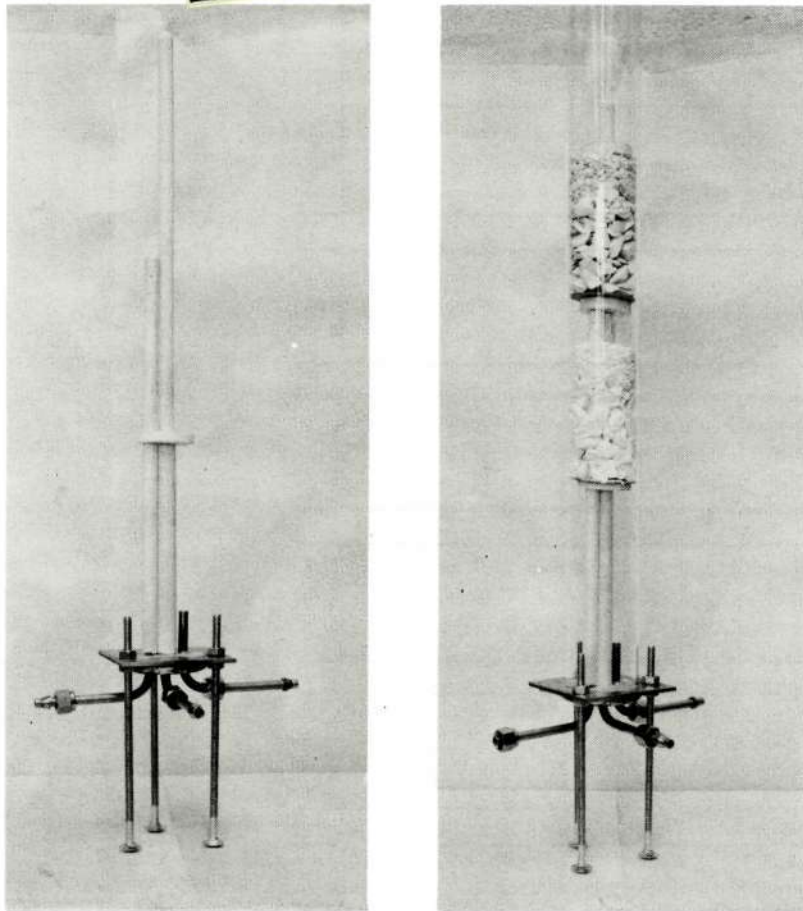


Fig. 40 - Double-Stage Chlorinator

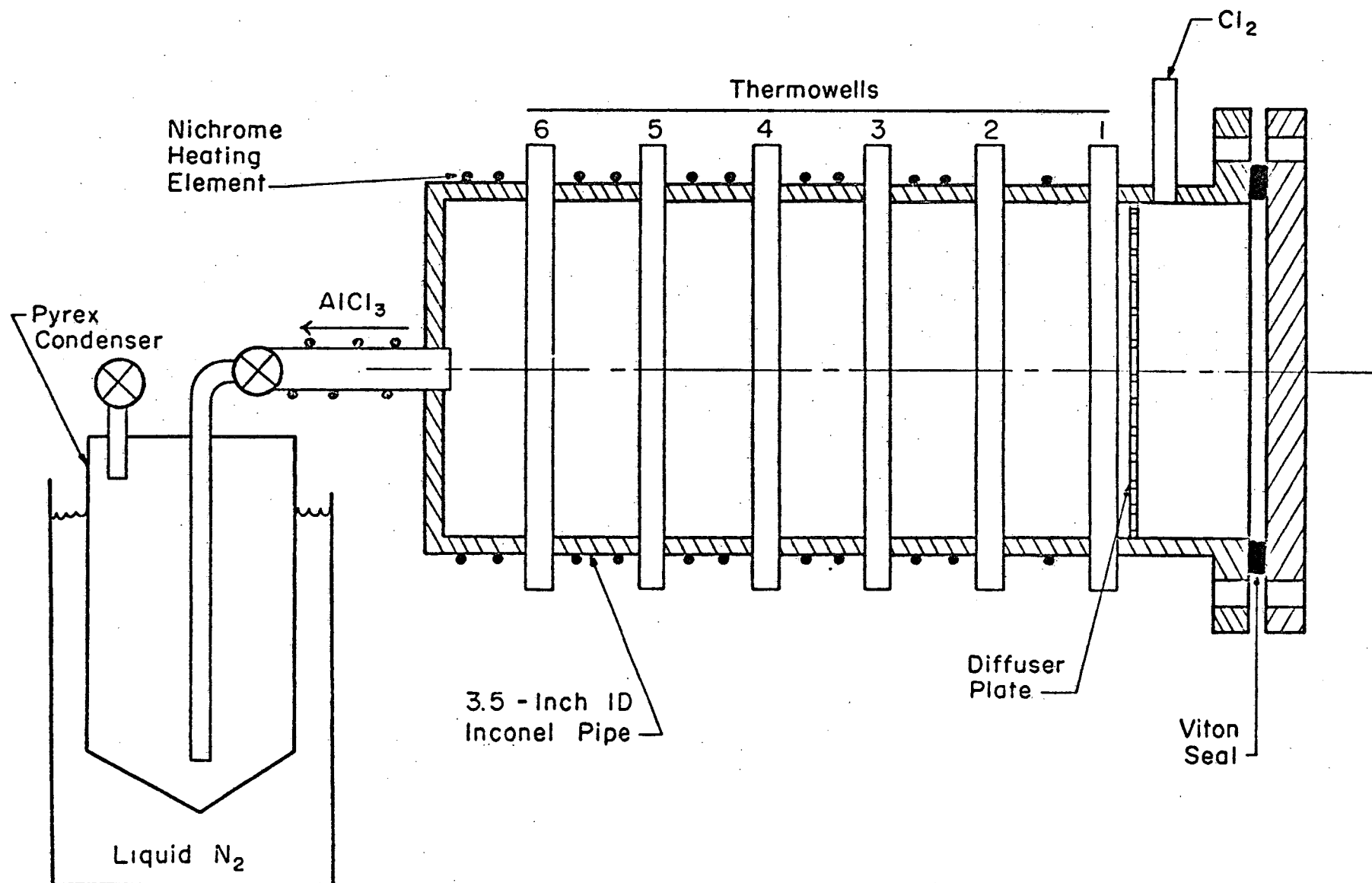


Fig. 41 - Apparatus for Chlorination Efficiency Determinations

5. Gas Temperature Measurement

Because prediction of reaction products using thermodynamic data is based on constant temperature, it was necessary to know the actual temperature of the gases to verify reaction temperature. An alumina tube (10 mm in diameter) was positioned in the center of the hot zone with a thermocouple placed next to it. The temperature of the alumina tube was obtained by sighting an optical pyrometer on a mirror reflection through the viewing port while at the same time recording the thermocouple temperature. This provided a calibration of the radiation loss due to the mirror and glass viewing port. The thermocouple was next positioned between the alumina reaction tube and the silicon carbide heating element at the center of the hot zone at the same height as the 10 mm alumina sight tube. The system was evacuated and temperature measurement of the interior alumina sight tube and the thermocouple outside the reaction chamber were recorded for a range of temperatures, pressures, and gas flow rates. Hydrogen, carbon monoxide, and carbon dioxide were used as flow gases in the temperature measurements because they would not form solid reaction products which would interfere with the optical pyrometer readings. The effects of gas flows and pressure on the reaction zone temperatures are shown in Fig. 42. The interior of the reaction zone was 10°C lower than the exterior when pressure was at a minimum and no gases were flowing. The interior temperature decreased as gas flow rates were increased. At the highest flow rate the interior temperature was approximately 40°C lower than the exterior temperature range of 1000°C to 1400°C. A temperature profile of the vapor reaction furnace is shown in Fig. 43.

6. Gas Flow Control

Reactant gas flows were monitored using low-flow rotameters. Chemically pure CO, welding grade CO₂, and 99.97 per cent H₂ were passed through calcium sulfate drying columns to remove moisture before monitoring. Chlorine (99.965 pure) was introduced into the system at three positions through three separate flowmeters and transfer lines. Refer to Figs. 44 through 46 for vapor phase apparatus, gas control panel, and a schematic of the system gas flow control, respectively.

To provide greater flexibility in gas flow rate ranges, two sets of flow meters were operated at different pressures. The low-flow rotameters were calibrated in cc/min at 0 psig and 5 psig for H₂, CO, and CO₂, and in cc/min at 0 psig and 25 psig for Cl₂. For calculation of desired flow rates, gas pressure through the rotameters had to be considered. Gas pressures through the rotameters and flow rates were adjusted by micrometer needle valves below the rotameters.

System pressure was controllable from atmospheric pressure to 5 μ using two Duoseal vacuum pumps in parallel and a bleed valve which opened to the atmosphere. Pressure was monitored with two absolute diaphragm gages which had ranges of 0-50 mm Hg and 0-760 mm Hg.

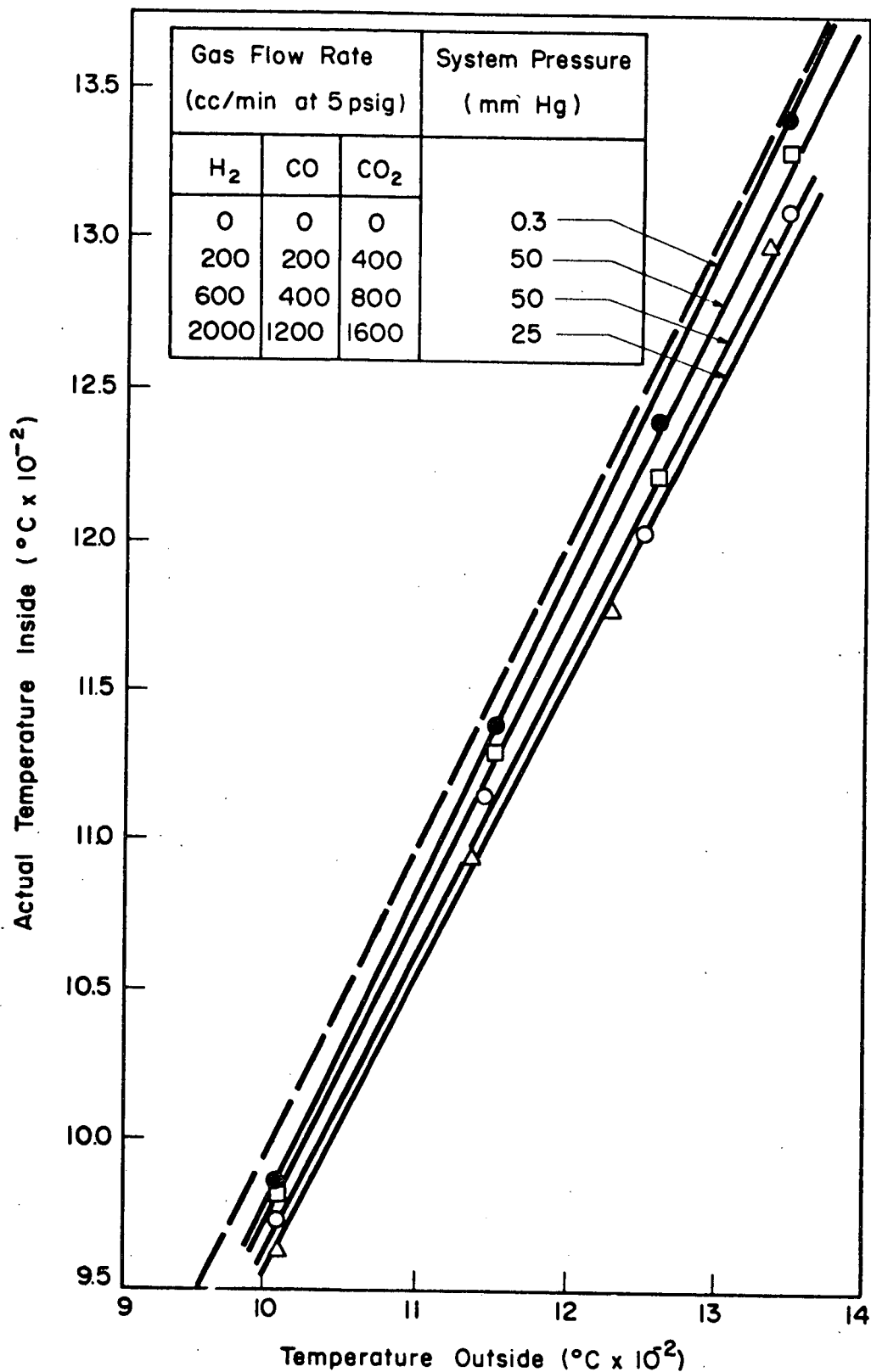


Fig. 42 - Actual Temperature Inside Reaction Tube vs Temperature Outside Reaction Tube for Various Gas Flow Rates

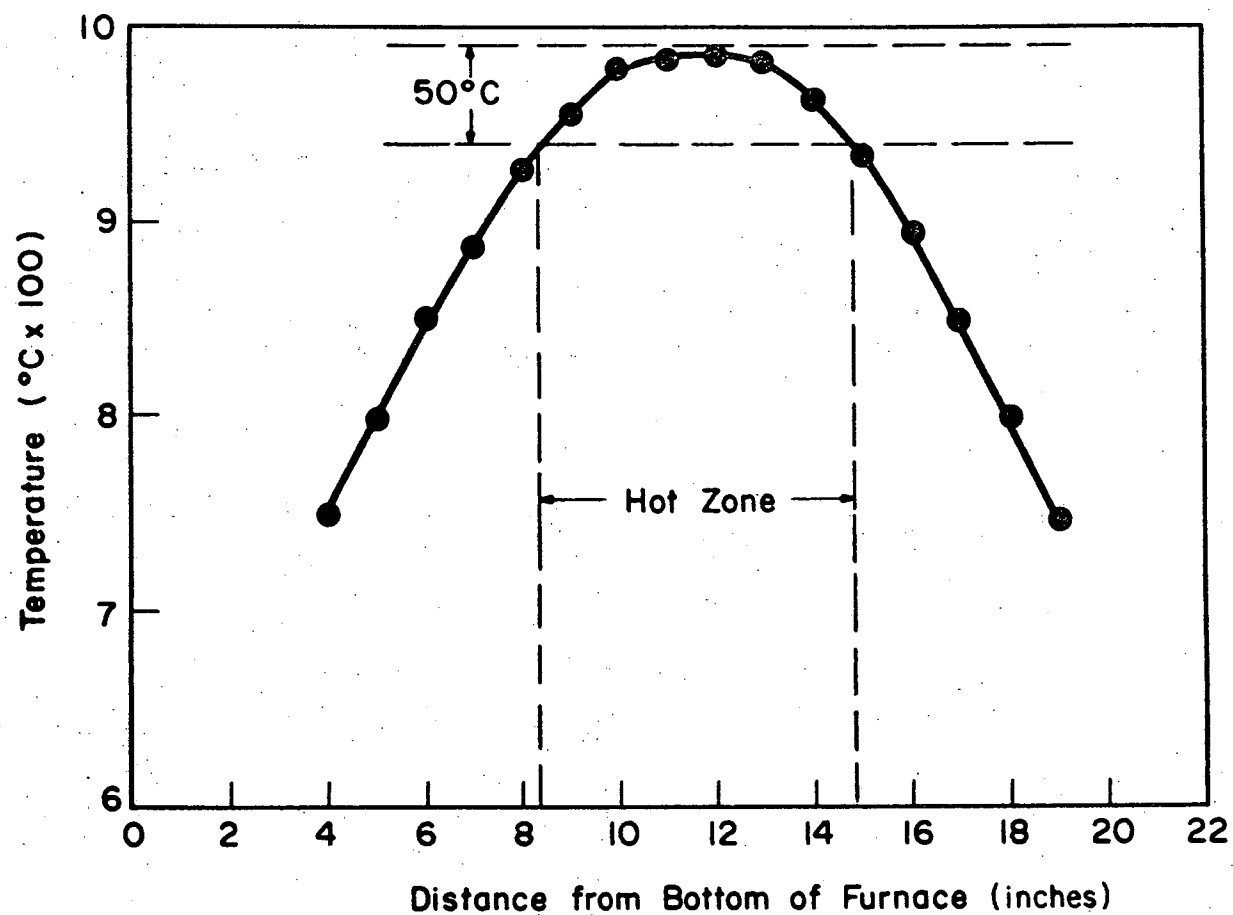


Fig. 43 - Temperature Profile of Vapor Phase Reaction Furnace

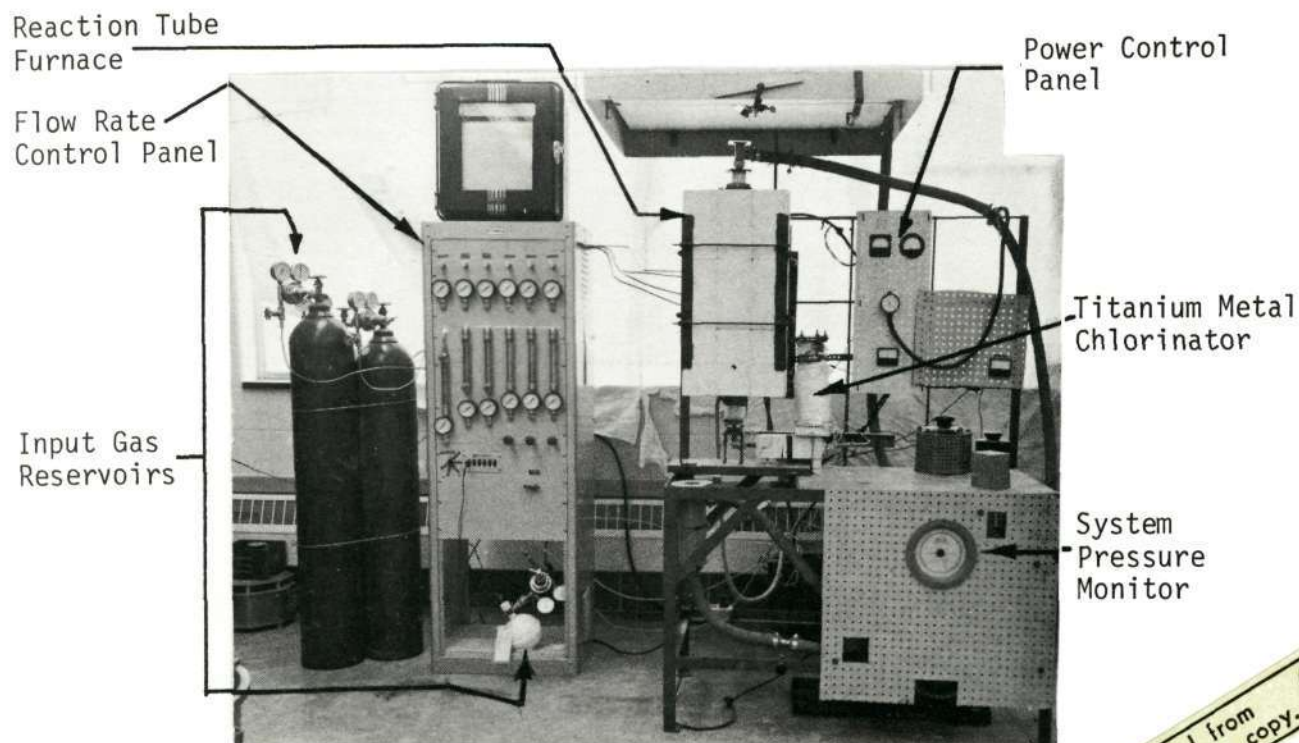


Fig. 44 - Vapor Phase Apparatus

Reproduced from
best available copy.

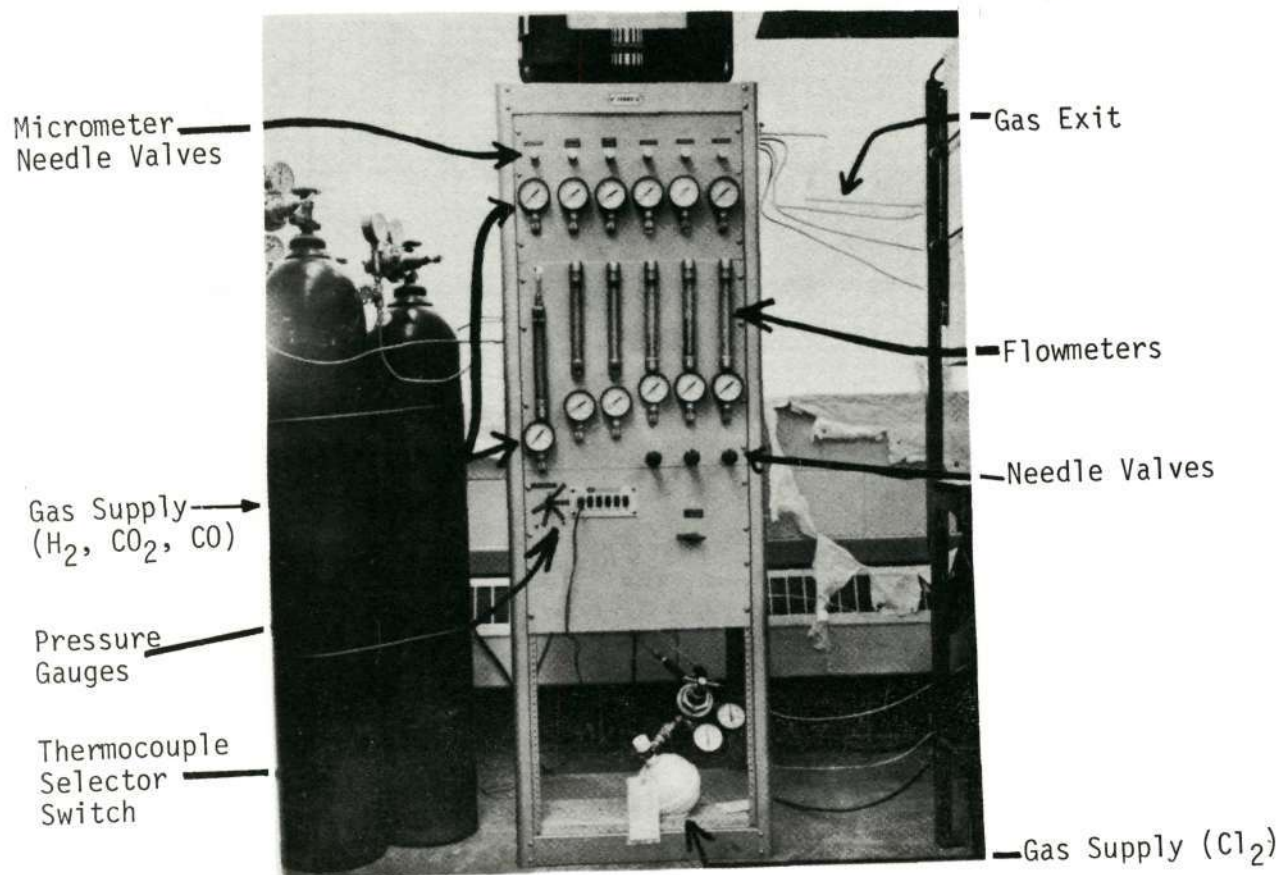


Fig. 45 - Gas Flow Control Panel

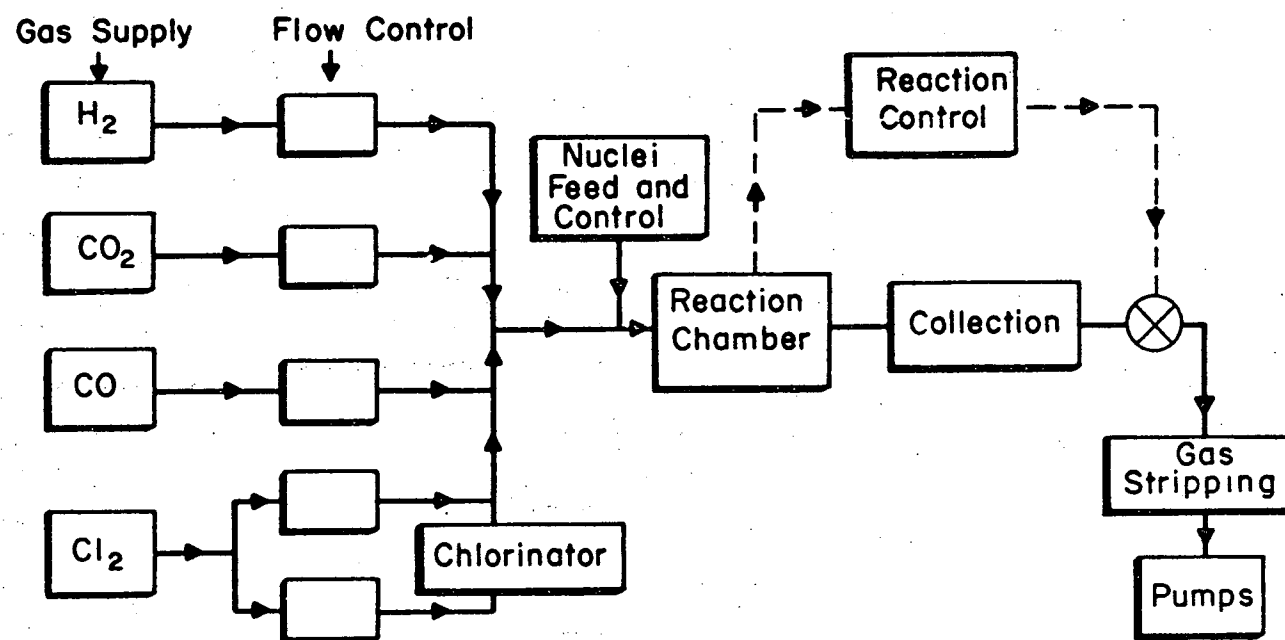


Fig. 46 - Vapor Phase System

7. Operation Procedure for Vapor Phase Runs

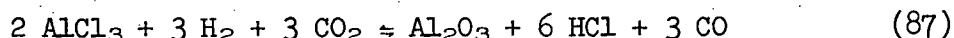
The source metals or metal oxides were weighed and placed in the reaction zone and chlorinator. The system was evacuated and all portions of the system were brought up to temperature and stabilized before each run. Liquid nitrogen was poured into the cold trap. Gas flows were initiated in the following order: Cl_2 to metal or oxides, CO_2 , and H_2 . At the completion of a run gases were stopped in the reverse order from initiation, the system was closed above the cold trap, and the cold trap was removed and placed in a hood while the trapped gases evaporated. Once the chlorinator cooled to room temperature, the reaction tube was removed and the reaction products analyzed.

IV. EXPERIMENTAL RESULTS

A. ALUMINUM OXIDE (Al_2O_3) PRODUCTION AND CHARACTERIZATION

1. Aluminum Oxide Production

Aluminum oxide powders were prepared by the following reaction:



The reaction free energy and equilibrium constant were calculated over the temperature range 500-2000°K. The thermodynamic data are summarized in Table XXII.

The growth conditions for the formation of aluminum oxide are given in Table XXIII. Aluminum chloride was generated as discussed previously. Weight-loss measurements on the source aluminum indicated a minimum chlorination efficiency of 80-95 per cent for the various runs.

Reactant gases were admitted to the reaction chamber through a central injector nozzle. The reaction chamber was a horizontal alumina tube, 38 millimeters in diameter. The tube was heated in a molybdenum-wound, hydrogen-protected furnace. Gases were reacted in a 10-cm long isothermal zone. Aluminum oxide powders nucleated and grew during residence in the isothermal zone, beyond which they deposited on the tube walls. Samples were carefully selected from various regions within the tube for characterization.

2. Aluminum Oxide Characterization

The crystalline phases in the powder samples were identified with x-ray diffraction (see Appendix D). In all samples, the principal phases were transition aluminas, predominantly gamma and delta. Alpha alumina (corundum) was present as a secondary phase. Traces of unreacted aluminum chloride were observed in a few samples collected near the cold end of the tube where the temperature would permit deposition.

The particle size of the powder samples was determined by lineal analysis of electron micrographs. Several typical micrographs are shown in Figs. 47-50.

Comparing the particle size with the growth conditions for each run, several trends appear.

In general, increasing system pressure decreases the gas velocity in the reaction chamber, allowing first a longer time for gas mixing and

Table XXII - Free-Energy Changes and Equilibrium Constants as a Function of Temperature for Aluminum Oxide Production

T (°C)	T (°K)	ΔG° Reaction* (kcal/mole)	K_p Reaction*
227	500	-63.3	3.3×10^{27}
727	1000	-75.8	3.0×10^{16}
927	1200	-80.2	3.4×10^{14}
1127	1400	-85.4	1.8×10^{13}
1227	1500	-87.6	5.0×10^{12}
1327	1600	-90.5	2.0×10^{12}
1427	1700	-92.6	6.9×10^{11}
1527	1800	-94.6	2.7×10^{11}
1627	1900	-97.4	1.4×10^{11}
1727	2000	-100.0	7.4×10^{10}

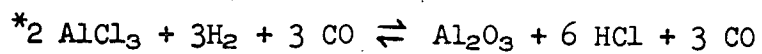
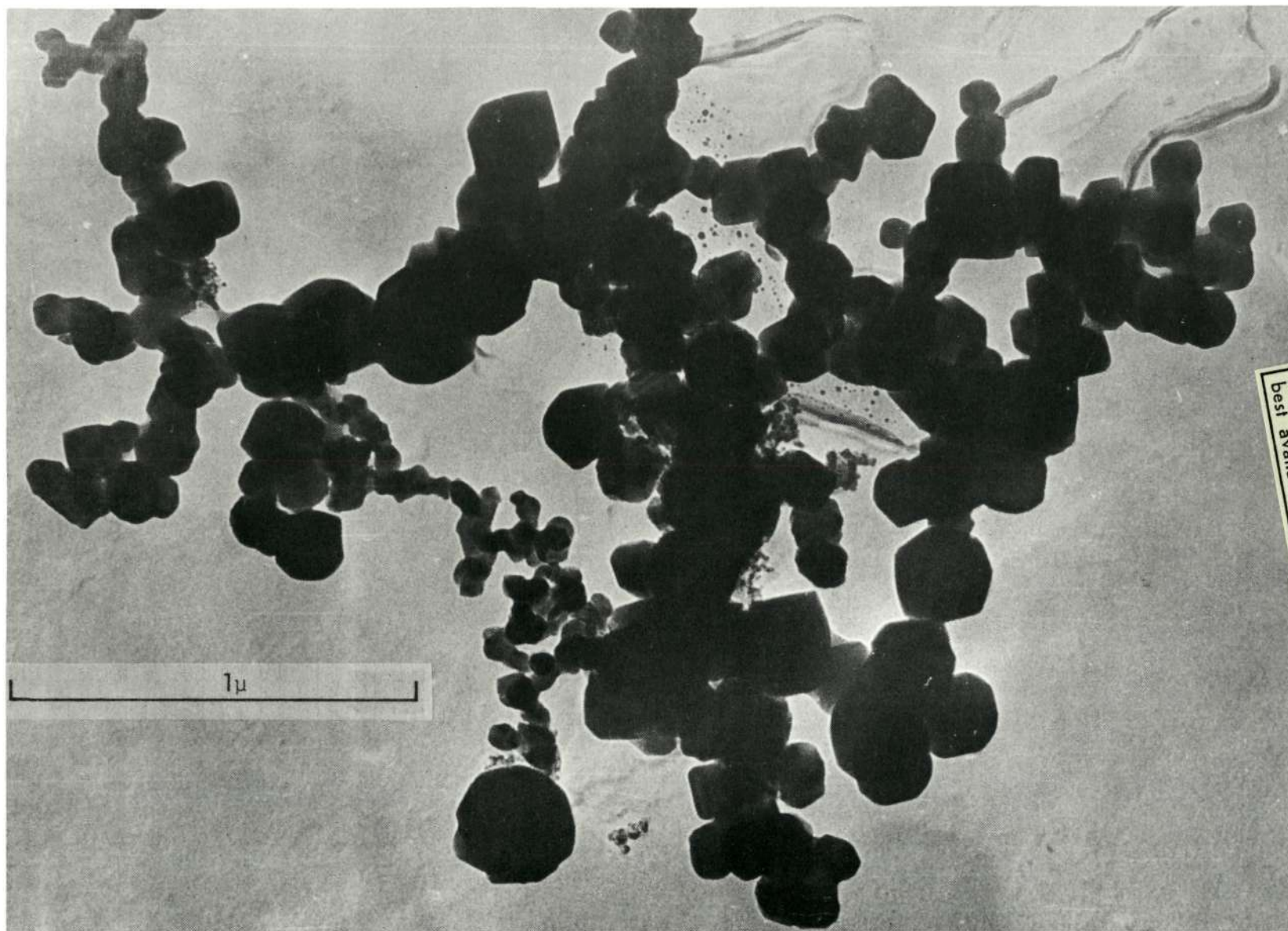


Table XXIII - Conditions for Aluminum Oxide Powder Production

Run No.	Flow Conditions (cc/min)					P _{Total} (Torr)	Temp. (°C)	Particle Size (μ)
	H ₂	CO ₂	CO	Cl ₂ xs	Cl ₂ Al			
VA-2	1000	200	-	-	30	15	1500	~ 0.01
VA-3	1000	200	-	-	30	200	1500	~ 0.01
VA-4	1000	200	-	-	40	350	1500	~ 0.01
VA-6	950	800	100	20	40	100	1750	0.05
VA-8	950	800	100	20	70	340	1700 1750 1800 1850	0.07
VA-9	950	800	100	20	70	260	1850	
VA-10	600	500	210	45	50	660	1800	0.13
VA-13	100	100	-	-	80	50	1700	0.02
VA-15	100	100	-	-	80	100	1750	0.09
VA-16	50	50	-	-	40	50	1750	0.05
VA-17	100	100	-	-	80	200	1750	0.12
VA-18	50	50	-	-	40	50	1600	0.14



Reproduced from
best available copy.



Fig. 47 - Electron Micrograph of Alumina Powder, 67,200X

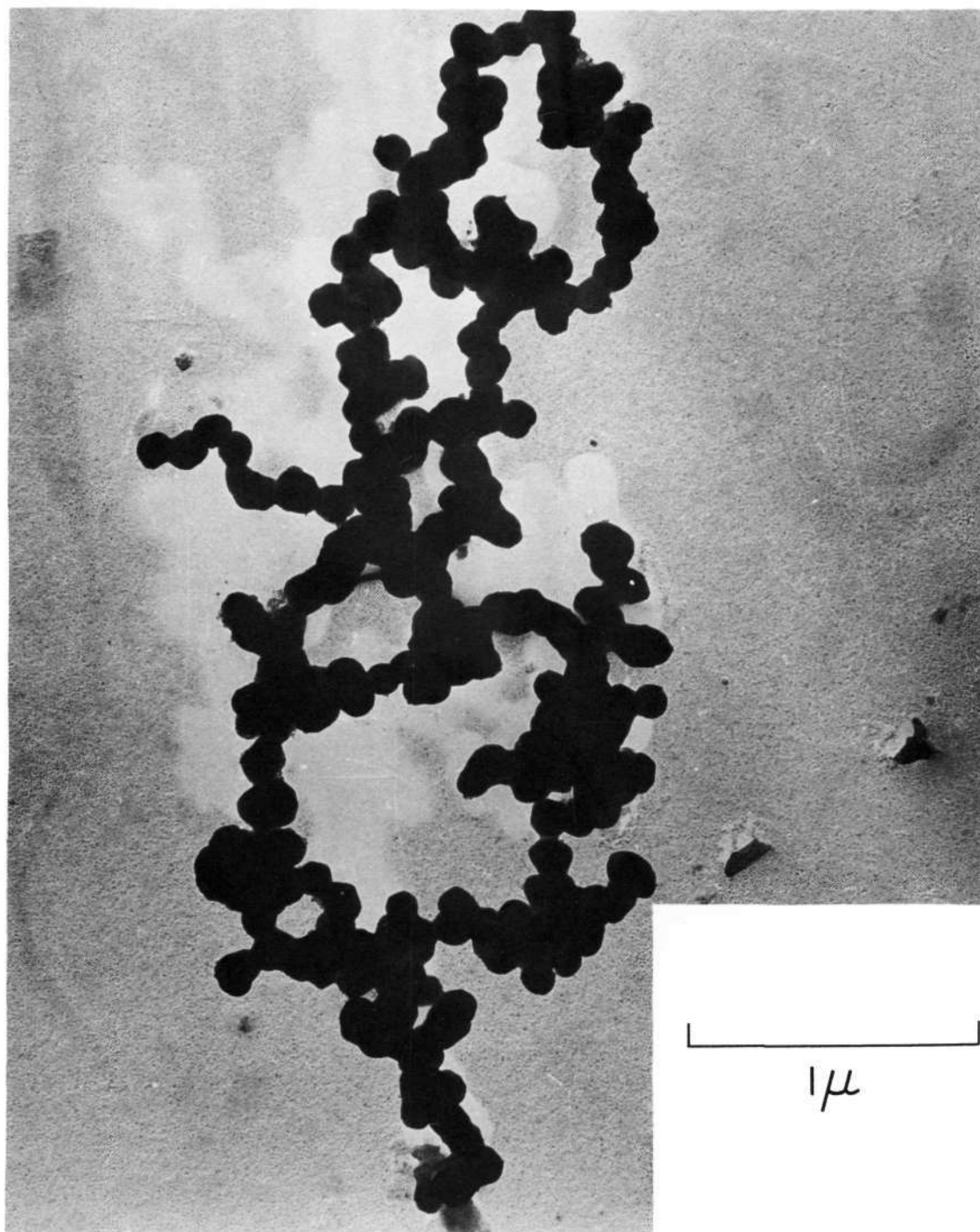


Fig. 48 - Electron Photomicrograph of Alumina Powder, 43,400X

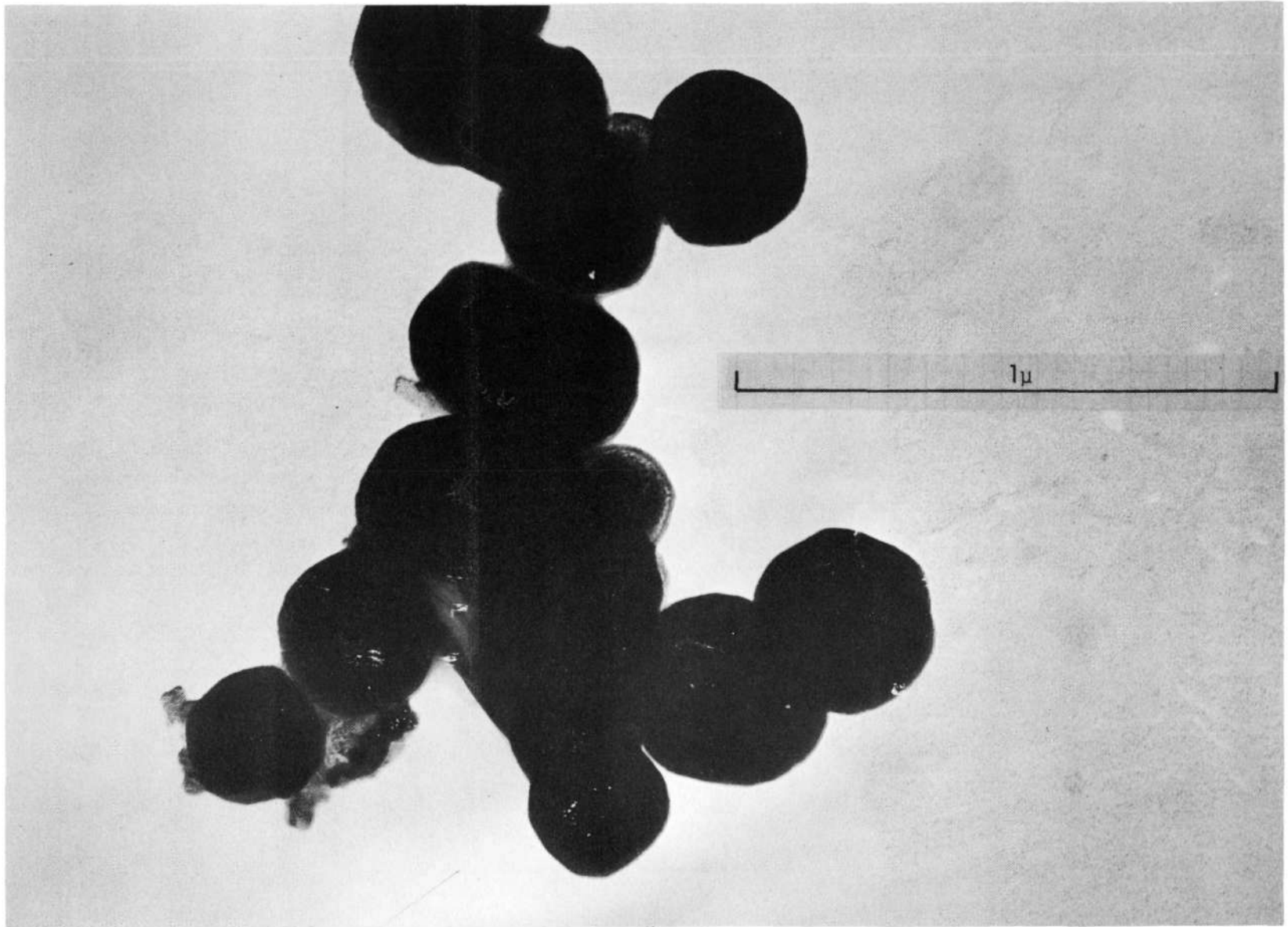


Fig. 49 - Electron Photomicrograph of Alumina Powder, 92,000X

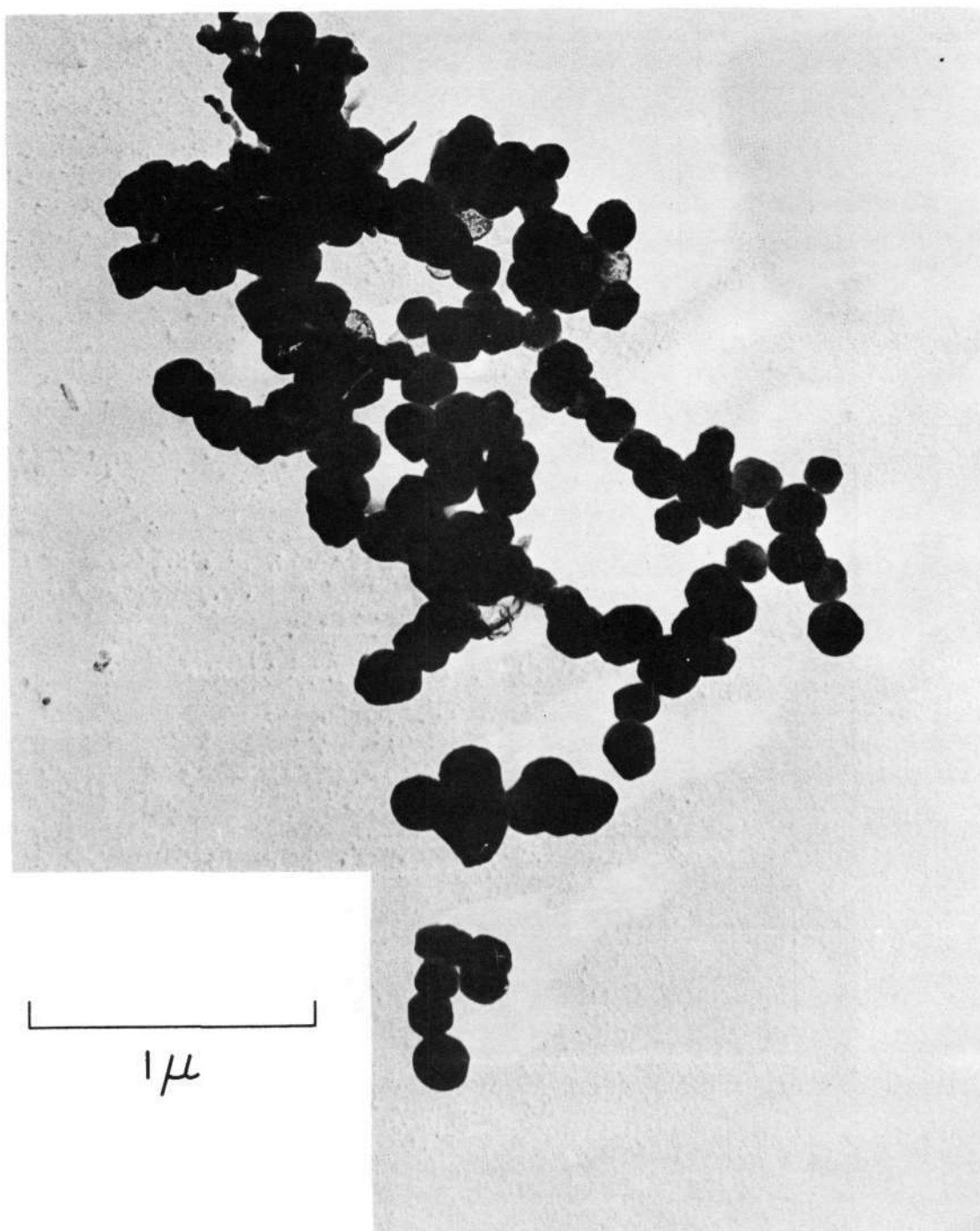


Fig. 50 - Electron Photomicrograph of Alumina Powder, 43,400X

heat transfer in the reactor entrance, and second a longer residence time for powder growth in the hot zone. Increased heat transfer to the gas stream and increased mixing should result in increased efficiency of conversion. This was substantiated by the increased amount of powder produced at higher pressures. In addition, the increase in residence time in the hot zone should result in an increase in average particle size. The increase in size from 0.09μ for Run No. VA-15 to 0.12μ for Run No. VA-17 verified this assumption.

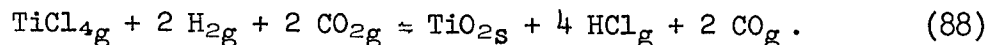
To determine the effect of temperature upon particle size, temperature was varied in VA-8 from 1700°C to 1850°C , in 50°C increments. The particle size distribution of the resulting powders was much wider than that obtained at fixed conditions. A range from 0.01 to 0.20 was observed with an average particle size of 0.07μ . From a probability plot of particle size versus per cent finer (Fig. 51), the particle size distribution appeared to be a sum of several individual normal distributions. The results of VA-9 suggest that the large size of VA-8 can be attributed to the higher temperatures. However, comparing VA-16 with VA-18, it is apparent that a decrease in temperature resulted in considerable increase in particle size for these particular input gas conditions. The effect of temperature on particle size is not precisely defined from the results of these experiments.

Comparing the results of VA-15 with VA-16, the effect on particle size of the number of moles input is apparent. Doubling the inputs and simultaneously doubling system pressure to maintain the same gas velocity results in approximately a two-fold increase in particle size from 0.05 to 0.09μ . Thus growth appears to be directly related to the availability or concentration of the growth species.

B. TITANIUM DIOXIDE (TiO_2) POWDER PRODUCTION AND CHARACTERIZATION

1. Titanium Dioxide Powder Production

The powder was formed by the following chemical reaction and the subsequent homogeneous nucleation of rutile:



The reaction free energy and equilibrium constant for the reaction (Table XXIV) show thermodynamic feasibility over the entire temperature range. Titanium chloride was generated by controlled chlorination of titanium sponge at 400°C , and transferred to the reaction chamber at 300°C to prevent condensation in the lines. Runs were made over the temperature range 800 - 1400°C . The silicon carbide furnace heated the reaction chamber. Gases were injected into the chamber through a five millimeter (inside diameter) alumina tube which extended

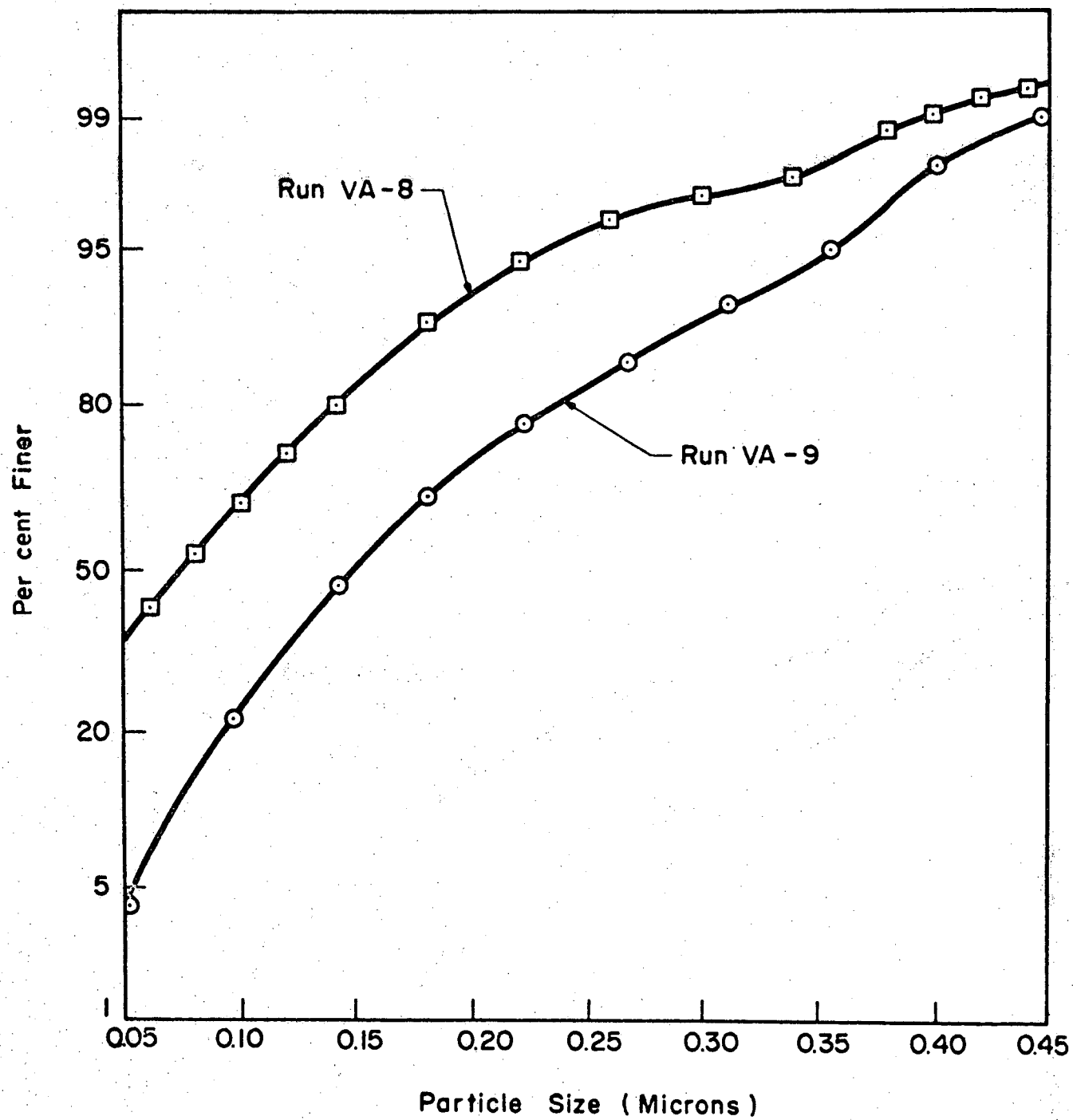
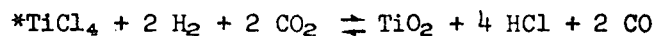


Fig. 51 - Particle Size Probability Plot of Alumina Powders

Table XXIV - Free-Energy Changes and Equilibrium Constants
as a Function of Temperature for Titanium
Dioxide Production

T (°C)	T (°K)	ΔG° Reaction * (kcal/mole)	K_p Reaction*
27	300	- 4.60	2.25×10^3
127	400	-10.55	5.82×10^5
227	500	-17.15	3.14×10^7
327	600	-18.20	4.27×10^8
427	700	-21.85	6.64×10^8
527	800	-25.45	8.98×10^8
627	900	-28.90	1.04×10^7
727	1000	-32.10	1.04×10^7
827	1100	-35.55	1.16×10^7
927	1200	-39.39	1.49×10^7
1027	1300	-42.30	1.29×10^7
1127	1400	-45.90	1.46×10^7
1227	1500	-49.15	1.45×10^7
1327	1600	-53.25	1.88×10^7
1427	1700	-56.45	1.81×10^7
1527	1800	-60.60	2.28×10^7
1627	1900	-64.50	2.63×10^7
1727	2000	-67.40	2.32×10^7



within two inches of the hot zone. Residence time was controlled with system pressure and was calculated for a 25-centimeter isothermal zone. System conditions and particle sizes for specific runs are listed in Table XXV. Analysis by x-ray diffraction of titania powders showed only rutile present at 1200°C and 1400°C. A minor amount of anatase was discovered in the 1000°C powders, and at 800°C specimens were about equal portions of rutile and anatase. The presence of anatase was confirmed by the appearance of the typical anatase morphology in powder micrographs, Figure 52. The dominance of pyramidal faces over prisms in anatase makes its octahedral habit readily distinguishable from the prismatic rutile modification.

2. Titanium Dioxide Powder Characterization

X-ray diffraction analyses of the powder from both runs, using both diffractometer and powder camera methods, showed the material to be rutile. No other phases were detectable. Typical micrographs of rutile powders, Figure 53-56, describe the range and uniformity of size obtained. Average particle size ranged from 0.06 to 0.38 micron. Distributions were narrow, Figure 57, comparing favorably with or superior to materials from other processes. Considerable improvement in surface roughness over commercial oxidation process rutile was observed. Surface areas from 2.3 to 6.6 square meters per gram resulted in surface roughness values of 1.3 to 1.7. This improved surface state should enhance the stability of the pigment in extraterrestrial thermal control coatings.

The effect of residence time and hot zone temperature on the particle size of vapor-grown rutile is presented in Figure 58. For three-dimensional growth, particle volume increased with residence time in the isothermal zone. Since the cube of the diameter provides some measure of particle volume, this parameter was chosen for the abscissa in Figure 58. It was apparent that particle volume increased linearly with residence time, indicating a constant volume growth rate for a constant temperature and reactant gas input. The variation in particle size for very short residence times was indeterminate, but a finite ordinate intercept would be anticipated, representing an induction time required for reaction and nucleation of the growth phase. The volume growth rates, or slopes, from Figure 57 were strongly influenced by temperature, Figure 59. A maximum in growth rate at 1000°C may be explained by considering separately the effects of nucleation and growth. Nucleation rate was qualitatively observed to decrease with temperature. Profuse powder production at 1400°C decreased slightly at 1200°C and was diminished still further at 1000°C. Very little powder was produced at 800°C. High nucleation rate may have depleted the gas stream of the growth species, and little material remained for growth at the higher temperatures. As reaction and nucleation rates decreased with temperature, fewer nuclei were produced and their resultant growth was less inhibited by concentration depletion. The net result was a

Table XXV - System Conditions for TiO₂ Pigment Production

Run No.	Temp. (°C)	Pressure (mm. Hg)	Gas Velocity (cm/sec)	Residence Time (sec)	Average Particle Size (microns)
T- 6	1400	50	62.2	0.4	0.09
T- 4	1400	200	15.5	1.6	0.18
T- 5	1400	400	7.8	3.2	0.18
T- 7	1400	660	4.7	5.3	0.16
T-18	1400	760	4.1	6.1	0.19
T-12	1200	50	54.8	0.45	0.06
T- 8	1200	100	27.4	0.91	0.07
T- 9	1200	200	13.7	1.8	0.17
T-10	1200	400	6.8	3.7	0.21
T-11	1200	660	4.1	6.1	0.27
T-17	1200	760	3.6	7.0	0.25
T-13	1000	87	27.2	0.92	0.15
T-14	1000	175	13.5	1.85	0.21
T-15	1000	350	6.8	3.7	0.29
T-16	1000	760	3.1	8.0	0.38
T-19	800	200	10.0	2.5	0.05
T-20	800	400	5.0	5.0	0.08

Flow Rates: H₂ = 200
 (std. cc./min.) CO₂ = 200
 Cl₂ = 100

Reproduced from
best available copy.

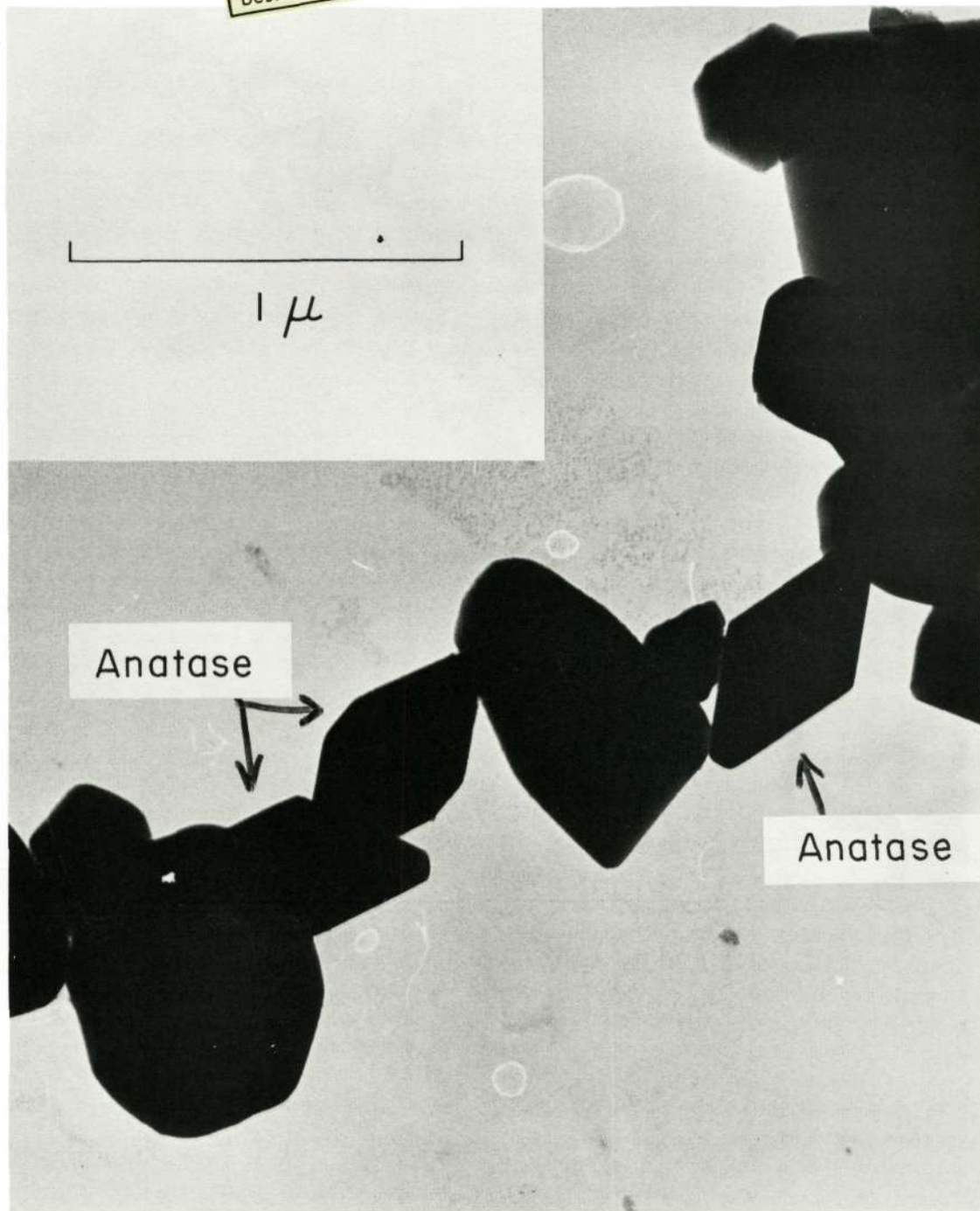


Fig. 52 - Anatase Morphology in Titania Powders, 59,000X

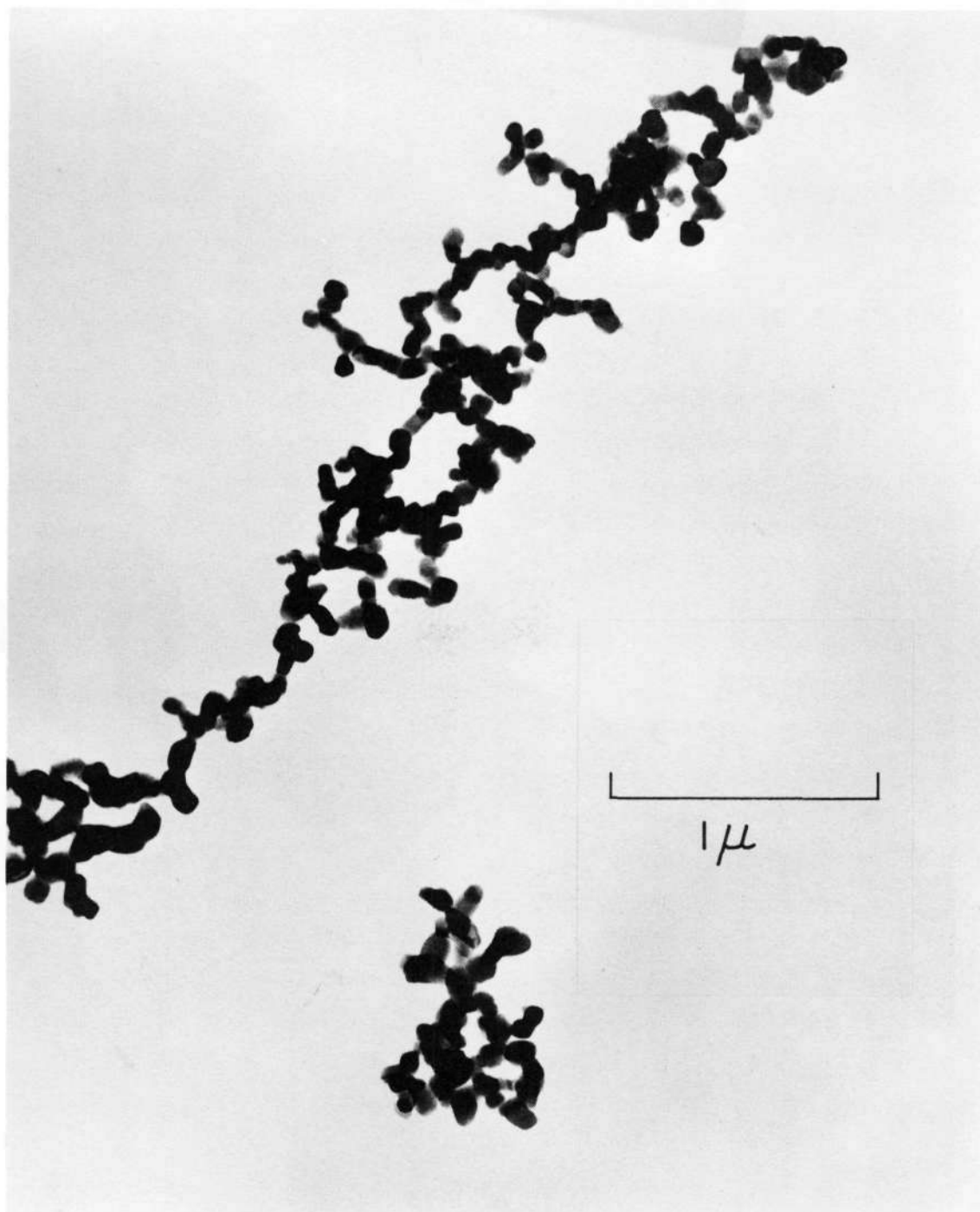


Fig. 53 - Typical Micrograph of Rutile Powder, Run T-8, 40,000X

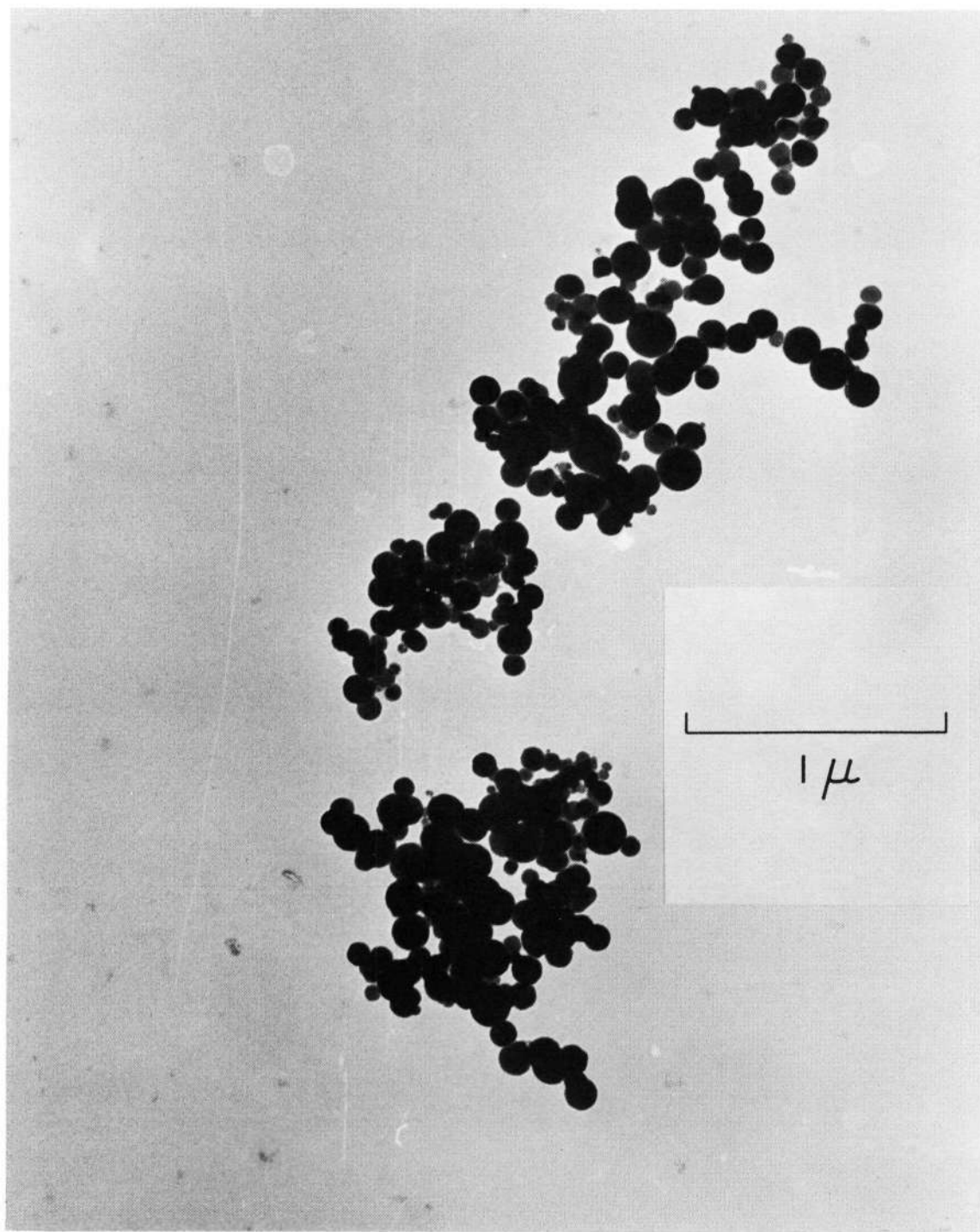


Fig. 54 - Typical Micrograph of Rutile Powder, Run T-6, 40,000X

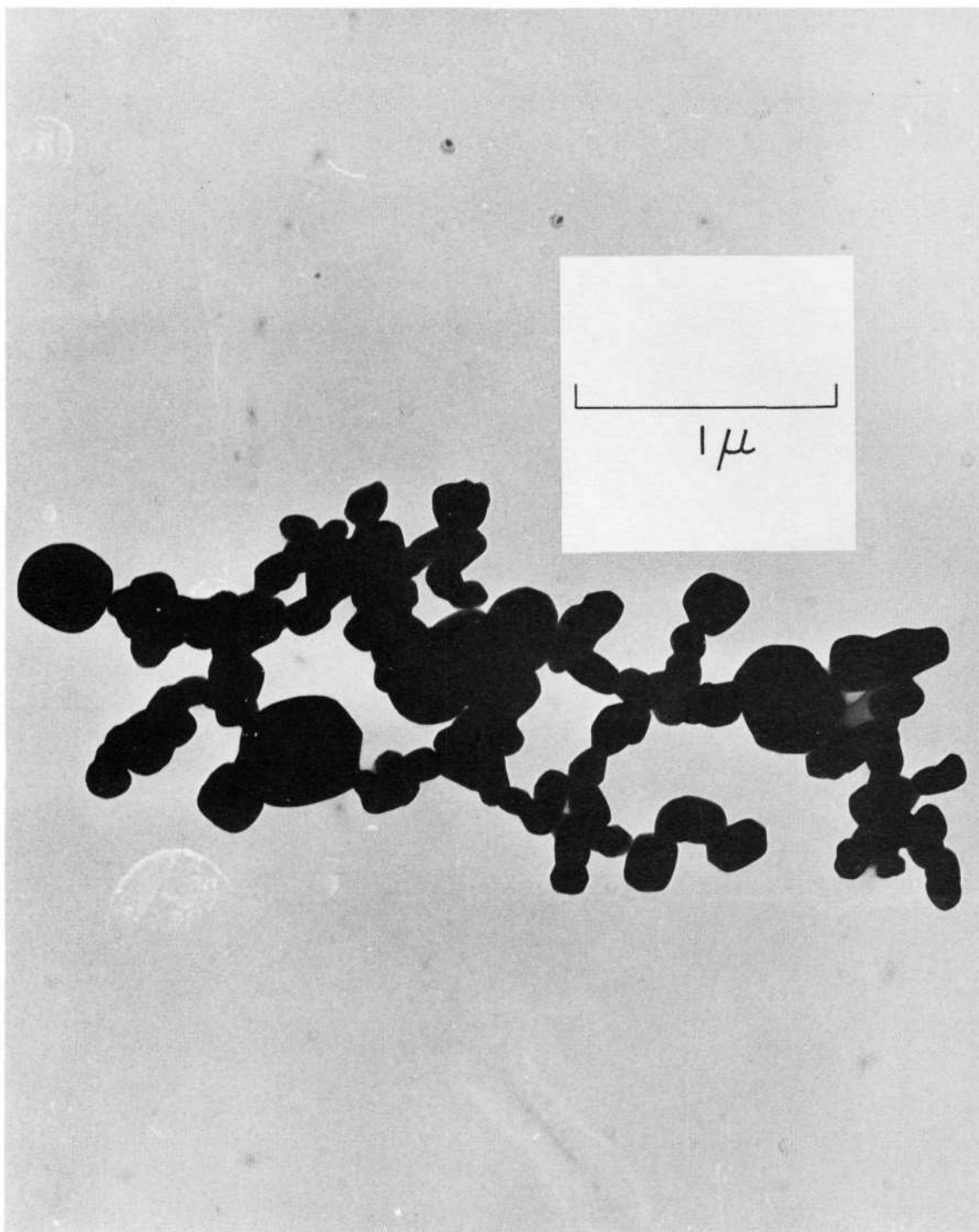


Fig. 55 - Typical Micrograph of Rutile Powder, Run T-10, 40,000X

Reproduced from
best available copy.

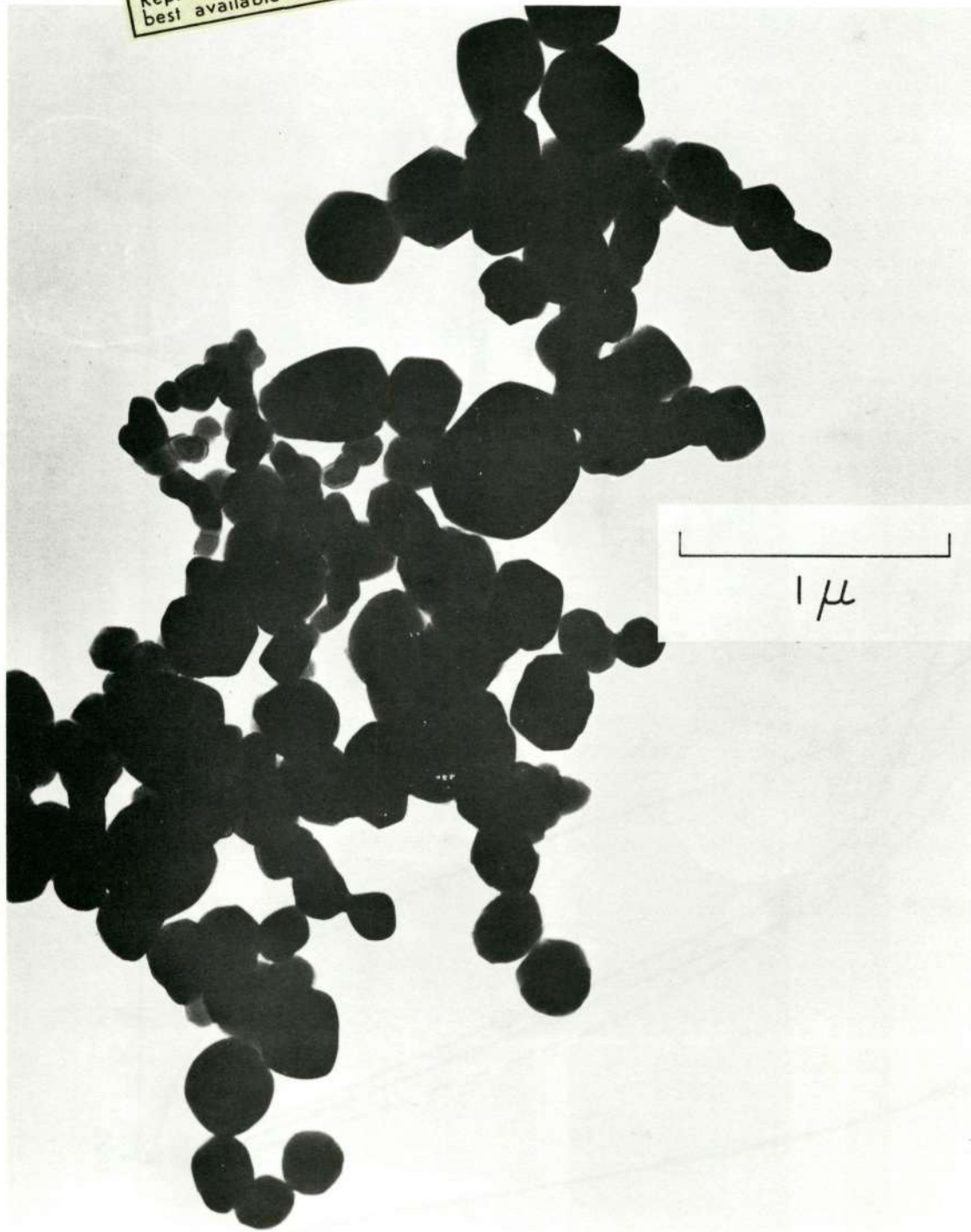


Fig. 56 - Typical Micrograph of Rutile Powder, Run T-11, 40,000X

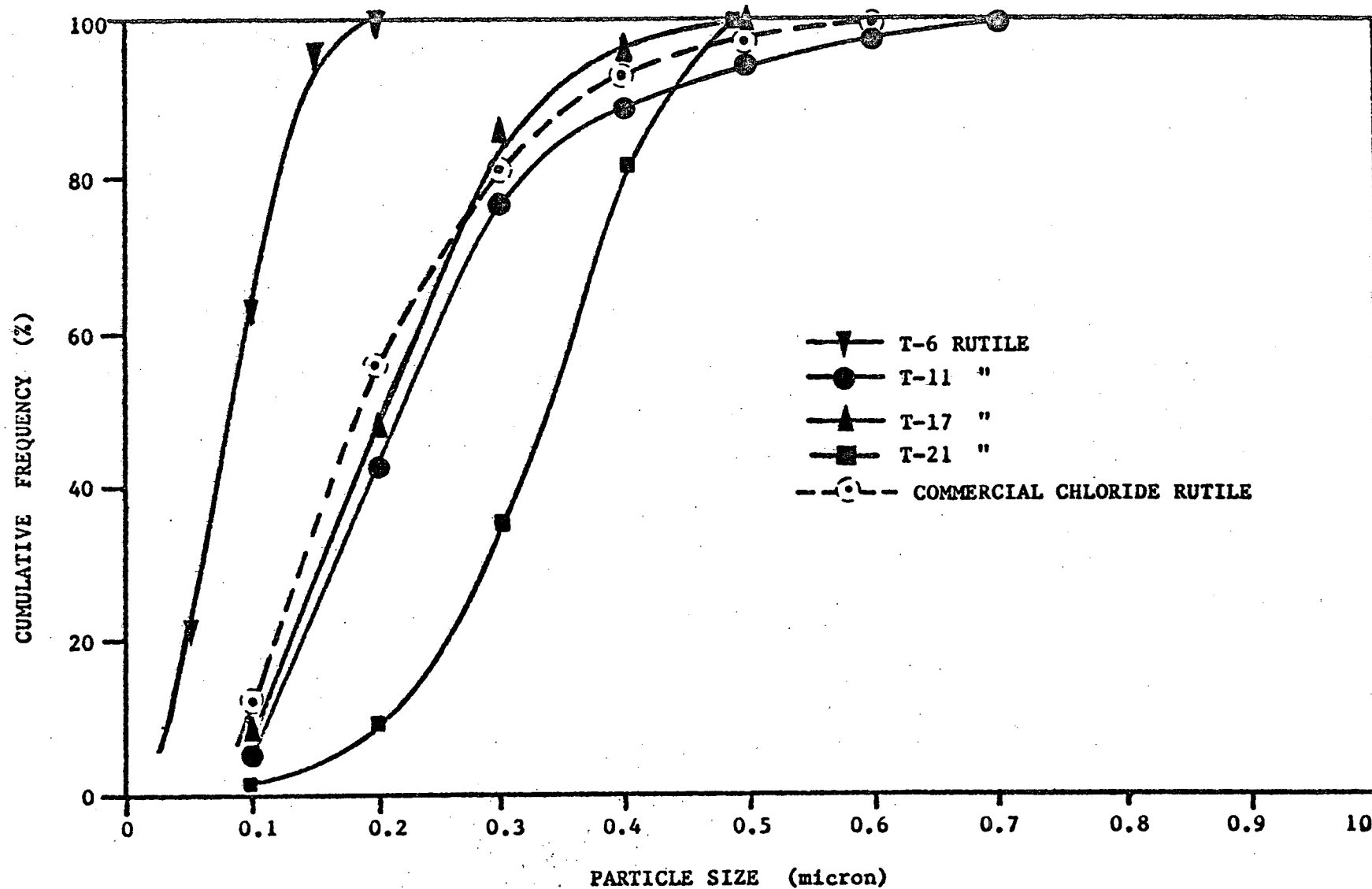


Fig. 57 - Typical Particle Size Distributions of Rutile Powders

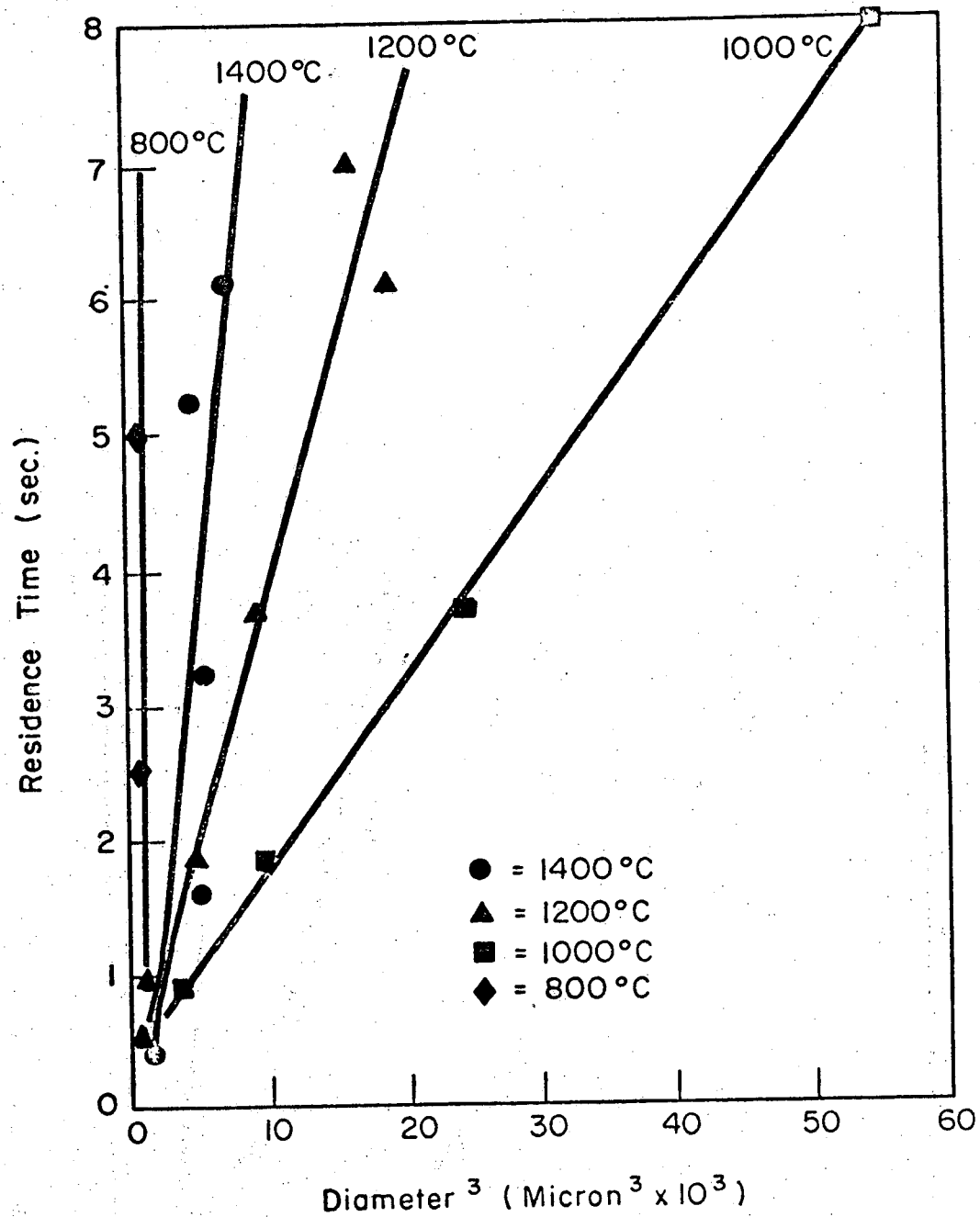


Fig. 58 - Effect of Temperature and Residence Time on Particle Size of Vapor-Grown Rutile

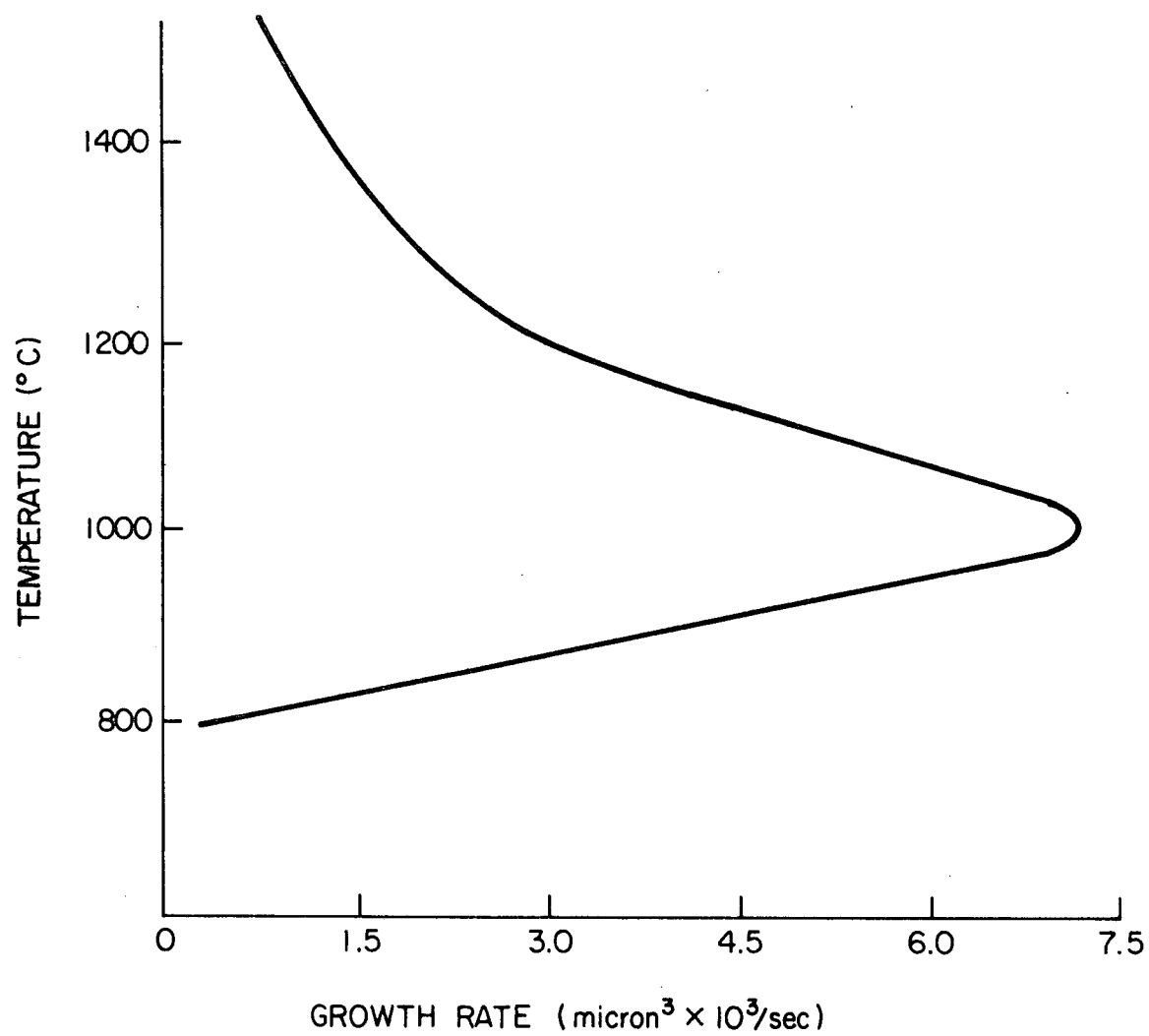


Fig. 59 - Volume Growth Rate versus Temperature for Titania Runs

decrease in particle size with increasing temperature, all other system conditions being fixed. The decrease in growth rate below 1000°C indicated that, in addition to the steadily diminishing nucleation rate, reaction and/or condensation kinetics were limiting growth. Few nuclei were formed, and their size was very small.

To test the validity of the assumption that nucleation was depleting the gas stream and inhibiting growth, a technique was required which would reduce the nucleation rate at a fixed temperature. One factor which may affect nucleation is the position of the injector tip. Smoke tube studies have been reported⁶⁴ which show considerable turbulence generated as reactant gases exit the injector. This turbulence enhances gas mixing and heat transfer and therefore it follows that inducing such turbulence near the hot zone may also promote nucleation kinetics. Injecting the gases further upstream in a cooler region may limit turbulence-induced nucleation by establishing laminar flow into and through the hot zone. If nucleation rate can be effectively reduced in this manner, a particle size increase would be anticipated.

Three additional rutile runs were made at 1200°C with the injector shortened 8 inches to inject the reactants 10 inches from the isothermal zone, Figure 60. Residence times of 0.9, 1.8 and 3.6 seconds were employed, corresponding to previous runs T-8, T-9 and T-10. Lineal analysis of electron micrographs, Figures 61 to 63, revealed a considerable size increase over earlier counterparts, Table XXVI. Graphical presentation of the two sets of runs, Figure 64, shows the cube of the diameter again varies linearly with time. The volume growth rate, G , has increased from 2.9 to 19.7 ($\text{micron}^3 \times 10^3/\text{second}$). This nearly sevenfold increase in growth rate indicates the importance of injection temperature in controlling nucleation and growth. Having confirmed the effect of nucleation rate on particle growth, and having negated to some extent the nucleation-depletion of the gas stream, a measurably broader range of particle sizes was produced.

Table XXVI - Particle Size Variation with Injector Length

Run No.	Residence Time (seconds)	Injection Distance from Hot Zone (inches)	Average Particle Size (micron)
T- 8	0.9	2	0.07
T-24	0.9	10	0.26
T- 9	1.8	2	0.17
T-21	1.8	10	0.33
T-10	3.7	2	0.21
T-25	3.6	10	0.42

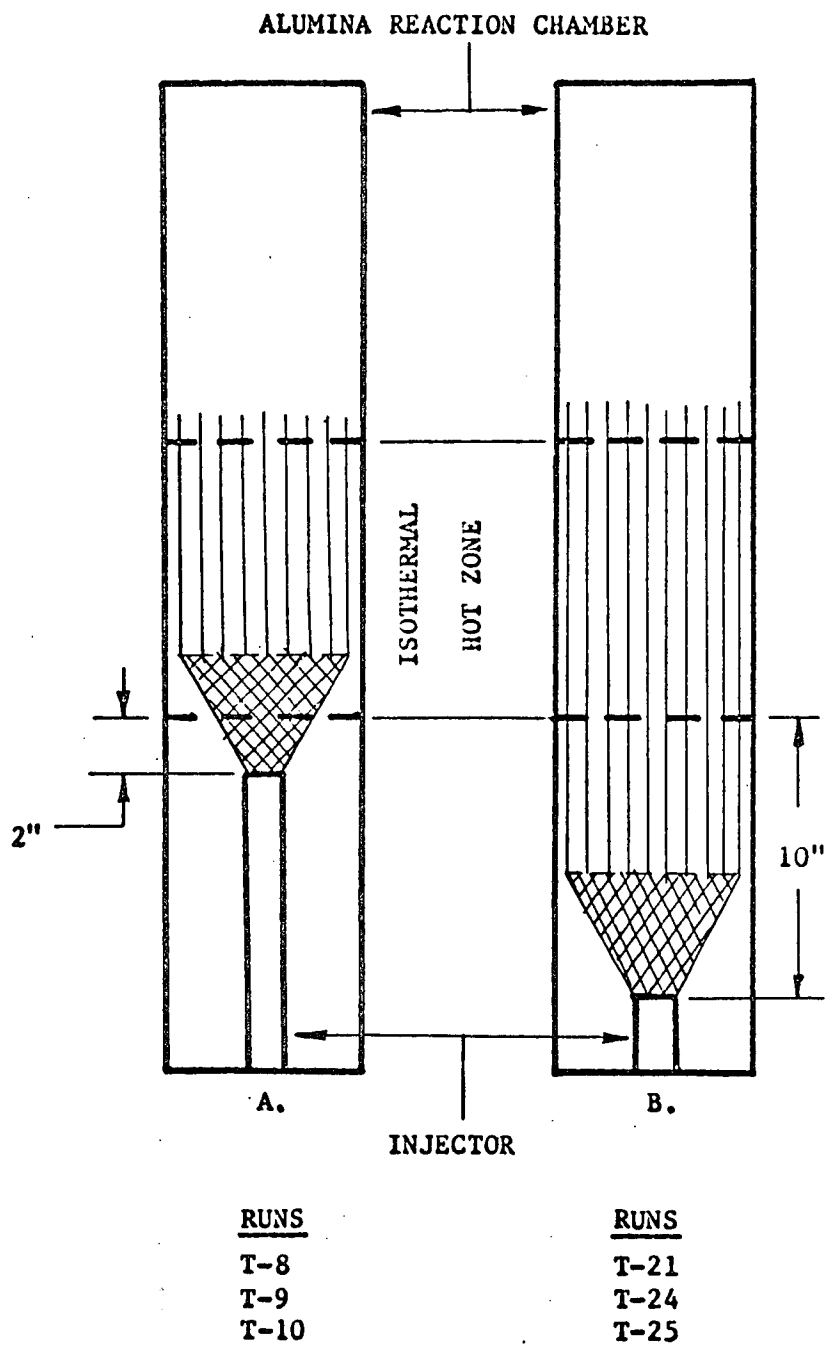
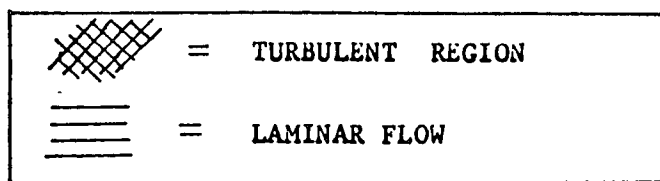


Fig. 60 - Injector Modification for Rutile Studies

Reproduced from
best available copy.

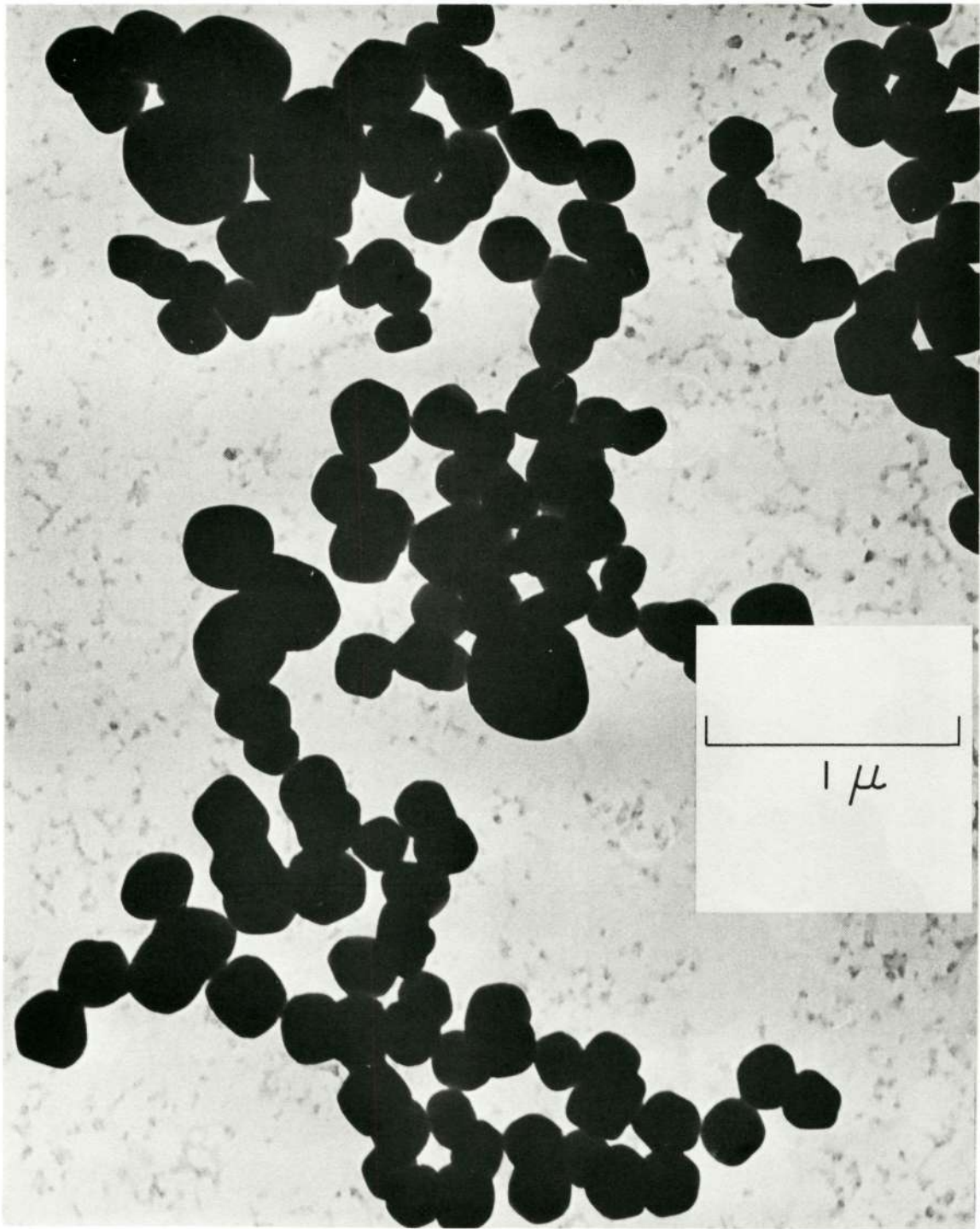


Fig. 61 - Typical Micrograph of Rutile Powder, Run T-24,
40,000X

Reproduced from
best available copy.

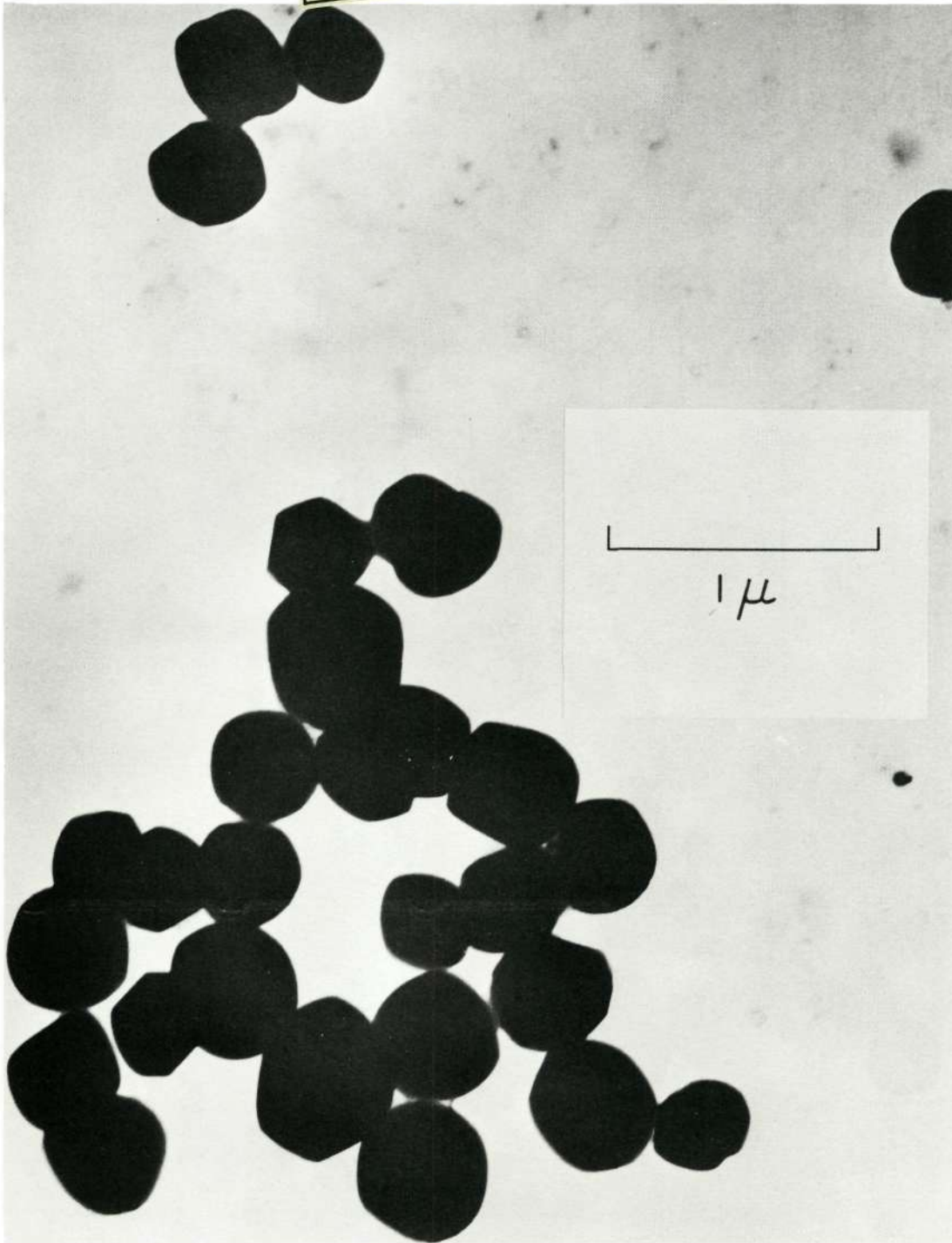


Fig. 62 - Typical Micrograph of Rutile Powder, Run T-21,
40,000X

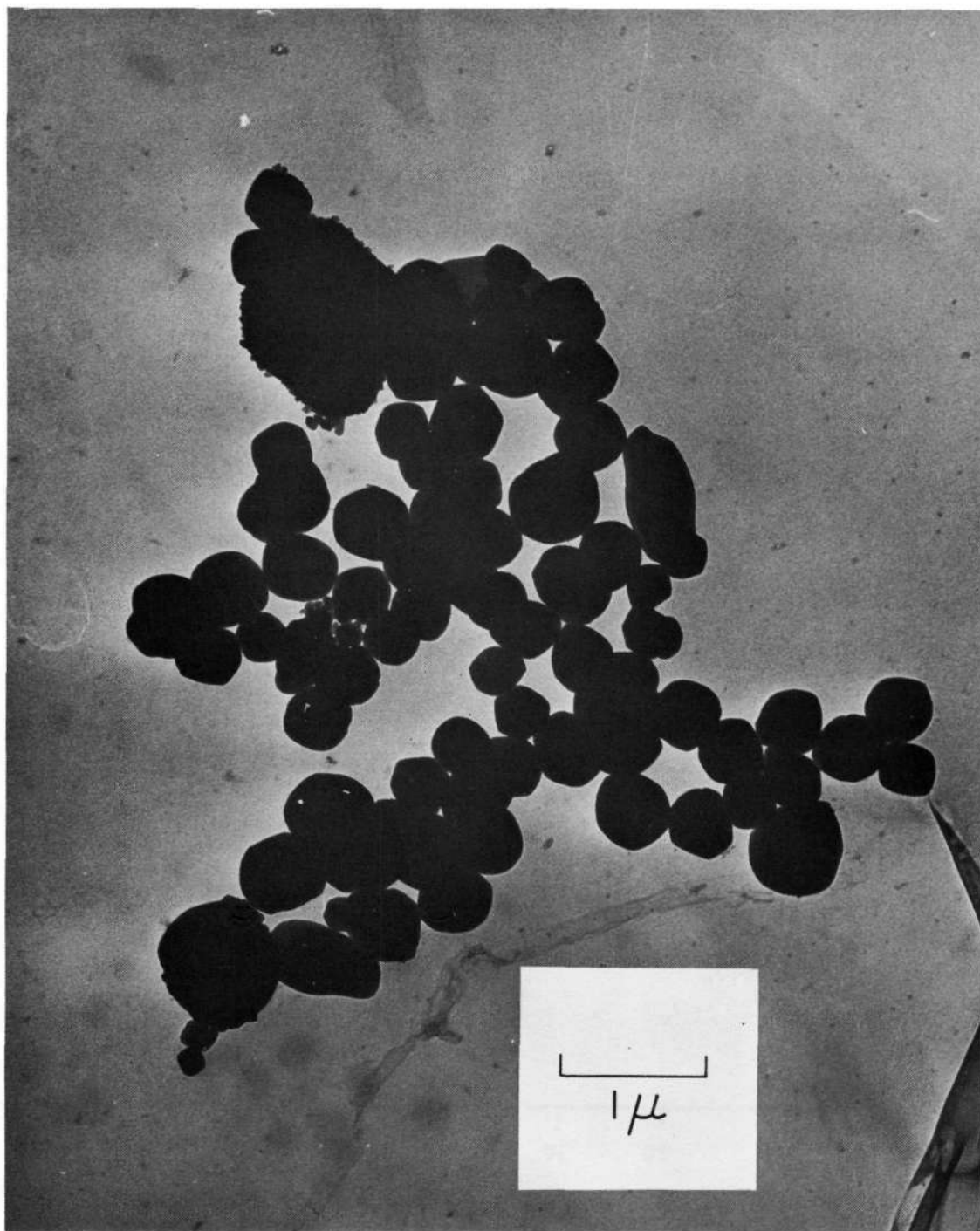


Fig. 63 - Typical Micrograph of Rutile Powder, Run T-25,
23,000X

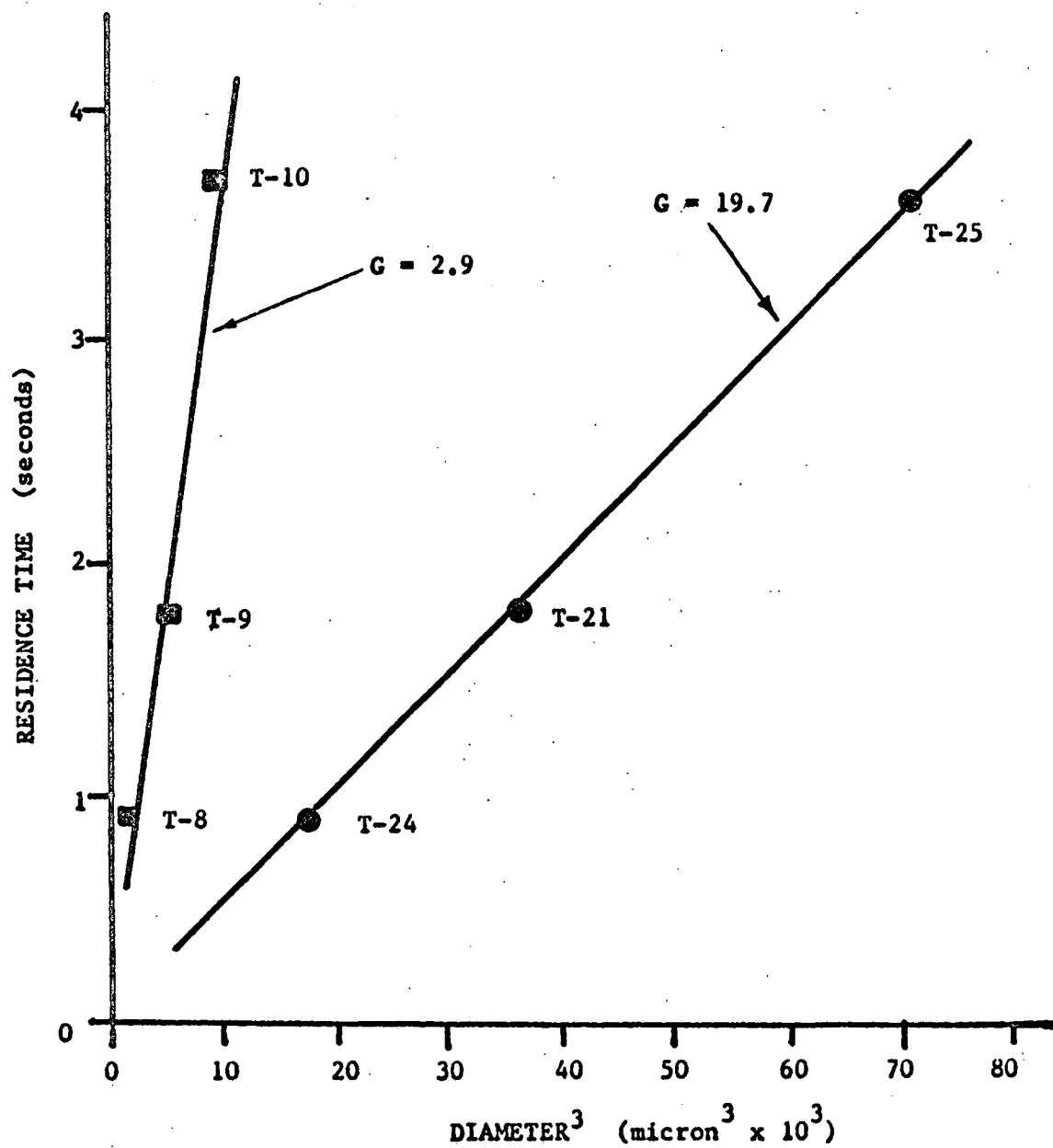
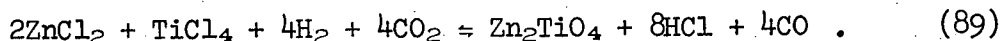


Fig. 64 - Effect of Residence Time and Injector Length on Particle Size of Rutile

C. ZINC ORTHOTITANATE (Zn_2TiO_4) POWDER PRODUCTION AND CHARACTERIZATION

1. Using Zinc Metal as the Zinc Vapor Species

Zinc orthotitanate powder was produced from homogeneous nucleation of gases using vaporization of metallic zinc as the zinc vapor species. The Zn/Ti ratio shown in Table XXVII is the ratio of the number of moles of Zn to number of moles of Ti introduced into the system during the run. For stoichiometric Zn_2TiO_4 , the Zn/Ti ratio should be 2.0. The overall reaction was



a. Zinc Vaporization - To establish the conditions for a controlled zinc evaporation rate, the system pressure was maintained at 50 mmHg for all runs. The zinc temperature was varied from 500 to 600°C. The recorded temperature was approximately 50°C lower than the actual temperature. This temperature difference was indicated by the observed melting of the metal which occurred at $370 \pm 11^\circ\text{C}$ for the runs recorded; zinc melts at 420°C . Although the temperature was low, temperature measurement gave a relative and reproducible control for establishing zinc evaporation conditions. Zinc evaporation rates at 50 mmHg system pressure is plotted versus temperature in Fig. 65. Because of gas flow rate variation it was difficult to establish a relation between evaporation rate and temperature; although in general, evaporation rate increased with temperature.

Several factors may be responsible for poor control of zinc evaporation. The first and most probable factor was variation in zinc partial pressure. Even though the system pressure was maintained constant, variation of other gas flow rates caused a variation in zinc partial pressure. Increasing gas flow rates would decrease zinc partial pressure and increase zinc evaporation rate. This was indicated in runs 2, 6, and 7 where zinc temperatures were fairly close and zinc evaporation seemed to be controlled by zinc partial pressure. The second factor was reduction of surface area because of powders settling on the evaporation surface. This could not be controlled and the magnitude of the effect could not be determined. Later runs were made using zinc chloride as the zinc vapor species.

b. Powder Characteristics - In the majority of the runs, powder was deposited in three distinct zones in the reaction tube above the hot zone. The zones were the top two inches of the reaction tube, Zone 1; approximately 2-4 inches below the top of the reaction tube, Zone 2; and from approximately 4 inches below the top of the reaction zone to the hot zone, Zone 3 (see Fig. 66 for sketch of zones). According to visual evidence in most runs Zone 1 contained mainly metallic zinc which was powdery and dark gray. Zone 2 contained large

Table XXVII - System Conditions and Phase Analysis for Runs Using
Metallic Zinc as the Zinc Vapor Species

Run No. Zn_2TiO_4	Reaction Zone Temp. (°C)	Gas Flow Rates			Zinc Evaporation Rate (g/min)	Zinc Temp. (°C)	Zn/Ti Ratio
		Cl_2 to Ti (cc/min at 25 psig)	H_2 (cc/min at 5 psig)	CO_2 (cc/min at 5 psig)			
1	1200	85	168	336	2.0	600	7.8
2	1200	100	200	400	0.40	575	1.1
3	1400	90	200	400	0.16	500	0.6
4	1040	27	570	111	0.12	540	1.3
5	1100	100	500	1000	—*	600	—
6	1300	95	300	600	0.75	560	2.6
7	1350	100	300	1600	1.90	570	5.6
8	1300	100	2000	1600	0.67	520	1.9

System Pressure (mmHg)		Phase Analysis and Color of Powder					
		Zone 1		Zone 2		Zone 3	
		Phases	Color	Phases	Color	Phases	Color
1	50	Not Analyzed		Not Analyzed		(1) Zn_2TiO_4 (2) TiO_2 (3) ZnO	light gray
2	50	Not Analyzed		TiO_2	white	(1) ZnO (2) TiO_2 (3) Zn_2TiO_4	white
3	50	Not Analyzed		Not Analyzed		(1) TiO_2 (2) ZnO (3) Zn_2TiO_4 Trace (4) $ZnTiO_3$ Trace	white
4	50	Not Analyzed		Not Analyzed		(1) TiO_2 (2) $ZnTiO_3$	light gray
5	50	(1) Zn (2) $ZnCl_2$ (3) TiO_2	dark gray	(1) Zn (2) $ZnCl_2$	dark gray	(1) TiO_2 (2) ZnO Trace	light gray
6	50	Not Analyzed		Not Analyzed		(1) ZnO (2) Zn_2TiO_4 (3) TiO_2 (4) Zn Trace (5) $ZnTiO_3$ Trace	light gray
7	50	Not Analyzed		(1) ZnO (2) Zn_2TiO_4 (3) TiO_2	gray	(1) TiO_2 (2) ZnO (3) $ZnTiO_3$	light gray
8	50	Not Analyzed		Not Analyzed		(1) TiO_2 (2) ZnO (3) $ZnTiO_3$	light gray

* All zinc evaporated due to variation in system pressure.

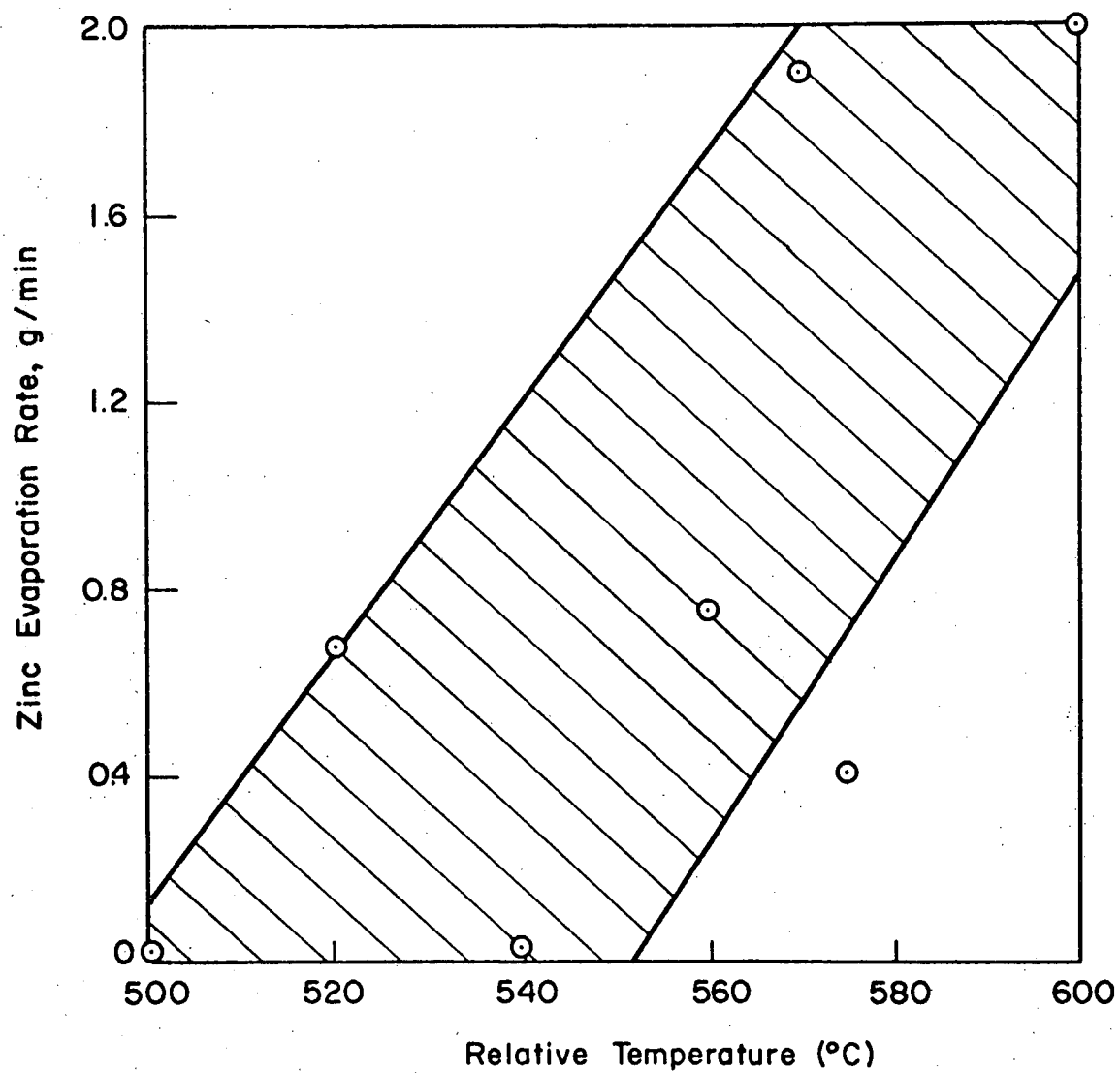


Fig. 65 - Zinc Evaporation Rate vs Temperature at 50 mmHg

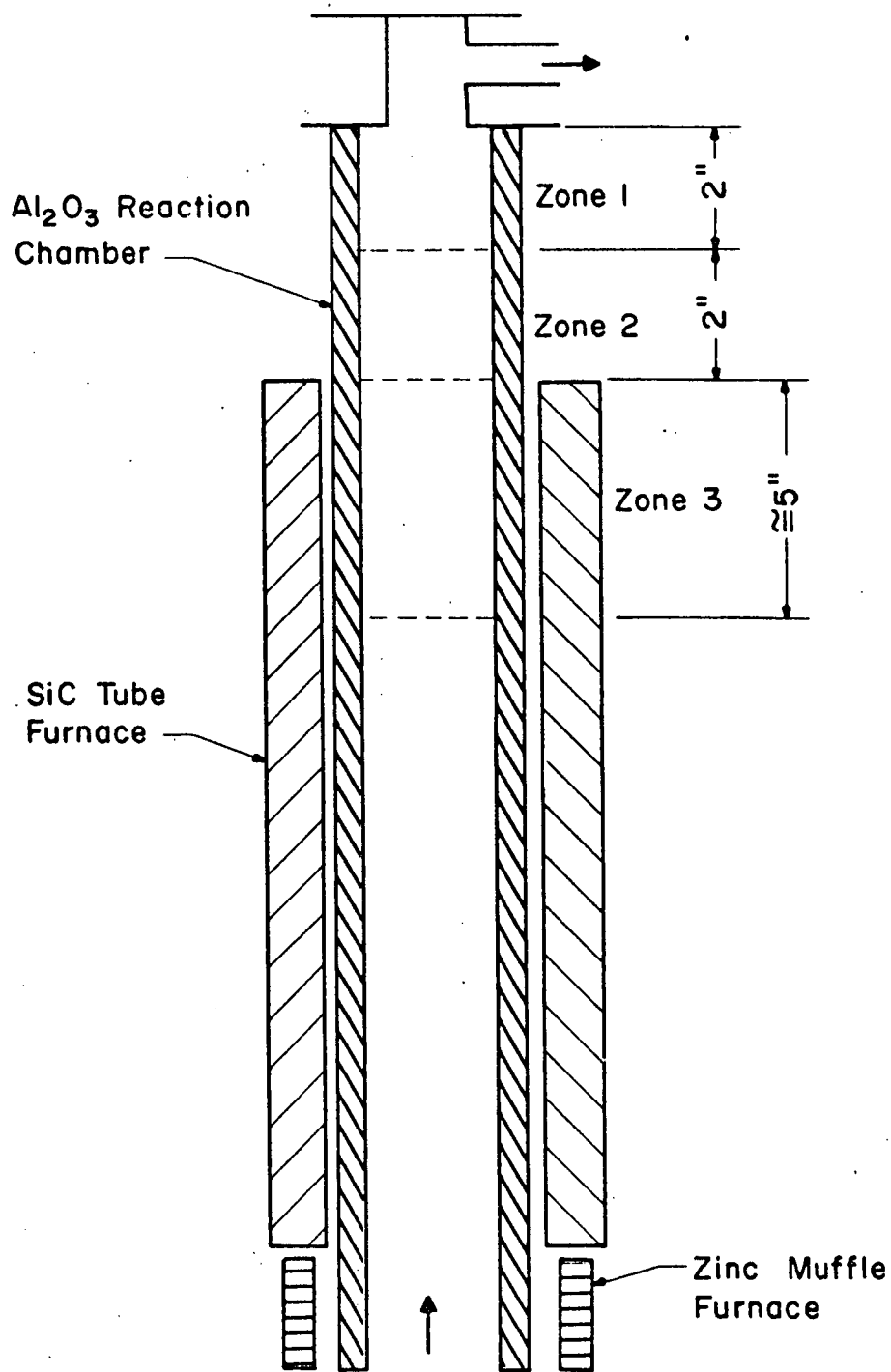


Fig. 66 - Schematic of Powder Deposition Zones

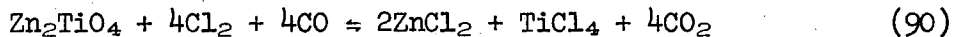
amounts of metallic zinc which condensed on the walls and flowed down the tube to the point that vaporization occurred again. The major oxides were found in Zone 3 and were evidenced by a light gray to white color. In no run was Zn_2TiO_4 the only oxide formed and in all runs TiO_2 and ZnO were found mixed with the Zn_2TiO_4 . The results of x-ray diffractometer phase analysis (see Appendix F) as well as material color for the different portions of the tube are listed in Table XXVII. The indicated phases are listed in order of peak height to indicate relative amounts of phases.

In four of the runs Zn_2TiO_4 was formed and in one run (#1) it was found to be the most abundant phase in Zone 3. Figures 67 and 68 are electron micrographs of run Zn_2TiO_4 -1, Zone 3. Although the characteristic morphology of Zn_2TiO_4 is not known and cannot be determined from the mixed phases in the micrographs, the micrographs do show a particle size in the 0.1 to 1.0 μ regions. The characteristic hexagonal morphology shown by rutile in earlier micrographs is apparent.

Although other oxide phases were formed besides Zn_2TiO_4 , its presence indicates that reaction was proceeding, at least to some degree. The most probable explanation is lack of mixing of the Zn vapor with the gases flowing through the central injection nozzle. The Reynolds number calculated for run Zn_2TiO_4 -8 for gas flow through the hot zone was 60. This indicates laminar flow and suggests a concentration gradient across the tube, with a high Zn concentration near the outside and a high TiCl_4 concentration in the center.

2. Using Zinc Chloride as the Zinc Vapor Species

Formation of Zn_2TiO_4 by homogeneous nucleation was achieved using ZnCl_2 as the zinc vapor species. The chloride was formed by chlorination of ZnO and Zn_2TiO_4 . In the former instance, zinc chloride was produced by the controlled chlorination of zinc oxide in the internal chlorinator below the reaction zone; simultaneously titanium sponge was chlorinated at 450°C and transferred at 350°C to the reaction chamber. The second method of halide generation involved the controlled chlorination of zinc orthotitanate in the internal chlorinator by the following reaction.



The feed stock was prepared by solid state reaction between stoichiometric amounts of ZnO and TiO_2 (anatase). The reactants were fired to 925°C for 24 hours with only 3 per cent ZnO remaining unreacted.

System conditions for ZnO source runs are shown in Table XXVIII. Flow gauge pressures were as indicated or 0 psig. Conditions for orthotitanate sources are shown in Table XXIX.

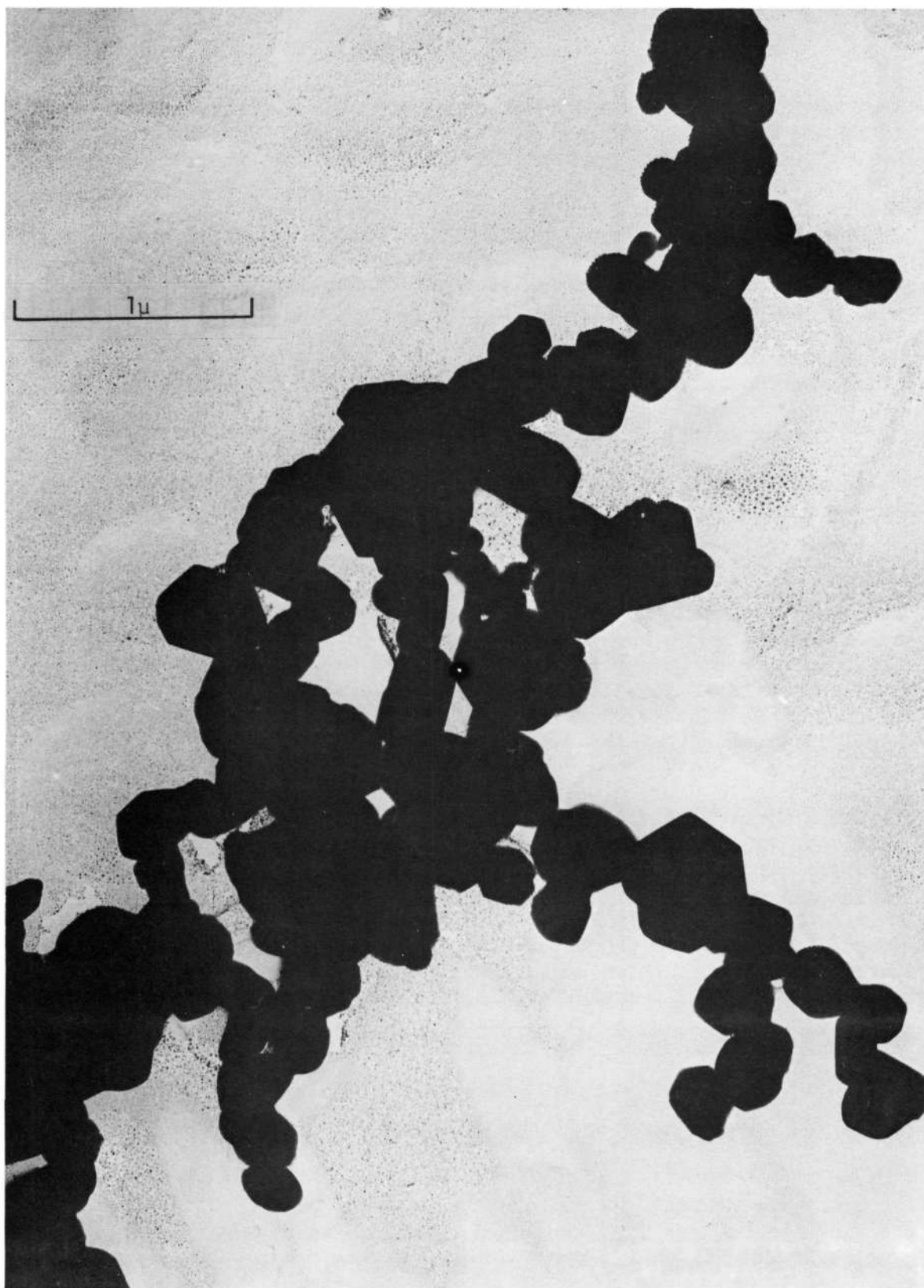


Fig. 67 - Electron Photomicrograph, Run Zn_2TiO_4 -1, Zone 3, 40,000X

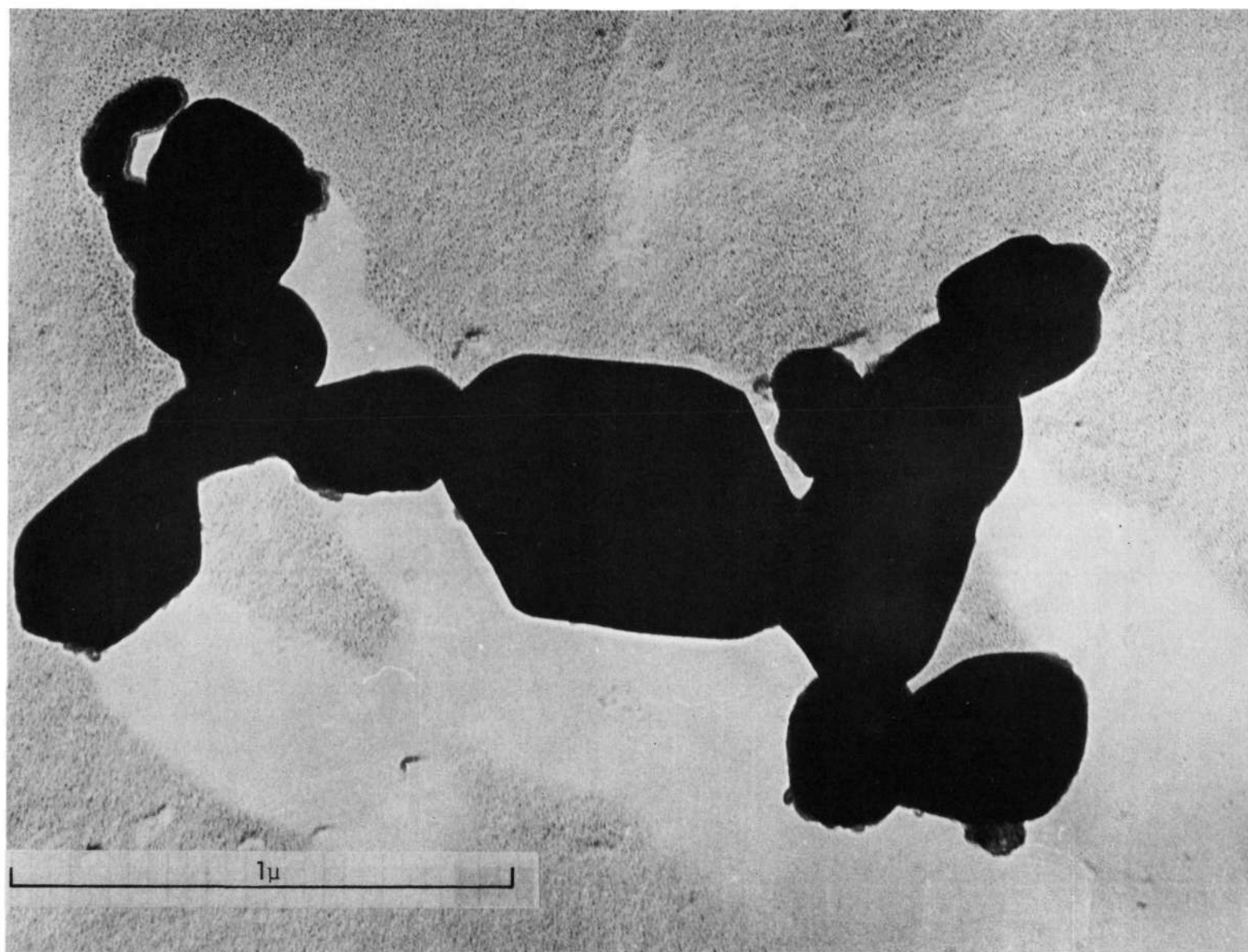


Fig. 68 - Electron Photomicrograph, Run Zn₂TiO₄-1, Zone 3, 82,000X

Table XXVIII - System Conditions and Phase Analysis for Runs Using Oxide to Produce Zinc Chloride

Material	Run No.	Reaction Zone Temperature (°C)	Gas Flow Rates									
			Cl ₂ to ZnO		Cl ₂ to TiO ₂		CO to ZnO		CO ₂		H ₂	
			Flow Gage Pressure (PSIG)	Flow Rate (cc/min)	Flow Gage Pressure (PSIG)	Flow Rate (cc/min)	Flow Gage Pressure (PSIG)	Flow Rate (cc/min)	Flow Gage Pressure (PSIG)	Flow Rate (cc/min)	Flow Gage Pressure (PSIG)	Flow Rate (cc/min)
ZnO	11	1300	25	40	25	0	5	80	5	0	5	80
Zn ₂ TiO ₄	12	1300	25	50	25	50	5	100	5	100	5	200
Zn ₂ TiO ₄	13	1300	25	50	25	50	5	100	5	100	5	200
Zn ₂ TiO ₄	14	1430	0	45	0	45	0	100	0	100	0	100
Zn ₂ TiO ₄	15	1400	0	38	0	38	0	90	0	100	0	130
Zn ₂ TiO ₄	16	1480	25	50	25	50	0	17	0	17	0	233
Zn ₂ TiO ₄	17	1450	25	40	25	40	0	100	0	100	0	200
Zn ₂ TiO ₄	18	1700	0	45	0	45	0	100	0	100	0	100

Material	Run No.	System Pressure (mm Hg)	ZnO Chlorination Efficiency (%)	Phase Analysis		
				Zone #1	Zone #2	Zone #3
ZnO	11	210	46	Not Analyzed	Not Analyzed	(1) ZnO (2) ZnCl ₂ 4Zn(OH) ₂
Zn ₂ TiO ₄	12	100	53	ZnCl ₂	Not Analyzed	Nothing Analyzed
Zn ₂ TiO ₄	13	200	61	ZnCl ₂	ZnCl ₂	TiO ₂
Zn ₂ TiO ₄	14	100	70	ZnCl ₂	ZnCl ₂	TiO ₂
Zn ₂ TiO ₄	15	90	101	ZnCl ₂	ZnCl ₂	TiO ₂
Zn ₂ TiO ₄	16	200	48	(1) ZnCl ₂ (2) TiO ₂	(1) ZnCl ₂ (2) TiO ₂	(1) TiO ₂ (2) ZnO (3) ZnTiO ₃
Zn ₂ TiO ₄	17	300	57	(1) ZnCl ₂ (2) TiO ₂	(1) TiO ₂ (2) ZnTiO ₃ (3) Trace ZnO (4) Trace Zn ₂ TiO ₄ or Zn ₂ Ti ₃ O ₈ or both	(1) TiO ₂ (2) ZnTiO ₃ (3) ZnO
Zn ₂ TiO ₄	18	200	99	(1) Zn (2) ZnCl ₂ (3) TiO ₂	(1) Zn (2) ZnCl ₂ (3) TiO ₂	(1) ZnO (2) TiO ₂ (3) ZnTiO ₃ (4) Trace Zn ₂ TiO ₄ or Zn ₂ Ti ₃ O ₈ or both

Table XXVIII - (Continued)

Run No.	Furnace	Temp. (°C)	Cl ₂ to ZnO (cc/min)	Cl ₂ to Ti (cc/min)	CO (cc/min)	CO ₂ (cc/min)	H ₂ (cc/min)	System Pressure (mmHg)
ZO 1	SC	1495	45	45	100	100	200	150
2	SC	1450	100	50	100	50	200	350
3	SC	1400	100	200	100	300	400	150
4	IF	1400	100	200	100	300	400	150
5	IF	1300	200	200	-	200	400	380
6	IF	1400	75	50	-	100	200	50
7	IF	1250	100	200	200	600	600	200
8	IF	1150	200	75	300	1200	600	150

Phase Analysis			
	Zone 1	Zone 2	Zone 3
ZO 1	ZnO Zn ₂ TiO ₄ (tr)	ZnCl ₂	No Powder
2	ZnO, ZnCl ₂ , Zn ₂ TiO ₄ (tr)	ZnCl ₂ , Zn	No Powder
3	ZnCl ₂ , Zn ₂ TiO ₄ (tr)	ZnO, Zn ₂ TiO ₄	No Powder
4	ZnO, TiCl ₃	ZnO, ZnCl ₂ ·Zn(OH) ₂ TiCl ₃	ZnO, TiCl ₃ , TiO ₂ ZnCl ₂ ·Zn(OH) ₂ Zn ₂ TiO ₄ (tr) Zn ₂ Ti ₃ O ₃ (tr) ZnTiO ₃ (tr)
5	Not Analyzed	ZnO, ZnTiO ₄ , TiCl ₃ , ZnTiO ₃ ZnCl ₂ ·Zn(OH) ₂	
6	ZnO, ZnCl ₂ , Zn(OH) ₂ , TiCl ₃	ZnO	No Powder
7	Not Analyzed	Not Analyzed	TiO ₂
8	Not Analyzed	Not Analyzed	ZnO

Table XXIX - System Conditions and Phase Analysis for Runs Using
Zinc Orthotitanate to Produce Zinc Chloride

Run	Temp. (°C)	Cl ₂ to Zn ₂ TiO ₄ (cc/min)	CO (cc/min)	CO ₂ (cc/min)	H ₂ (cc/min)	System Pressure (mmHg)	O ₂ (cc/min)	Furnace Type	Zone 1	Zone 2	Zone 3
ZOT 9	1500	400	400	200	400	100	-	IF	NA	No Powder	Al ₂ TiO ₅ TiO ₂ Zn ₂ TiO ₄ ZnTiO ₃ (tr)
10	1450	200	200	100	200	20	-	MF		ZnCl ₂ TiCl ₃ ZnO Zn ₂ TiO ₄ (tr)	No Powder
11	1450	100	300	500	300	140	-	MF		ZnCl ₂ ZnO TiO ₂ ZnTiO ₄ (tr)	TiO ₂ Zn ₂ TiO ₄ ZnO
12	1200	400	400	400	400	100	-	IF		No Powder	TiO ₂ Al ₂ TiO ₅ Zn ₂ TiO ₄
13	1300	400	400	200	600	380	150	IF		TiO ₂ Al ₂ TiO ₅ TiCl ₃	TiO ₂ Al ₂ TiO ₅
14	1150	400	400	400	400	100	-	IF		No Powder	Al ₂ TiO ₅ Zn ₂ TiO ₄ TiO ₂
15	1250	400	100	600	1000	100	-	IF	ZnCl ₂ TiO ₂ (tr)	No Powder	Al ₂ TiO ₅ Zn ₂ TiO ₄
16	1300	400	400	200	400	380	-	IF	NA	NA	TiO ₂ ZnTiO ₃ Al ₂ TiO ₅ Zn ₂ Ti ₃ O ₈
17	1300	100	100	100	200	200	-	MF	NA	ZnCl ₂ TiO ₂ Zn ₂ TiO ₄ (tr)	

Powder was typically deposited in three zones. Zone 1 was the top six inches of the reactor, Zone 2 extended to 12 inches below the top of the reactor, and Zone 3 continued to 25 inches from the top. Regions listed as "not analyzed" were not barren but contained hydroscopic material identified as zinc chloride. Zinc orthotitanate was formed in every run as a minor phase, except in the case of predicted mixing conditions which produced 15 weight per cent.

Figures 69-72 show scanning electron micrographs of sample ZOT-12.

D. CALCIUM TUNGSTATE (CaWO_4) POWDER

Calcium tungstate powder was produced by homogeneous nucleation using the chlorination of CaO and W to provide the halide gases. The conditions and phase identification for products of formation are listed in Table XXX. Figures 73-75 show scanning electron micrographs of the products.

Table XXX - System Conditions and Phase Analysis of CaWO_4 Run

Temperature	°C	1500		
Cl_2 to CaO	cc/min	100		
Cl_2 to W	cc/min	200		
CO to CaO	cc/min	100		
CO_2	cc/min	700		
H_2	cc/min	700		
System Pressure	mmHg	100		
Phase Analysis	Collector	Zone 1	Zone 2	Reactor
	CaO	CaO	CaO	CaO
	CaWO_4	CaCO_3		
	CaCl_2	CaWO_4		

E. LANTHANUM OXIDE (La_2O_3) POWDER

Lanthanum oxide powders were produced over the range of 1650°C to 1750°C in the molybdenum element reactor. The furnace heated both the reactor and the chlorinator. In runs 1-4, chlorine was passed over pure La_2O_3 ; in subsequent runs carbon was mixed with La_2O_3 to promote reduction and chlorination. With the carbon-free source materials, only a trace of La_2O_3 was detected in a quantity of LaCl_3 ; thus indicating the need for stronger reduction conditions by the addition of CO .

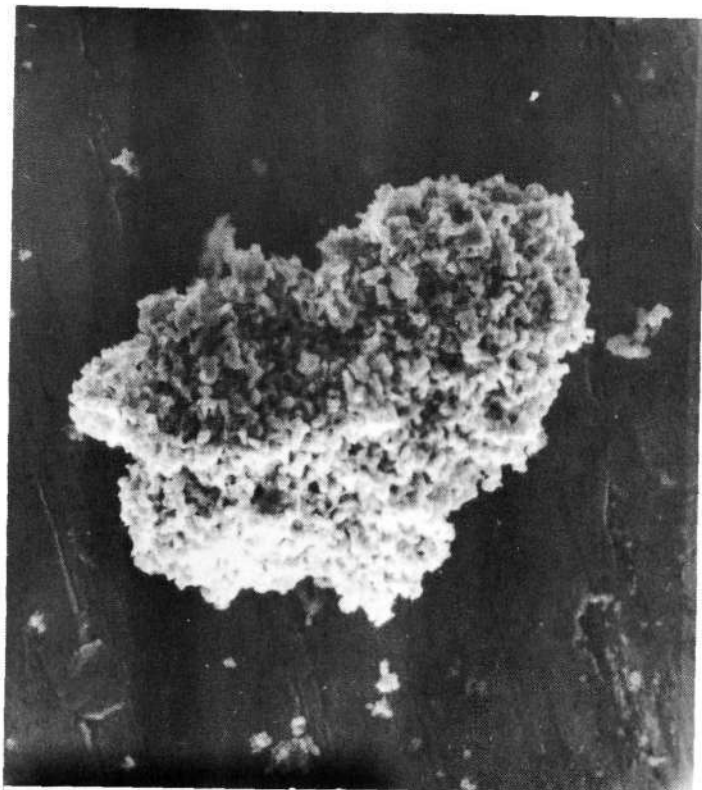


Fig. 69 - Scanning Electron Micrograph, Sample ZOT-12
500X

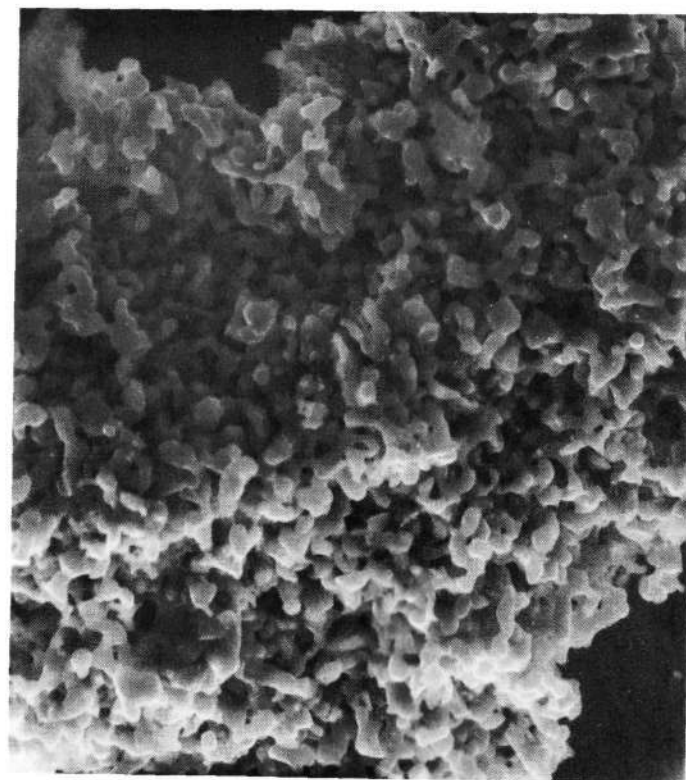


Fig. 70 - Scanning Electron Micrograph, Sample ZOT-12
1000X

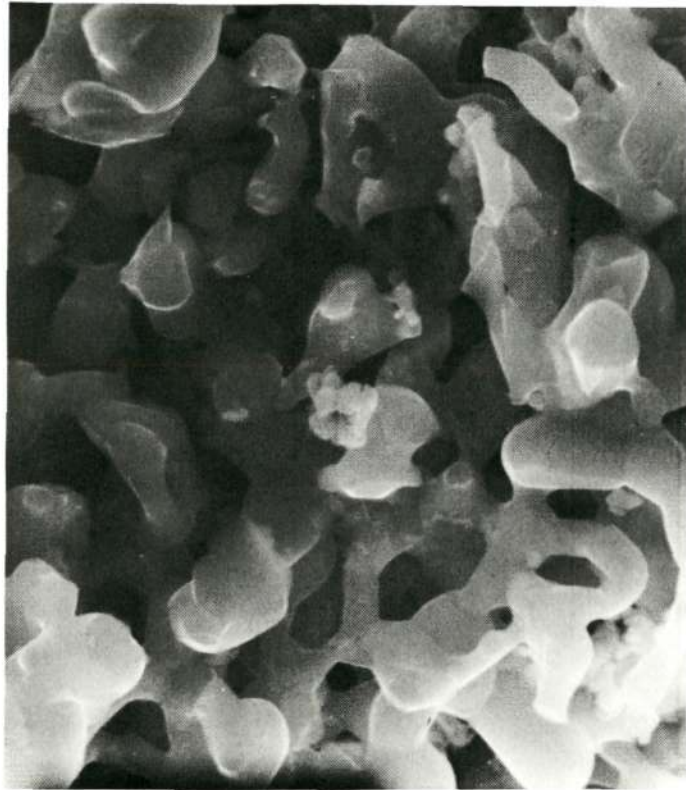


Fig. 71 - Scanning Electron Micrograph, Sample ZOT-12
5000X



Fig. 72 - Scanning Electron Micrograph, Sample ZOT-12
10,000X

Reproduced from
best available copy.

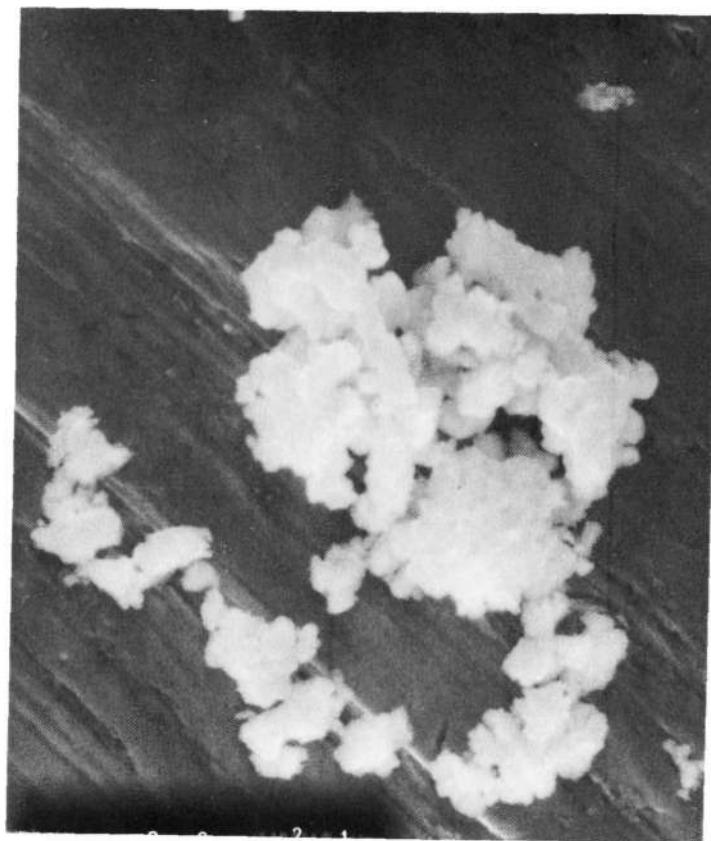


Fig. 73 - Scanning Electron Micrograph, Sample CW-1
1000X

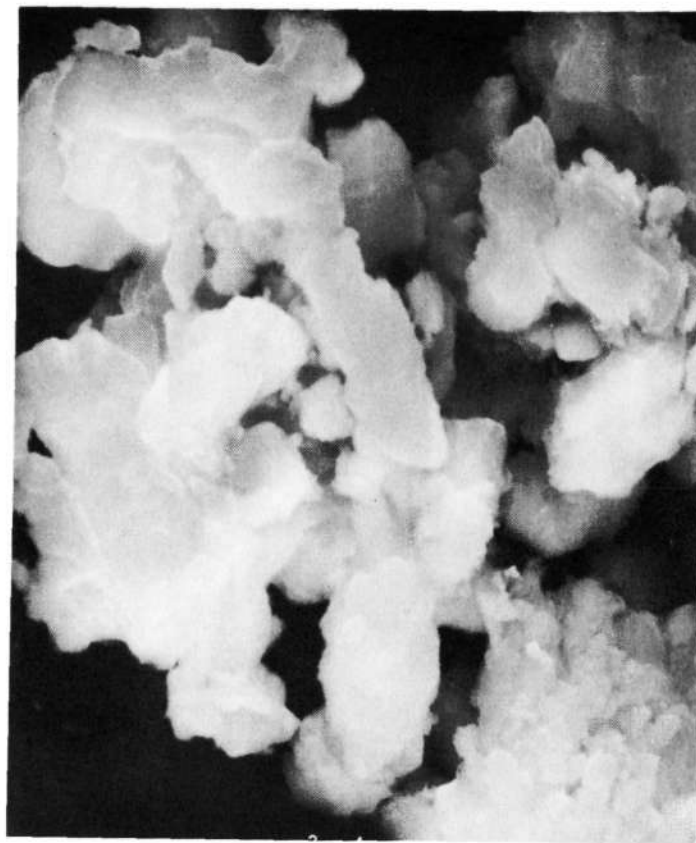


Fig. 74 - Scanning Electron Micrograph, Sample CW-1
3000X



Fig. 75 - Scanning Electron Micrograph, Sample CW-1
5000X

Table XXXI - System Conditions and Phase Analysis for La₂O₃ Runs

Run	Temp. °C	Cl ₂ cc/min	CO	CO ₂ cc/min	H ₂ cc/min	Carbon	System Pressure mmHg	Xs Cl ₂	Zone 1	Zone 2
1	1750	45	-	100	100	No	150	-		LaOCl LaCl ₃ La ₂ O ₃ (tr)
2	1750	100	-	500	500	No	300	-		LaCl ₃ ·7H ₂ O LaOOH
3	1700	100	-	300	300	No	50	-		LaOCl LaCl ₃ ·7H ₂ O LaOOH La ₂ O ₃ (tr)
4	1700	100	-	800	600	No	500	-	LaOCl LaAlO ₃	LaOCl LaAlO ₃
5	1700	300	100	-	300	No	30	-	LaOCl LaCl ₃ ·7H ₂ O	LaOCl LaCl ₃ ·7H ₂ O
6	1700	300	400	-	300	No	250	-	LaOCl LaCl ₃ La ₂ O ₃	LaOCl LaCl ₃ La ₂ O ₃
7	1750	300	-	500	300	Yes	50	-	LaCl ₃ LaOCl La ₂ O ₃	LaCl LaOCl La ₂ O ₃
8	1750	300	-	500	300	Yes	100	-	LaOCl LaCl ₃ LaAlO ₃	LaOCl LaCl ₃ LaAlO ₃ La ₂ O ₃
9	1650	300	300	500	500	Yes	50	-	LaOCl	LaOCl
10	1700	300	200	-	300	Yes	50	-	LaOCl La ₂ O ₃ (tr)	LaOCl LaOOH LaAlO ₃ La ₂ O ₃ (tr)
11	1750	100	100	700	700	No	100	-	LaOCl La ₂ O ₃ LaCl ₃ ·7H ₂ O	LaOCl LaOOH
12	1750	200	100	300	300	Yes	100	-	LaOCl LaOOH LaAlO ₃ LaCl ₃ ·7H ₂ O	LaOCl LaOOH LaAlO ₃ LaCl ₃ ·7H ₂ O
13	1750	150	300	300	300	No	150	-	LaOCl LaCl ₃ ·7H ₂ O LaAlO LaOOH	LaOCl LaCl ₃ ·7H ₂ O LaAlO ₃
14	1750	50	300	300	300	No	150	-	NA	LaOCl LaCl ₃ ·7H ₂ O La ₂ O ₃ (tr) LaAlO ₃
15	1750	150	500	300	300	No	380	50	LaOCl La ₂ O ₃ LaCl ₃ ·7H ₂ O (tr)	LaOCl La ₂ O ₃ LaCl ₃ ·7H ₂ O(tr)
16	1700	100	300	300	300	No	380	50	LaOCl	LaOCl
17	1750	200	100	-	300	No	100	50	LaCl ₃ ·7H ₂ O LaOCl LaOOH	LaCl ₃ ·7H ₂ O(tr) LaOCl LaOOH
18	1700	200	200	-	500	No	380	50	LaCl ₃ ·7H ₂ O LaOCl La ₂ O ₃ (tr)	LaOCl
19	1750	150	400	200	500	No	250	-	LaOCl	LaOCl
20	1750	220	-	500	300	Yes	480	-	LaCl ₃ ·7H ₂ O	LaOCl LaCl ₃ ·7H ₂ O La ₂ O ₃ (tr)
21	1700	220	200	200	300	No	100	-	LaCl ₃ LaOOH	LaCl ₃ LaOOH
22	1750	100	-	300	300	Yes	380	-	LaOCl La ₂ O ₃ (tr)	LaOCl La ₂ O ₃



Fig. 76 - Scanning Electron Micrograph, Sample LA-16
500X

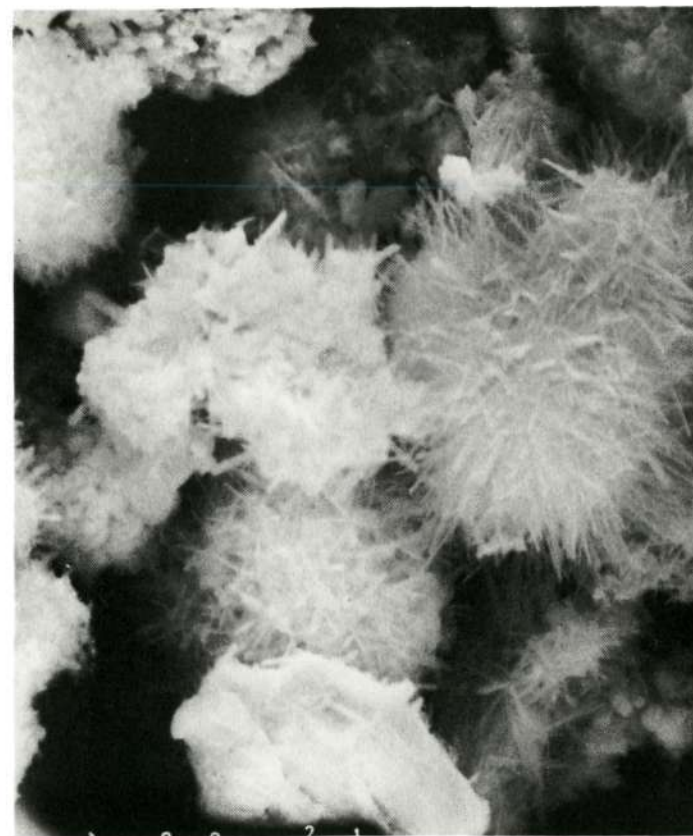


Fig. 77 - Scanning Electron Micrograph, Sample LA-16
3000X

Reproduced from
best available copy.

Reproduced from
best available copy.



Fig. 78 - Scanning Electron Micrograph, Sample LA-20
500X

V. CONCLUSIONS AND RECOMMENDATIONS

A. CONCLUSIONS

The following conclusions can be made concerning this effort in the development and preparation of space-stable pigments for thermal control coatings:

1. Aluminum Oxide Powder

- a. For constant reactant gas inputs and reaction zone temperature, increasing reaction zone pressure increases the average particle size of alumina powder.
- b. Increasing reactant gas inputs and increasing system pressure to maintain constant gas velocities at constant temperature increases the average particle size of alumina powder.
- c. The particle size range for the various alumina runs was 0.1 to 0.50 μ .

2. Titanium Dioxide

- a. Systematic variations of particle size were controlled with hot zone temperatures, residence time, and injector design. Sizes from 0.06 - 0.42 micron were produced, with distributions as narrow as any yet reported.
- b. A constant volume growth rate of particles at a specific temperature was observed. Variation of growth rate with temperature reflected the effect of changing super-saturation and nucleation rate. Additional flexibility in controlling nucleation was achieved by varying injector length.

3. Zinc Orthotitanate

- a. Improvements in the yield of zinc orthotitanate have been attained by reactor design improvements that incorporate maximized jet action.
- b. Gas mixing must be increased to eliminate the mixed species.

4. Calcium Tungstate

Calcium tungstate was produced as the major phase.

5. Lanthanum Oxide

- a. Lanthanum oxide has been produced as a minor phase only.
- b. Lanthanum oxychloride kinetics prevents the formation of lanthanum oxide in large amounts.

B. RECOMMENDATIONS

Gas mixing remains the major limitation to high yields of multiple oxides. A plasma cell should be incorporated into the present reactor as an upstream turbulence and heating source. Further reaction system improvements should permit pilot production studies at an early date.

IV. REFERENCES

1. Zerlaut, G. A., and Ashford, N., "Development of Space-Stable Thermal-Control Coatings," Report No. IITRI-U6002-73, Contract NAS8-5379, (January, 1969).
2. Zerlaut, G. A., Gilligan, J. E., and Ashford, N., "Investigation of Environmental Effects on Coatings for Thermal Control of Large Space Vehicles," Report No. IITRI-U6002-97, Contract NAS8-5379 (October, 1971).
3. Plunkett, J. D., "NASA Contributions to the Technology of Inorganic Coatings," NASA-SP-S014, U. S. Government Printing Office, Washington, D. C., (November, 1964).
4. Kingery, W. D., Introduction to Ceramics, John Wiley & Sons, Inc., N.Y., N.Y. p. 511-545 (1963).
5. Dulin, F. H., and Rase, D. E., "Phase Equilibrium in the System ZnO-TiO_2 ," J. Am. Cer. Soc., 43:3 (1960), 125-131.
6. Bartram, S. F., and Slepety's, R. A., "Compound Formation and Crystal Structure in the System ZnO-TiO_2 ," J. Am. Cer. Soc., 44 (1961), 493.
7. Campbell, W. B., "Determination of the Feasibility of Forming Refractory Fibers by a Continuous Process," AMRA CR 63-03/8F, (1966).
8. Schaffer, P. S., and Jones, D. W., "Development of Pigments for Thermal Control Coatings," NASA Contract No. NAS8-20162, Lexington Laboratories, Inc., (1966).
9. Wicks, C. E., and Block, F. E., "Thermodynamic Properties of 65 Elements - Their Orders, Halides, Carbides and Nitrides," Bull. 305, Bureau of Mines, (1963).
10. Stull, D. R., "JANAF Thermochemical Tables," National Bureau of Standards Report PBI68370, (August, 1965).
11. Kubo, T., Kato, M., Mitarai, Y., and Uchida, K., "Solid State Reaction of the $\text{TiO}_2\text{-ZnO}$ System," Kogys Kagaku Zasshi, 66:4 (1963), 403.
12. Bird, R. B., Stewart, W. E., and Lightfoot, E. N., Transport Phenomena, p. 23, J. Wiley (1960).
13. Bird, R. B., loc. cit., p. 746.
14. Wilke, C. R., J. Chem. Phys., 18, pp. 517-519 (1950).
15. Bird, R. B., op. cit., p. 259.

16. Bird, R. B., op. cit., p. 511.
17. Campbell, W. B., et al., "Preparation of Pigments for Space-Stable Thermal Control Coatings," The Ohio State University Research Foundation, NASA Contract No. NAS 8-21317, July 1970.
18. Brodkey, R. S., The Phenomena of Fluid Motions, p. 327, Addison-Wesley (1967).
19. Danchwerts, I. V., Chem. Eng. Sci. 8, p. 93 (1958).
20. Brodkey, op. cit.
21. Lee J. and Brodkey, R. S., "Turbulent Motion and Mixing in a Pipe," A.I.Ch.E. Journal 10, pp. 187-193 (1964).
22. Gegner, J. P., and Brodkey, R. S., "Dye Injection at the Centerline of a Pipe," A.I.Ch.E. Journal 12, pp. 817-819 (1966).
23. Brodkey, R. S., "Turbulent Motion, Mixing and Kinetics." Professional Development Lectures. Vol. 1, No. 2, November 1968, West Virginia University, Nitro, W. Va.
24. Pai, S. I., "On Turbulent Jet Mixing of Two Gases at Constant Temperature," J. of Appl. Mech., pp. 41-47, March (1955).
25. Corrsin, S., A.I.Ch.E. Journal 3, p. 329 (1957).
26. Ibid. 10, p. 870 (1964).
27. Danchwerts, op. cit.
28. Brodkey, op. cit., p. 331.
29. Brodkey, R. S., "Turbulent Motion, Mixing and Kinetics", op. cit.
30. Wilke, C. R., op. cit.
31. Hinze, J. O., "Non-isotropic Free Turbulence," Chapter 6, Turbulence, McGraw-Hill (1959).
32. Champagne, F. H. and Wygnanskii, I. J., "Coaxial Turbulent Jets." Boeing Sci. Res. Lab. Document DL-82-0958. Flight Sciences Laboratory, February 1970.
33. Hinz, J. O., op. cit.
34. Ibid.
35. Champagne, F. H., op. cit.

36. Ibid.
37. Hinze, loc. cit., p. 425.
38. Brodkey, R. S., O.S.U. Chemical Engineering Department, Private Communication.
39. Rose, H. E., and Wood, A. J., An Introduction to Electrostatic Precipitation in Theory and Practice, London Constable, (1966).
40. Ruheman, M., The Separation of Gases, (1940).
41. Schoen, H. M., New Chemical Engineering Separation Techniques, N. Y. Interscience Publisher, (1962).
42. Oliver, E. D., Diffusional Separation Processes, N. Y. Wiley and Sons, (1966).
43. Poole, J. B., and Doyle, D., Solid-Liquid Separation, London H. M. S. O. (1966).
44. Pownell, J. H., "Cyclones in the Chemical and Process Industries," Chem. and Ind., (Rev.), 47 (1961), 1888-96.
45. Darby, G. M., "Classification in Hydrocyclones," Bull. Am. Cen. Soc., 34, (1955), 287-90.
46. Bradley, D., The Hydroclone, International Series of Monographs, Chem. Engr., Vol. 4, Pergamon Press, (1965).
47. Rietema, K., and Verven, C. G., Cylcones in Industry, Elsevier Publishing Co., (1961).
48. Wilkinson, B. W., "The Performance Characteristics of Cyclone Dust Collectors," Ph.D. Dissertation, The Ohio State University, (1958).
49. Trowbridge, M. E., "Centrifugation," in Solid Liquid Separation, London HMSO, Chp. 6, (1966).
50. Perry, J. H., Ed., Chemical Engineers Handbook, Section 20, (1965).
51. Ibid., p. 64, Section 20.
52. Boucher, R. M.-G., "Ultrasonics in Processing." Chem. Eng. pp 83-100. October 2, (1961).
53. Ibid., p. 1034-1039, (1950 Edition).
54. Encyclopedia of Chemical Technology, Vol. 10, Interscience Publisher, p. 329-352.

55. Berg, E. W., Physical and Chemical Methods of Separation, N. Y. McGraw-Hill, (1963).
56. Oliver, E. D., Diffusion Separation Processer, N. Y. Wiley and Sons, (1966).
57. Pratt, H. R. C., Counter Current Separation Processes, Elsevier Publisher, (1967).
58. Schoen, H. M., New Chemical Engineering Separation Techniques, N. Y. Interscience Publisher, (1962).
59. Pirie, J. M., "Symposium on the Less Common Means of Separation," Institution of Chemical Engineers, London, (1969).
60. Gibbs, H. D., "The Production of Hydrochloric Acid from Chlorine and Water," J. Ind. Engr. Chem., 12:6 (1962), 538.
61. The Handbook of Chemistry and Physics, (1960).
62. Vivian, J. E. and Whitney, R. P., "Absorption of Chlorine in Water," Chemical Engineering Progress, 43:12, (1947), 691-702.
63. Schoen, op. cit.
64. Campbell, W. B., "Determination of the Feasibility of Forming Refractory Fibers by a Continuous Process," AMRA-CR-G3-03/8F, June 1966.

APPENDIX A

FREE ENERGY VALUES USED IN THERMODYNAMIC CALCULATIONS

Table XXXII - Free Energy Values Used in Thermodynamic Calculations

T °C	T °K	ΔG° -																		
		AlCl ₃	Al ₂ O ₃	Cl ₂	CO	CO ₂	HCl	H ₂	TiCl ₄	TiO ₂	Zn	ZnCl ₂	ZnO	Zn ₂ TiO ₄	La ₂ O ₃	Ca ₂ NO ₄	LaOCl (est)	LaCl ₃	CaCl ₂	WCl ₆
27	300	-136.08	-378.00	0	-32.80	-94.25	-22.75	0	-175.90	-212.00	0	-88.45	-76.10	-369.60	-402.60	-331.80	-223.63	-238.30	-179.65	-60.00
127	400	-134.85	-370.30	0	-35.00	-94.30	-22.95	0	-170.55	-207.90	0	-84.80	-74.65	-362.20	-393.10	-323.00	-218.70	-233.00	-175.95	-52.50
227	500	-133.61	-362.80	0	-37.10	-94.40	-23.90	0	-167.45	-203.60	0	-81.10	-71.30	-351.20	-384.50	-314.60	-213.97	-227.40	-172.50	-45.00
327	600	-132.36	-355.30	0	-39.35	-94.45	-23.40	0	-164.50	-199.30	0	-78.80	-68.95	-342.20	-376.60	-306.15	-209.77	-222.70	-169.05	-40.40
427	700	-131.09	-347.80	0	-41.55	-94.45	-23.60	0	-161.60	-194.95	0	-76.60	-66.60	-333.15	-368.10	-297.80	-205.13	-217.30	-165.75	-37.80
527	800	-129.81	-340.40	0	-43.70	-94.50	-23.75	0	-158.70	-190.75	0	-74.40	-64.00	-323.75	-360.00	-289.50	-200.43	-211.30	-162.35	-35.20
627	900	-128.51	-332.90	0	-45.85	-94.55	-23.90	0	-155.85	-186.55	0	-72.20	-61.50	-314.50	-351.30	-281.30	-196.10	-207.00	-159.15	-32.60
727	1000	-127.01	-325.20	0	-47.95	-94.60	-24.00	0	-152.95	-182.35	0	-70.00	-59.00	-305.35	-342.40	-273.10	-191.10	-200.90	-155.70	-30.00
827	1100	-125.41	-317.20	0	-50.10	-94.60	-24.15	0	-150.05	-178.00	0	-66.72	-56.10	-295.20	-334.90	-265.10	-186.90	-195.86	-152.80	-27.30
927	1200	-123.80	-309.40	0	-52.15	-94.65	-24.40	0	-147.10	-173.89	0	-63.44	-53.40	-285.69	-326.90	-256.95	-182.83	-191.60	-150.30	-24.70
1027	1300	-122.10	-301.50	0	-54.35	-94.70	-24.40	0	-144.15	-169.55	0	-60.16	-50.70	-275.95	-319.00	-248.80	-179.00	-188.00	-147.70	-22.10
1127	1400	-120.57	-293.80	0	-56.25	-94.75	-24.65	0	-141.15	-165.45	0	-56.88	-47.90	-266.25	-310.50	-240.60	-175.00	-184.50	-145.10	-19.50
1227	1500	-118.95	-286.10	0	-58.40	-94.75	-24.70	0	-138.15	-161.20	0	-53.60	-45.10	-256.40	-302.50	-232.35	-171.13	-180.90	-142.40	-17.00
1327	1600	-117.31	-278.10	0	-60.60	-94.80	-24.90	0	-135.20	-157.25	0	-51.50	-42.40	-246.65	-294.50	-224.50	-167.23	-177.20	-139.60	-14.20
1427	1700	-115.67	-270.60	0	-62.65	-94.85	-25.00	0	-132.25	-153.10	0	-49.50	-39.40	-236.90	-286.00	-216.45	-163.23	-173.70	-137.00	-11.50
1527	1800	-114.03	-263.10	0	-64.65	-94.90	-25.25	0	-129.25	-149.35	0	-47.50	-36.60	-227.55	-278.00	-209.05	-159.40	-170.20	-134.30	-9.00
1627	1900	-112.38	-255.50	0	-66.75	-94.90	-25.45	0	-126.25	-145.25	0	-45.50	-33.80	-217.85	-270.00	-202.00	-155.57	-166.70	-131.70	-6.40
1727	2000	-110.73	-247.90	0	-68.75	-95.00	-25.50	0	-123.25	-141.15	0	-43.50	-31.00	-208.15	-262.00	-195.05	-151.67	-163.00	-129.00	-3.80

Preceding page blank

Preceding page blank

APPENDIX B

COMPUTER PROGRAM SOURCE LIST FOR CALCULATION OF
EQUILIBRIUM CONSTANTS AND FREE ENERGY VALUES


```

0001      DIMENSION IDLGR(20,20),IDLGP(20,20),IR(15),IP(15)
0002      DIMENSION IA(15),IB(15),IC(15),MA(15),MB(15),MC(15)
0003      DIMENSION JA(15),JB(15),JC(15),KA(15),KB(15),KC(15)
0004      999 FORMAT(15,15I5)
0005      998 FORMAT(3X,3A4,9I7)
0006      997 FORMAT(' DELTA G IS',I8,' CALORIES AT',I3,'00 DEGREES KELVIN AND T
      THE EQUILIBRIUM CONSTANT IS',F12.4)
0007      995 FORMAT('0 THE FOLLOWING DATA IS FOR THE REACTION ')
0008      994 FORMAT('0REACTANTS',4X,I2,3A4,I2,3A4,I2,3A4,I2,3A4,I2,3A4,I2,3A4)
0009      993 FORMAT('0PRODUCTS',5X,I2,3A4,I2,3A4,I2,3A4,I2,3A4,I2,3A4,I2,3A4//)
0010      992 FORMAT('1 THE DATA USED IN THESE CALCULATIONS IS ')
0011      991 FORMAT('0',2X,3A4,9I7)
0012      READ(5,999)IRCTN,((IR(I),I=1,IRCTN)
0013      READ(5,999)IPRDT,((IP(I),I=1,IPRDT)
0014      READ(5,998)((IA(I),IB(I),IC(I),((IDLGR(I,M),M=3,11),MA(I),MB(I),MC(
      11),((IDLGR(I,M),M=12,20)),I=1,IRCTN)
0015      READ(5,998)((JA(I),JB(I),JC(I),((IDLGP(I,M),M=3,11),KA(I),KB(I),KC(
      11),((IDLGP(I,M),M=12,20)),I=1,IPRDT)
0016      90 WRITE(6,992)
0017      92 WRITE(6,991)((IA(I),IB(I),IC(I),((IDLGR(I,M),M=3,11),MA(I),MB(I),MC
      1(I),((IDLGR(I,M),M=12,20)),I=1,IRCTN)
0018      91 WRITE(6,991)((JA(I),JB(I),JC(I),((IDLGP(I,M),M=3,11),KA(I),KB(I),KC
      1(I),((IDLGP(I,M),M=12,20)),I=1,IPRDT)
0019      95 WRITE(6,995)
0020      94 WRITE(6,994)((IR(I),IA(I),IB(I),IC(I)),I=1,IRCTN)
0021      93 WRITE(6,993)((IP(I),JA(I),JB(I),JC(I)),I=1,IPRDT)
0022      99 DO96M=3,20
0023      A=0
0024      DO98K=1,IRCTN
0025      98 A=A+IR(K)*IDLGR(K,M)
0026      B=0
0027      DO97K=1,IPRDT
0028      97 B=B+IP(K)*IDLGP(K,M)
0029      IDLG=B-A
0030      DLG=IDLG
0031      R=1.987
0032      DENM=R*M*100
0033      X=-DLG/DENM
0034      C=EXP(X)
0035      96 WRITE(6,997)IDLG,M,C
0036      STOP
0037      [ ]

```

Preceding page blank

APPENDIX C

Preceding page blank

```
// (3000,0),CLASS=C
//ST1 FYEC PROC=FORTRAN,
// REGION.GD=252K,TIME.GD=(0,50),
// PARM.GD='S17F=150K'
//CMP.SYSIN DD *
  DIMENSION C(70,20), CTMP (70,20), RCTMP(20,20), INDEXR(70),
  1LTEMP(20), LPR(20),LPC(20),RNV(70,20),G(70),RLNK(70),RK(70),
  2GAMMA(70),IVECTR(70),PARP(70),IFLEM(20)
  COMMON NCOLM1,RNV,C,DELTAZ,INDEXR,NCOL
  EPSLON=1.0E-08
  1 READ 1000,NROW,NCOL,ITMAX,NCASE
  1000 FORMAT (4I10)
  IF (FOF,60) 10,11
  10 CALL FX11
  11 NCOLM1=NCOL-1
  READ 3000,(IFLEM(I),I=1,NCOLM1)
  3000 FORMAT (8A10)
  READ 1001,((C(I,J),J=1,NROW),J=1,NCOLM1)
  1001 FORMAT (8F10.1)
  READ 1001,(GAMMA(I),I=1,NROW)
  DO 500 ICASE=1,NCASE
  READ 1002,P,T
  1002 FORMAT (2F10.1)
  READ 1001,(G(I),I=1,NROW)
  READ 1001,(C(I,NCOL),I=1,NROW)
  PRINT 1999,P,T
  1999 FORMAT (1H1,8HPRESSURE ,E20.8,10X,11HTEMPERATURE ,E20.8)
  PRINT 2000
  2000 FORMAT (10X,18HCOMPOSITION MATRIX)
  PRINT 3001,(IFLEM(I),I=1,NCOLM1)
  3001 FORMAT (8A10)
  DO 12 I=1,NROW
  12 PRINT 2001,(C(I,J),J=1,NCOLM1)
  2001 FORMAT (1X,10F10.2)
  PRINT 2002
  2002 FORMAT (///1X,20H GIBBS FREE ENERGIES )
  PRINT 2003,(G(I),I=1,NROW)
  2003 FORMAT (1X,8F14.6)
  PRINT 2004
  2004 FORMAT (///1X,17H PHASE PARAMETERS )
  PRINT 2001, (GAMMA(I),I=1,NROW)
  PRINT 2005
  2005 FORMAT (///1X,30H FIRST ESTIMATE OF COMPOSITION )
  PRINT 2003,(C(I,NCOL),I=1,NROW)
  PRINT 2006
  2006 FORMAT(//13X,7HSPECIES,9X,11HCOMPOSITION,5X,20HEQUILIBRIUM CONSTAN
  1T,5X,16HPARTIAL PRESSURE,10X,8HC VECTOR)
C
C DO INITIALIZATION
C
  IRASIS=1
  ICONV =0
  ITER=0
  20 IF(ICONV) 21,21,22
  22 TOTP=0
  DO 18 I=1,NROW
  PARP(I)=A*C(I,NCOL)*GAMMA(I)
  18 TOTP=TOTP+PARP(I)
  PRINT 2022,(I,C(I,NCOL),RK(I),PARP(I),IVECTR(I),I=1,NROW)
  2022 FORMAT (1X,119,2F20.8,F24.8,I20)
  PRINT 2223,A,TOTP
  2223 FORMAT (//10X,12HVALUE OF A =,F20.7,10X,14HTOTAL PRESSURE ,F20.7)
```

```

      PRINT 2222,ITER
2222 FORMAT(/10X,33HTHESE RESULTS WERE OBTAINED AFTER 14,12H ITERATIO
      INS )
      GO TO 500
21  ICONV =1
      IF (ITER-ITMAX) 25,23,22
23  PRINT 2023,ITMAX
2023 FORMAT (10X,15HITERATION LIMIT,15,10H REACHED )
      GO TO 22
25  ITER=ITER+1
      IF (IBASIS) 199, 199, 49
C
C   STORE THE COMPOSITION MATRIX AND THE VECTOR ESTIMATES OF COMPOSITION
C   IN THE ARRAY CTEMP
C
49  DO 40 J=1,NROW
      DO 41 I=1,NCOL
41  CTEMP(J,I)=C(J,I)
40  INDEXR(J)=J
C
C   CONSTRUCTION OF OPTIMUM BASIS
C
      NROW1=NROW
      I=1
50  IF (I-NROW1) 69,69,68
68  PRINT 2068
2068 FORMAT (1X,37HNO NONSINGULAR B MATRIX CAN BE FOUND )
      GO TO 500
69  MAX=1
      DO 51 K=1,NROW1
          IF (CTEMP(MAX,NCOL)-CTEMP(K,NCOL))52,51,51
52  MAX=K
51  CONTINUE
      DO 56 N=1,NCOLM1
56  RCTEMP(I,N)=CTEMP(MAX,N)
C
C   CHECK FOR LINEAR DEPENDENCE
C
      IF (I-1) 54,661,54
54  IM=I-1
      DO 57 N=1,IM1
          RTERM=0.0
          DO 58 ISUM=1,NCOLM1
              RTERM=RTERM+RCTEMP(I,ISUM)*RCTEMP(N,ISUM)
          DO 59 J=1,NCOLM1
              RCTEMP(I,J)=RCTEMP(I,J)-RTERM*RCTEMP(N,J)
          57 CONTINUE
661  RTERM=0
          DO 60 J=1,NCOLM1
              RTERM=RTERM+RCTEMP(I,J)**2
          RTERM=SQRT(RTERM)
          IF (RTERM-EPSLON) 62,62,61
C
C   RTERM-EPSLON LESS THAN OR EQUAL ZERO IMPLIES DEPENDENCE
C   RTERM-EPSLON POSITIVE IMPLIES INDEPENDENCE
C
62  DO 63 J=1,NCOL
          TEMP=CTEMP(NROW1,J)
          CTEMP(NROW1,J)=CTEMP(MAX,J)
63  CTEMP(MAX,J)=TEMP
          ITEMP=INDEXR(MAX)
          INDEXR(MAX)=INDEXR(NROW1)

```

```

      INDEXR(NROW1)=ITEMP
      NROW1=NROW1-1
      GO TO 50
61 DO 662 J=1,NCOLM1
662 RCTEMP(I,J)=RCTEMP(I,J)/RTERM
      IF (J-MAX) 66,65,66
66 DO 64 N=1,NCOL
      TEMP=CTEMP(I,N)
      CTEMP(I,N)=CTEMP(MAX,N)
64 CTEMP(MAX,N)=TEMP
      ITEMPT=INDEXR(MAX)
      INDEXR(MAX)=INDEXR(I)
      INDEXR(I)=ITEMPT
65 IF (J-NCOLM1) 67,70,67
67 I=I+1
      GO TO 50
70 CONTINUE
C
C      CONSTRUCTION OF REACTION COEFFICIENT MATRIX AND EQUILIBRIUM
C      CONSTANT VECTOR
C      COMPUTE B INVERSE AND STORE THE RESULT IN CTEMP
C
      CALL INV1 (CTEMP,NCOLM1,70,0,LTEMP,IERR,DET,NPIV,PIV,LPR,LPC)
      IF(IERR) 91,92,91
91 PRINT 2091,IERR
2091 FORMAT (1X,4H IERR,15,5X,36HTROUBLE CONSULT DEFINITION OF IERR )
      GO TO 500
92 DO 80 I=1,NCOLM1
      DO 80 J=1,NROW
      TEMP=0
      DO 81 N=1,NCOLM1
81 TEMP=TEMP+C(J,N)*CTEMP(N,I)
80 RNV(J,I)=TEMP
      DO 85 I=1,NROW
      TEMP=0
      DO 86 J=1,NCOLM1
86 IN=INDEXR(J)
      TEMP=TEMP+RNV(I,J)*G(IN)
      R=1.98726
      RLNK(I)=-1.0/(R*T)*(G(I)-TEMP)
85 RK(I)=EXP(RLNK(I))
C
C      EQUILIBRIUM PROCEDURE
C
199 TEMP=0
      DO 200 I=1,NROW
200 TEMP=TEMP+GAMMA(I)*C(I,NCOL)
      A=P/TEMP
      DO 19 J=1,NROW
19 IVECTR(J)=0
      DO 301 J=1,NCOLM1
      IF (I-INDEXR(J)) 301,400,301
301 CONTINUE
      TEMP=0
      DO 302 J=1,NCOLM1
      IN=INDEXR(J)
      IF (GAMMA(IN)*RNV(I,J)) 307,308,307
308 TERM=0
      GO TO 302
307 TERM=GAMMA(IN)*RNV(I,J)*ALOG(A*C(IN,NCOL))
302 TEMP=TEMP+TERM
      IF (GAMMA(I)) 306,309,306

```

```

309 TERM=0
    GO TO 255
306 TERM=GAMMA(I)*ALOG(A*C(I,NCOL))
255 RLNO=-TEMP+TERM
    RO=EXP(RLNO)
    IF (GAMMA(I)) 303,320,303
303 DO 304 J=1,NCOLM1
    IF (RNV(I,J)) 305,304,305
305 IN=INDEXR(J)
    IF (C(I,NCOL)-0.01*C(IN,NCOL)) 304,304,320
304 CONTINUE

```

C
C
C TREATMENT OF MINOR SPECIES

```

    NMULT=ITER/4
    IF (ITER-NMULT*4) 350,310,350
310 IF (ABS(1-RK(I)/RO)-1.0E-04) 300,300,312
312 ETAP=C(I,NCOL)*RK(I)/RO
    DELTAZ=ETAP-C(I,NCOL)
    CALL FUDGE(I)
    C(I,NCOL)=C(I,NCOL)+DELTAZ
    IVECTR(I)=J
    DO 313 J=1,NCOLM1
    IN=INDEXR(J)
313 C(IN,NCOL)=C(IN,NCOL)-RNV(I,J)*DELTAZ
350 ICONV=0
    GO TO 300

```

C
C
C TREATMENT OF MAJOR SPECIES

```

320 IF (ABS(1-RK(I)/RO)-1.0E-05) 300,300,321
321 IVECTR(I)=2
    IF (GAMMA(I)) 322,323,322
322 TEMP=0
    DO 327 J=1,NCOLM1
    IN=INDEXR(J)
324 TEMP=TEMP+GAMMA(IN)*RNV(I,J)**2/C(IN,NCOL)
327 CONTINUE
    TEMP=TEMP+GAMMA(I)/C(I,NCOL)
333 DELTAZ=(RLNK(I)-RLNO)/TEMP
    CALL FUDGE(I)
340 C(I,NCOL)=C(I,NCOL)+DELTAZ
    DO 325 J=1,NCOLM1
    IN=INDEXR(J)
325 C(IN,NCOL)=C(IN,NCOL)-RNV(I,J)*DELTAZ
    GO TO 350

```

C
C
C CONDENSED PHASE PROCEDURE

```

323 IF (C(I,NCOL)-1.0E-06) 330,330,331
330 IF (RLNK(I)-RLNO) 337,331,331
337 IVECTR(I)=4
    GO TO 300
331 TEMP=0
    IVECTR(I)=3
    DO 334 J=1,NCOLM1
    IN=INDEXR(J)
    IF (C(IN,NCOL)) 332,334,332
332 TEMP=TEMP+GAMMA(IN)*RNV(I,J)**2/C(IN,NCOL)
334 CONTINUE
    IF (C(I,NCOL)) 386,385,386
386 TEMP=TEMP+GAMMA(I)/C(I,NCOL)

```

```

INDEXR(NROW1)=IITEMP
NROW1=NROW1-1
GO TO 50
61 DO 662 J=1,NCOLM1
662 RCTEMP(I,J)=RCTEMP(I,J)/RTERM
IF (I-MAX) 66,65,66
66 DO 64 N=1,NCOL
TEMP=CTEMP(I,N)
CTEMP(I,N)=CTEMP(MAX,N)
64 CTEMP(MAX,N)=TEMP
IITEMP=INDEXR(MAX)
INDEXR(MAX)=INDEXR(I)
INDEXR(I)=IITEMP
65 IF (I-NCOLM1) 67,70,67
67 I=I+1
GO TO 50
70 CONTINUE
C
C CONSTRUCTION OF REACTION COEFFICIENT MATRIX AND EQUILIBRIUM
C CONSTANT VECTOR
C COMPUTE B INVERSE AND STORE THE RESULT IN CTEMP
C
CALL INVI (CTEMP,NCOLM1,70,0,LTEMP,IERR,DET,NPIV,PIV,LPR,LPC)
IF(IERR) 91,92,91
91 PRINT 2091,IERR
2091 FORMAT (1X,4HIFERR,15,5X,36HTROUBLE CONSULT DEFINITION OF IERR )
GO TO 500
92 DO 80 I=1,NCOLM1
DO 80 J=1,NROW
TEMP=0
DO 81 N=1,NCOLM1
81 TEMP=TEMP+C(I,N)*CTEMP(N,I)
80 RNV(J,I)=TEMP
DO 85 I=1,NROW
TEMP=0
DO 86 J=1,NCOLM1
IN=INDEXR(J)
86 TEMP=TEMP+RNV(I,J)*G(IN)
R=1.98726
RLNK(I)=-1.0/(R*T)*(G(I)-TEMP)
85 RK(I)=EXP(RLNK(I))
C
C EQUILIBRIUM PROCEDURE
C
199 TEMP=0
DO 200 I=1,NROW
200 TEMP=TEMP+GAMMA(I)*C(I,NCOL)
A=P/TEMP
DO 19 J=1,NROW
19 IVECTR(J)=0
DO 301 J=1,NCOLM1
IF (I-INDEXR(J)) 301,400,301
301 CONTINUE
TEMP=0
DO 302 J=1,NCOLM1
IN=INDEXR(J)
IF (GAMMA(IN)*RNV(I,J)) 307,308,307
308 TERM=0
GO TO 302
307 TERM=GAMMA(IN)*RNV(I,J)*ALOG(A*C(IN,NCOL))
302 TEMP=TEMP+TERM
IF (GAMMA(I)) 306,309,306

```

```

385 CONTINUE
    IF (TEMP) 333,335,333
335 RMIN=C(I,NCOL)
    DO 380 J=1,NCOLM1
        IN=INDEXR(J)
        IF (RNV(I,J)) 381,380,381
381 IF (RMIN-C(IN,NCOL)/ABS(RNV(I,J))) 380,380,351
351 RMIN=C(IN,NCOL)/ABS(RNV(I,J))
380 CONTINUE
    IF (RLNK(I)) 353,300,354
353 DELTAZ=-RMIN
    GO TO 340
354 DELTAZ=RMIN
    GO TO 340
300 CONTINUE
C
C CHECK IF UPDATING OF BASIS IS NECESSARY
C
    DO 400 J=1,NCOLM1
        IN=INDEXR(J)
        IF (RNV(I,J)) 410,400,410
410 IF (C(I,NCOL)-C(IN,NCOL)) 400,400,420
420 IBASIS=1
400 CONTINUE
    GO TO 20
500 CONTINUE
    GO TO 1
END
SUBROUTINE FUDGE(I)
COMMON NCOLM1,RNV,C,DELTAZ,INDEXR,NCOL
DIMENSION INDEXR(70),C(70,20),RNV(70,20)
IF (C(I,NCOL)+DELTAZ) 1,1,2
1 DELTAZ=-C(I,NCOL)/2.0
2 CONTINUE
    DO 3 J=1,NCOLM1
        IN=INDEXR(J)
        IF(C(IN,NCOL)-RNV(I,J)*DELTAZ) 4,4,3
4 IF (C(IN,NCOL)) 5,6,5
6 DELTAZ=0.0
    GO TO 3
5 DELTAZ=C(IN,NCOL)/(2.0*RNV(I,J))
3 CONTINUE
    RETURN
    END
C N-THE ORDER OF A 7046A023
C 7046A024
SUBROUTINE INVI(A,N,NN,FPS,LTEMP,IERR,DET,NPIV,PIV,LPR,LPC)
DIMENSION A(MN,NN)
DIMENSION LTEMP(1),LPR(1),LPC(1)
C 7046A004
C DECK 7046A 7046A005
C 7046A006
C SUBROUTINES CALLED - NONE 7046A007
C 7046A008
C THIS ROUTINE INVERTS MATRIX A IN ITS OWN SPACE. IT ALSO COMPUTES THE 7046A009
C THE DETERMINANT OF A. 7046A010
C 7046A011
C THE METHOD IS THE USUAL GAUSSIAN EXCHANGE PROCESS. BOTH ROWS AND 7046A012
C COLUMNS ARE SEARCHED FOR MAXIMAL PIVOTS. THERE IS NO UNNECESSARY 7046A013
C INTERCHANGING OF ROWS OR COLUMNS, ALL SUCH INTERCHANGES BEING CARRIED 7046A014
C OUT AFTER THE EXCHANGE PROCESS IS COMPLETE. CHAPTER 1 OF E.L. STIEGLF, 7046A015
C INTRODUCTION TO NUMERICAL MATHEMATICS, ACADEMIC PRESS, N.Y., 1963, SHOULD 7046A016

```


C BE HELPFUL IN FOLLOWING THE CODE.	7046A017
C	7046A018
C THE CALLING PROGRAM MUST SET A,N,NN,EPS,AND LTEMP TO-	7046A019
C	7046A020
C A-THE MATRIX TO BE INVERTED	7046A021
C	7046A022
C NN-THE NUMBER OF WORDS OF STORAGE PROVIDED FOR EACH COLUMN	7046A025
C OF ARRAY A BY THE CALLING PROGRAM	7046A026
C	7046A027
C EPS-A NON-NEGATIVE NUMBER WHICH EACH PIVOT IS REQUIRED TO EXCEED	7046A028
C IN ABSOLUTE VALUE %CUSTOMARILY ZERO<	7046A029
C	7046A030
C LTEMP-A BLOCK OF AT LEAST N WORDS OF TEMPORARY INTEGER STORAGE	7046A031
C	7046A032
C IN ADDITION TO OVERWRITING A WITH ITS INVERSE,THE ROUTINE ALSO SETS	7046A033
C IERR,DET,NPIV,PIV,LPR,AND LPC TO-	7046A034
C	7046A035
C IERR- 0 IF INVERSION IS COMPLETED AND NO TROUBLE IS DETECTED	7046A036
C	7046A037
C 2 IF MAGNITUDE OF CURRENT PIVOT FAILS TO EXCEED EPS	7046A038
C %INVERSION WILL NOT BE COMPLETED<	7046A039
C	7046A040
C DET-PLUS OR MINUS THE PRODUCT OF THE CURRENT AND ALL PREVIOUS	7046A041
C PIVOTS	7046A042
C	7046A043
C NPIV-THE NUMBER OF THE CURRENT PIVOT %FIRST,SECOND,ETC.<	7046A044
C	7046A045
C PIV-THE CURRENT PIVOT	7046A046
C	7046A047
C LPR-THE FIRST NPIV POSITIONS LIST THE PIVOT ROW INDICES IN ORDER	7046A048
C OF USE	7046A049
C	7046A050
C LPC-THE FIRST NPIV POSITIONS LIST THE PIVOT COLUMN INDICES IN	7046A051
C ORDER OF USE	7046A052
C	7046A053
C DO INITIALIZATIONS	7046A054
C	7046A055
IERR=0	
DET=1.0	
DO 2 I=1,N	
LPR(I)=I	
2 LPC(I)=I	
C	
C BEGIN EXCHANGE PROCESS	
C	
DO 17 NP=1,N	
NPIV=NP	
C	
C SELECT PIVOT	
C	
PIV=0.0	
DO 4 K=NP,N	
I=LPR(K)	
DO 4 L=NP,N	
J=LPC(L)	
IF(ABS(A(I,J))-ABS(PIV))4,3,3	
3 KPIV=K	
LPIV=L	
IPIV=I	
JPIV=J	
PIV=A(I,J)	
4 CONTINUE	

```

C
C  UPDATE DETERMINATE AND PIVOT ROW AND COLUMN LISTS
C
      DET=DET*PIV
      ITEMP=LPR(NP)
      LPR(NP)=LPR(KPIV)
      LPR(KPIV)=ITEMP
      JTEMP=LPC(NP)
      LPC(NP)=LPC(LPIV)
      LPC(LPIV)=JTEMP
C
C  EXIT IF PIVOT TOO SMALL
C
      IF(EPS-ABS(PIV))8,7,7
7  IERR=2
   RETURN
C
C  MODIFY PIVOT ROW
C
      DO 9 J=1,N
      9 A(IPIV,J)=-A(IPIV,J)/PIV
C
C  MODIFY OTHER ROWS
C
      DO 14 I=1,N
      IF(I-IPIV)10,14,10
10  TEMP=A(I,JPIV)
      IF(TEMP)11,14,11
11  DO 13 J=1,N
      IF(J-JPIV)12,13,12
12  A(I,J)=A(I,J)+A(IPIV,J)*TEMP
13  CONTINUE
14  CONTINUE
C
C  MODIFY PIVOT COLUMN
C
      DO 15 I=1,N
15  A(I,JPIV)=A(I,JPIV)/PIV
      A(IPIV,JPIV)=-A(IPIV,JPIV)
17  CONTINUE
C
C  END EXCHANGE PROCESS
C
C  UNSCRAMBLE ROWS OF INVERSE AND ADJUST SIGN OF DETERMINANT
C
      DO 18 I=1,N
      L=LPR(I)
18  LTEMP(L)=LPC(I)
      DO 22 I=1,N
19  K=LTEMP(I)
      IF(I-K)20,22,20
20  DET=-DET
      DO 21 J=1,N
      TEMP=A(I,J)
      A(I,J)=A(K,J)
21  A(K,J)=TEMP
      LTEMP(I)=LTEMP(K)
      LTEMP(K)=I
      GO TO 19
22  CONTINUE
C
C  UNSCRAMBLE COLUMNS OF INVERSE

```

```

C
DO 23 J=1,N
L=LPC(I)
23 LTEMP(L)=LPR(I)
DO 27 I=1,N
24 K=LTEMP(I)
IF(I-K)25,27,25
25 DO 26 J=1,N
TEMP=A(J,I)
A(J,I)=A(J,K)
26 A(J,K)=TEMP
LTEMP(I)=LTEMP(K)
LTEMP(K)=K
GO TO 24
27 CONTINUE
RETURN
END
/*
//GO.SYSIN DD *

```

Preceding page blank

APPENDIX D

ALUMINUM OXIDE X-RAY DIFFRACTION PATTERNS

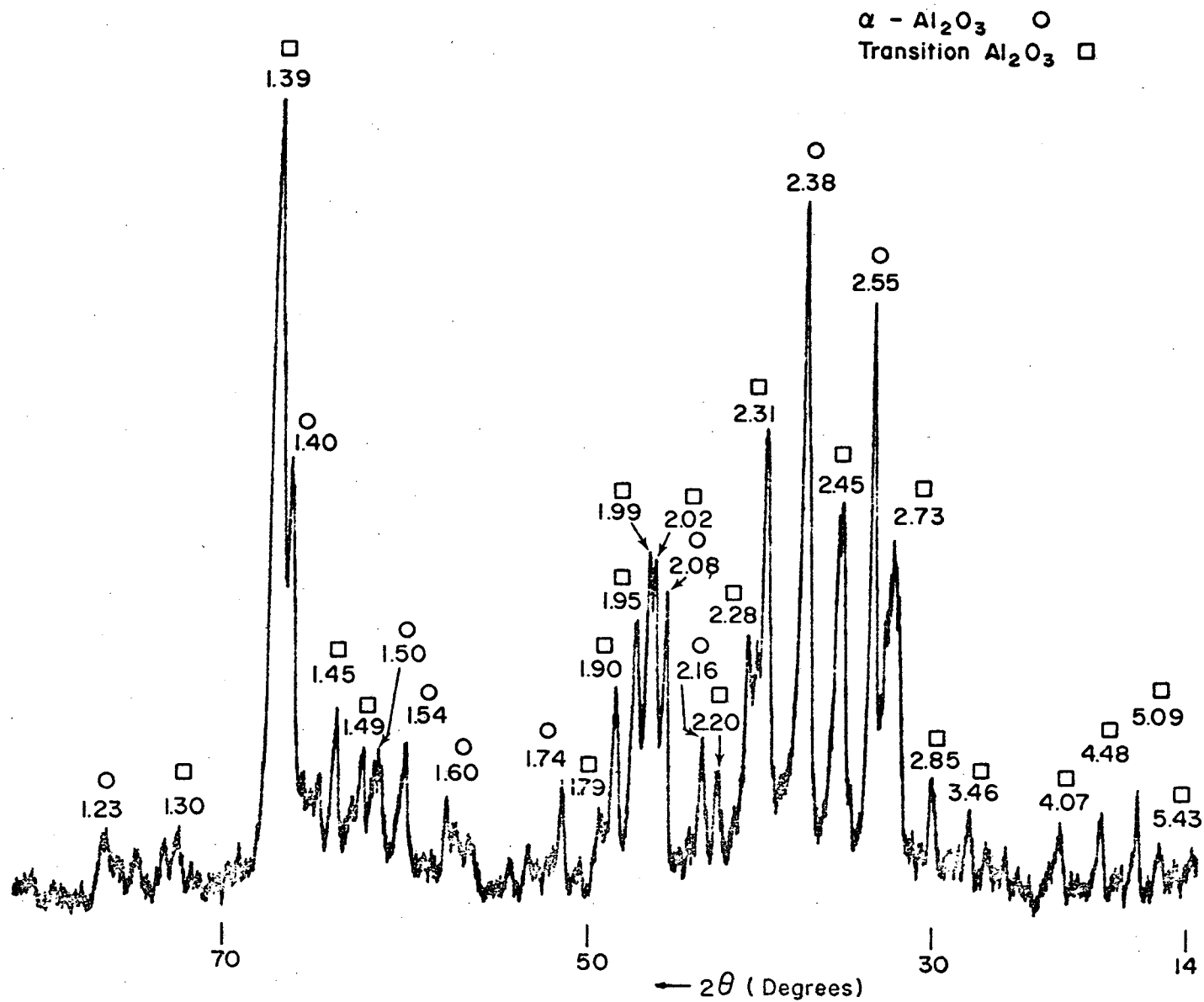


Fig. 79 - X-ray Diffractometer Trace of Vapor Grown Aluminum Oxide Powder from Run VA-10

Table XXXIII X-ray Powder Diffraction Data for Alumina, Run No. VA-10

Line No.	2 θ	d spacing	I	Phase	Line No.	2 θ	d spacing	I	Phase
1	17.2	5.15	M	$\Delta\theta$	21	64.4	1.45	M	K, θ
2	19.7	4.50	S	Δ,γ,N,K,θ	22	65.4	1.43	W	K, θ
3	22.2	4.00	M	Δ	23	67.4	1.39	S	$\alpha,\Delta,\gamma,N,K,\theta$
4	25.2	3.53	W	α,θ	24	72.6	1.30	W	K
5	27.5	3.24	W		25	73.5	1.29	M	Δ,θ
6	29.4	3.04	W	K	26	74.3	1.28	M	
7	31.5	2.84	S	Δ,N,K,θ	27	75.8	1.25	W	Δ,θ
8	33.1	2.70	M	Δ,K,θ	28	76.9	1.24	W	
9	34.6	2.59	S	α,Δ,K,θ	29	77.7	1.23	M	N, θ
10	36.9	2.43	S	Δ,γ,N,K,θ	30	81.9	1.18	W	
11	39.1	2.30	M	Δ,γ,N,K,θ	31	83.9	1.15	W	γ,Δ
12	42.6	2.12	W	α,K,θ	32	85.6	1.13	M	N
13	45.9	1.98	M	Δ,γ,N,K,θ	33	88.5	1.10	W	
14	46.9	1.94	M	Δ,K	34	94.1	1.05	M	
15	48.2	1.89	M	K, θ	35	96.5	1.03	M	γ,N
16	51.0	1.79	W	K	36	99.6	1.01	M	
17	57.4	1.60	W	α,θ	37	101.6	.993	M	
18	60.4	1.53	M	γ,N,θ	38	102.5	.988	W	γ
19	61.7	1.50	M	K	39	104.7	.979	M	
20	62.7	1.48	M	θ	40	108.1	.951	M	
					41	111.2	.934	M	

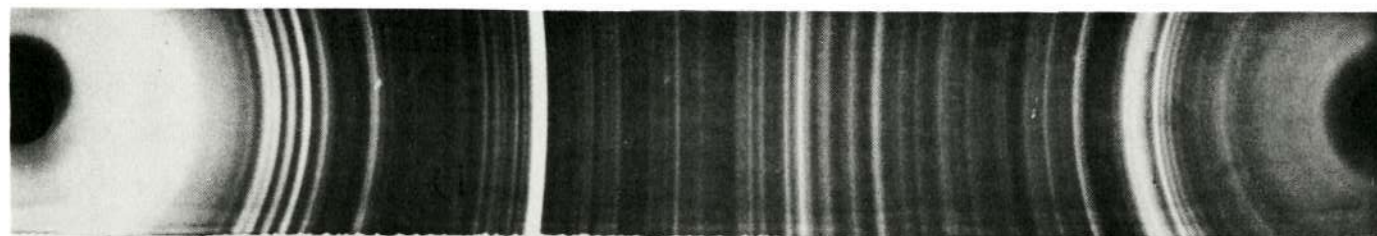


Fig. 80 - X-ray Diffraction Pattern for Alumina, Run VA-10

Reproduced from
best available copy.

Preceding page blank

APPENDIX E

TITANIUM DIOXIDE X-RAY DIFFRACTION PATTERNS

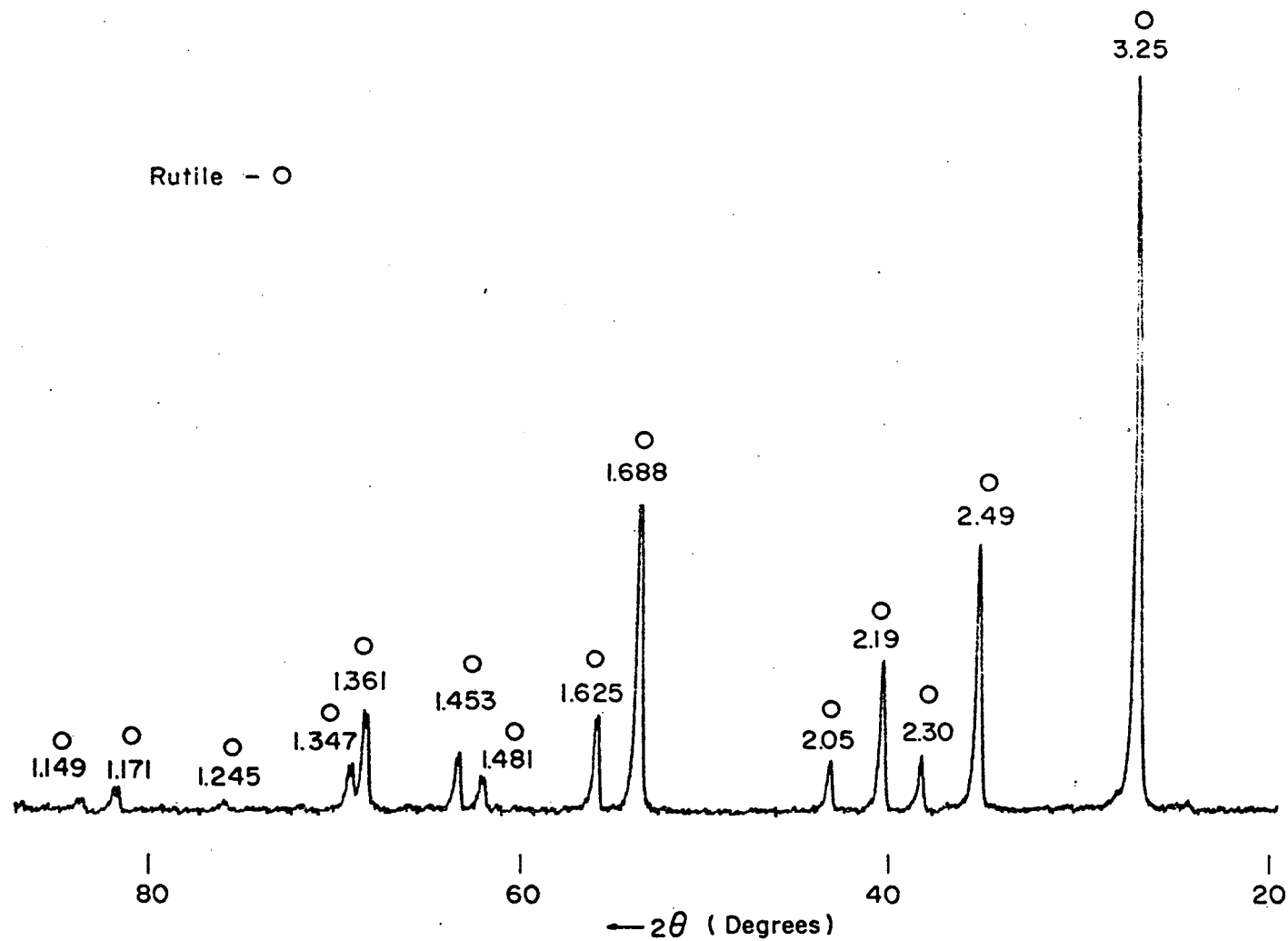


Fig. 81 - X-ray Diffractometer Trace of Vapor Grown Rutile Powder
from Run TiO₂-1

Table XXXIV - X-ray Powder Diffraction Data for Titanium, Run No. TiO₂-1

Line No.	2θ	d spacing	I	Phase	Line No.	2θ	d spacing	I	Phase
1	27.63	3.225	S	TiO ₂	19	95.53	1.040	W	TiO ₂
2	36.28	2.474	M	TiO ₂	20	97.48	1.0246	VW	TiO ₂
3	39.43	2.283	W	TiO ₂	21	106.18	.9633	VW	TiO ₂
4	41.48	2.175	M	TiO ₂	22	116.53	.9056	W	TiO ₂
5	44.23	2.046	W	TiO ₂	23	117.88	.8992	W	TiO ₂
6	45.73	1.982	W	Camera	24	120.28	.8882	M	TiO ₂
7	54.53	1.681	S	TiO ₂	25a	122.88	.8770	M	TiO ₂
8	56.78	1.620	M	TiO ₂	25b	123.63	.8739	W	TiO ₂
9	62.98	1.475	W	TiO ₂	26a	131.88	.8459	W	TiO ₂
10	64.18	1.450	W	TiO ₂	26b	132.58	.8413	VW	TiO ₂
11	69.13	1.357	M	TiO ₂	27a	136.68	.8288	W	TiO ₂
12	69.93	1.344	W	TiO ₂	27b	137.43	.8266	VW	doublet
13	76.63	1.242	VW	TiO ₂	28a	140.08	.8195	M	TiO ₂
14	82.48	1.168	W	TiO ₂	28b	140.98	.8172	W	doublet
15	84.38	1.147	W	TiO ₂	29a	155.78	.7879	VW	
16	87.78	1.111	VW	TiO ₂	30a	162.13	.7797	W	
17	89.73	1.092	W	TiO ₂	30b	163.88	.7779	VW	
18	90.93	1.080	W	TiO ₂					

Fig. 82 - X-ray Diffraction Pattern for Titania, Run TiO₂-1
Reproduced from
best available copy.


Preceding page blank

APPENDIX F

ZINC ORTHOTITANATE X-RAY DIFFRACTION PATTERNS

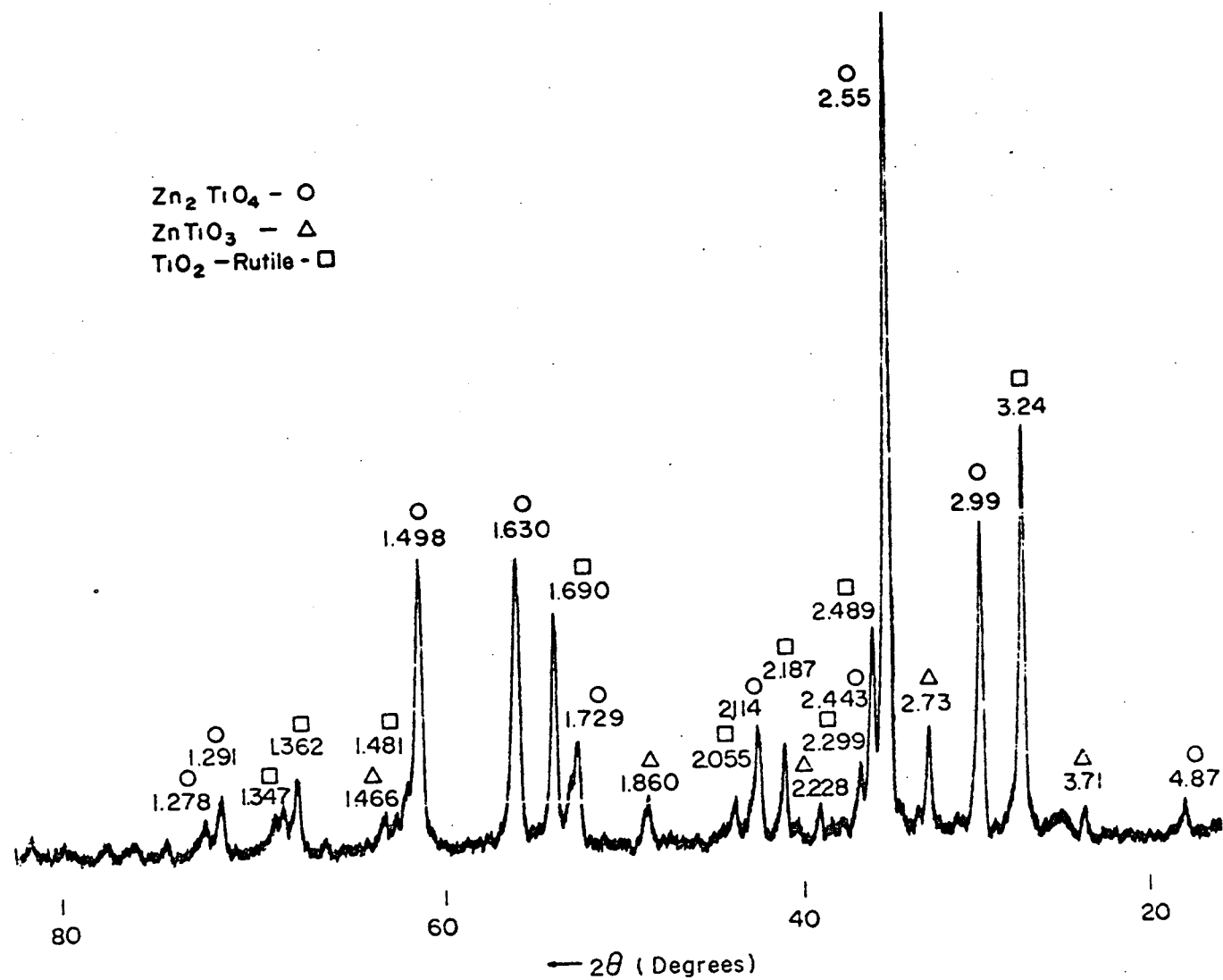


Fig. 83 - X-Ray Diffractometer Trace of Oxides from Run Zn_2TiO_4 -2, Showing Zn_2TiO_4 as the Major Phase

Table XXXV - X-ray Powder Diffraction Data for Zinc Orthotitanate, Run Zn₂TiO₄-1

Line No.	2θ	d spacing	I	Phase	Line No.	2θ	d spacing	I	Phase
1	27.45	3.250	S	TiO ₂	24	85.90	1.133	W	Zn ₂ TiO ₄
2	29.90	2.989	S	Zn ₂ TiO ₄	25	87.45	1.117	VW	TiO ₂ , ZnTiO ₃
3	32.90	2.723	M	ZnTiO ₃	26	88.75	1.103	M	Zn ₂ TiO ₄
4	35.25	2.547	VS	ZnTiO ₃ , Zn ₂ TiO ₄	27	89.40	1.097	VW	TiO ₂
5	36.10	2.489	W	TiO ₂	28	90.70	1.084	VW	TiO ₂
6	39.20	2.299	VW	TiO ₂	29	93.50	1.060	W	Zn ₂ TiO ₄
7	40.70	2.218	VW	ZnTiO ₃	30	95.15	1.045	VW	TiO ₂
8	41.35	2.185	W	TiO ₂	31	97.05	1.030	VW	TiO ₂
9	42.80	2.114	W	Zn ₂ TiO ₄	32	101.20	0.999	W	Zn ₂ TiO ₄
10	44.10	2.055	VW	TiO ₂	33	104.00	0.979	W	Zn ₂ TiO ₄
11	49.00	1.860	W	ZnTiO ₃	34	105.10	0.972	VW	
12	53.05	1.728	M	ZnTiO ₃ , Zn ₂ TiO ₄	35	109.10	0.947	VW	
13	54.40	1.688	S	TiO ₂	36	116.40	0.908	VW	TiO ₂
14	56.55	1.629	S	Zn ₂ TiO ₄ , TiO ₂ , ZnTiO ₃	37	117.30	0.904	VW	
15	62.05	1.497	S	ZnTiO ₃ , Zn ₂ TiO ₄	38	120.35	0.889	W	TiO ₂
16	69.00	1.362	W	TiO ₂	39	122.50	0.880	VW	
17	73.35	1.292	W	Zn ₂ TiO ₄	40	123.30	0.876	VW	TiO ₂
18	74.30	1.278	VW	Zn ₂ TiO ₄	41	126.00	0.866	W	
19	76.60	1.245	VW	TiO ₂	42	131.65	0.846	VW	TiO ₂
20	78.20	1.224	VW	Zn ₂ TiO ₄	43	136.30	0.831	W	TiO ₂
21	79.65	1.205	VW	ZnTiO ₃ , TiO ₂	44	136.90	0.829	VW	TiO ₂
22	82.35	1.172	VW	TiO ₂ , ZnTiO ₃	45	139.70	0.822	S	TiO ₂
23	84.10	1.152	VW	ZnTiO ₃	46	140.50	0.821	VW	TiO ₂

Fig. 84 - X-ray Diffraction Pattern for Zinc Orthotitanate, Run Zn₂TiO₄-1Reproduced from
best available copy.